# GEMS & GEMOLOGY

WINTER 2015
VOLUME LI

THE QUARTERLY JOURNAL OF THE GEMOLOGICAL INSTITUTE OF AMERICA


Pyrope Garnet with Color-Change Phenomenon

The Origin of Montana's Alluvial Sapphires

The Grand Sapphire: Provenance and Properties

In Search of Australian Opal

GEMS & GEMOLOGY

Winter 2015
VOLUME 51, No. 4


pg. 352


pg. 371

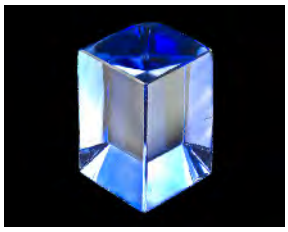
pg. 392


pg. 443

## Editorial



## Feature Articles



## Notes and New Techniques



## Field Reports



## Regular Features

GEMS & GEMOLOGY®

gia.edu/gems-gemology

**Subscriptions**
Copies of the current issue may be purchased for $29.95 plus shipping. Subscriptions are $79.99 for one year (4 issues) in the U.S. and $99.99 elsewhere. Canadian subscribers should add GST. Discounts are available for group subscriptions, GIA alumni, and current GIA students. To purchase print subscriptions, visit store.gia.edu or contact Customer Service. For institutional rates, contact Customer Service.

**Database Coverage**
*Gems & Gemology*'s impact factor is 0.778, according to the 2013 Thomson Reuters Journal Citation Reports (issued July 2014). *G&G* is abstracted in Thomson Reuters products (Current Contents: Physical, Chemical & Earth Sciences and Science Citation Index—Expanded, including the Web of Knowledge) and other databases. For a complete list of sources abstracting *G&G*, go to gia.edu/gems-gemology, and click on "Publication Information."

**Manuscript Submissions**
*Gems & Gemology*, a peer-reviewed journal, welcomes the submission of articles on all aspects of the field. Please see the Author Guidelines at gia.edu/gems-gemology or contact the Managing Editor. Letters on articles published in *G&G* are also welcome. Please note that Field Reports, Lab Notes, Gem News International, and Micro-World entries are not peer-reviewed sections but do undergo technical and editorial review.





*Gems & Gemology* is published quarterly by the Gemological Institute of America, a nonprofit educational organization for the gem and jewelry industry.

Postmaster: Return undeliverable copies of *Gems & Gemology* to GIA, The Robert Mouawad Campus, 5345 Armada Drive, Carlsbad, CA 92008.

Our Canadian goods and service registration number is 126142892RT.




## About the Cover

*The lead article in this issue analyzes the color-change phenomenon displayed by a pink pyrope garnet believed to be of Tanzanian origin. The cover photo shows two pieces of pyrope garnet from Morogoro, Tanzania, that exhibit the reported color-change characteristics. The round "Super Spiral cut" specimen, weighing 15.25 ct, comes from the same material as the 42.42 ct rough nodule. The gems were photographed on a glass tile that provides an organic look to the scene. Photo by Robert Weldon/GIA, courtesy of Meg Berry.*


Printing is by L+L Printers, Carlsbad, CA.
GIA World Headquarters The Robert Mouawad Campus 5345 Armada Drive Carlsbad, CA 92008 USA



ISSN 0016-626X

# **Garnets, Sapphires, Opals,** and Tarnish on High-Purity Gold

Welcome to the final *Gems & Gemology* of 2015. Colored gems—garnet, sapphire, and opal—are prominent in this issue. The Tanzanian garnet on our cover projects a rich, bold pink and demonstrates just how fine this material can be. It's profiled in our lead article. The issue also offers insight into the origin of Montana's alluvial sapphires, a gemological study of the historic Grand Sapphire, an investigation into tarnish spots on high-purity gold, and a field report on Australian opal.

Our first paper—by three of GIA's young research scientists, Ziyin "Nick" Sun, Aaron Palke, and Nathan Renfro—examines interesting "color-change" pyrope garnet from Tanzania. Under fluorescent-equivalent lighting, larger gems have the color of fine purple amethyst, while under incandescent they resemble hot pink tourmaline. The authors provide a comprehensive review of this material's inclusions along with a quantitative analysis of its color under different lighting conditions.

*Amethyst purple under fluorescent-equivalent lighting, hot pink under incandescent...*

Alluvial sapphires from the U.S. state of Montana have long been celebrated for their kaleidoscope of colors, but so far no one has located these gems' primary source rocks. In our second paper, a team of researchers led by Dr. J.C. "Hanco" Zwaan focuses on mineral inclusions and geochemistry to propose a metasomatic origin for Montana's alluvial sapphires.

Next, Dr. François Farges and his colleagues profile the fascinating history and gemology of Louis XIV's 135.74 ct Grand Sapphire, which was added to the French crown jewels in 1669, around the same time as the fabled Tavernier Blue diamond. On the basis of microscopic examination and spectroscopy, the authors suggest that this magnificent blue sapphire originated in Sri Lanka's gem fields.

Our fourth paper investigates unsightly tarnish spots in high-purity (99.9% Au) gold jewelry. Dr. Taijin Lu and his team from the National Gems & Jewellery Technology Administrative Center (NGTC) in Beijing use a combination of advanced techniques to detect the presence of silver and sulfur in the tarnish spots. The authors recommend careful cleaning during the gold manufacturing process to eliminate the possibility of silver contamination.

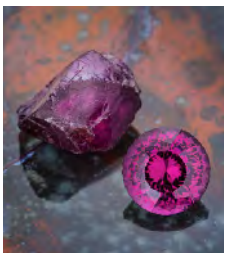

In June 2015, a GIA team consisting of Tao Hsu, Andrew Lucas, and Vincent Pardieu visited four important opal fields at the rugged fringes of Australia's arid Great Artesian Basin: Lightning Ridge, Koroit, Yowah, and Quilpie. Their field report documents mining activity and the growing importance of the revenue and employment brought to these remote outback communities by "opal tourism."

As usual, you'll find our regular Lab Notes and Gem News International sections along with the third installment of the Micro-World column. Our GNI section includes an update from field gemologist Vincent Pardieu on rubies from a new deposit in Zahamena National Park, Madagascar. There are also reports from the 2015 Geological Society of America (GSA) annual meeting in Baltimore, the first International Emerald Symposium in Bogotá, Colombia, and the 34th International Gemological Conference (IGC) in Vilnius, Lithuania.

Finally, you'll notice this issue includes a ballot card for the Dr. Edward J. Gübelin Most Valuable Article Award. We had a fantastic response to our 2014 reader ballot, so please do vote again for your favorite 2015 articles.

Please enjoy the Winter issue!

Duncan Pay | Editor-in-Chief | dpay@gia.edu

# VANADIUM- AND CHROMIUM-BEARING PINK PYROPE GARNET: CHARACTERIZATION AND QUANTITATIVE COLORIMETRIC ANALYSIS

Ziyin Sun, Aaron C. Palke, and Nathan Renfro

A type of pink pyrope garnet containing vanadium and chromium, believed to have been mined in Tanzania, appeared at the 2015 Tucson shows. The material shows a noticeable color difference from purplish pink under incandescent light (A) to purple under daylight-equivalent light (D65). This study reports a quantitative analysis of the difference in color between the two lighting conditions, based on the use of high-quality visible absorption spectroscopy to calculate CIELAB 1976 colorimetric coordinates. L*, a*, and b* colorimetric parameters were calculated for a wide range of path lengths as extrapolated from visible absorption spectra of thinner samples. Using this method, the path length of light through the stone that produces the optimal color difference can be calculated. This path length can then be used to determine the optimal depth range to maximize color change for a round brilliant of a specific material. The pink pyrope studied here can be designated as "color-change" garnet according to certain classification schemes proposed by other researchers. In many of these schemes, however, the material fails to exceed the minimum requirements for quantitative color difference and hue angle difference to be described as "color-change." Nonetheless, there is no simple solution to the problem of applying color coordinates to classify color-change phenomena. Also presented is a method by which spectra can be corrected for reflection loss and accurately extrapolated to stones with various path lengths.

Garnets are a group of isometric nesosilicates with the general chemical formula $X_3Y_2Z_3O_{12}$. X, Y, and Z represent dodecahedral, octahedral, and tetrahedral sites in the crystal structure, respectively. Natural rock-forming silicate garnets with the Z-site occupied by $Si^{4+}$ are commonly divided into the pyralspite and ugrandite groups. In pyralspite, $Al^{3+}$ occupies the Y-site and the X-site may contain $Mg^{2+}$, $Fe^{2+}$, or $Mn^{2+}$; these garnets are dominantly composed of the pyrope ($Mg_3Al_2Si_3O_{12}$), almandine ($Fe^{2+}{}_3Al_2Si_3O_{12}$), and spessartine ($Mn_3Al_2Si_3O_{12}$) end members. The ugrandite garnets have $Ca^{2+}$ on the X-site and $Cr^{3+}$, $Al^{3+}$, or $Fe^{3+}$ on the Y-site, giving uvarovite ($Ca_3Cr_2Si_3O_{12}$), grossular ($Ca_3Al_2Si_3O_{12}$), or andradite ($Ca_3Fe^{3+}{}_2Si_3O_{12}$) end members. Stockton and Manson (1985) proposed a classification scheme for separating the pyralspite group into the gemological species of pyrope, almandine, spessartine, pyrope-almandine, pyrope-spessartine, and almandine-spessartine. Previously, two types of color-change garnets have been reported: pyrope with very high $Cr^{3+}$ (Hysingjord, 1971; Carstens, 1973; Amthauer, 1975) and pyrope-spessartine containing both $Cr^{3+}$ and $V^{3+}$ (Crowningshield, 1970; Jobbins et al., 1975; Schmetzer and Ottemann, 1979; Manson and Stockton, 1984; Johnson and Koivula 1998; Krzemnicki et al., 2001; Schmetzer et al., 2009). $Cr^{3+}$-bearing pyrope, however, has not been observed in sizes large enough for faceting. In the trade, almost all color-change garnets are referred to as pyrope-spessartine.

A noticeable and attractive color change under

See end of article for About the Authors and Acknowledgments.
GEMS & GEMOLOGY, Vol. 51, No. 4, pp. 348–369,
http://dx.doi.org/10.5741/GEMS.51.4.348.

*Figure 1. An interesting type of pink pyrope garnet, probably mined in Morogoro, Tanzania, is shown under incandescent light A (left) and daylight-equivalent light $D_{65}$ (right). A noticeable difference in color can be seen. Left to right: a 2.51 ct modified round brilliant faceted by Todd Wacks, a 7.61 ct modified round brilliant faceted by Meg Berry, a 13.09 ct modified round brilliant faceted by Todd Wacks, and 31.90 ct and 6.00 ct rough. The 2.51 ct and 13.09 ct faceted stones were included as part of this study. Photos by Robert Weldon/GIA.*

different lighting conditions (i.e., daylight vs. incandescent light) significantly increases the value of a gem, and the decision of whether to apply the "color-change" descriptor is becoming a more important consideration in the trade. The two major systems established to quantitatively analyze color are CIE 1931 (developed in 1931 by the Commission Internationale de l'Éclairage) and CIELAB 1976 (published by the commission in 1976). They have been used to study color-change behavior of pyrope-spessartine garnets from Madagascar (Krzemnicki et al., 2001; Schmetzer et al., 2009). Both articles emphasized that color difference and hue angle difference under various lighting conditions are the most important factors affecting the strength of a stone's color change (see "Colorimetric Parameters in CIELAB 1976 Color Circle" below).

An interesting observation made after inspecting several faceted stones is that this pink pyrope garnet appears to show a more noticeable "color change" in larger stones. The phenomenon of color-change under a constant lighting but with varying light path length is known as the Usambara effect (Halvorsen and Jensen, 1997; Halvorsen, 2006). Björn (2002) used colorimetric calculations to quantitatively predict the color change caused by the Usambara effect in tourmaline, alexandrite, and color-change garnet. The underlying cause is the relative difference between two transmission windows in the visible absorption spectrum with changing path length.

As noted by previous studies, the presence of two transmission windows in the visible absorption spectrum is also the fundamental cause of a color change under different lighting conditions. Therefore, we sought to determine how a change in path length influences the color difference and hue angle difference under two lighting conditions and how this relates to the greater difference in color seen in the larger pyropes from this study. Liu et al. (1999b) quantitatively calculated the change of hue angle difference under daylight-equivalent light ($D_{65}$) and incandescent light (A) in a gem tourmaline with varying thickness from the Umba Valley, Tanzania. Liu et al. (1999b) suggested that this tourmaline should only be considered a color-change stone within a certain range of path lengths. Schmetzer et al. (2013) studied a synthetic alexandrite crystal and analyzed the relationship between the "alexandrite effect" and the Usambara effect in this pleochroic mineral with varying thickness. To shed more light on this phenomenon, we have carried out a detailed quantitative study of the influence of path length on color difference and hue angle difference under both lighting conditions for three different garnets. In doing so, we developed a new method to correct the UV-Vis-NIR spectra for reflection loss so that spectra for stones with a short path length could be accurately extrapolated to longer path lengths.

## MATERIALS AND METHODS

**Samples.** Twenty-three stones with inclusions provided by Todd Wacks, Jason Doubrava, Jeff Hapeman, and Meg Berry, some of which are shown in figure 1, were used to identify typical inclusions in this material. Among the samples were 21 rough pieces, ranging from 4.04 to 31.90 ct, and two faceted stones weighing 13.88 ct and 13.09 ct. Additionally,

**TABLE 1.** Chemical composition of pyrope and pyrope-spessartine samples by LA-ICP-MS.

| | Pyrope 3 | Pk1 | Pyrope 11 | Pyrope 6 | Pyrope 8 | Pyrope 9 | Pyrope 5 | Pyrope 7 | Pyrope 10 | Bl1 | Gr1 |
|---|---|---|---|---|---|---|---|---|---|---|---|
| |  |  |  |  |  |  |  |  |  |  |  |
| Carat weight | 12.26 | 2.63 | 2.51 | 0.29 | 0.36 | 0.67 | 1.41 | 1.02 | 14.79 | 0.70 | 0.86 |
| ppmw of different elements | | | | | | | | | | | |
| Mg | 125,000 | 124,000 | 121,000 | 117,000 | 118,000 | 117,000 | 120,000 | 120,000 | 123,000 | 83,800 | 62,100 |
| Ca | 16,700 | 18,400 | 18,400 | 15,800 | 15,100 | 15,500 | 19,200 | 18,100 | 15,000 | 14,300 | 26,100 |
| Mn | 45,400 | 45,800 | 43,200 | 57,700 | 57,700 | 57,800 | 42,000 | 36,700 | 51,300 | 134,000 | 163,000 |
| Fe | 32,500 | 34,300 | 33,800 | 31,600 | 32,400 | 31,800 | 35,600 | 41,200 | 31,400 | 18,600 | 15,600 |
| Al | 128,000 | 132,000 | 134,000 | 133,000 | 133,000 | 132,000 | 132,000 | 136,000 | 133,000 | 124,000 | 119,000 |
| Cr | 845 | 897 | 697 | 450 | 468 | 476 | 850 | 877 | 615 | 2210 | 708 |
| V | 1430 | 1490 | 1350 | 947 | 979 | 981 | 1430 | 1220 | 1010 | 5740 | 5830 |
| Si | 197,000 | 191,000 | 192,000 | 191,000 | 191,000 | 192,000 | 194,000 | 191,000 | 192,000 | 183,000 | 181,000 |
| Ti | 358 | 386 | 360 | 299 | 274 | 283 | 362 | 280 | 206 | 453 | 715 |
| wt.% oxides, converted from LA-ICP-MS | | | | | | | | | | | |
| MgO | 20.73 | 20.56 | 20.07 | 19.40 | 19.57 | 19.40 | 19.90 | 19.90 | 20.40 | 13.90 | 10.30 |
| CaO | 2.34 | 2.57 | 2.57 | 2.21 | 2.11 | 2.17 | 2.69 | 2.53 | 2.10 | 2.00 | 3.65 |
| MnO | 5.86 | 5.91 | 5.58 | 7.45 | 7.45 | 7.46 | 5.42 | 4.74 | 6.62 | 17.30 | 21.05 |
| FeO | 4.18 | 4.41 | 4.35 | 4.07 | 4.17 | 4.09 | 4.58 | 5.30 | 4.04 | 2.39 | 2.01 |
| $Al_2O_3$ | 24.19 | 24.94 | 25.32 | 25.13 | 25.13 | 24.94 | 24.94 | 25.70 | 25.13 | 23.43 | 22.48 |
| $Cr_2O_3$ | 0.12 | 0.13 | 0.10 | 0.07 | 0.07 | 0.07 | 0.12 | 0.13 | 0.90 | 0.32 | 0.10 |
| $V_2O_3$ | 0.21 | 0.22 | 0.20 | 0.14 | 0.14 | 0.14 | 0.21 | 0.18 | 0.15 | 0.84 | 0.86 |
| $SiO_2$ | 42.14 | 40.86 | 41.08 | 40.86 | 40.86 | 41.08 | 41.50 | 40.86 | 41.08 | 39.15 | 38.72 |
| $TiO_2$ | 0.06 | 0.06 | 0.06 | 0.05 | 0.05 | 0.05 | 0.06 | 0.05 | 0.03 | 0.08 | 0.12 |
| Total | 99.83 | 99.68 | 99.32 | 99.37 | 99.55 | 99.40 | 99.43 | 99.38 | 100.45 | 99.41 | 99.29 |
| mol.% end members | | | | | | | | | | | |
| Pyrope | 72.90 | 72.64 | 70.94 | 68.95 | 69.43 | 68.92 | 70.66 | 70.42 | 72.12 | 51.54 | 38.90 |
| Grossular | 4.69 | 5.22 | 5.43 | 4.84 | 4.59 | 4.72 | 5.61 | 5.32 | 4.48 | 1.12 | 6.08 |
| Spessartine | 11.76 | 11.86 | 11.23 | 15.08 | 15.07 | 15.08 | 10.92 | 9.55 | 13.30 | 36.38 | 45.26 |
| Almandine | 8.28 | 5.66 | 8.65 | 7.93 | 7.57 | 7.97 | 9.09 | 10.14 | 6.56 | 4.02 | 4.01 |
| Uvarovite | 0.35 | 0.37 | 0.29 | 0.19 | 0.20 | 0.20 | 0.35 | 0.37 | 0.26 | 0.96 | 0.31 |
| Goldmanite | 0.73 | 0.76 | 0.69 | 0.49 | 0.50 | 0.50 | 0.73 | 0.63 | 0.51 | 3.07 | 3.18 |
| Schorlomite-Al | 0.16 | 0.17 | 0.16 | 0.13 | 0.12 | 0.13 | 0.16 | 0.13 | 0.09 | 0.21 | 0.34 |
| Remainder[a] | 1.15 | 3.33 | 2.63 | 2.42 | 2.53 | 2.50 | 2.50 | 3.47 | 2.68 | 2.73 | 1.94 |
| Total | 100.00 | 100.00 | 100.01 | 100.01 | 100.00 | 100.00 | 100.01 | 100.01 | 100.00 | 100.01 | 100.00 |

[a] *The "remainder" in the end-member components is what is left over after assigning all the atoms to a stoichiometric garnet formula. This value is related to analytical error in the chemical measurements.*

eight rough pyrope specimens, ranging from 0.29 to 14.79 ct, and one 2.51 ct faceted pyrope modified round brilliant were provided by Mr. Wacks for chemical analysis. One blue (Bl1) and one green (Gr1) faceted pyrope-spessartine garnet were selected from the authors' own collection (table 1) for colorimetric analysis, along with one of the rough pink pyrope samples used for chemical analysis (Pk1). A total of 11 stones underwent chemical analysis as part of this study. According to Mr. Wacks, this material may have been mined some 30 years ago in Morogoro, Tanzania (Pay, 2015), and could represent the material documented by Stockton (1988).

**Standard Gemological Properties.** This study began when GIA's Carlsbad laboratory received a 2.51 ct transparent purple pink modified round brilliant stone for scientific examination (pyrope 11 in table

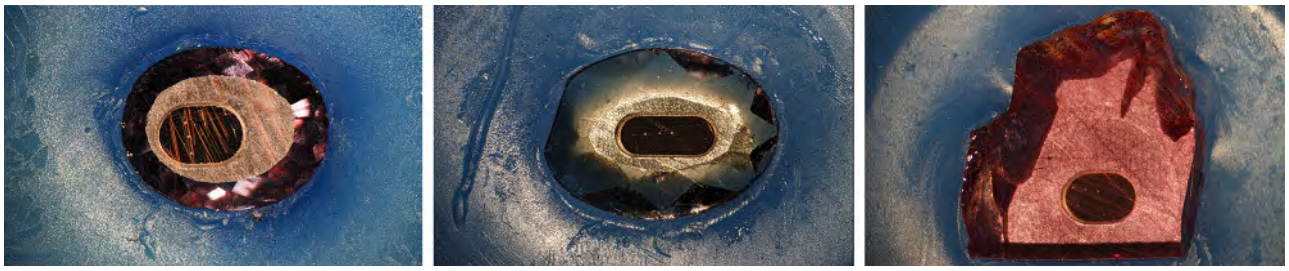

*Figure 2. Three flat wafers with two parallel polished surfaces were prepared and attached in wax to collect UV-Vis-NIR spectra. Wafer Bl1 (left, 1.478 mm in thickness) showed the most intersecting rutile needles in the optical path. Gr1 (middle, 1.416 mm in thickness) showed the fewest interfering rutile needles. The density of the rutile needles blocking the aperture in Pk1 (right, 3.500 mm in thickness) was intermediate between Bl1 and Gr1. Three laser ablation marks are shown in the center of the wafers through the aperture. Photos by Nathan Renfro; fields of view: 11.58 mm (left), 12.17 mm (center), and 14.58 mm (right).*

1). Standard gemological testing revealed a refractive index (RI) of 1.736 and no birefringence. The specific gravity (SG), obtained hydrostatically, was 3.75. No fluorescence was observed under either long-wave (LW) or short-wave (SW) UV light. Using a handheld spectroscope, weak absorption lines were observed in the blue and violet section—a 505 nm absorption line, and very weak absorption bands at 520 and 573 nm. Microscopic examination showed intersecting long and short needles throughout. All of these properties were consistent with pyrope garnet based on the gemological classification system devised by Stockton and Manson (1985). The stone exhibited a noticeable difference in color between incandescent light and daylight-equivalent light.

## In Brief

- Vanadium, chromium, and manganese are responsible for the presence of two visible-light transmission windows in a particular type of pink pyrope garnet. This is the cause of the color difference seen under daylight-equivalent light (D65) and incandescent light (A).
- This material has lower concentrations of vanadium, chromium, and manganese than normal color-change pyrope-spessartine, and a much higher pyrope component. These cause the unique color properties.
- There should be a range of path lengths (sizes) with which the garnet shows the best color change. Below or above this range, the saturation is too low or the hue angle change or saturation change is too small to produce an observable color change.
- There is no unique and simple solution to the problem of classifying color-change stones based on their CIELAB color coordinates, as the entire concept of "color change" is inherently subjective.

**Photomicrography.** The rough stones were fabricated to wafers with parallel windows using standard lapidary equipment, which oriented the inclusions in the best possible position for photomicrography. Photomicrographs were taken using various Nikon microscopes, including an Eclipse LV100, SMZ1500, and SMZ10 (Renfro, 2015a).

**Raman Spectroscopy Analysis.** Raman spectra were collected with a Renishaw inVia Raman microscope system. The Raman spectra of the inclusions were excited by a Stellar-REN Modu Ar-ion laser producing highly polarized light at 514 nm and collected at a nominal resolution of 3 $cm^{-1}$ in the 2000–200 $cm^{-1}$ range. Each spectrum of the inclusions was accumulated three times at 20× or 50× magnification. In many cases the confocal capabilities of the Raman system allowed inclusions beneath the surface to be analyzed. Several other stones were polished to expose the inclusion to the surface.

**LA-ICP-MS Analysis.** The chemical composition for each sample, listed in table 1, was obtained with a ThermoFisher X-series II ICP-MS coupled with a New Wave Research UP-213 laser ablation unit with a frequency-quintupled Nd:YAG laser (213 nm wavelength) running at 4 ns pulse width. NIST (National Institute of Standards and Technology) glass standards SRM 610 and 612 and USGS (United States Geological Survey) glass standards BHVO-2G, BIR-1, NKT-1G, and BCR-2 were used for external calibration. Ablation was achieved using a 55 µm diameter laser spot size, a fluence of around 10 $J/cm^2$, and a 15 Hz repetition rate. The garnets were initially internally standardized with $^{29}Si$ using an educated guess based on the EDXRF analyses. The data was converted to wt.% oxides and normalized to 100 wt.%

and then converted back to ppmw. The ppmw concentration of $^{29}Si$ obtained in this manner was then used for internal standardization to recalculate the chemical compositions. The ppmw values obtained in this final calculation were identical within <1% to those obtained after normalizing to 100 wt.% with the guessed value of $^{29}Si$ used for internal standardization, demonstrating the validity of this method. We selected six spots on each pyrope sample for general chemical composition. For the three garnet wafers on which we collected UV-Vis spectra (Pk1, Bl1, and Gr1; see table 1 and figures 2 and 13), the LA-ICP-MS analyses were performed in the same region where the spectroscopic data was collected. The EDXRF data agreed with the LA-ICP-MS analyses, generally within 5–10%.

**Energy-Dispersive X-Ray Fluorescence (EDXRF) Analysis.** In addition to LA-ICP-MS, the composition of three garnet wafers (Bl1, Gr1, and Pk1) was analyzed on an ARL Quant'X EDXRF analyzer from Thermo Electron Corporation. USGS glass NKT-1G was used for external calibration.

**UV-Vis-NIR Spectroscopy.** Three garnets (samples Bl1, Gr1, and Pk1) were prepared as wafers with parallel polished surfaces and various thicknesses (figure 2). UV-Vis-NIR spectra were collected with a Hitachi U-2910 spectrometer. The spectra were collected in the 190–1100 nm range with a 1 nm spectral resolution at a scan speed of 400 nm/min.

## RESULTS AND DISCUSSION

**Microscopic Internal Characteristics.** The pink pyrope garnets studied here contain a wide range of inclusions in addition to their interesting color properties. An example is the 13.88 ct faceted pyrope in figure 3, which exhibits a black inclusion that can be seen through the table.

Quartz, apatite, sulfides, graphite, rutile, fingerprint-like inclusions, growth tubes, and negative crystals were observed. Surface features—etch markings and trigons—were also visible. Each type of mineral inclusion was identified by Raman spectroscopy.

**Quartz.** Quartz is a common inclusion in the pink pyrope garnets from this study. Pyrope-rich garnet is in general associated with magnesium-bearing basic rocks from the lower crust to the upper mantle. In figure 4A, the morphology of a small colorless transparent quartz crystal with conspicuous surface markings appears to be constrained by step-like growth of the garnet's (110) faces. This crystal is also surrounded by very fine rutile needles, rendering a pseudohexagonal contour. This syngenetic crystal showed strong birefringent color under polarized lighting (figure 4B). In figure 4C, some yellowish foreign mineral (possibly goethite, dolomite, or a limonitic mineral) and a tiny black prism (possibly hematite, ilmenite, or senaite) were captured by a transparent quartz crystal. Under polarized lighting, the mineral-filled area showed strong birefringent color (figure 4D). No Raman signal could be obtained for this material, but large clusters of quartz crystal with similar yellowish foreign mineral filler were observed in another stone (figure 4E and 4F). In figure 4G, a very large quartz crystal shows a hexagonal crystal habit. Large quartz crystals with irregular shape were also found (figure 4H). Quartz is also a prevalent mineral inclusion in other garnets such as almandine, umbalite (mainly composed of pyrope and spessartine with small amounts of almandine, lacking color change), and color-change pyrope-spessartine garnet (Gübelin and Koivula, 2005).

*Figure 3. A black inclusion with a whitish tension halo rim, likely graphite, was observed under the table facet of the 13.88 ct modified cushion brilliant. The presence of the inclusion makes the stone a collector's piece. The cut stone, faceted by Meg Berry, is shown along with a 43.30 ct rough nodule provided by Jason Doubrava. Photo by Robert Weldon.*

**Apatite and Other Phosphate Minerals.** Apatite and other phosphate minerals have been found in rhodolite, almandine, spessartine, umbalite, and color-change pyrope-spessartine (Gübelin and Koivula, 2005). To isolate the weak apatite Raman scattering signal from the pink garnet host studied here, a bluish

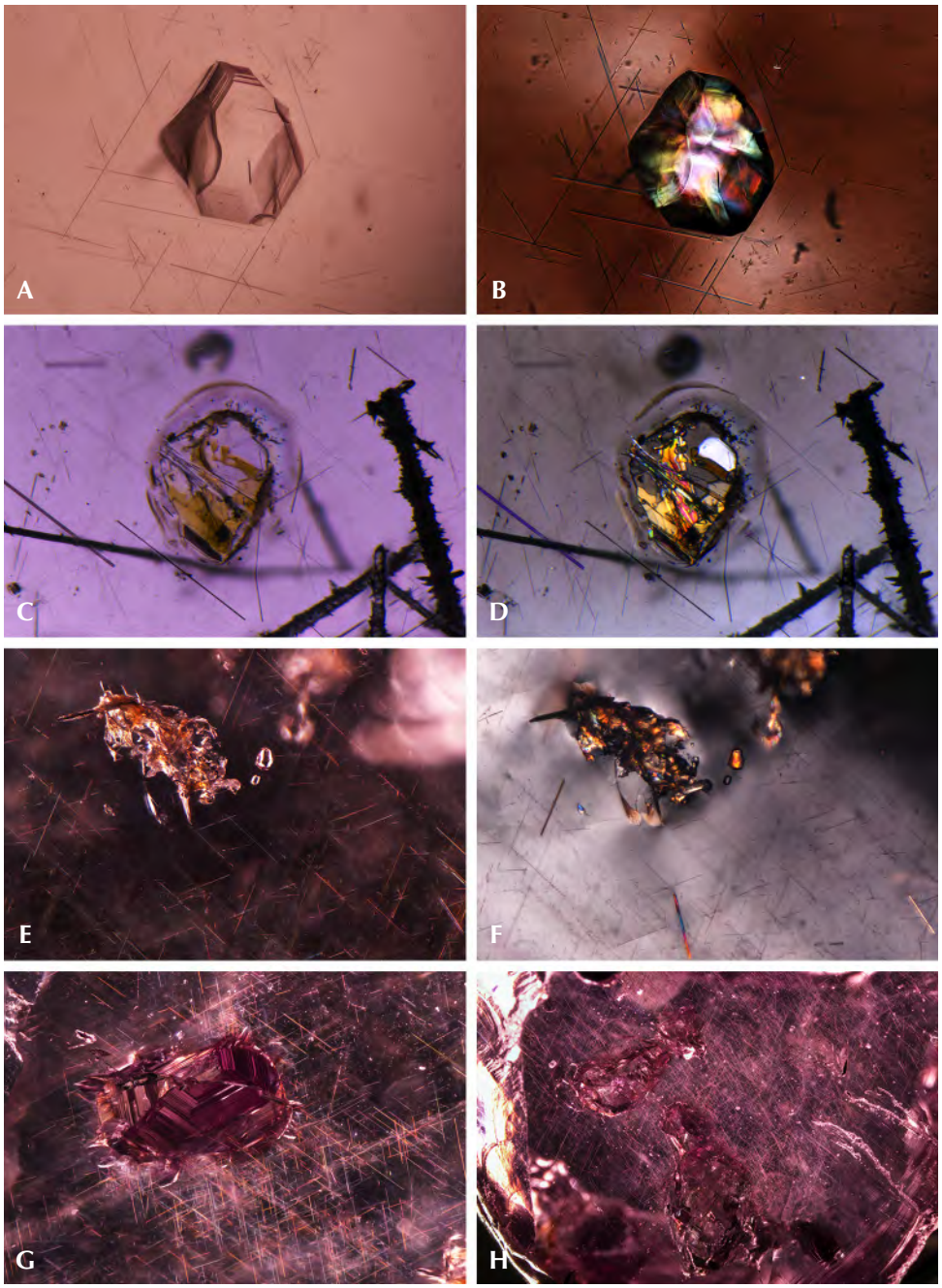


*Figure 4. A: Transparent quartz crystal with sharp euhedral crystal faces under diffused transmitted lighting. B: The same crystal with bright interference colors under cross-polarized lighting. C: Quartz crystal filled with foreign yellowish material under diffused transmitted lighting. D: The foreign yellowish material showed interference colors under cross-polarized lighting. E: Cluster of quartz crystals with foreign yellowish material under darkfield illumination. F: The quartz host and foreign yellowish material both showed interference colors under cross-polarized light. G: The hexagonal geometry of a large quartz crystal became very distinct under darkfield illumination. H: Two large quartz crystals with irregular shape under darkfield illumination. Fields of view: 0.62 mm (A and B), 1.92 mm (C and D), 1.99 mm (E and F), 2.34 mm (G), and 7.19 mm (H). Photomicrographs Ziyin Sun (A and B), Nathan Renfro (C and D), and Jonathan Muyal (E–H).*

hexagonal prismatic apatite crystal was partially polished through to reach the surface (figure 5A). The outline of the crystal was distinct under polarized lighting (figure 5B). Figures 5C and 5D show a group of rounded apatite crystals whose morphology suggests they were partially corroded before being captured by the garnet. An extremely large euhedral apatite crystal showed a greenish yellow bodycolor (figure 5E) with a fingerprint-like halo extending around its perimeter. Another whitish mineral gave an unidentifiable Raman spectrum, which nonetheless seemed to share many similarities with Raman spectra of other phosphate minerals (figure 5F).

**Sulfides.** Sulfide crystals are another very common mineral inclusion in these pink pyrope garnets. Raman spectroscopy was inconclusive, even when the inclusions were polished to the surface; the closest match was for chalcocite, although other sulfides and sulfosalts gave reasonable matches as well. Figure

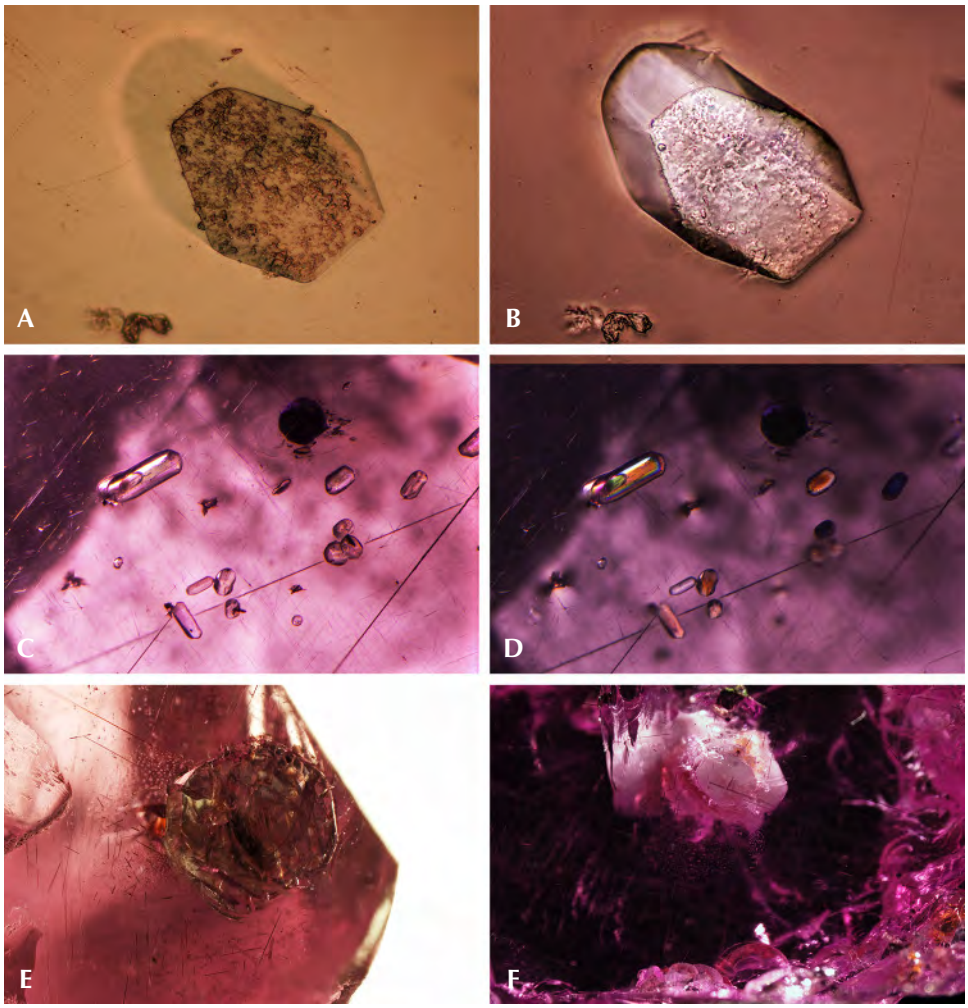


*Figure 5. A: This bluish apatite crystal, shown in reflected lighting and weak diffused transmitted lighting, displays a hexagonal crystal outline where it breaks the surface. B: The entire shape of the same crystal is distinct under cross-polarized lighting. C: This group of rounded apatite crystals is shown under diffused transmitted lighting. D: All the crystals in 5C showed interference colors under cross-polarized lighting. E: This large greenish yellow tabular apatite crystal with a liquid fingerprint extending from it is seen in diffused transmitted and fiber-optic lighting. F: A large opaque whitish phosphate mineral under darkfield illumination. Fields of view: 0.25 mm (A and B), 2.52 mm (C and D), 4.92 mm (E), and 7.19 mm (F). Photomicrographs Ziyin Sun (A, B, and E), Nathan Renfro (C and D), and Jonathan Muyal (F).*

6A shows a rounded sulfide crystal that was partially exposed and showed a metallic luster under reflected light. The depression next to the crystal suggests that there was originally another sulfide crystal. The crystal outline is distinct under darkfield illumination (figure 6B). All the sulfides showed a reddish reflected color when illuminated by a fiber-optic light from the side of the wafer (figure 6C, 6D, and 6E), although this may represent the red color of the light transmitted through the garnet. Some of these inclusions have associated fingerprint-like inclusions showing birefringent color under cross-polarized lighting (figure 6F and 6G), and many are surrounded by clusters of rutile needles (figure 6F). An orange iron oxide mineral is also associated with fractures near some of these sulfide inclusions (figure 6F). The flow lines next to the rutile cluster on the top part of figure 6G may be the result of excess titanium in the mineralization environment, which causes $TiO_2$ to precipitate and coalesce as "silk" as the garnet cools.

**Graphite.** Black tablets of graphite represent one of the more frequent inclusions of the pink pyrope garnets in this study. The partially exposed graphite crystal in figure 7A showed a dull luster. The outline of the crystal and a surrounding tension halo became distinct under darkfield illumination (figure 7B). Some of the graphite showed a very uniform layered pseudohexagonal crystal structure (figure 7C). The whitish tension halo is always present around the graphite (figure 7C). The presence of graphite suggests a relatively high-grade metamorphic formation process. It is also a frequent guest mineral in almandine and color-change pyrope-spessartine. The common association of V-bearing gem material with graphite, as found in this pink pyrope in many gem-bearing metamorphic deposits from East Africa (e.g., tanzanite and tsavorite), is of interest.

**Rutile.** Strong fiber-optic lighting revealed a three-dimensional network of (presumably) rutile needles and unknown mineral platelets that showed flashes of iri-

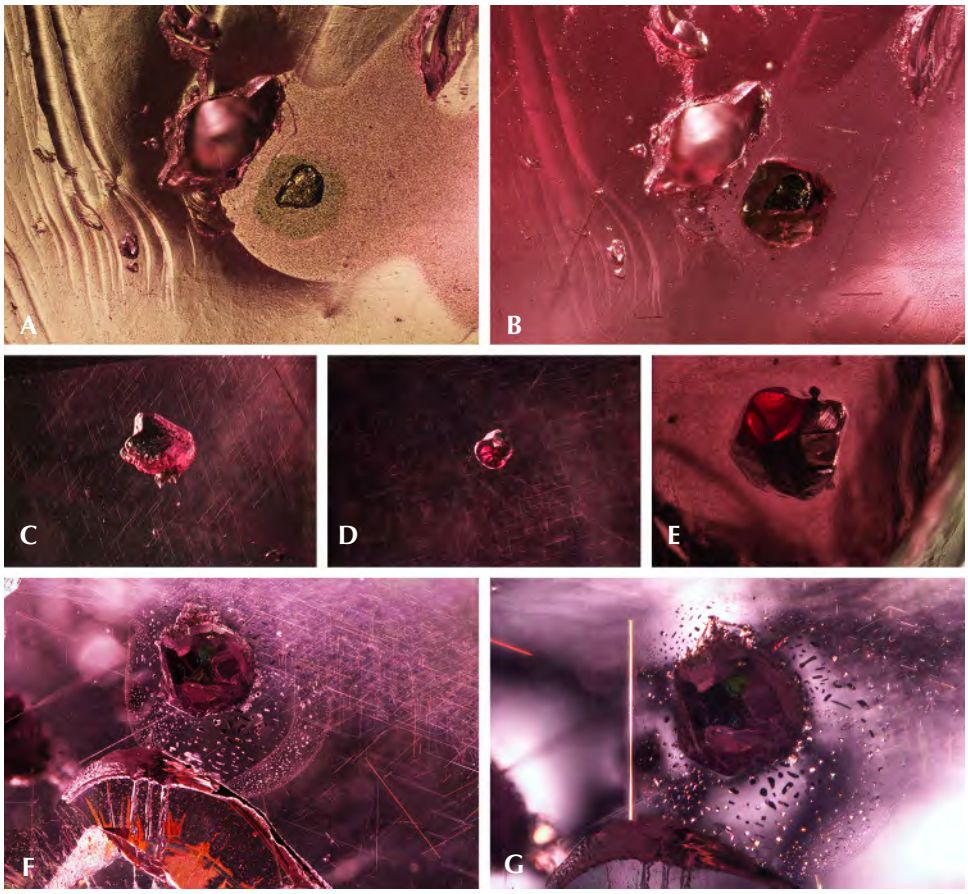


*Figure 6. A: An opening next to a surface-reaching sulfide crystal, shown under reflected lighting and weak transmitted lighting. B: The outline of the crystal became distinct under darkfield illumination. C, D, and E: These sulfides showed reddish color when illuminated with strong fiber-optic lighting from the side. F: This well-formed sulfide crystal with extended partially healed tension halo is shown under darkfield and fiber-optic illumination. G: Fingerprint-like inclusions in the partially healed tension halo displayed birefringent color under cross-polarized lighting. Fields of view: 2.47 mm (A and B), 2.96 mm (C and D), 5.85 mm (E), 3.57 mm (F), and 2.85 mm (G). Photomicrographs by Ziyin Sun (A, B, and E), Aaron C. Palke, (C and D), and Jonathan Muyal (F and G).*

descent color (figure 8A). The slender needles appeared to outline the edges of a rhombododecahedron (probably aligned along <110>). Under cross-polarized lighting, the needles showed birefringent color (figure 8B). One blocky rutile crystal that presented itself along a fracture surface appeared to have a metallic luster under reflected lighting (figure 8C). Observing this mineral from the opposite side revealed how it would look like as an inclusion in a stone (figure 8D). This blocky rutile crystal appeared black and opaque.

**Fingerprint-Like Inclusions.** Fingerprint-like fluid inclusions are common features in the pyrope garnets. In figure 9A, a large secondary inclusion plane is

*Figure 7. A: This graphite crystal with tension halo is shown under reflected lighting and weak diffused transmitted lighting. B: The outline of the same black graphite crystal became distinct under darkfield illumination. C: The layered structure of the graphite inclusion is visible under diffused fiber-optic lighting. Fields of view: 1.24 mm (A and B) and 0.62 mm (C). Photomicrographs by Jonathan Muyal and Ziyin Sun.*

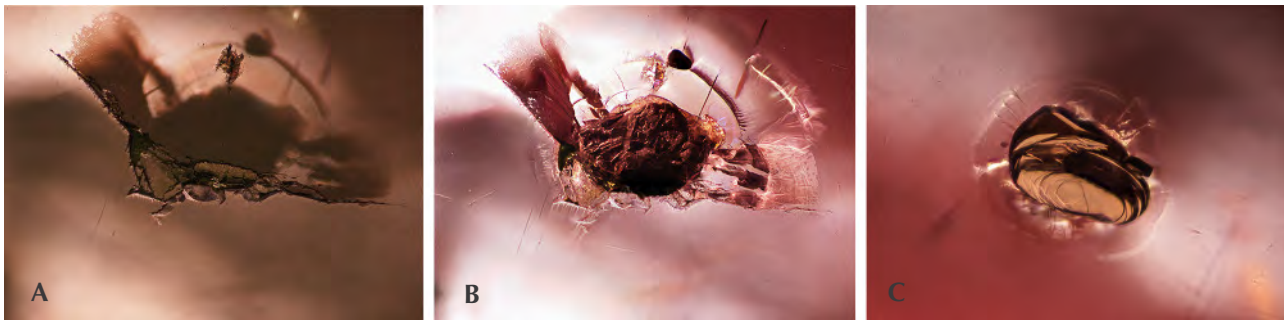

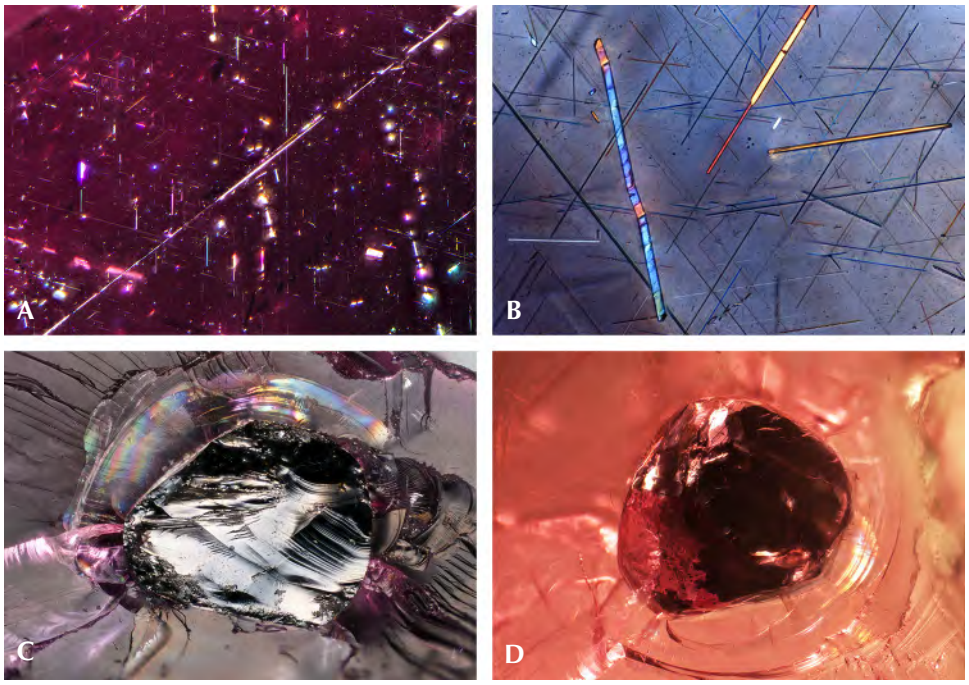


*Figure 8. A: Iridescent intersecting rutile needles under fiber-optic illumination. B: Three needle-like mineral inclusions showing birefringent color under cross-polarized lighting. C: A large rutile crystal breaking the surface shows a metallic luster under reflected lighting. D: The same crystal observed from the opposite side under darkfield illumination. Fields of view: 3.48 mm (A), 0.62 mm (B), and 2.47 mm (C and D). Photomicrographs by Nathan Renfro (A), Jonathan Muyal (B), and Ziyin Sun (C and D).*

partly filled by some foreign material, possibly quartz. Viewed in cross-polarized light, the inclusions appear to show birefringent colors, suggesting the presence of some mineral phase that presumably precipitated from the fluid that originally occupied a partially healed fracture plane (figure 9B). The interference colors in this photomicrograph are all of low intensity, and the image is quite dark. The picture immediately takes on an array of vivid colors with the insertion of the first-order red compensator (figure 9C; see Koivula, 1984; Renfro, 2015a).

**Growth Tubes and Negative Crystals.** These pink pyrope garnets are also characterized by the presence of many hollow tubes whose sides appear to be confined by the crystal structure. It is possible that rutile or another needle-like mineral inclusion originally occupied these spaces but was later dissolved. Alternatively, these could be growth tubes caused by some defect in the crystal lattice that blocked garnet growth in a specific zone while the bulk of the garnet continued to grow around it, resulting in a hollow tube. Many of the hollow tubes were later filled with epigenetic yellowish limonitic material (figure 10, left). Some tabular rounded negative crystals were also observed (figure 10, right). Those voids do not show an interference color under cross-polarized lighting and are thus probably filled with some fluid or vapor phase.

*Figure 9. A: Partially healed fingerprint-like inclusions under diffused transmitted lighting. B: The same inclusion under polarized lighting. C: The same inclusion under polarized lighting with insertion of the first-order red compensator. Field of view: 3.16 mm. Photomicrographs by Nathan Renfro.*

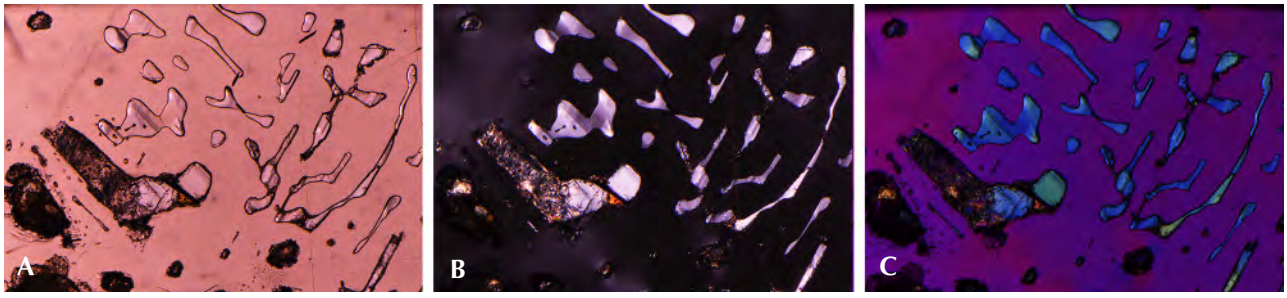

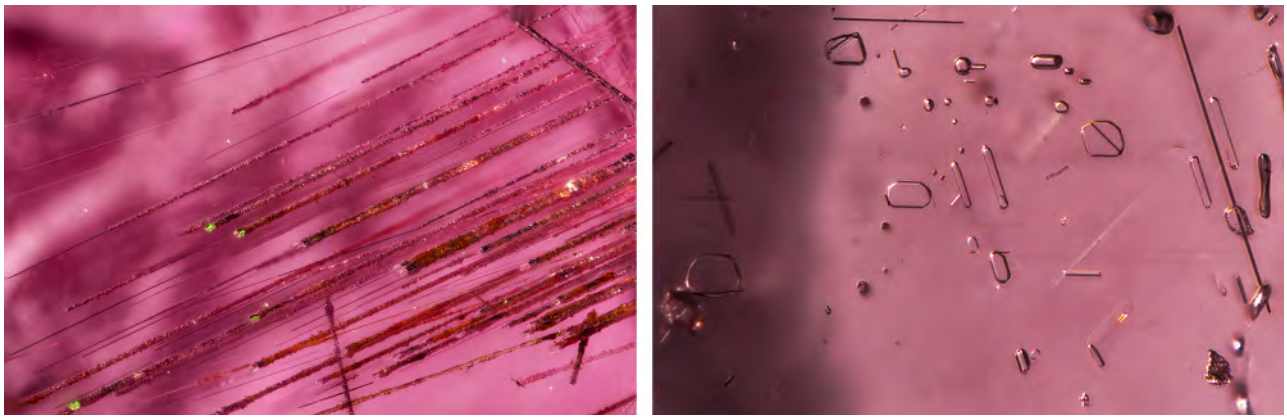

*Figure 10. Left: Hollow growth tubes filled with limonitic iron compound minerals, viewed in diffused transmitted and fiber-optic illumination. Right: Rounded negative crystals and voids viewed in diffused transmitted illumination. Fields of view: 4.33 mm (left) and 1.26 mm (right). Photomicrographs by Nathan Renfro (left) and Jonathan Muyal (right).*

**Surface Features: Etch Markings and Trigons.** Unusual slightly rounded and circuitous channels were observed on the surface of one piece of pink garnet rough. To our knowledge, such a pattern has not been described in garnet or any other gem material. One possible explanation is that a larger piece of garnet broke along a large secondary fluid inclusion plane, and the pattern left by the fluid inclusion plane was corroded and rounded, ultimately forming the channels seen in figures 11A and 11B. Other fresh pink pyrope surfaces show trigon-shaped depressions that can be effectively imaged using episcopic differential interference contrast (DIC), as shown in figure 11C (see also Koivula, 2000; Renfro, 2015b). The formation process of those large trigons is still unknown, although such features are presumed to be caused by late-stage dissolution or etching.

*Figure 11. A: Numerous channels on the surface of a garnet rough under diffused reflected lighting. B: The same channels, seen at higher magnification under diffused reflected lighting. C: An episcopic differential interference contrast (DIC) image of large trigons on the surface of a garnet rough under reflected lighting. Fields of view: 5.98 mm (a), 4.79 mm (b), and 0.62 mm (c). Photomicrographs by Nathan Renfro.*

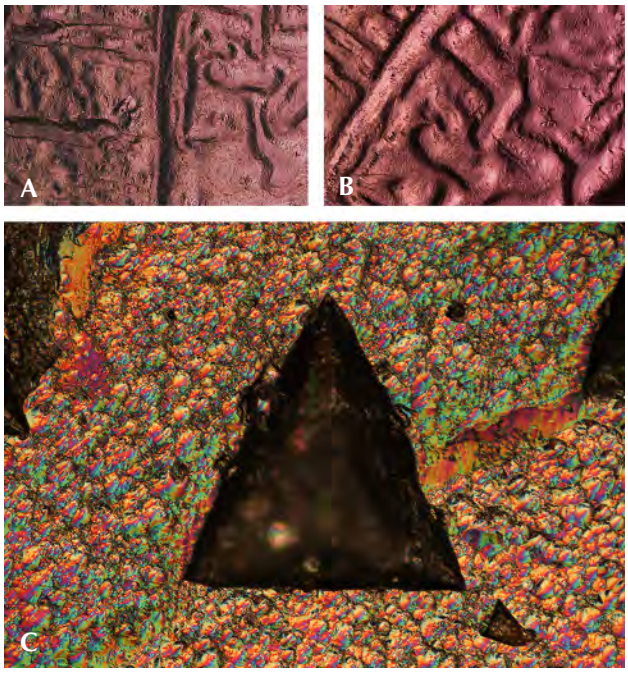


The inclusions observed suggest that this pink pyrope garnet is a product of high-grade metamorphic formation processes. Weak to strong corrosion probably also occurred sometime after the crystal growth, likely after peak metamorphic conditions.

**Chemical Analysis.** Table 1 shows the chemical composition of nine pyrope and two pyrope-spessartine garnets, expressed as ppmw (parts per million by weight), oxide percent by weight (as derived from ppmw values from LA-ICP-MS measurements; other trace elements are not reported here), and mole percent end members (mol.%), calculated using the spreadsheet method of Locock (2008). We conclude that this type of pink pyrope garnet has the following end-member composition: pyrope 68.92–72.90 mol.%, grossular 4.48–5.61 mol.%, spessartine 9.55–15.08 mol.%, almandine 5.66–10.14 mol.%, uvarovite 0.19–0.37 mol.%, and goldmanite 0.49–0.76 mol.%. The composition of two pyrope-spessartine garnets (Bl1 and Gr1) is also listed for comparison in table 1. As a secondary check on the

accuracy of the LA-ICP-MS results, the composition of the three garnet wafers (Bl1, Gr1, and Pk1) was also analyzed by EDXRF. The EDXRF results generally agreed with the LA-ICP-MS measurements within 5–10% for the elements listed in table 1.

**Visible Absorption Spectrum Analysis.** Accurate visible spectroscopic measurement relies on correctly identifying the spectral baseline. This is especially true in the present study, where spectra for stones with long path lengths were produced by multiplying the spectrum collected from thin wafers (approximately 1–4 mm) by an appropriate factor. In this case, the baseline must be carefully corrected to avoid amplifying any errors inherent in fitting the baseline.

Absorbance, A, in our UV-Vis-NIR spectra is the sum of $A_c$ (chromophore light loss), $A_{rl}$ (reflection light loss, surface of the gem), and $A_{isl}$ (inclusion-scattering light loss). An equation can be written simply as

$$A = A_c + A_{rl} + A_{isl} \qquad (1)$$

Samples Bl1, Gr1, and Pk1 were polished into wafers with thicknesses of 1.478, 1.416, and 3.500 mm, respectively. After UV-Vis-NIR spectra were collected (red traces in figure 12), the three wafers were further polished down to thicknesses of 0.906, 0.842, and 2.278 mm. UV-Vis-NIR spectra were collected on the thinner wafers (green traces in figure 12). When the short path length traces are subtracted from the long path length traces, the resulting spectra (blue traces in figure 12) have the $A_{rl}$ reflection light loss removed because $A_{rl}$ is expected to be the same regardless of the stone's thickness. These spectra, corrected for reflection light loss, correspond to path lengths equal to the difference between the long and short path lengths for each stone. Now we can use these reflection-corrected spectra to produce the spectra of any desired path length by multiplying by an appropriate constant. We can also calculate the spectra of the reflection light loss (purple traces in figure 12) by renormalizing the reflection-corrected spectra to the original path lengths and taking the difference between the corrected and uncorrected spectra, as discussed below.

The baselines of the reflection-corrected spectra are not equal to 0 at 850 nm, which would be expected with an absolutely perfect correction. The magnitude of the residual baseline correlates with the relative amount of rutile inclusions observed in the garnets, with Bl1 having the highest concentration and Gr1 the

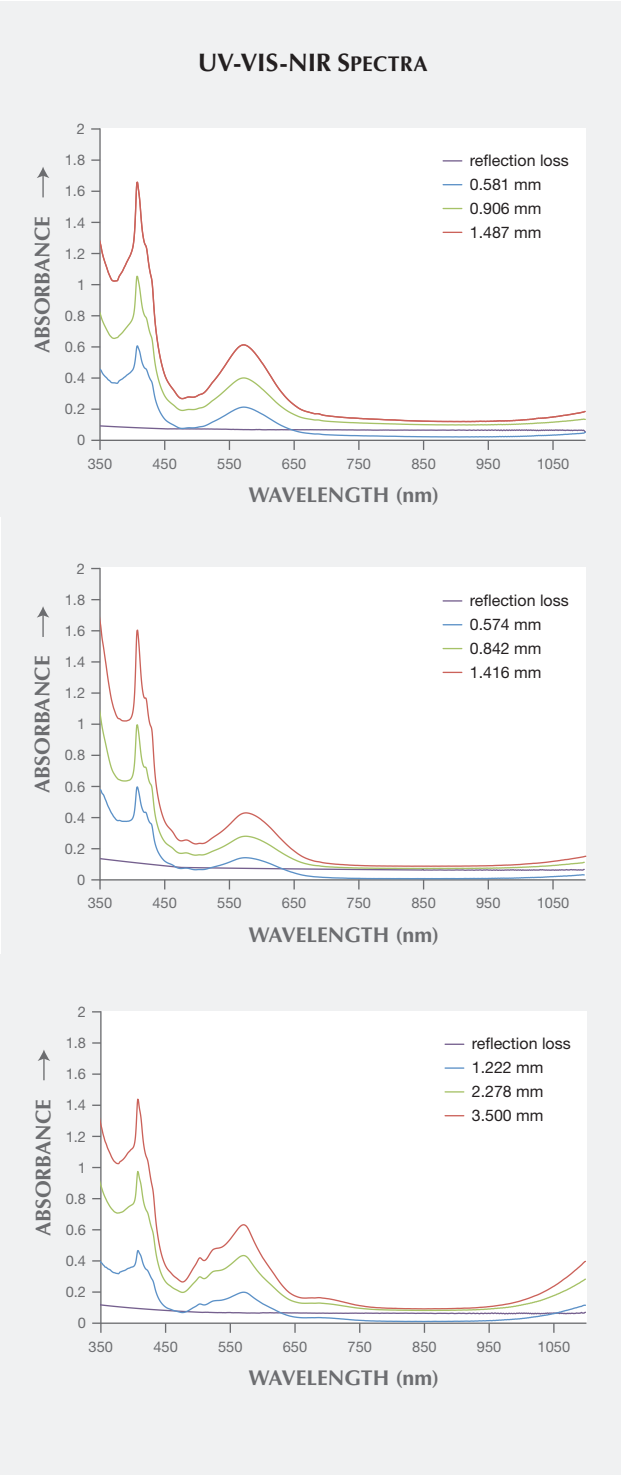


*Figure 12. For samples Bl1 (top), Gr1 (middle), and Pk1 (bottom), the red traces are the absorption spectra for the wafer. The green traces are the absorption spectra for the same wafer polished down to a thickness of 0.906, 0.842, and 2.278 mm. The blue traces are the absorption spectra created by subtracting the green traces from the red traces. Finally, the purple traces are the spectra of the reflection light loss.*


*Figure 13. These photos show polished wafers under daylight-equivalent light (top) and incandescent light (bottom). Left to right: Samples Bl1 (1.487 mm thick), Gr1 (1.416 mm thick), and Pk1 (3.500 mm thick). Composite photo by Robison McMurtry.*

lowest. Thus, we can conclude that the residual baseline is mainly caused by inclusion-scattering absorption ($A_{isl}$ in equation 1). Note that no attempt is made to correct the spectra for $A_{isl}$. If we assume that light scattering particles are evenly distributed and have uniform orientation, size, and shape within a certain stone, then the magnitude of this term is expected to be dependent on the thickness of the stone. While this assumption will not be strictly correct for most gem materials, a more rigorous correction for $A_{isl}$ is not feasible at the moment, and will probably not have a significant impact on the results.

The calculated visible spectra for samples Bl1, Gr1, and Pk1 share many of the same features, as shown in figures 13 and 14. The absorption bands at 410, 422, and 430 nm are caused by $Mn^{2+}$, while those at 504 and 521 nm are caused by $Fe^{2+}$ (Moore and White, 1972). A wide absorption band between 550 and 600 nm is caused by contributions from both $Cr^{3+}$ and $V^{3+}$ (Geiger et al., 2000). Sample Bl1 shows two transmission windows: Window A lies in the red section from 650 to 700 nm; window C, with its transmission maximum at 477 nm, lies in the blue section of the spectrum (figure 14). Sample Gr1 shows the same transmission window in the red section of the spectrum (window A), but the higher-energy transmission window is more open to wavelengths of light in the green section, with its transmission maximum at 510 nm (window B). The red transmission window for Pk1 is wider than for the other two samples. The higher-energy window has a transmission maximum at 477 nm, similar to Bl1, but with more transmission in the higher-energy (violet) section due to the lower $Mn^{2+}$ content (again,

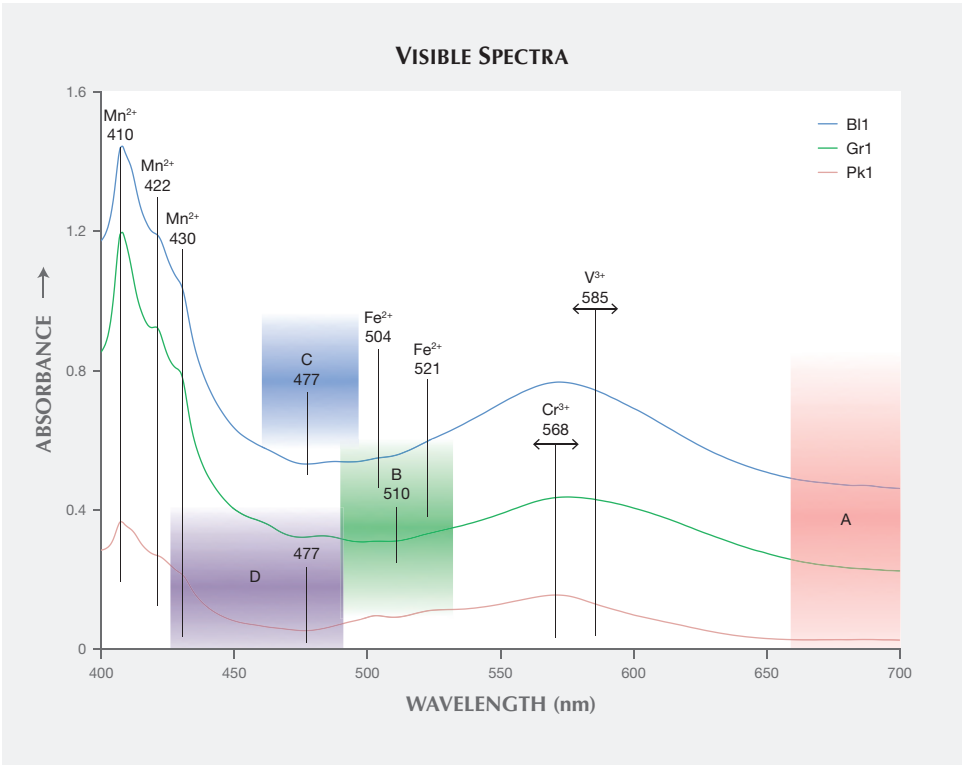


*Figure 14. The calculated visible absorption spectra of three garnets with 1 mm thickness revealed absorption bands at 410, 422, and 430 nm caused by $Mn^{2+}$; absorption bands at 504 and 521 nm caused by $Fe^{2+}$; and a wide absorption band between 550 and 600 nm caused by $Cr^{3+}$ and $V^{3+}$. Transmission windows A, B, C, and D are labeled. The green trace and the blue trace are offset by 0.2 and 0.4 absorbance units, respectively.*

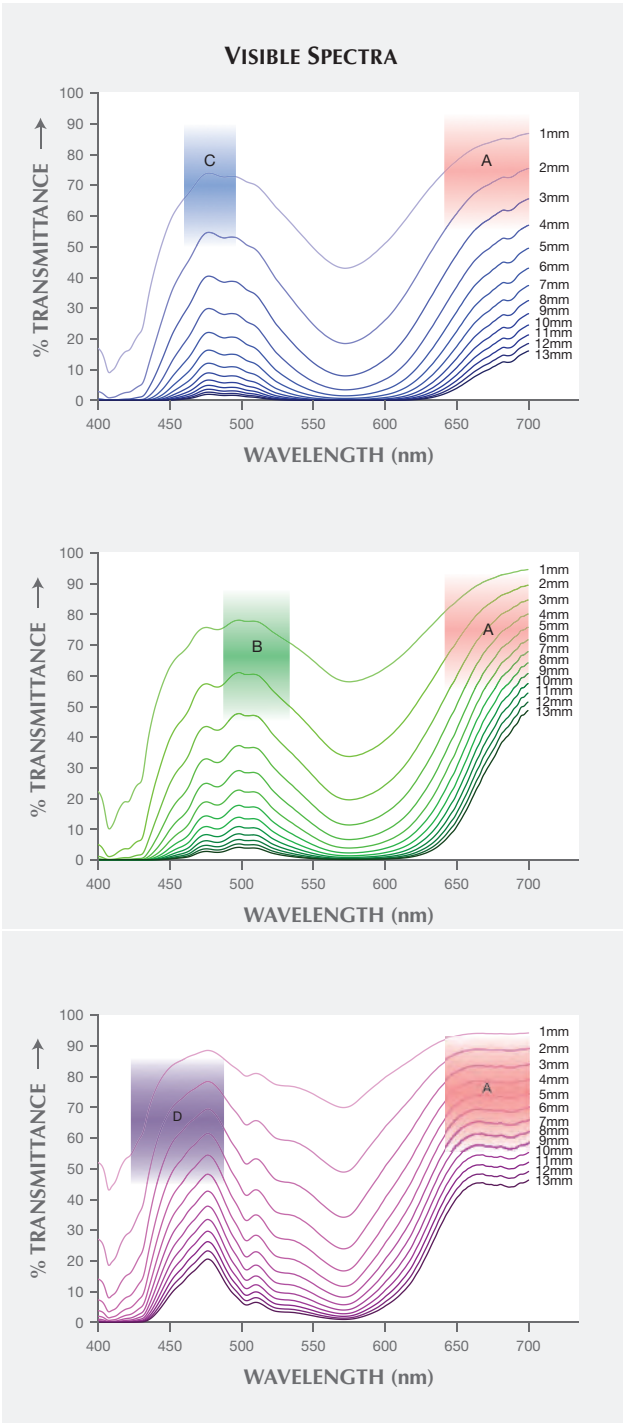


*Figure 15. Top: Visible transmission spectra of Bl1 with path length from 1 to 13 mm; transmission windows A and C become smaller with increasing wafer thickness. Middle: Visible transmission spectra of Gr1 with path length from 1 to 13 mm; transmission windows A and B become smaller with increasing wafer thickness. Bottom: Visible transmission spectra of Pk1 with path length from 1 to 13 mm; transmission windows A and D become smaller with increasing wafer thickness.*

see figure 14). The transmission windows described here are similar to those mentioned by Schmetzer et al. (2009).

## SPECTRUM AND COLORIMETRIC DATA ANALYSIS

**Visible Transmission Spectra.** The spectra of three garnets were converted to transmission spectra with path lengths from 1 to 13 mm by multiplying the spectra by an appropriate value ($l/l_0$, where "l" is the desired path length and "$l_0$" is the path length of the reflection-corrected spectrum—0.581 mm, 0.574 mm, and 1.222 mm for Bl1, Gr1, and Pk1, respectively). For all samples, the transmission windows became smaller as the path length increased (figure 15). CIELAB 1976 L*, a*, b* color space coordinates were calculated for each spectrum under incandescent and daylight-equivalent light with the GRAMS software using the relative spectral power distribution of CIE standard illuminant $D_{65}$ and A, and CIE 1931 2° standard observer (CIE, 2004).

**Colorimetric Parameters in CIELAB 1976 Color Circle.** Thorough discussions of the principles behind the CIELAB 1976 color circle have appeared elsewhere (CIE, 2004; Schmetzer et al., 2009). Therefore, we present a brief introduction and direct the reader to other sources for more detailed explanations.

The color circle has three axes in a three-dimensional space. L* represents lightness and is perpendicular to the plane of the paper. A low L* value signifies a darker color, a high value a lighter color. The variables a* and b* lie in the plane of the paper and define a two-dimensional Cartesian coordinate system that represents the different colors and color saturations possible within the color circle. The coordinates a* and b* can also be converted to polar coordinates $C^*_{ab}$ and $h_{ab}$.

The variable $C^*_{ab}$ represents chroma or saturation, and a higher $C^*_{ab}$ value means a more saturated color. It is calculated by the equation

$$C^*_{ab} = \sqrt{a^{*2}+b^{*2}}$$

The hue angle, $h_{ab}$, is calculated by the equation

$$h_{ab} = \arctan(a^*/b^*)$$

Variations in $h_{ab}$ cause changes in hue, starting from purple-red at 0°, yellow at 90°, bluish green at 180°, and blue at 270°.

Finally, $E^*_{ab}$ signifies the geometric distance of a specific L*a*b* color coordinate in three-dimensional

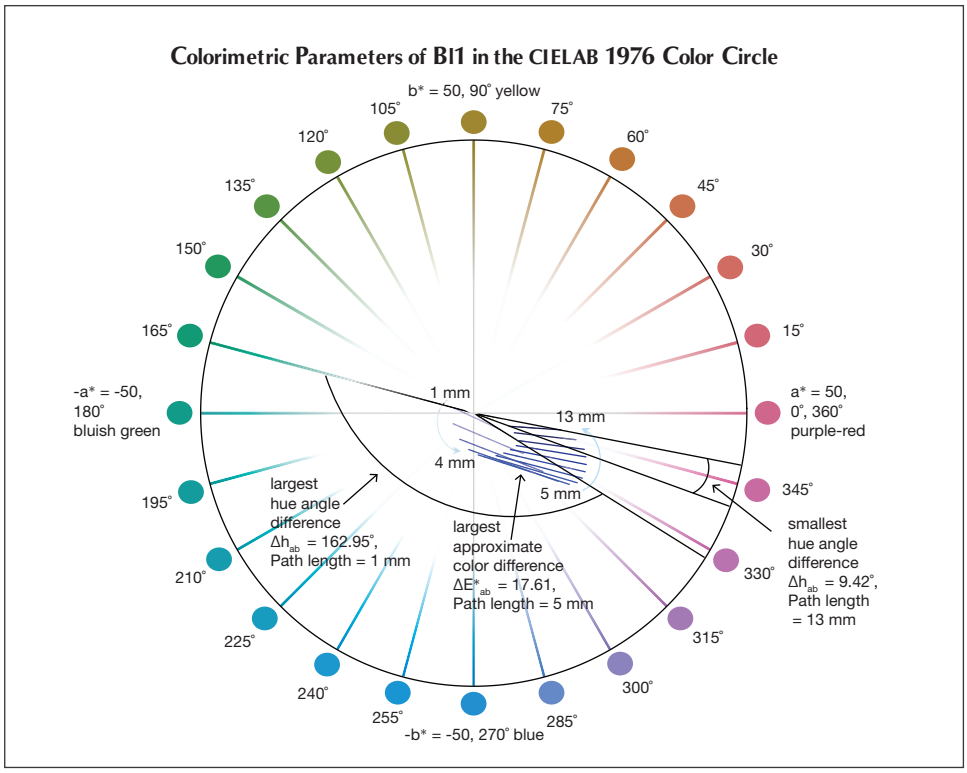


*Figure 16. Bl1 showed the largest approximate color difference $\Delta E^*_{ab}$ = 17.61 at a path length of 5 mm, the largest hue angle difference $\Delta h_{ab}$ = 162.95° at a path length of 1 mm, and the smallest hue angle difference $\Delta h_{ab}$ = 9.42° at a path length of 13 mm.*

CIELAB color space from the origin at L* = 0, a*= 0, and b*= 0. $E^*_{ab}$ is calculated by the equation

$$E^*_{ab} = \sqrt{a^{*2}+b^{*2}+L^{*2}}$$

The utility of $E^*_{ab}$ lies in the fact that the difference in this value for two different color coordinates, $\Delta E^*_{ab}$, is a reliable measurement of the absolute color difference between, for instance, the color of a stone under two different lighting conditions.

The color difference between daylight-equivalent ($D_{65}$) and incandescent (A) lighting, $\Delta E^*_{ab}$, is calculated by the equation

$$\Delta E^*_{ab} = \sqrt{\Delta a^{*2}+\Delta b^{*2}+\Delta L^{*2}}$$

where $\Delta a^* = a^*_{D65} - a^*_A$, $\Delta b^* = b^*_{D65} - b^*_A$, and $\Delta L^* = L^*_{D65} - L^*_A$.

$\Delta h_{ab}$(°), the hue angle difference between daylight-equivalent ($D_{65}$) and incandescent (A) lighting, is calculated by the equation

$$\Delta h_{ab} = |h_{ab,D65} - h_{ab,A}|$$

$\Delta C^*_{ab}$, the chroma (saturation) difference between daylight-equivalent and incandescent lighting, is calculated by the equation

$$\Delta C^*_{ab} = |C^*_{ab,D65} - C^*_{ab,A}|$$

Table 2 shows values of $C^*_{ab}$, $h_{ab}$, $\Delta C^*_{ab}$, $\Delta h_{ab}$, and $\Delta E^*_{ab}$ of three garnet samples (Pk1, Bl1, and Gr1) under daylight-equivalent and incandescent lighting with path lengths from 1 to 13 mm.

**The CIELAB 1976 Color Circle Plots (Schmetzer et al., 2009 and 2013).** A convenient way to represent the color difference between daylight-equivalent ($D_{65}$) and incandescent (A) lighting for a sample is to project the three-dimensional L*a*b* coordinates into the two-dimensional a*b* plane (the color circle) and draw a tie-line between the $D_{65}$ and A lighting coordinates. Furthermore, if one wants to track the color difference between $D_{65}$ and A lighting with increasing light path length, such tie lines could be drawn for each path length and plotted on the same color circle. We did so for garnet samples Bl1, Gr1, and Pk1, with path lengths from 1 to 13 mm (figures 16–18). The right ends of the tie lines represent the color coordinates under incandescent lighting (A). The left ends of the tie lines represent the color coordinates under daylight-equivalent lighting (D65).

Alternatively, one could isolate a specific variable such as $\Delta E^*_{ab}$, $\Delta h_{ab}$, or $\Delta C^*_{ab}$ and plot its changes with the light path length. Such plots are shown for samples Pk1, Bl1, and Gr1 in figure 19. All three show similar behavior in their color difference vs. path

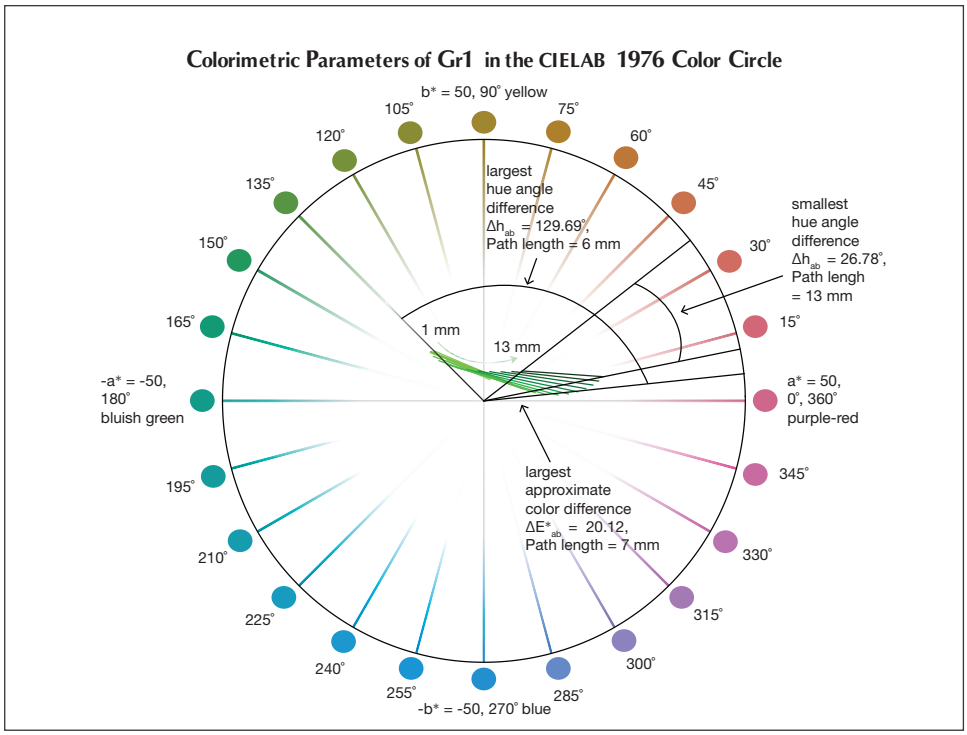


*Figure 17. Gr1 showed the largest approximate color difference $E^*_{ab}$ = 20.12 at a path length of 7 mm, the largest hue angle difference $\Delta h_{ab}$ =129.69° at a path length of 6 mm, and the smallest hue angle difference $\Delta h_{ab}$ = 26.78° at a path length of 13 mm.*

length plots, with $\Delta E^*_{ab}$ steadily rising with path length until reaching a critical point and falling again (figure 19, left column). However, these three stones all showed different behavior in hue angle difference vs. path length plots and chroma difference vs. path length plots (figure 19, center and right columns). The hue angle difference $\Delta h_{ab}$ of sample Bl1 decreases steadily as the stone becomes thicker. The hue angle

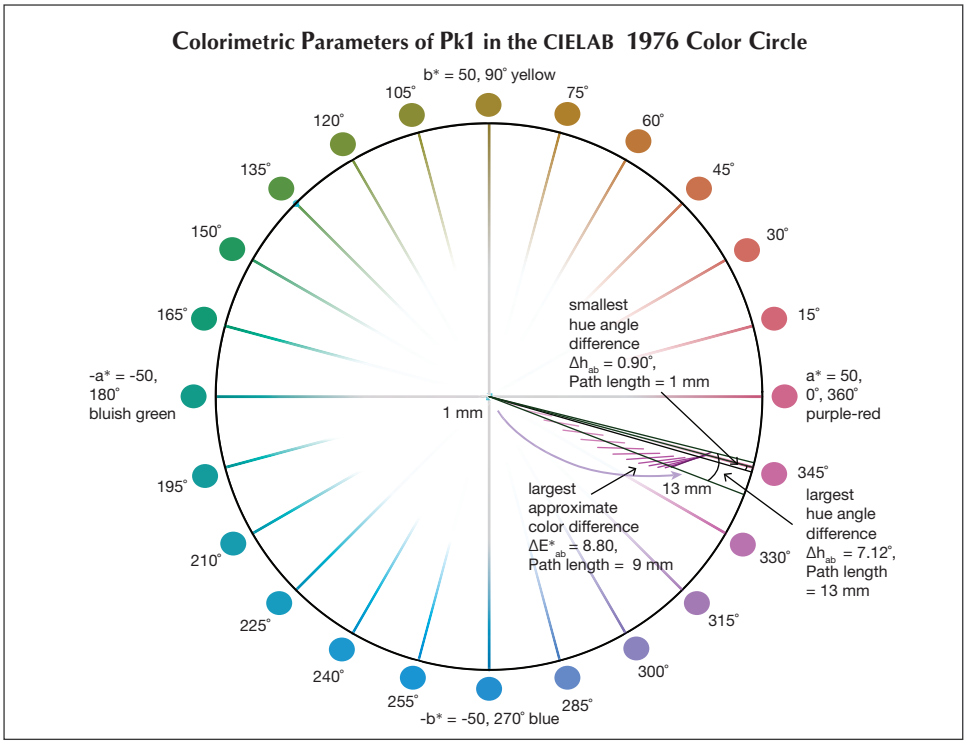


*Figure 18. Pk1 showed the largest approximate color difference $\Delta E^*_{ab}$ = 8.80 at a path length of 9 mm, the largest hue angle difference $\Delta h_{ab}$ = 7.12° at a path length of 13 mm, and the smallest hue angle difference $\Delta h_{ab}$ = 0.90° at a path length of 1 mm. The path length = 1 mm tie line is obscured because it is almost parallel to the black lines indicating the smallest hue angle.*

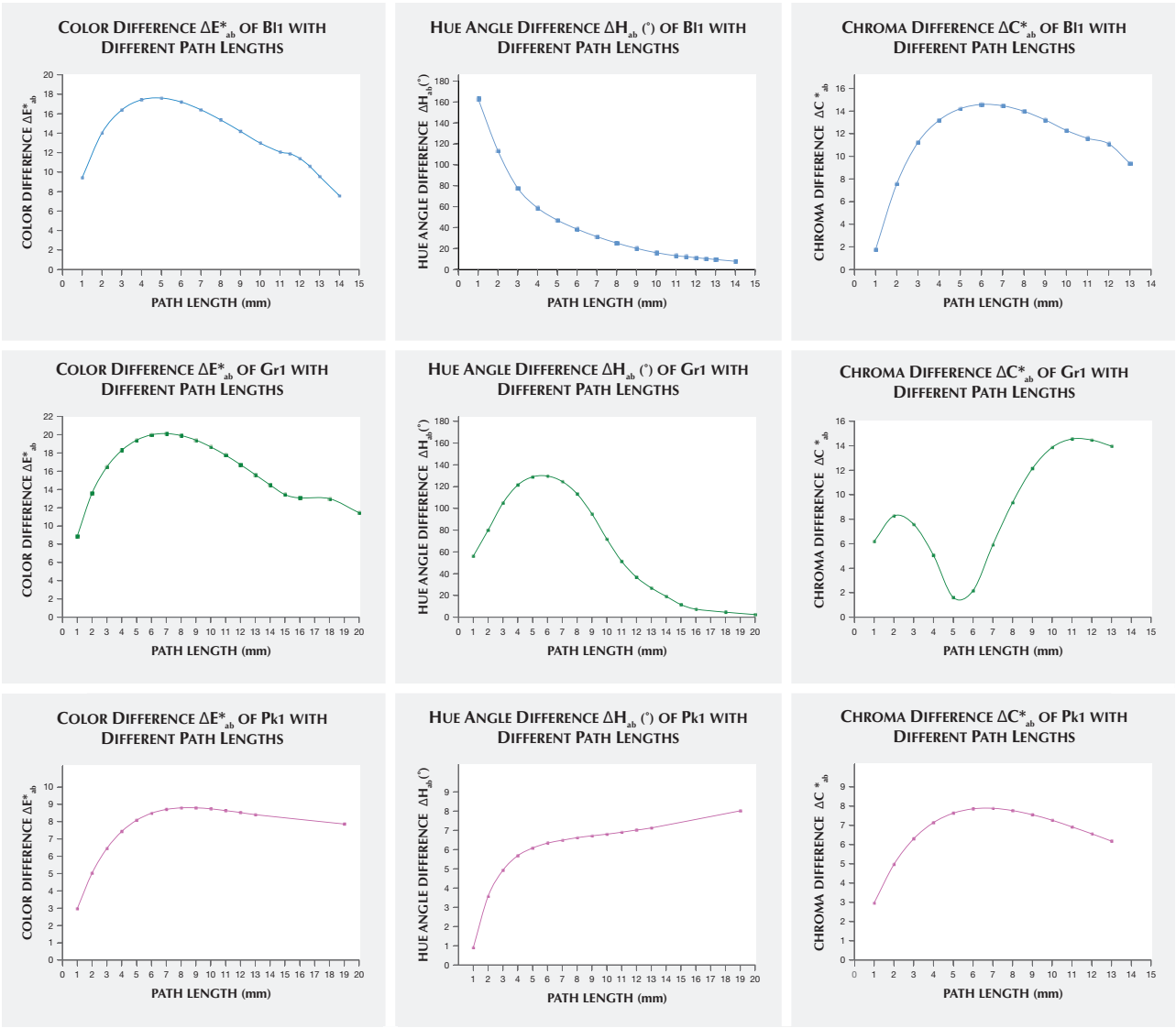


*Figure 19. The color difference vs. path length, hue angle difference vs. path length, and chroma difference vs. path length plots of Bl1 (top row) show that $\Delta E^*_{ab}$ and $\Delta C^*_{ab}$ reach their maximum at a path length of 5 mm and 6 mm, respectively, and $\Delta h_{ab}$ continues to decrease as path length increases. For Gr1 (middle row), $\Delta E^*_{ab}$, $\Delta h_{ab}$, and $\Delta C^*_{ab}$ reach their maximum at path lengths of 7 mm, 6 mm, and 10 mm, respectively. For Pk1 (bottom row), $\Delta E^*_{ab}$ and $\Delta C^*_{ab}$ reach their peak at path lengths of 9 mm and 6 mm, respectively, and $\Delta h_{ab}$ continues to increase with path length.*

difference $\Delta h_{ab}$ of Gr1 increases until reaching its highest value when the path length is 6 mm, after which it begins to decrease. On the other hand, the hue angle difference $\Delta h_{ab}$ of Pk1 simply continues to rise with the thickness of the stone until reaching a 13 mm path length (figure 19, middle column). The chroma difference $\Delta C^*_{ab}$ of Bl1 and Pk1 increases until reaching their maximum values, after which they decrease again (figure 19, right column, top and bottom rows). The chroma difference $\Delta C^*_{ab}$ of Gr1 increases first, then decreases before rising again to form a wave shape (figure 19, right column, middle row). At greater path length, the magnitude of the color change increases at first as the chroma (saturation), chroma difference, or hue angle difference increases and then decreases as the chroma, chroma difference, or hue angle difference decreases. This occurs because one of the transmission windows is preferentially "closed" as the stone becomes thicker. This type of behavior is related to the strength of two transmission windows (figure 14) and the complex relationship between them. It is difficult to predict

**TABLE 2.** Colorimetric data of three garnets with wafer thickness from 1 to 13 mm.

| Path Length | | Bl1 | Gr1 | Pk1 | Path Length | | Bl1 | Gr1 | Pk1 |
|---|---|---|---|---|---|---|---|---|---|
| 1 mm | $L^*$ for daylight $D_{65}$ | 79.33 | 85.59 | 90.54 | 6 mm | $L^*$ for daylight $D_{65}$ | 26.13 | 39.59 | 55.61 |
| | $a^*$ for daylight $D_{65}$ | −3.76 | −6.97 | 3.07 | | $a^*$ for daylight $D_{65}$ | 2.54 | −7.07 | 19.88 |
| | $b^*$ for daylight $D_{65}$ | 0.99 | 7.89 | −0.90 | | $b^*$ for daylight $D_{65}$ | −7.97 | 6.99 | −9.28 |
| | $L^*$ for incandescent light A | 78.94 | 85.32 | 90.77 | | $L^*$ for incandescent light A | 25.92 | 39.34 | 57.09 |
| | $a^*$ for incandescent light A | 4.79 | 1.10 | 5.94 | | $a^*$ for incandescent light A | 19.05 | 12.05 | 28.23 |
| | $b^*$ for incandescent light A | −2.97 | 4.20 | −1.64 | | $b^*$ for incandescent light A | −12.80 | 1.19 | −9.55 |
| | $C^*_{ab}$ for daylight $D_{65}$ | 3.89 | 10.53 | 3.20 | | $C^*_{ab}$ for daylight $D_{65}$ | 8.36 | 9.94 | 21.94 |
| | $h_{ab}$ (°) for daylight $D_{65}$ | 165.25 | 131.46 | 343.66 | | $h_{ab}$ (°) for daylight $D_{65}$ | 287.68 | 135.33 | 334.98 |
| | $C^*_{ab}$ for incandescent light A | 5.64 | 4.34 | 6.16 | | $C^*_{ab}$ for incandescent light A | 22.95 | 12.11 | 29.80 |
| | $h_{ab}$ (°) for incandescent light A | 328.20 | 75.32 | 344.57 | | $h_{ab}$ (°) for incandescent light A | 326.10 | 5.64 | 341.31 |
| | $\Delta C^*_{ab}$ | 1.75 | 6.19 | 2.96 | | $\Delta C^*_{ab}$ | 14.59 | 2.17 | 7.86 |
| | $\Delta h_{ab}$ (°) | 162.95 | 56.13 | 0.90 | | $\Delta h_{ab}$ (°) | 38.43 | 129.69 | 6.33 |
| | $\Delta E^*_{ab}$ | 9.43 | 8.88 | 2.97 | | $\Delta E^*_{ab}$ | 17.20 | 19.98 | 8.48 |
| 2 mm | $L^*$ for daylight $D_{65}$ | 63.26 | 73.33 | 82.02 | 7 mm | $L^*$ for daylight $D_{65}$ | 20.78 | 33.86 | 50.55 |
| | $a^*$ for daylight $D_{65}$ | −3.75 | −9.48 | 6.51 | | $a^*$ for daylight $D_{65}$ | 4.12 | −5.24 | 22.67 |
| | $b^*$ for daylight $D_{65}$ | −1.96 | 9.60 | −2.47 | | $b^*$ for daylight $D_{65}$ | −7.80 | 6.43 | −10.50 |
| | $L^*$ for incandescent light A | 62.65 | 72.89 | 82.49 | | $L^*$ for incandescent light A | 20.81 | 33.80 | 52.27 |
| | $a^*$ for incandescent light A | 9.15 | 3.02 | 11.40 | | $a^*$ for incandescent light A | 19.99 | 14.17 | 31.20 |
| | $b^*$ for incandescent light A | −7.44 | 4.26 | −3.53 | | $b^*$ for incandescent light A | −11.95 | 1.13 | −10.36 |
| | $C^*_{ab}$ for daylight $D_{65}$ | 4.23 | 13.49 | 6.96 | | $C^*_{ab}$ for daylight $D_{65}$ | 8.82 | 8.29 | 24.98 |
| | $h_{ab}$ (°) for daylight $D_{65}$ | 207.59 | 134.64 | 339.22 | | $h_{ab}$ (°) for daylight $D_{65}$ | 297.84 | 129.18 | 335.15 |
| | $C^*_{ab}$ for incandescent light A | 11.79 | 5.22 | 11.93 | | $C^*_{ab}$ for incandescent light A | 23.29 | 14.21 | 32.88 |
| | $h_{ab}$ (°) for incandescent light A | 320.88 | 54.67 | 342.79 | | $h_{ab}$ (°) for incandescent light A | 329.13 | 4.56 | 341.63 |
| | $\Delta C^*_{ab}$ | 7.56 | 8.27 | 4.97 | | $\Delta C^*_{ab}$ | 14.47 | 5.92 | 7.89 |
| | $\Delta h_{ab}$ (°) | 113.29 | 79.97 | 3.57 | | $\Delta h_{ab}$ (°) | 31.29 | 124.62 | 6.48 |
| | $\Delta E^*_{ab}$ | 14.03 | 13.60 | 5.03 | | $\Delta E^*_{ab}$ | 16.40 | 20.12 | 8.70 |
| 3 mm | $L^*$ for daylight $D_{65}$ | 50.65 | 62.87 | 74.35 | 8 mm | $L^*$ for daylight $D_{65}$ | 16.33 | 28.89 | 45.97 |
| | $a^*$ for daylight $D_{65}$ | −2.53 | −10.08 | 10.05 | | $a^*$ for daylight $D_{65}$ | 5.54 | −3.20 | 25.17 |
| | $b^*$ for daylight $D_{65}$ | −4.80 | 9.35 | −4.29 | | $b^*$ for daylight $D_{65}$ | −7.33 | 6.03 | −11.47 |
| | $L^*$ for incandescent light A | 49.99 | 62.36 | 75.07 | | $L^*$ for incandescent light A | 16.60 | 29.06 | 47.94 |
| | $a^*$ for incandescent light A | 12.73 | 5.22 | 16.37 | | $a^*$ for incandescent light A | 20.51 | 16.14 | 33.72 |
| | $b^*$ for incandescent light A | −10.73 | 3.29 | −5.38 | | $b^*$ for incandescent light A | −10.78 | 1.34 | −10.88 |
| | $C^*_{ab}$ for daylight $D_{65}$ | 5.43 | 13.75 | 10.93 | | $C^*_{ab}$ for daylight $D_{65}$ | 9.19 | 6.83 | 27.66 |
| | $h_{ab}$ (°) for daylight $D_{65}$ | 242.21 | 137.15 | 336.88 | | $h_{ab}$ (°) for daylight $D_{65}$ | 307.08 | 117.95 | 335.50 |
| | $C^*_{ab}$ for incandescent light A | 16.65 | 6.17 | 17.23 | | $C^*_{ab}$ for incandescent light A | 23.17 | 16.20 | 35.43 |
| | $h_{ab}$ (°) for incandescent light A | 319.87 | 32.22 | 341.81 | | $h_{ab}$ (°) for incandescent light A | 332.27 | 4.75 | 342.12 |
| | $\Delta C^*_{ab}$ | 11.22 | 7.58 | 6.30 | | $\Delta C^*_{ab}$ | 13.98 | 9.37 | 7.77 |
| | $\Delta h_{ab}$ (°) | 77.67 | 104.93 | 4.92 | | $\Delta h_{ab}$ (°) | 25.19 | 113.21 | 6.62 |
| | $\Delta E^*_{ab}$ | 16.38 | 16.46 | 6.45 | | $\Delta E^*_{ab}$ | 15.36 | 19.90 | 8.79 |
| 4 mm | $L^*$ for daylight $D_{65}$ | 40.65 | 53.92 | 67.45 | 9 mm | $L^*$ for daylight $D_{65}$ | 12.58 | 24.57 | 41.84 |
| | $a^*$ for daylight $D_{65}$ | −0.90 | −9.66 | 13.52 | | $a^*$ for daylight $D_{65}$ | 6.79 | −1.06 | 27.37 |
| | $b^*$ for daylight $D_{65}$ | −6.69 | 8.55 | −6.12 | | $b^*$ for daylight $D_{65}$ | −6.69 | 5.77 | −12.18 |
| | $L^*$ for incandescent light A | 40.07 | 53.42 | 68.42 | | $L^*$ for incandescent light A | 13.09 | 25.00 | 44.05 |
| | $a^*$ for incandescent light A | 15.52 | 7.51 | 20.83 | | $a^*$ for incandescent light A | 20.70 | 17.92 | 35.82 |
| | $b^*$ for incandescent light A | −12.52 | 2.30 | −7.04 | | $b^*$ for incandescent light A | −9.44 | 1.76 | −11.14 |
| | $C^*_{ab}$ for daylight $D_{65}$ | 6.75 | 12.90 | 14.84 | | $C^*_{ab}$ for daylight $D_{65}$ | 9.53 | 5.87 | 29.96 |
| | $h_{ab}$ (°) for daylight $D_{65}$ | 262.34 | 138.49 | 335.65 | | $h_{ab}$ (°) for daylight $D_{65}$ | 315.43 | 100.41 | 336.01 |
| | $C^*_{ab}$ for incandescent light A | 19.94 | 7.85 | 21.99 | | $C^*_{ab}$ for incandescent light A | 22.75 | 18.01 | 37.51 |
| | $h_{ab}$ (°) for incandescent light A | 321.11 | 17.03 | 341.33 | | $h_{ab}$ (°) for incandescent light A | 335.49 | 5.61 | 342.72 |
| | $\Delta C^*_{ab}$ | 13.19 | 5.05 | 7.15 | | $\Delta C^*_{ab}$ | 13.22 | 12.14 | 7.55 |
| | $\Delta h_{ab}$ (°) | 58.77 | 121.46 | 5.68 | | $\Delta h_{ab}$ (°) | 20.06 | 94.80 | 6.71 |
| | $\Delta E^*_{ab}$ | 17.43 | 18.28 | 7.43 | | $\Delta E^*_{ab}$ | 14.19 | 19.40 | 8.80 |
| 5 mm | $L^*$ for daylight $D_{65}$ | 32.64 | 46.22 | 61.22 | 10 mm | $L^*$ for daylight $D_{65}$ | 9.40 | 20.79 | 38.10 |
| | $a^*$ for daylight $D_{65}$ | 0.84 | −8.59 | 16.82 | | $a^*$ for daylight $D_{65}$ | 7.84 | 1.13 | 29.27 |
| | $b^*$ for daylight $D_{65}$ | −7.67 | 7.71 | −7.81 | | $b^*$ for daylight $D_{65}$ | −5.96 | 5.64 | −12.65 |
| | $L^*$ for incandescent light A | 32.22 | 45.81 | 62.45 | | $L^*$ for incandescent light A | 10.12 | 21.49 | 40.54 |
| | $a^*$ for incandescent light A | 17.59 | 9.81 | 24.78 | | $a^*$ for incandescent light A | 20.63 | 19.48 | 37.53 |
| | $b^*$ for incandescent light A | −13.09 | 1.58 | −8.45 | | $b^*$ for incandescent light A | −8.04 | 2.35 | −11.17 |
| | $C^*_{ab}$ for daylight $D_{65}$ | 7.72 | 11.54 | 18.54 | | $C^*_{ab}$ for daylight $D_{65}$ | 9.85 | 5.75 | 31.89 |
| | $h_{ab}$ (°) for daylight $D_{65}$ | 276.25 | 138.09 | 335.09 | | $h_{ab}$ (°) for daylight $D_{65}$ | 322.76 | 78.67 | 336.63 |
| | $C^*_{ab}$ for incandescent light A | 21.93 | 9.94 | 26.18 | | $C^*_{ab}$ for incandescent light A | 22.14 | 19.62 | 39.16 |
| | $h_{ab}$ (°) for incandescent light A | 323.34 | 9.15 | 341.17 | | $h_{ab}$ (°) for incandescent light A | 338.71 | 6.88 | 343.43 |
| | $\Delta C^*_{ab}$ | 14.21 | 1.61 | 7.64 | | $\Delta C^*_{ab}$ | 12.29 | 13.87 | 7.27 |
| | $\Delta h_{ab}$ (°) | 47.09 | 128.94 | 6.08 | | $\Delta h_{ab}$ (°) | 15.95 | 71.79 | 6.80 |
| | $\Delta E^*_{ab}$ | 17.61 | 19.40 | 8.08 | | $\Delta E^*_{ab}$ | 12.98 | 18.66 | 8.74 |

| Path Length | | Bl1 | Gr1 | Pk1 |
|---|---|---|---|---|
| 11 mm | $L^*$ for daylight $D_{65}$ | 6.74 | 17.49 | 34.72 |
| | $a^*$ for daylight $D_{65}$ | 8.40 | 3.28 | 30.89 |
| | $b^*$ for daylight $D_{65}$ | −5.07 | 5.60 | −12.92 |
| | $L^*$ for incandescent light A | 7.60 | 18.46 | 37.37 |
| | $a^*$ for incandescent light A | 20.34 | 20.82 | 38.88 |
| | $b^*$ for incandescent light A | −6.65 | 3.05 | −11.00 |
| | $C^*_{ab}$ for daylight $D_{65}$ | 9.81 | 6.49 | 33.48 |
| | $h_{ab}$ (°) for daylight $D_{65}$ | 328.89 | 59.64 | 337.30 |
| | $C^*_{ab}$ for incandescent light A | 21.40 | 21.04 | 40.41 |
| | $h_{ab}$ (°) for incandescent light A | 341.90 | 8.33 | 344.20 |
| | $\Delta C^*_{ab}$ | 11.59 | 14.55 | 6.92 |
| | $\Delta h_{ab}$ (°) | 13.01 | 51.31 | 6.90 |
| | $\Delta E^*_{ab}$ | 12.07 | 17.75 | 8.63 |
| 12 mm | $L^*$ for daylight $D_{65}$ | 4.85 | 14.58 | 31.65 |
| | $a^*$ for daylight $D_{65}$ | 7.49 | 5.35 | 32.23 |
| | $b^*$ for daylight $D_{65}$ | −3.60 | 5.65 | −13.00 |
| | $L^*$ for incandescent light A | 5.68 | 15.84 | 34.50 |
| | $a^*$ for incandescent light A | 18.79 | 21.92 | 39.92 |
| | $b^*$ for incandescent light A | −4.88 | 3.82 | −10.66 |
| | $C^*_{ab}$ for daylight $D_{65}$ | 8.31 | 7.78 | 34.75 |
| | $h_{ab}$ (°) for daylight $D_{65}$ | 334.33 | 46.56 | 338.03 |
| | $C^*_{ab}$ for incandescent light A | 19.41 | 22.25 | 41.32 |
| | $h_{ab}$ (°) for incandescent light A | 345.44 | 9.89 | 345.05 |
| | $\Delta C^*_{ab}$ | 11.10 | 14.47 | 6.57 |
| | $\Delta h_{ab}$ (°) | 11.11 | 36.68 | 7.02 |
| | $\Delta E^*_{ab}$ | 11.40 | 16.72 | 8.53 |
| 13 mm | $L^*$ for daylight $D_{65}$ | 3.53 | 12.03 | 28.86 |
| | $a^*$ for daylight $D_{65}$ | 6.53 | 7.29 | 33.32 |
| | $b^*$ for daylight $D_{65}$ | −2.41 | 5.76 | −12.91 |
| | $L^*$ for incandescent light A | 4.30 | 13.55 | 31.90 |
| | $a^*$ for incandescent light A | 16.04 | 22.79 | 40.66 |
| | $b^*$ for incandescent light A | −3.07 | 4.65 | −10.18 |
| | $C^*_{ab}$ for daylight $D_{65}$ | 6.96 | 9.29 | 35.73 |
| | $h_{ab}$ (°) for daylight $D_{65}$ | 339.74 | 38.31 | 338.82 |
| | $C^*_{ab}$ for incandescent light A | 16.33 | 23.26 | 41.92 |
| | $h_{ab}$ (°) for incandescent light A | 349.16 | 11.53 | 345.94 |
| | $\Delta C^*_{ab}$ | 9.37 | 13.97 | 6.18 |
| | $\Delta h_{ab}$ (°) | 9.42 | 26.78 | 7.12 |
| | $\Delta E^*_{ab}$ | 9.56 | 15.61 | 8.40 |

| | |
|---|---|
| $L^*$ | lightness parameter in the three-dimensional CIELAB color space |
| $a^*$, $b^*$ | rectangular parameters in the three-dimensional CIELAB color space |
| $C^*_{ab}$ for daylight $D_{65}$ | chroma (saturation) for daylight $D_{65}$ |
| $h_{ab}$ (°) for daylight $D_{65}$ | hue angle for daylight $D_{65}$ |
| $C^*_{ab}$ for incandescent light A | chroma (saturation) for incandescent light A |
| $h_{ab}$ (°) for incandescent light A | hue angle for incandescent light A |
| $\Delta h_{ab}$ (°) | hue angle difference between daylight and incandescent light |
| $\Delta C^*_{ab}$ | chroma difference between daylight and incandescent light |
| $\Delta E^*_{ab}$ | color difference between daylight and incandescent light in the three-dimensional CIELAB color space |

without an accurate quantitative calculation, and this behavior is expected to vary between different gem materials.

An interesting phenomenon was observed in the color difference vs. path length plots of Bl1 and Gr1. When the stone becomes darker with increasing path length, a small bump forms instead of a smooth curved line (figure 19, left column). Presently, we cannot offer an explanation for this unusual behavior.

**Color Difference $\Delta E^*_{ab}$ vs. Hue Angle Difference $\Delta h_{ab}$ Plots, and the Problem of "Color Change."** Color difference vs. hue angle difference plots reveal that Bl1 and Gr1 show a larger color difference $\Delta E^*_{ab}$ and hue angle difference $\Delta h_{ab}$ than Pk1 at nearly all path lengths (figure 20).

Liu et al. (1994, 1999a) suggested that a stone should have a hue angle difference $\Delta h_{ab}$ larger than 20° and a chroma difference $\Delta C^*_{ab}$ higher than 5 to be considered a color-change stone. Schmetzer et al. (2009) proposed three different sets of criteria that could be used to decide whether to describe a stone as having a "color change." The first set of criteria suggests that a stone should have a hue angle difference $\Delta h_{ab}$ larger than 60° or a color difference $\Delta E^*_{ab}$ larger than 9. The second and third set of criteria are shown graphically in figures 20 and 21, respectively, and offer a distinction between "color change" and "color variation" depending on where the stone plots in a specific region of the $\Delta E^*_{ab}$ vs. $\Delta h_{ab}$ space.

To facilitate discussion of color change and its relationship to path length in these three stones, the color of Bl1, Gr1, and Pk1 under daylight-equivalent light and incandescent light was quantitatively reproduced for path lengths from 1 mm to 13 mm by converting CIE L*, a*, and b* color space coordinates into color swatches using Adobe Photoshop (figure 22).

According to the classification of Liu et al. (1994, 1999a), Bl1 can be considered to have a color change when the path length of light passing through the stone is between 3 and 9 mm. Likewise, Gr1 is a color-change garnet when the path length is between 2 and 13 mm. Because Pk1's hue angle difference $\Delta h_{ab}$ is never larger than 20°, it cannot be considered a color-change stone according to this classification.

According to the first classification of Schmetzer et al. (2009) described above, Bl1 is a color-change stone when path length is between 1 and 13 mm, Gr1 is a color-change stone when path length is between 2 and 13 mm, and Pk1 is never a color-change

garnet because its $\Delta E^*_{ab}$ is never larger than 9 and its $\Delta h_{ab}$ is never larger than 60°. According to the second classification scheme of Schmetzer et al. (2009), Bl1 is a color-change stone when path length is between 1 and 13 mm, as are Gr1 when path length is between 1 and 13 mm and Pk1 when path length is between 4 and 13 mm (again, see figure 20). According to the third classification scheme of Schmetzer et al. (2009), Bl1 is a color-change stone at path lengths between 1 and 13 mm, as is Gr1 at path lengths between 1 and 13 mm, and Pk1 is never a color-change garnet (figure 21).

Considering the $\Delta E^*_{ab}$ vs. $\Delta h_{ab}$ plots used by Schmetzer et al. (2009) as criteria, it makes sense intuitively that stones with low $\Delta E^*_{ab}$ and $\Delta h_{ab}$ values do not possess a color change. Likewise, stones with high $\Delta E^*_{ab}$ but very low $\Delta h_{ab}$ should probably not be described as "color-change"—even though the saturation and/or lightness may change between daylight-equivalent and incandescent lighting, there will be no significant change in hue, which is likely the most important factor. Nor do samples with large $\Delta h_{ab}$ but very small $\Delta E^*_{ab}$ values qualify as color-change stones, because their saturation is too low for color differences to be readily observed. It should be pointed out that there is no unique solution to the problem of classifying color-change stones based on their CIELAB color coordinates, as the entire concept of "color change" is inherently subjective. A more objective boundary for color-change stones might be achieved through a comprehensive survey of gemologists, jewelers, collectors, and gem enthusiasts. But even the most comprehensive survey cannot be expected to provide an absolute classification scheme for color-change gems.

**TABLE 3.** Proportions of the round brilliant cut garnet used to demonstrate the relationship between carat weight and path length.

| | |
|---|---|
| Crown angle (°) | 35.00 |
| Pavilion angle (°) | 38.50 |
| Total height (%) | 59.35 |
| Crown height (%) | 15.06 |
| Pavilion height (%) | 39.79 |
| Table (%) | 57.02 |
| Girdle height bezel (%) | 4.50 |
| Star angle (°) | 20.75 |
| Upper girdle angle (°) | 41.10 |
| Lower girdle angle (°) | 39.56 |

**The Relationship Between Carat Weight and Actual Path Length in a Standard Round Brilliant.** To relate the path lengths used in our color calculations above to the size of faceted stones, we report here the results of calculations, using DiamCalc software, that show the relationship between carat weight and actual path length for a 57-facet round brilliant garnet. The stone has an RI of 1.750 and an SG of 3.875; its proportions are listed in table 3. The path length represents a ray of light entering the garnet at approxi-

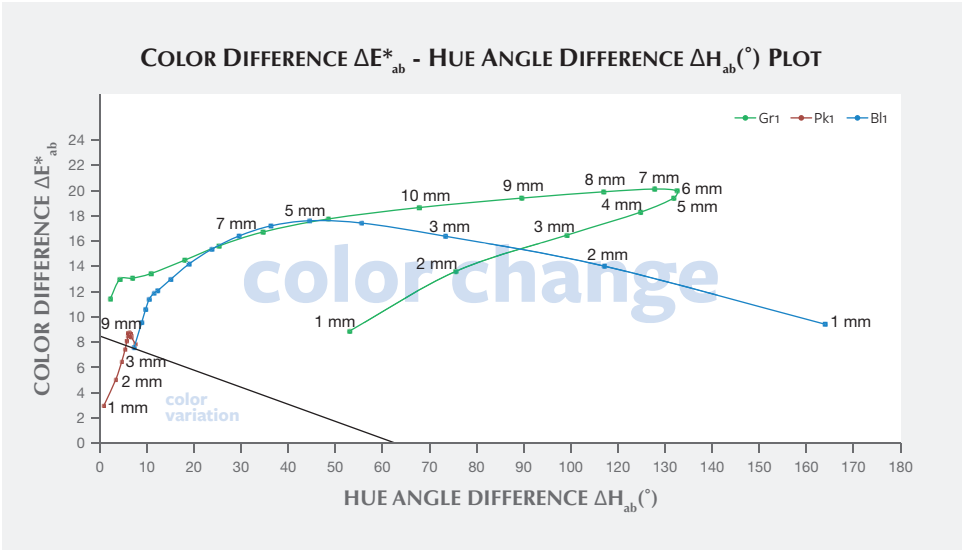


*Figure 20. Color difference $\Delta E^*_{ab}$ vs. hue angle difference $\Delta h_{ab}$ plot of three garnets with different path lengths (modified after Schmetzer et al., 2009).*

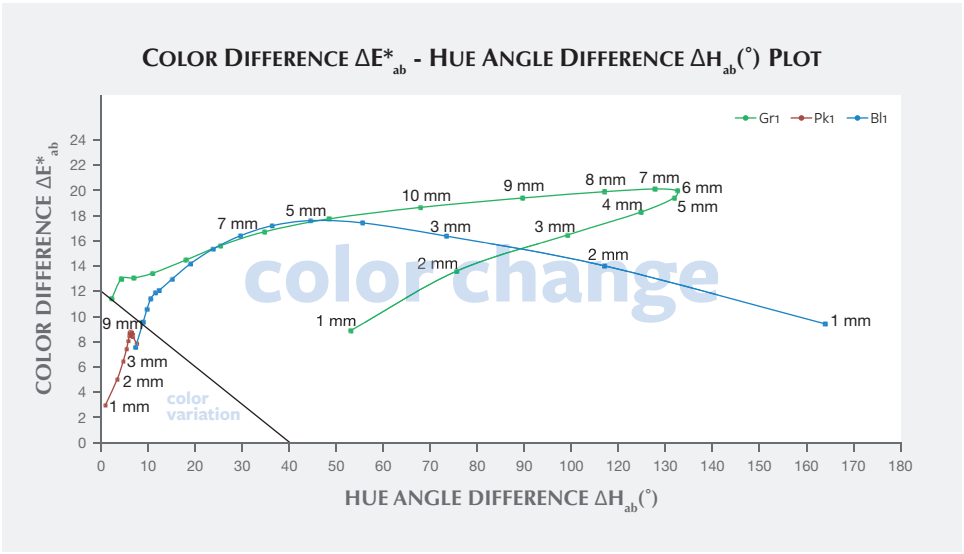


*Figure 21. Color difference $\Delta E^*_{ab}$ vs. hue angle difference $\Delta h_{ab}$ plot of three garnets with different path lengths (modified after Schmetzer et al., 2009).*

mately 70° to the plane of the girdle (from over the shoulder of the observer). The light passes through the middle of a bezel facet, strikes the middle of a pavilion main facet, and is reflected to the opposing pavilion main facet before exiting through the table to the eye of the observer directly overhead (red line in figure 23). The carat weight of each path length from 1 to 13 mm was calculated and is reported in figure 22. This calculation is only for round brilliants of the specific proportions presented in table 3. The path length will vary with the way the stone is cut. The concentration, distribution, and orientation of the inclusions will influence how the light passes through and is absorbed into the stone. This factor has not been corrected for individual stones in this study.

*Figure 22. The color of three stones under daylight-equivalent light (D65) and incandescent light (A) is quantitatively reproduced by converting CIE L*, a*, b* color space coordinates into color swatches using Adobe Photoshop. The colors of Bl1, Gr1, and Pk1 are shown at different path lengths and carat weights. For each sample, the two rows represent the color under incandescent lighting (top), and daylight-equivalent light (bottom).*

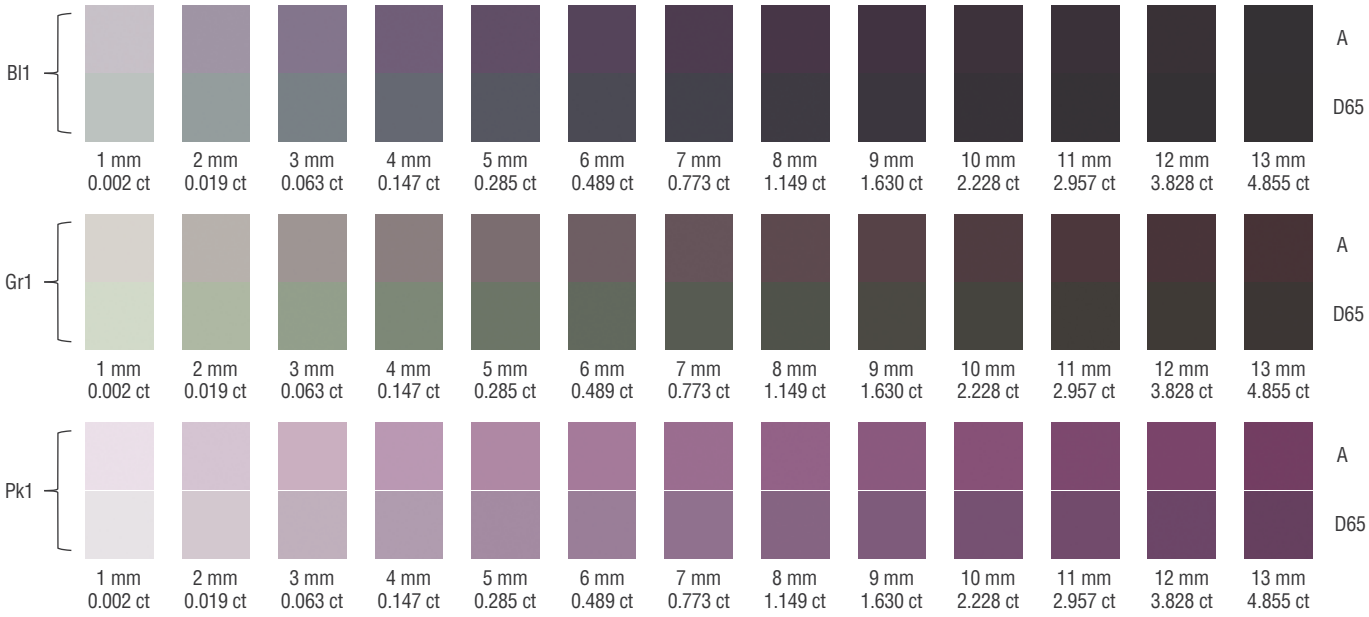

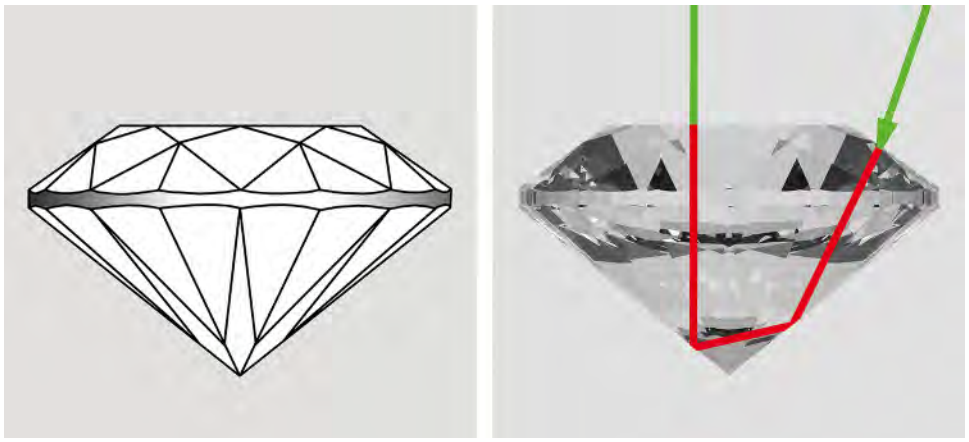

*Figure 23. Diagram of the round brilliant garnet (left) and the calculated path length inside the stone (right, red line). Photo by Al Gilbertson.*

## CONCLUSIONS

What sets this type of pink pyrope garnet apart from other color-change pyrope-spessartine garnets is the somewhat lower concentration of vanadium and chromium and also the much higher pyrope component ($Mg_3Al_2Si_3O_{12}$). From the colorimetric analysis of three different samples, we have the following thoughts.

The Usambara effect and color change are two manifestations of the phenomenon of having two distinct transmission windows in the visible spectrum. This study quantitatively described the interplay between color change and the Usambara effect (Schmetzer et al., 2013).

To make this comparison between the Usambara effect and color change, a reflection loss correction method was developed. This method allowed us to accurately manipulate the UV-Vis spectra to calculate color under different lighting conditions for various path lengths.

As path length increases, the difference in color between incandescent and daylight-equivalent lighting increases at first as chroma (saturation), chroma difference, or hue angle difference increases. The color difference then decreases as chroma, chroma difference, or hue angle difference decreases. This latter effect occurs because one of the transmission windows is preferentially "closed" in the thicker portions of the stone.

By this reasoning, there is one path length that should show the greatest difference in color between incandescent and daylight-equivalent lighting, another with the greatest hue angle variation, and still another with the greatest saturation variation. While this path length may not be the same in all cases, there should be a range of path lengths that show the best color change. Below or above this range, the saturation is too low or the hue angle change or saturation change is too slight to produce an observable color change.

ABOUT THE AUTHORS

*Mr. Sun is a staff gemologist, Dr. Palke is a postdoctoral research associate, and Mr. Renfro is the analytical manager of the gem identification department and analytical microscopist in the inclusion research department, at GIA in Carlsbad, California.*

ACKNOWLEDGMENTS

*The authors thank Todd Wacks from Todd's Gems, Jason Doubrava from Jason Doubrava Gems & Minerals, Meg Berry from Megagem and Jeff Hapeman from Earth's Treasury, for providing samples for chemical analyses and inclusion photomicrography. Assistance from Jonathan Muyal in polishing the garnet wafers and taking photomicrographs of inclusions is greatly appreciated. The authors thank two anonymous reviewers for their constructive comments and criticism, which helped to improve this article. The authors thank Al Gilbertson for using DiamCalc software to calculate the relationship between path length and carat weight; Dino DeGhionno, Shane McClure, Mike Breeding, David Nelson, Troy Ardon, Yun Luo, and Tao Hsu for many helpful mineralogical and colorimetric discussions. Virginia Schwartz, Philip York, Amy Cooper, Heidi Breitzmann, Philip Owens, Claire Ito, Rebecca Tsang, Najmeh Anjomani, Johna Lippert, and Jenni Rieger provided invaluable assistance in gemological testing and discussions. The photos of the samples in table 1 are by Robison McMurtry.*

## REFERENCES


Amthauer G. (1975) Kristallchemie und Farbe chromhaltiger Granate. *Neues Jarbuch für Mineralogie Abhandlungen*, Vol. 126, No. 2, pp. 158–186 [in German].

Björn L. O. (2002) *Photobiology: The Science of Light and Life*. Kluwer Academic Publishers, Dordtrecht, Netherlands.

Carstens H. (1973) The red-green change in chromium-bearing garnets. *Contributions to Mineralogy and Petrology*, Vol. 41, pp. 273–276, http://dx.doi.org/10.1007/BF00371036

CIE Commission Internationale de l'Éclairage (2004) CIE 15: Technical Report: Colorimetry. 3rd edition

Crowningshield R. (1970) A rare alexandrite garnet from Tanzania. *G&G*, Vol. 13, No. 6, pp. 174–177.

Geiger C.A., Stahl A., Rossman G.R. (2000) Single-crystal IR- and UV/VIS-spectroscopic measurements on transition-metal bearing pyrope: the incorporation of hydroxide in garnet. *European Journal of Mineralogy*, Vol. 12, No. 2, pp. 259–271, http://dx.doi.org/10.1127/0935-1221/2000/0001-0259

Gübelin E.J., Koivula J.I. (2005) *Photoatlas of Inclusions in Gemstones*, Vol. 2, Opinio, Basel, Switzerland, pp. 430–469.

Halvorsen A. (2006) The Usambara effect and its interaction with other color change phenomena. *Journal of Gemmology*, Vol. 30, No. 1/2, pp. 1–21.

Halvorsen A., Jensen B.B. (1997) A new color change effect. *Journal of Gemmology*, Vol. 25, No. 5, pp. 325–330.

Hysingjord J. (1971) A gem garnet from the island of Otteroy. *Journal of Gemmology*, Vol. 12, No. 7, pp. 296–299.

Jobbins E.A., Saul J.M., Tresham A.E., Young B.R. (1975) Blue color-change gem garnet from East Africa. *Journal of Gemmology*, Vol. 14, No. 5, pp. 201–208.

Johnson M.L., Koivula J.I., Eds. (1998) Gem News: Color change pyrope-spessartine garnet, also from Madagascar. *G&G*, Vol. 34, No. 3, pp. 222–223.

Koivula J.I. (1984) The first-order red compensator: an effective gemological tool. *G&G*, Vol. 20, No. 2, pp. 101–105, http://dx.doi.org/10.5741/GEMS.20.2.101

——— (2000) *The Microworld of Diamonds*. Gemworld International. Northbrook, IL.

Krzemnicki M.S., Hänni H.A., Reusser E. (2001) Color-change garnets from Madagascar: comparison of colorimetric with chemical data. *Journal of Gemmology*, Vol. 27, No. 7, pp. 395–408.

Liu Y., Shigley J.E., Fritsch E., Hemphill S. (1994) The "alexandrite effect" in gemstones. *Color Research and Application*, Vol. 19, No. 3, pp. 186–191.

Liu Y., Shigley J.E., Fritsch E., Hemphill S. (1999a) A colorimetric study of the alexandrite effect in gemstones. *Journal of Gemmology*, Vol. 26, No. 6, pp. 371–385.

Liu Y., Shigley J.E., Halvorsen A. (1999b) Colour hue change of a gem tourmaline from the Umba Valley, Tanzania. *Journal of Gemmology*, Vol. 26, No. 6, pp. 386–396.

Locock A.J. (2008) An Excel spreadsheet to recast analyses of garnet into end-member components, and a synopsis of the crystal chemistry of natural silicate garnets. *Computers & Geosciences*, Vol. 34, pp. 1769–1780, http://dx.doi.org/10.1016/j.cageo.2007.12.013

Manson D.V., Stockton C.M. (1984) Pyrope-spessartine garnets with unusual color behavior. *G&G*, Vol. 20, No. 4, pp. 200–207, http://dx.doi.org/10.5741/GEMS.20.4.200

Moore R.K., White W.B. (1972) Electronic spectra of transition metal ions in silicate garnets. *Canadian Mineralogist*, Vol. 11, pp. 791–811.

Pay D. (2015) Gem News International: Color-change garnets from Tanzania. *G&G*, Vol. 51, No. 1, pp. 88–89.

Renfro N. (2015a) Digital photomicrography for gemologists. *G&G*, Vol. 51, No. 2, pp. 144–159, http://dx.doi.org/10.5741/GEMS.51.2.144

——— (2015b) The application of differential interference contrast microscopy to gemmology. *Journal of Gemmology*, Vol. 34, No. 7, pp. 616–620.

Schmetzer K., Ottemann J. (1979) Kristallchemie und Farbe Vanadium-haltiger Granate. *Neues Jarbuch für Mineralogie Abhandlungen*, Vol. 136, No. 2, pp. 146–168 [in German].

Schmetzer K., Bernhardt H.-J., Bosshart G., Hainschwang T. (2009) Color-change garnets from Madagascar: variation of chemical, spectroscopic and colorimetric properties. *Journal of Gemmology*, Vol. 31, No. 5–8, pp. 235–282.

Schmetzer K., Bernhardt H.-J., Balmer W.A., Hainschwang T. (2013) Synthetic alexandrites grown by the HOC method in Russia: internal features related to the growth technique and colorimetric investigation. *Journal of Gemmology*, Vol. 33, No. 5–6, pp. 113–129.

Stockton C.M. (1988) Pastel pyropes. *G&G*, Vol. 24, No. 2, pp. 104–106, http://dx.doi.org/10.5741/GEMS.24.2.104

Stockton C.M., Manson D.V. (1985) A proposed new classification for gem-quality garnets. *G&G*, Vol. 21, No. 4, pp. 205–218, http://dx.doi.org/10.5741/GEMS.21.4.205

# Alluvial Sapphires from Montana: Inclusions, Geochemistry, and Indications of a Metasomatic Origin

J.C. (Hanco) Zwaan, Eric Buter, Regina Mertz-Kraus, and Robert E. Kane

Although the source rocks of alluvial sapphires in Montana have never been discovered, inclusions and geochemistry of material from this location may give clues to their original source. Mineral inclusions in alluvial Montana sapphires, mainly from Rock Creek, were identified and compared with existing data. Topaz was a remarkable find in one of these samples; other newly identified mineral inclusions in Montana sapphire were allanite, anatase, chalcopyrite, and monazite. Together with the presence of calcium-rich plagioclase, alkali-feldspar, apatite, barite, phlogopite, a pyrochlore-group mineral previously called uranpyrochlore, and chromite/spinel, these inclusions may reflect a metasomatic origin for the sapphires. This is supported by their chemical composition, which largely coincides with sapphires of plumasitic/metasomatic origin. The secondary Montana sapphires analyzed in this study are characterized by mean values of Fe (4686 ppmw), Ti (58 ppmw), Ga (51 ppmw), Mg (35 ppmw), and Cr (21 ppmw). Fe-Mg-Ga ratios help to distinguish them from sapphires with overlapping properties, such as those from Umba, Tanzania, and Rio Mayo, Colombia.

While Yogo Gulch is Montana's only primary sapphire deposit, alluvial deposits occur near Philipsburg (Rock Creek), Deer Lodge (Dry Cottonwood Creek), and Helena (Missouri River; figure 1). Eldorado Bar is the largest and best known of the approximately 14-mile-long Missouri River deposits. Other historically mined sapphire deposits—in gravel bars on both sides of the river, as well as the riverbed itself—are American Bar, Dana Bar, Metropolitan Bar, Spokane Bar, French Bar, Magpie Gulch, and Emerald Bar.

*Figure 1. Locations of sapphire deposits in the U.S. state of Montana. Yogo Gulch is the only primary deposit, while Rock Creek is the most important alluvial deposit.*


Rock Creek, popularly known as Gem Mountain, is the most important of Montana's secondary deposits (Kane, 2004, 2008; Berg, 2014). Huge quantities of sapphire have been produced in this area. Between 1906 and 1923, 190 million carats were shipped from Rock Creek, and during the mid-1990s more than 3.5 million carats were produced (Kane, 2004). Between the 1920s and 1990s there was very little to no production, if any. Production stopped in the 1930s, mainly because of fierce competition from synthetic sapphires used in the watch industry. By the 1970s the public could screen gravel for sapphires. Despite favorable sampling results obtained from a 3,700-cubic-yard sample between 1974 and 1976, the pale-colored material was not considered marketable. Production resumed only after it was discovered that heat treatment induced appealing colors (compare

See end of article for About the Authors and Acknowledgments.
GEMS & GEMOLOGY, Vol. 51, No. 4, pp. 370–391,
http://dx.doi.org/10.5741/GEMS.51.4.370.

*Figure 2. Montana sapphires occur at three commercial secondary deposits: Rock Creek, Dry Cottonwood Creek, and the Missouri River area. These rough and faceted Rock Creek stones show the range of permanent colors after routine heat treatment without the addition of chemicals. The largest faceted gem weighs 0.43 ct, and the largest rough stone weighs 1.86 ct. Courtesy of Fine Gems International, © Robert E. Kane.*

Berg, 2014). Yet the source and origin of these alluvial deposits remains unclear, despite more than 100 years of searching (e.g., Pratt, 1906; Clabaugh, 1952; Garland, 2002; Berg, 2011).

To avoid confusion within the gem trade, specific nomenclature is used to differentiate Montana sapphires by rarity, the nature of the deposit (primary versus secondary), and the application of heat treatment (a common practice in enhancing the colors of the alluvial sapphires). The sapphires from the primary deposit at Yogo Gulch, routinely called "Yogo sapphires," are unique in that they have a very uniform, intense color and thus do not require heating. The sapphires that come from the secondary deposits of the Missouri River, Dry Cottonwood Creek, and Rock Creek are simply referred to as "Montana sapphires" (figure 2). Throughout the present article, the authors follow this convention.

The geology of western Montana is dominated by Cenozoic episodes of basin development and deformation (resulting in a fold-thrust belt and *foreland basin**), in response to subduction of the Pacific plate

*Italicized geochemical terms are defined in the glossary on p. 389.

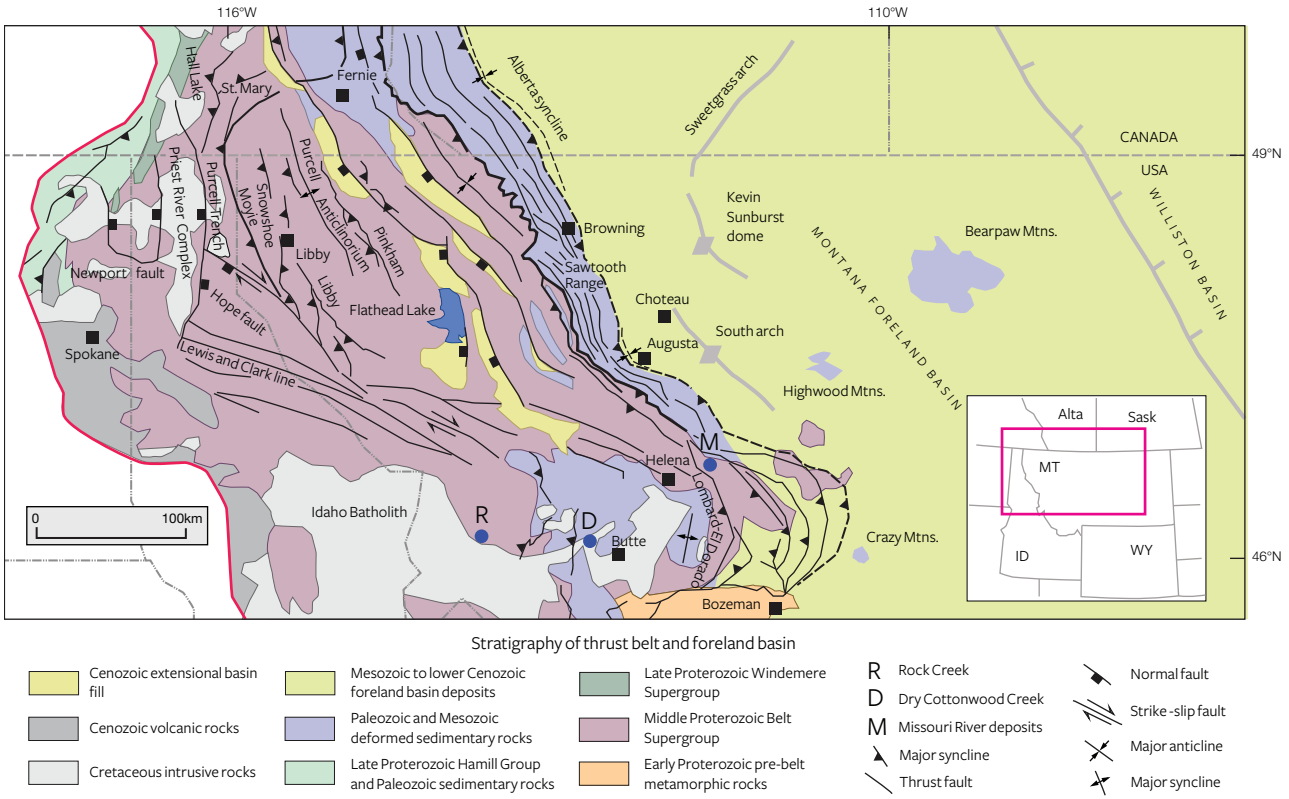


*Figure 3. Simplified regional tectonic map of the fold-thrust belt and foreland basin of northwestern Montana (MT) and adjacent areas (Idaho – ID, Wyoming – WY, Alberta – Alta., and Saskatchewan – Sask.) From Fuentes et al. (2012).*

along the western continental margin (figure 3; Garland, 2002; Fuentes et al., 2012). The geological framework has a foundation in the Archean and Proterozoic development of the North American continent. The Proterozoic basin formed a large trough trending northwest, and most of the sediments accumulated in the basin from 1470 to 1400 Ma at a relatively rapid rate (Evans et al., 2000). Locally, Paleozoic and Mesozoic sediments are exposed (though often poorly, as the large sedimentary basins of these periods have mostly been overprinted by Cenozoic tectonics). Large sections of Proterozoic belt sediments uplifted by Cretaceous thrust faulting compose most of the bedrock in the Rock Creek area (Garland, 2002; Fuentes et al., 2012). After an onset of igneous activity during the Late Cretaceous and Paleocene epochs (approximately 80–58 Ma), resulting in the emplacement of the Idaho *batholith* (figure 3), Eocene and younger mafic to ultramafic alkalic, igneous rocks (< 54 Ma) intruded the region. Of these rocks, a lamprophyric ultramafic dike (called ouachitite, a variety of monchiquite, characterized by the abundance of black mica and brown amphibole, olivine, clinopyroxene, analcime) and *hydrothermal breccia* host the Yogo sapphire deposit (e.g., Clabaugh, 1952; Baker, 1992; Baker, 1994; Giuliani et al., 2007). In the Rock Creek area, tertiary sediments and volcanics lie *nonconformably* (with a substantial gap in the geological record) on tilted Proterozoic Belt series sediments (figure 4). Here, the main unit of the Eocene volcanic rocks (approximately 50 Ma) is a porphyritic rhyolite or rhyodacite flow

## In Brief

- Mineral inclusions and geochemical features of alluvial Montana sapphires may reflect a metasomatic origin.
- Geochemistry is also useful in differentiating sapphires of Montana origin from sapphires from other localities.
- Fe-Mg-Ga ratios help to distinguish Montana sapphires from material with overlapping properties originating in Umba, Tanzania and Rio Mayo, Colombia.
- Topaz inclusions within sapphire may also indicate a Montana origin.

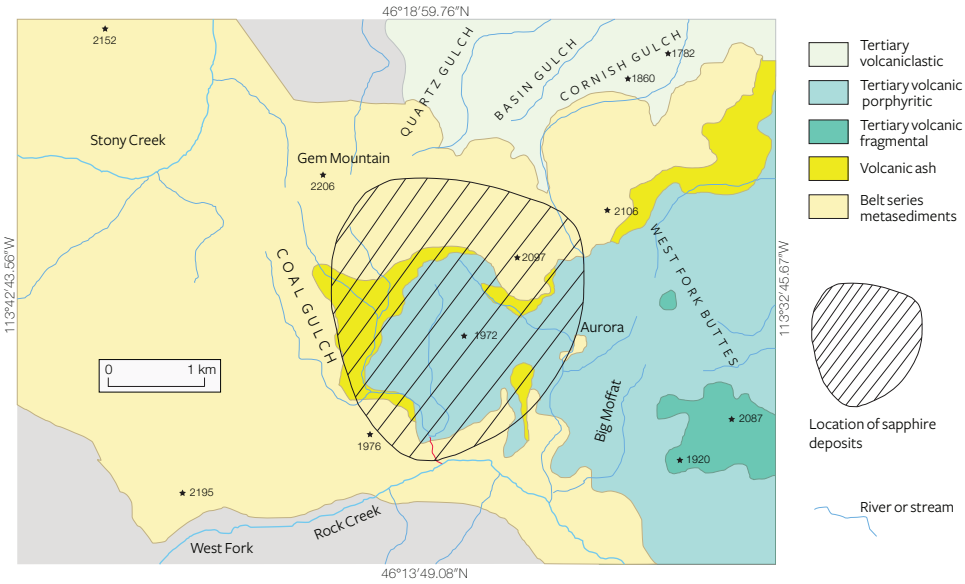


*Figure 4. Geological sketch map of the Rock Creek area showing the location of the alluvial sapphire deposits. Modified from Garland (2002).*

(Garland, 2002; Berg, 2011, Berg, 2014) or, close by, a felsic lapilli tuff (Berger and Berg, 2006; Berg, 2007).

The Yogo primary sapphire deposit is well characterized. Although several hypotheses have been presented for the origin of these gems, the chemical composition of garnet inclusions strongly supports the idea that the sapphires are xenocrysts, formed in a mantle eclogite and subsequently brought to the surface by lamprophyric magma (Cade and Groat, 2006; Giuliani et al., 2007; also compare Baker, 1994; Mychaluk, 1995). The sub-euhedral to euhedral pale reddish orange garnets were Cr-poor (0.02 wt.%), low in $TiO_2$ (0.12 wt.%) and $Na_2O$ (0.02 wt.%), and had average values of MgO (10.7 wt.%), FeO (14.0 wt.%), and CaO (11.2 wt.%) (Cade and Groat, 2006). This indicates that the garnet inclusions were formed in the mantle in group II eclogite, according to Schulze (2003), and that the Yogo sapphires are xenocrysts in the melt, also originating from the mantle.

In contrast, the source and origin of the alluvial deposits are highly enigmatic. The Pleistocene in most of North America was marked by several periods of glaciation, and Garland (2002) suggested that the distribution of the alluvial sapphires in the Rock Creek deposit is due to a post-glacial redistribution of a previously existing paleoplacer of the Pliocene age. The erosion of the paleoplacer resulted in concentrations of sapphires through increased fluvial activity. Garland (2002) further advocated a metamorphic origin, *sensu stricto*, at mid-crustal levels, with an inferred minimum temperature of corundum formation at 600–700°C (deducted from hercynite inclusions in Rock Creek sapphires), with magnetite exsolved around the contact. Based on the assumption of equilibrium of the corundum-anorthite-clinozoisite-muscovite assemblage, and working with the composition of a garnet inclusion, $Grs_{10}Alm_{42}Pyr_{47}$, pressure-temperature (P-T) diagrams indicate approximate formation conditions of 13 kbar and 720°C at $aH_2O = 1$, and 9 kbar and 580°C at $aH_2O = 0.5$. The dominance of $CO_2$ in the fluid inclusions indicates a $CO_2$-rich and/or high-grade metamorphic crystal growth environment. These formation conditions suggest a crystallization depth of approximately 30 km.

Berg (2011) proposed that in the Rock Creek area, the rhyolitic volcanic rocks are the bedrock source—based on the concentration of sapphires in alluvial deposits proximal to or surrounded by rhyolite, the occurrence of sapphires with attached rhyolite, and the lack of fractures and abrasion—indicating limited fluvial transport. At Silver Bow, a minor alluvial occurrence south of Dry Cottonwood Creek, Berger and Berg (2006) and Berg (2007) distinguished two populations of sapphires, in which pastel sapphires (mainly with shades of green, blue, and yellow) showed signs of resorption at the surface and, in some cases, reaction rims with spinel. Fragments of corundum-bearing biotite-sillimanite schist were also found at Silver Bow. Based on these observations, pastel sapphires were interpreted as xenocrysts of metamorphic origin. Berger and Berg (2006) further argued that dark blue sapphires did not show evidence of resorption or reaction minerals, and postulated them to be magmatic phenocrysts, the source melt of which is represented by a 5 mm fragment of dark blue sapphire–bearing igneous rock, recovered from the debris-flow deposits.

When source rocks of sapphire are largely unidentified, inclusions and chemical composition may give additional clues to their original source and genesis. We identified mineral inclusions, characterized the sapphires chemically, and compared our results with existing data.

## MATERIALS AND METHODS

A parcel of approximately 400 faceted sapphires, with a total weight of 702.63 carats, was studied. These samples had been previously removed from the faceted sapphire inventory of the American Gem Corporation (AGC) because of their many large mineral inclusions, which made them ideal for the present study. The samples were mostly brilliant cut, of variable size (mostly between 0.9 and 2.6 ct) and color (see figure 5). Their color ranged from pale to dark blue, yellow to orange, colorless to pale green, and parti-colored (blues and greens with yellow to orange portions). Although most of the parcel was from Rock Creek, a few stones from Dry Cottonwood Creek and the Eldorado Bar deposit on the Missouri River were also included, due to mixing of sapphires from those deposits by the AGC. During the mid-1990s, AGC mined more than 3.5 million carats from Rock Creek and 500,000 carats from Dry Cottonwood Creek. A test mining program at the Eldorado Bar deposit produced several kilograms of rough. All the stones were routinely heat treated.

*Figure 5. A selection of alluvial Montana sapphires from this study. These samples weigh between 0.88 and 1.38 ct. The entire parcel ranged from approximately 0.9 and 2.6 ct and weighed 702.63 carats total. Courtesy of Fine Gems International, © Robert E. Kane.*

**Microscopic Analysis.** Internal features were observed with a standard gemological microscope and a Nikon Eclipse E600 POL polarizing microscope. After selecting sapphires that contained recognizable mineral inclusions, we analyzed 98 dark blue samples, along with 18 green and 9 yellow to orange stones, with a Thermo DXR micro-Raman spectrometer using 532 nm laser excitation. Raman spectra were collected at room temperature in confocal mode, which is necessary for analysis of individual inclusions on a micron scale (1–2 µm). A grating of 1800 grooves/mm and a pinhole size of 25 µm, combined with the optical path length, yielded a spectral resolution of 1.0 $cm^{-1}$. The Raman spectra were interpreted with the help of the RRUFF Raman database of minerals (rruff.info) and other sources (e.g., Wang et al., 2004; Freeman et al., 2008). Depending on the size, position, and orientation of the inclusion analyzed relative to the surface of the host material, the sapphire's Raman peaks at 416 and (rarely) 378 $cm^{-1}$ sometimes appeared in the inclusion's spectrum.

**Laser Ablation–Inductively Coupled Plasma–Mass Spectrometry (LA-ICP-MS).** LA-ICP-MS was used to determine the trace-element composition of 52 of the faceted alluvial sapphires, which were selected after microscopic analysis. Analyses were performed at the Institute of Geosciences, Johannes Gutenberg University (Mainz, Germany), using an ESI NWR 193 nm Excimer laser with an output wavelength of 193 nm coupled to an Agilent 7500ce quadrupole ICP-MS.

Three spot analyses were performed on each sample. We used a spot size of 100 µm and a pulse repetition rate of 10 Hz. The energy density was about 2.6 $J/cm^2$. Ablation was carried out under a helium atmosphere, and the sample gas was mixed with Ar before entering the plasma. Background signals were measured for 15 seconds, followed by 60 seconds of ablation and 20 seconds of washout. We used the multi-element synthetic glass NIST SRM 610 for calibration of the element concentrations, applying the preferred values for NIST SRM 610 reported in the GeoReM database (http://georem.mpch-mainz.gwdg.de; Jochum et al., 2005, 2011) to calculate the element concentrations of the samples. We analyzed USGS BCR-2G and NIST SRM 612 at least nine times during each sequence as quality control materials (QCM) to monitor the precision and accuracy of the measurements. A high-purity synthetic corundum sample was analyzed in addition to the unknown samples to validate the measurements. The calibration with NIST SRM 610 yielded a Ca concentration of several hundred ppmw for the

high-purity synthetic corundum, as it did for the unknown samples. Therefore, we assume Ca to be below the detection limit in all of the unknown samples. The measured Ca values are probably due to interference from the corundum matrix ($^{16}O + {}^{27}Al$) on $^{43}Ca$ (May and Wiedmeyer, 1998).

Glitter 4.4.1 software (www.glitter-gemoc.com) was used for data reduction. Measured isotope intensities were normalized to $^{27}Al$, applying an $Al_2O_3$ content of 100 wt.% for the corundum samples and the values reported in the GeoReM database for the QCM. For most elements, the measured concentrations on the QCM agreed within 15% with the preferred values reported in the GeoReM database (Jochum et al., 2005, 2011). With the QCM, relative standard deviations for the averaged element concentrations determined during the experiment were typically less than 7%. Element/Al ratios were calculated using the element concentrations determined and the assumed $Al_2O_3$ content of 100 wt.%.

## RESULTS

**Mineral Inclusions.** The sapphire samples were selected for their prominent mineral inclusions, as well as other features such as fissures and an abundance of negative crystals, which often showed characteristic dendritic-like surfaces (figure 6). Rutile was the dominant mineral inclusion identified by Raman spectroscopy. Needles exsolved along the crystal plane directions of corundum were observed in a

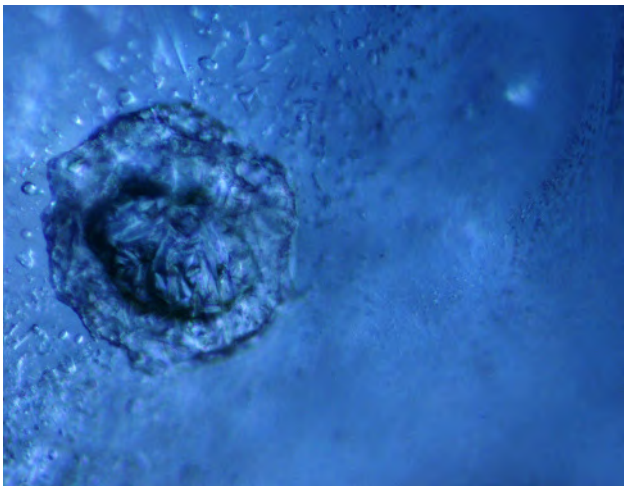

*Figure 6. Negative crystals in a blue sapphire showed dendritic surfaces. Photomicrograph by Hanco Zwaan; field of view 0.35 mm.*

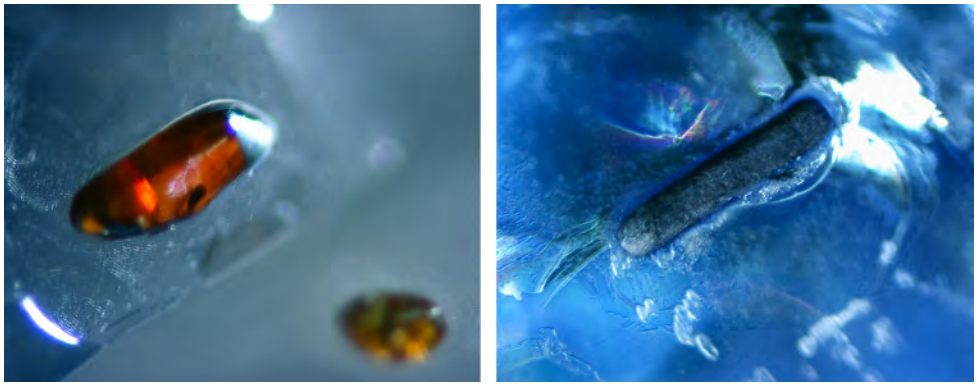

*Figure 7. Prismatic and rounded rutile crystals, both orangy brown (left) and black (right), were encountered using a combination of dark-field and oblique illumination. Photomicrographs by Hanco Zwaan; field of view 0.7 mm (left) and 1.4 mm (right).*

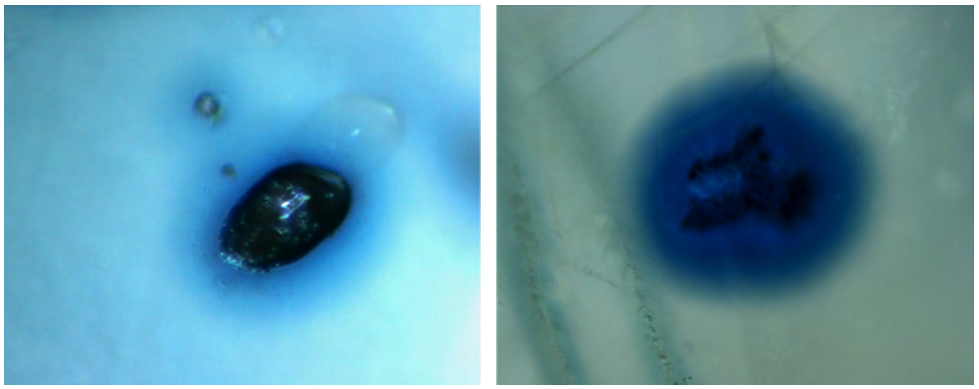

*Figure 8. Blue halos were seen around prismatic rutile, but more often around irregularly shaped grains (using transmitted light and oblique illumination on the left and transmitted light on the right). Photomicrographs by Hanco Zwaan; field of view 0.35 mm (left) and 0.7 mm (right).*

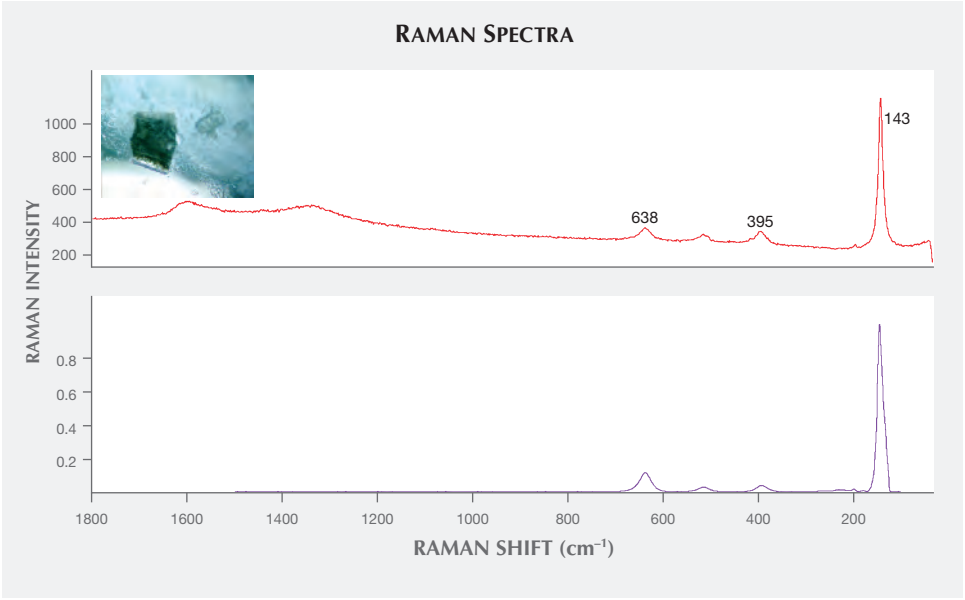


*Figure 9. Anatase, another polymorph of $TiO_2$, is seen here using a combination of oblique and darkfield illumination (inset). The Raman spectrum (top) showed a perfect match with spectra of anatase in the RRUFF database (bottom). Photomicrograph by Hanco Zwaan; field of view 0.7 mm.*

number of sapphires, but prismatic and rounded transparent (orangy) brown or black crystals were more common (figure 7), occasionally with a blue halo (figure 8, left). Moreover, we encountered irregularly shaped rutile grains that usually occurred with a blue halo (figure 8, right). Anatase, the relatively rare polymorph of $TiO_2$, was also found in three sapphires (figure 9).

Ca-rich plagioclase (spectral matches with anorthite and bytownite) and alkali feldspar (with most spectral matches closest to orthoclase) were occasionally encountered. The orientation and prismatic shape of a plagioclase crystal located in the core of a sapphire crystal suggests a protogenetic origin (figure 10). Apart from the spectral matches with the RRUFF database, spectra with bands at 503 and 487 $cm^{-1}$, with a very weak feature at 460 $cm^{-1}$ (group I) and bands at 282 $cm^{-1}$ and 197 $cm^{-1}$ (figure 11), showed a close match with the anorthite spectra of Freeman et al. (2008). The separation between the main group I bands was approximately 17 $cm^{-1}$, close to the average of 19.5 $cm^{-1}$ for anorthite and bytownite compositions. For other members of the plagioclase series with an intermediate composition (labradorite, andesine, and oligoclase), the separation between the main group I bands was about 30 $cm^{-1}$, closer to that of Na-feldspar than Ca-feldspar. Also as in Freeman et al. (2008), the spectra with bands at 512, 480, and 452 $cm^{-1}$ (group I) and bands at 282 and 175 $cm^{-1}$ matched closely with orthoclase, confirming the presence of a potassium-rich feldspar.

Allanite, a black to brown epidote-group mineral with a spectral match closest to allanite-Ce (figure 12), was found in four sapphires. Spectra of the inclusions were similar to those in the RRUFF database for allanite-Ce from Arendal, Norway, and allanite

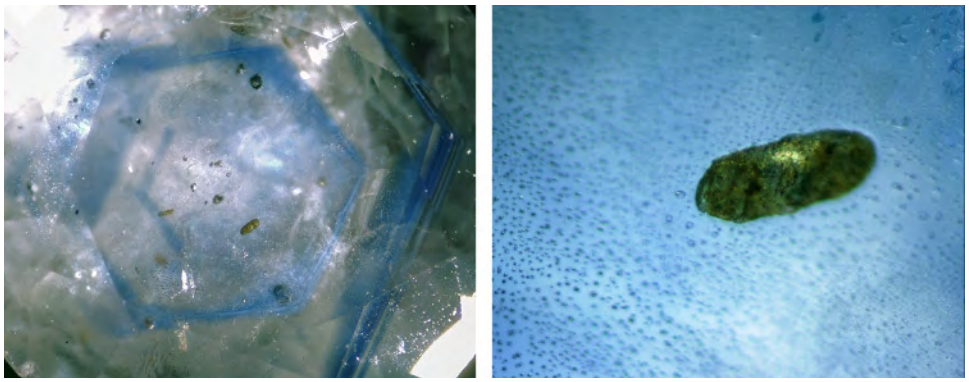

*Figure 10. Calcium-rich plagioclase in the core of a sapphire crystal with hexagonal growth zoning. The prismatic shape (enlarged on the right) and orientation suggest a protogenetic origin. Photomicrographs by Hanco Zwaan, using combination oblique and darkfield illumination; field of view 6.4 mm (left) and 0.7 mm (right).*

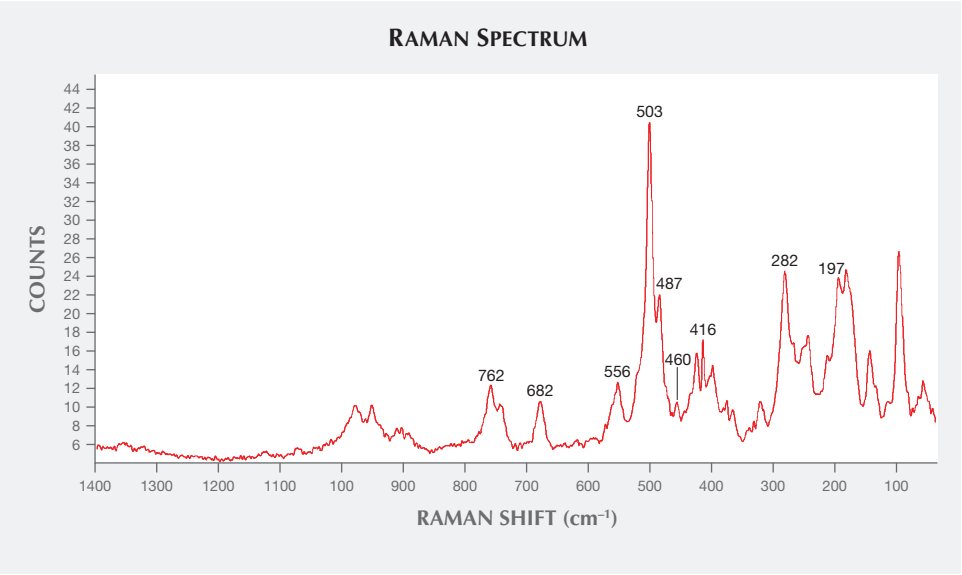


*Figure 11. A Raman spectrum of calcium-rich plagioclase, with main peaks at 503 and 487 cm$^{-1}$, is typical for plagioclase with anorthite and bytownite compositions. The small peak at 416 cm$^{-1}$ is due to the corundum host.*

found in marble from Chillagoe, in northern Queensland, Australia (Lopez and Frost, 2015), showing major bands around 660, 610, 409, 294, and 225 cm$^{-1}$.

In alphabetical order, the other mineral inclusions identified were aluminite ($Al_2SO_4(OH)_4 \cdot 7H_2O$); anhydrite; apatite; barite (figure 13); chalcopyrite (figure 14); cristobalite ($SiO_2$); hematite; ilmenite; magnetite; near-colorless mica; monazite (figure 15); nahcolite ($NaHCO_3$); phlogopite, a pyrochlore-group mineral; spinel; and topaz. Monazite was found in one sample; the spectral match was closest to monazite-Ce, with a main band at 975 cm$^{-1}$ and peaks at 226, 468, 623, 994, 1032, and 1060 cm$^{-1}$ (figure 16; also compare Poitrasson et al., 2000; Nasdala et al., 2010). Topaz was only found in one sapphire (figure 17), but two isolated subhedral grains could be identified within it. Our Raman spectra were in good agreement with the reference spectra of topaz, showing main bands at 238, 265, 285, 331, 402, 455, and 925 cm$^{-1}$ (figure 18).

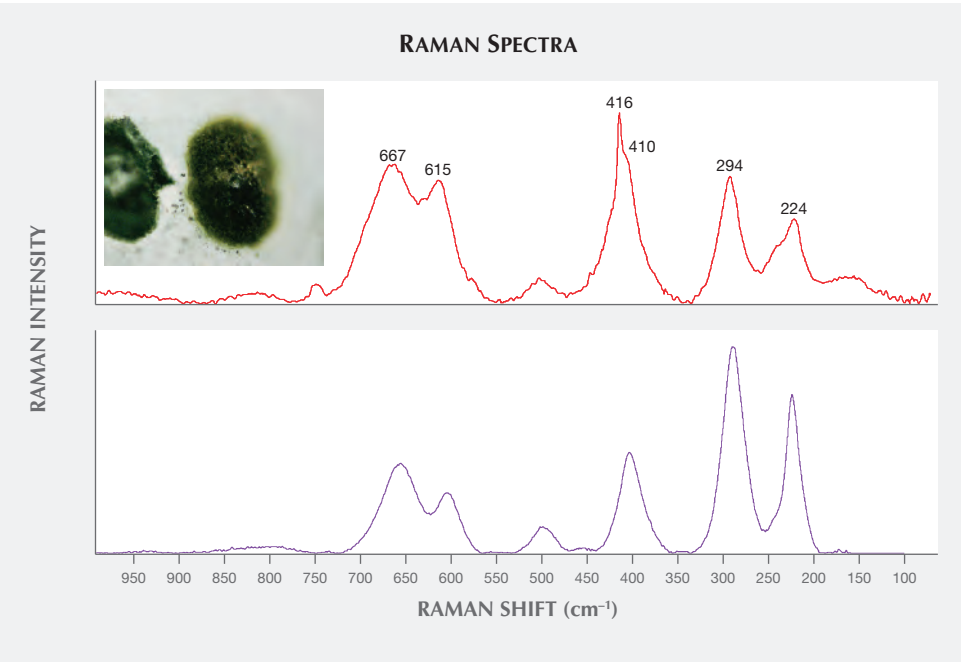


*Figure 12. Allanite, a rare mineral inclusion (shown in transmitted light and oblique illumination, inset), was found in four of the sapphires examined. The Raman spectrum (top) gave a close match with allanite-Ce in the RRUFF database (bottom). The peak at 416 cm$^{-1}$ was caused by the corundum host. Photomicrograph by Hanco Zwaan; field of view 0.7 mm.*

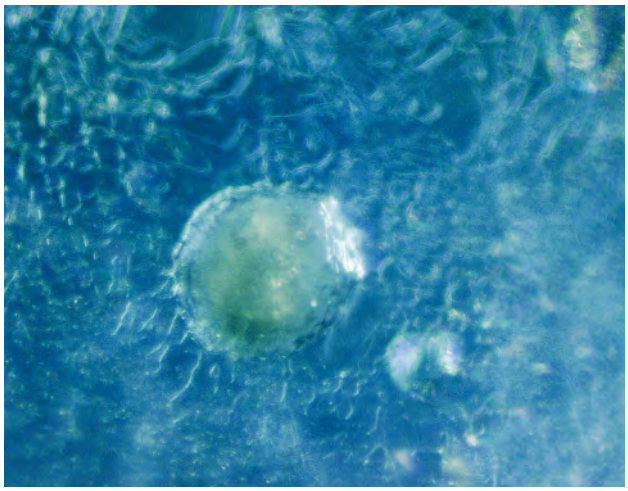

*Figure 13. Barite, seen here using darkfield and oblique illumination, was found in a few samples and showed a rounded and corroded surface in all instances. Photomicrograph by Hanco Zwaan; field of view 0.35 mm.*

*Figure 15. Monazite, shown using transmitted light and oblique illumination, has not been reported before as a mineral inclusion in alluvial Montana sapphires. Photomicrograph by Eric Buter; field of view 0.4 mm.*

Raman spectra of some micas were difficult to interpret. There were spectral matches with muscovite, $KAl_2(AlSi_3O_{10})(OH,F)_2$, and often a slightly better match with the closely related (but Li-bearing) trilithionite, $K(Li,Al)_3(AlSi_3O_{10})(F,OH)_2$. For the pyrochlore-group mineral in one sapphire, a spectral match was found with "uranpyrochlore," a mineral name that has been discredited (Atencio, 2010) but essentially indicates a pyrochlore composition of $Ca_2Nb_2O_7$, possibly close to $(U,Ca,Ce)_2(Nb,Ta)_2O_6(OH,F)$. The encountered spinel-group mineral (figure 19) is difficult to characterize correctly due to existing solid solution series. When comparing spectra with principal peaks at 692 $cm^{-1}$ (Wang et al., 2004), it can either be magnesiochromite $[Mg(Cr,Al,Fe)_2O_4]$ or an Fe-Cr spinel, with a hercynite $[FeAl_2O_4]$ and chromite $[FeCr_2O_4]$ component. The presented spectrum (figure 20) showed a principal peak with a full width at half maximum (FWHM) of about 70 $cm^{-1}$, which was broader than the principal peak of the matching magnesiochromite (FWHM of about 30 $cm^{-1}$), and another reference of chromite (FWHM of about 50 $cm^{-1}$; Wang et al., 2004). This could be due to heat treatment, which is known to cause lattice disorder in spinel at temperatures above 750°C, resulting in a dramatic increase of the width of the prominent feature (Saeseaw et al., 2009). The hexagonal crystal shapes appeared to be strongly determined by the host material (figure 19), indicating a syngenetic growth of spinel and corundum.

*Figure 14. Chalcopyrite grains, shown here in oblique illumination, rarely occur in alluvial sapphires from Montana. Photomicrograph by Hanco Zwaan; field of view 0.7 mm.*

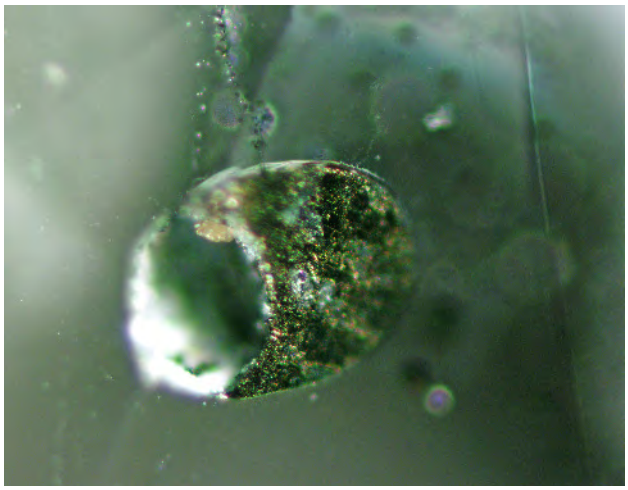

Many atoll-like inclusions, with a central mineral surrounded by a discoid stress halo, did not show clear mineral shapes but had indistinct, roundish, or elongated forms (figure 21). These inclusions did not reveal clear Raman spectra and were interpreted to be of amorphous nature, probably as a result of heat treatment.

**TABLE 1.** Mineral inclusions in Montana sapphires.

| Minerals | Localities | | | | | | | | |
|---|---|---|---|---|---|---|---|---|---|
| | Data from literature* | | | | | | | | |
| | Yogo Gulch | Rock Creek | Dry Cottonwood | Silver Bow | French Bar | Browns Gulch | Eldorado Bar | Montana unspecified | This study (mainly Rock Creek) |
| Albite | | | | Y | | Y | | Y | |
| Alkali feldspar | | | | | | | | Y | Y |
| Allanite | | | | | | | | | Y |
| Almandine garnet | Y | Y | Y | | | | Y | | |
| Aluminite | | | | | | | | | Y |
| Analcime | Y | Y | | | | | Y | Y | |
| Anatase | | | | | | | | | Y |
| Andesine | | | | | | | | Y | |
| Anhydrite | | | Y | | | | | Y | Y |
| Anorthite | | | | | | | | | Y |
| Apatite | | | Y | Y | | Y | | Y | Y |
| Baddeleyite | | | | | | | | Y | |
| Barite | | Y | | | | | | Y | Y |
| Biotite | Y | | Y | | | | | Y | |
| Boehmite | | | | | | | Y | | |
| Bytownite | | | | | | | | | Y |
| Calcite | Y | | Y | | | | Y | Y | |
| Carbon (amorphous) | | | Y | | | | | | |
| Carbonate | | Y | | | | | | | |
| Chalcopyrite | | | | | | | | | Y |
| Clinozoisite | | Y | Y | | | | Y | Y | |
| Cristobalite | | | | | | | | | Y |
| Diaspore | | Y | Y | | | | | | |
| Diopside | | | | | | | | Y | |
| Epidote | | Y | | | | | | | |
| Ferro-columbite | | | | | | | | Y | |
| Fuchsite | | | Y | | | | | | |
| Gibbsite | | Y | | | | | | | |
| Graphite | | Y | | | | | | | |
| Hematite | | Y | | | | | | Y | Y |
| Hercynite | | Y | | | | | Y | Y | |
| Ilmenite | | Y | Y | Y | | Y | | Y | Y |
| Labradorite | Y | Y | Y | | | | | | |
| Magnetite | | Y | | | | | | Y | Y |
| Monazite | | | | | | | | | Y |
| Muscovite*/Lithian mica | | Y | Y | | | | | Y | Y |
| Nahcolite | | | | | | | | | Y |
| Orthoclase | | | Y | | | | | | Y |
| Phlogopite | Y | | Y | Y | | Y | Y | Y | Y |
| Plagioclase | | | | | | | Y | Y | Y |
| Pyrite | Y | | | | | | | Y | |
| Pyrochlore | | | | | | | | Y | Y |
| Pyroxene | | | | | | | | Y | |
| Pyrrhotite | | | Y | | | | | | |
| Rutile | Y | Y | Y | Y | | Y | Y | Y | Y |
| Sphalerite | | | Y | | | | | | |
| Spinel | Y | | | Y | | Y | | Y | Y |
| Topaz | | | | | | | | | Y |
| Uraninite | | | | | | | | Y | |
| Zircon | Y | Y | Y | | Y | Y | | Y | |
| Zoisite | | Y | | | | | | | |

**Berg, 2007; Berg, 2014; Berger and Berg, 2006, Garland, 2002; Giuliani et al., 2007; Gübelin and Koivula, 1986; Gübelin and Koivula, 2008; Williams and Walters, 2004.*

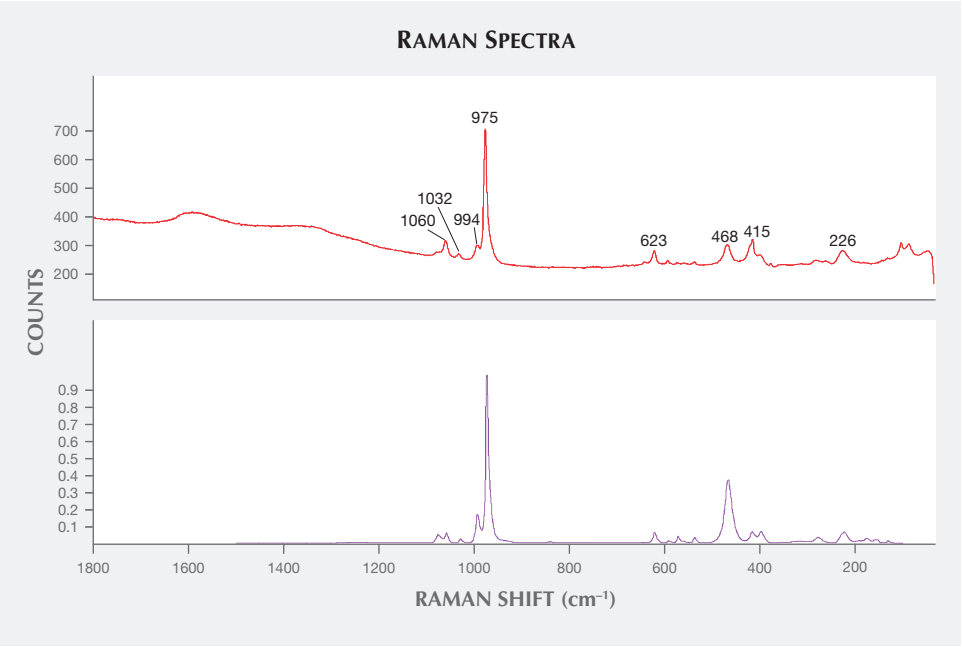


*Figure 16. The Raman spectrum of the monazite inclusion (top) corresponds to a reference spectrum for monazite-Ce (bottom). The peak at 415 $cm^{-1}$ is due to the corundum host.*

The mineral inclusions found are listed along with previously published data in table 1. All of the inclusions were found in blue sapphires. Allanite, apatite, and alkali feldspar also occurred in yellow-orange and green sapphires, and Ca-rich plagioclase was encountered in green samples as well. Apart from mineral inclusions, pronounced hexagonal growth zoning (figure 10, left) and parallel growth structures (planes or lines) were encountered in many stones. These parallel growth lines may or may not be associated with color zoning (see Schmetzer and Schwarz, 2005).

*Figure 17. This topaz crystal, shown using oblique illumination, was observed as a mineral inclusion in an alluvial Montana sapphire; another grain of topaz was found in the same sample. This is the first report of topaz as an inclusion in sapphire. Photomicrograph by Hanco Zwaan; field of view 1.2 mm.*

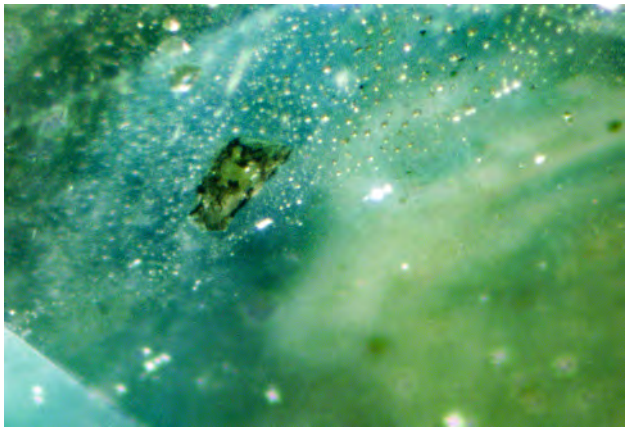

**Chemical Composition.** As summarized in table 2, the alluvial sapphires from Montana showed a rather consistent composition regardless of color. Whether their color was medium to dark blue, green (in some cases caused by blue and yellow zones within one stone), or orange to yellow, they had medium to high Fe (2191–7687 ppmw), low Ti and Ga (18–153 ppmw and 38–65 ppmw, respectively), and medium Mg content (35 ppmw). A green sapphire showed a low Mg content around 10 ppmw, while a dark blue sample that otherwise showed Mg values of 20 and 35 ppmw, very close to the mean value, contained one spot with a very high content of 391 ppmw. This one high value does not appear to be related to the presence of an inclusion or a different color, as values of other elements in the same spot did not reveal similar anomalies.

The higher mean Cr content in yellow to orange samples (43 ppmw) compared to blue and green (19 and 16 ppmw, respectively) is caused by one orange sapphire showing 139–155 ppmw. The other yellow and orange-yellow stones had much lower values, like most blues and greens; one dark blue sapphire also showed elevated Cr values between 91 and 100 ppmw.

Many elements had values below detection limits, with some spots giving higher values. One spot on a dark green stone showed 10 ppmw Mn. For Ni, a sin-

**TABLE 2.** Trace-element concentrations of Montana alluvial sapphires by LA-ICP-MS.[a]

| Color | All colors | | Blue | | Green | | Yellow-orange | | |
|---|---|---|---|---|---|---|---|---|---|
| Number of samples | 52 | | 39 | | 9 | | 4 | | |
| Number of analyses | 156 | | 117 | | 27 | | 12 | | |
| Trace elements (ppmw)[b] | **Range** | **Mean** | **Range** | **Mean** | **Range** | **Mean** | **Range** | **Mean** | **Detection limits** |
| Li | bdl[c]–1.6 | | bdl | | bdl–1.6 | | bdl | | 0.56–1.0 |
| Be | bdl–0.6 | | bdl–0.6 | | bdl | | bdl | | 0.31–1.4 |
| B | bdl–5.4 | | bdl–5.4 | | bdl | | bdl | | 2.2–3.4 |
| Mg | 7.1–391 | 35 | 9.4–391 | 37 | 7.1–58 | 29 | 23–49 | 36 | 0.54–1.0 |
| Ca | bdl | | bdl | | bdl | | bdl | | 107–547 |
| Sc | bdl–1.2 | | bdl–1.2 | | bdl | | bdl | | 0.81–1.3 |
| Ti | 18–153 | 58 | 23–142 | 59 | 18–128 | 50 | 28–153 | 55 | 0.95–4.7 |
| V | 1.1–15 | 5.8 | 1.9–15 | 6.1 | 2.1–10 | 5.2 | 1.1–6.5 | 3.9 | 0.05–0.26 |
| Cr | bdl–155 | 21 | bdl–100 | 19 | 2.3–48 | 16 | 4.1–155 | 43 | 1.4–4.3 |
| Mn | bdl–10 | | bdl | | bdl–10 | | bdl | | 0.72–1.14 |
| Fe | 2191–7687 | 4686 | 2191–7687 | 4598 | 4308–7628 | 5689 | 2259–4046 | 3294 | 4.2–6.2 |
| Co | bdl–0.28 | | bdl–0.28 | | 0.19–0.26 | | bdl | | 0.16–0.39 |
| Ni | bdl–44 | | bdl–1.8 | | bdl–44 | | bdl–1.2 | | 0.48–1.7 |
| Zn | bdl–1.3 | | bdl–1.3 | | bdl–0.9 | | bdl–1.0 | | 0.59–1.8 |
| Ga | 38–65 | 51 | 38–65 | 50 | 45–65 | 54 | 43–59 | 49 | 0.26–0.59 |
| As | bdl–5.7 | | bdl–5.7 | | bdl–5.0 | | bdl–5.5 | | 2.5–4.3 |
| Rb | bdl–0.18 | | bdl–0.18 | | bdl | | bdl | | 0.14–0.39 |
| Sr | bdl–1.4 | | bdl–1.0 | | bdl–1.4 | | bdl–0.5 | | 0.04–0.15 |
| Y | bdl–0.56 | | bdl | | bdl–0.56 | | bdl | | 0.04–0.15 |
| Zr | bdl–0.15 | | bdl–0.14 | | bdl–0.15 | | bdl | | 0.09–0.30 |
| Nb | bdl–0.42 | | bdl–0.42 | | bdl | | bdl | | 0.04–0.14 |
| Mo | bdl–2.4 | | bdl | | bdl | | bdl–2.4 | | 0.19–0.68 |
| Sn | bdl–13 | | bdl–13 | | bdl–11 | | bdl | | 0.10–1.3 |
| Sb | bdl–0.73 | | bdl–0.49 | | bdl | | bdl–0.73 | | 0.29–0.78 |
| Cs | bdl–1.1 | | bdl | | bdl–1.1 | | bdl | | 0.07–0.80 |
| Ba | bdl–28 | | bdl | | bdl–28 | | bdl | | 0.19–0.59 |
| La | bdl–6.5 | | bdl | | bdl–6.5 | | bdl | | 0.03–0.09 |
| Ce | bdl–15 | 0.12 | bdl–1.6 | | bdl–15 | | bdl | | 0.02–0.07 |
| Nd | bdl–4.5 | | bdl–0.18 | | bdl–4.5 | | bdl | | 0.11–0.34 |
| Sm | bdl–0.72 | | bdl | | bdl–0.72 | | bdl | | 0.14–0.44 |
| Eu | bdl–0.7 | | bdl–0.7 | | bdl | | bdl | | 0.03–0.11 |
| W | bdl–15 | | bdl–15 | | bdl | | bdl | | 0.06–0.19 |
| Tl | bdl–0.68 | | bdl–0.68 | | bdl | | bdl | | 0.03–0.10 |
| Pb | bdl–0.19 | | bdl–0.07 | | bdl–0.19 | | bdl–0.18 | | 0.03–0.15 |
| Th | bdl–1.48 | | bdl | | bdl–1.48 | | bdl | | 0.02–0.04 |

[a]*Rock Creek is the main source (see "Materials and Methods").*
[b]*The left column gives the range of concentrations for all stones; the other columns give the ranges according to color. Detection limits may vary with each analysis. Minimum detection limits are given with 99% confidence; Cu, Ge, Yb, Hf, Ta, Ir, Pt, Au, and U were below detection limits in all analyses.*
[c]*Abbreviation: bdl=below detection limit.*

gle spot on a dark green sapphire gave a value of 44 ppmw, while a few spots had values just above the detection limits. In a dark blue sample, the highest recorded value was 1.8 ppmw. Only three spots in three different stones had values ≥1 ppmw Sr. For Mo, a single spot gave 2.4 ppmw. A few measurements showed >1 ppmw Sn and Ba, while two spots were above 1 ppmw for Ce. For La and Nd, only one spot gave 6.5 ppmw and 4.5 ppmw, respectively. One analysis gave 15 ppmw W, while another indicated >1

**TABLE 3.** Trace-element concentrations of Montana alluvial sapphires: comparison with other data.[a]

| Analytical technique | LA-ICP-MS (this study) | | PIXE (Garland, 2002) | | | | | |
|---|---|---|---|---|---|---|---|---|
| Locality | Rock Creek[b] | | Rock Creek | | Dry Cottonwood Creek | | Eldorado Bar | |
| Number of samples | 52 | | 43 | | 15 | | 9 | |
| Number of analyses | 156 | | | | | | | |
| Trace elements (ppmw) | Range | Mean | Range | Mean | Range | Mean | Range | Mean |
| Ti | 18–153 | 58 | 23–118 | 71 | 5–46 | 28 | 15–72 | 40 |
| V | 1.1–15 | 5.8 | bdl[c]–18 | 7 | bdl–40 | 6 | bdl–12 | 5 |
| Cr | bdl–155 | 21 | bdl–551 | 65 | bdl–182 | 26 | bdl–181 | 44 |
| Fe | 2191–7687 | 4686 | 1120–7587 | 4782 | 1575–4596 | 3420 | 2631–6700 | 3866 |
| Ga | 38–65 | 51 | 42–58 | 49 | 39–77 | 50 | 46–55 | 51 |

[a]*Cu, Ge, Yb, Hf, Ta, Ir, Pt, Au, and U were below the detection limits in all analyses.*
[b]*Rock Creek is the main source (see "Materials and Methods").*
[c]*Abbreviation: bdl=below detection limit.*

ppmw Th. All other elements analyzed showed values below or only slightly above detection limits (table 2).

Proton-induced X-ray emission (PIXE) analyses of a similar number of samples (Garland, 2002) for Ti, V, Cr, Fe, and Ga (table 3), showed comparable ranges and mean values. The only exception was Cr, for which PIXE analysis showed a wider range of values in the Rock Creek samples. This is because the suite of 43 sapphires analyzed by Garland (2002) contained six pink samples along with the blue, green, and yellow varieties.

## DISCUSSION

**Mineral Inclusions.** The inclusions are listed in table 1 and compared with previously published data by Gübelin and Koivula (1986, 2008), Garland (2002), Williams and Walters (2004), Berger and Berg (2006), Berg (2007, 2014), and Giuliani et al. (2007). Our study showed the presence of allanite, anatase, chalcopyrite, monazite, and topaz, which were previously unreported, although Berg (2014) inferred the presence of allanite in one sapphire using EDX analysis. Orthoclase and Ca-rich plagioclase (anorthite-

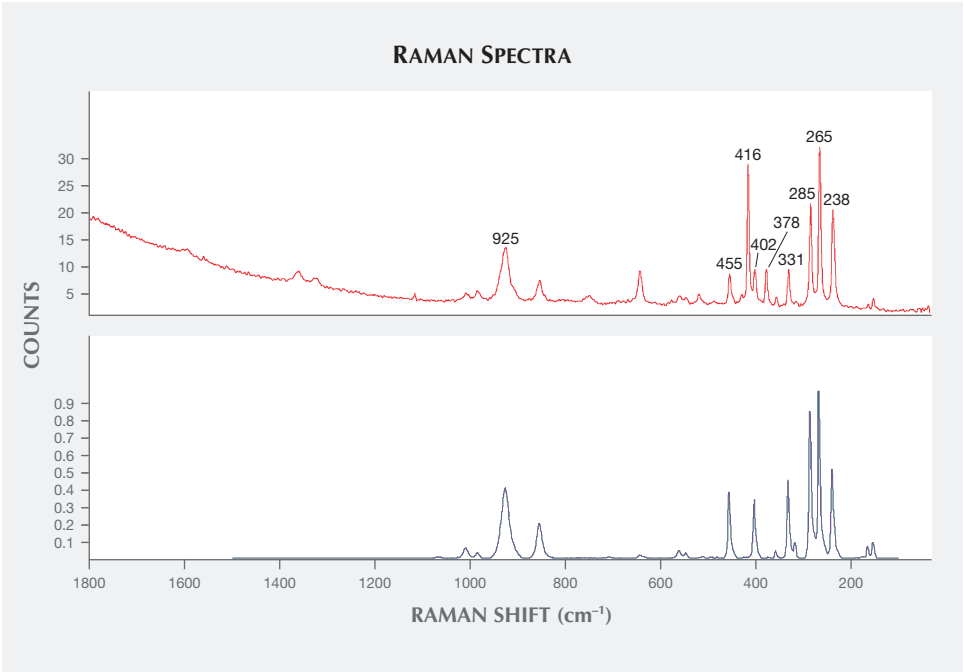


*Figure 18. The Raman spectrum of the topaz inclusions (top) compared well with the reference spectrum (bottom). The peaks at 416 and 378 $cm^{-1}$ are due to the sapphire host.*

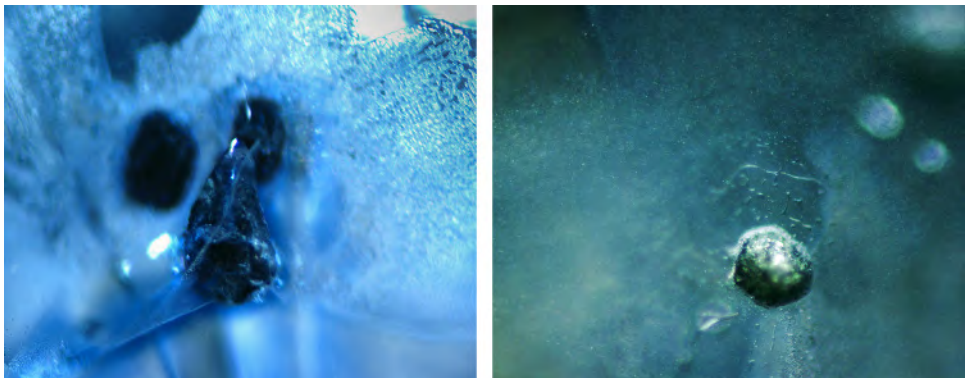

*Figure 19. Spinel inclusions showed a hexagonal outline, indicating syngenetic growth. Rutile inclusions appear in the background of the photomicrograph on the left. The images are shown in transmitted light (left) and oblique illumination (right). Photomicrographs by Hanco Zwaan; field of view 1.4 mm (left) and 0.7 mm (right).*

bytownite) were similar to earlier reported alkali feldspar and labradorite, respectively, whereas phlogopite was consistent with the earlier mention of biotite. In the gemological literature, allanite has been described as an inclusion indicative of a Kashmir origin (Schwieger, 1990), but obviously can no longer be considered a hallmark for that locality. Moreover, allanite has also been found in corundum from Rio Mayo, Colombia (Sutherland et al., 2008).

The predominance of rutile—in many cases the only mineral present—appears to confirm Rock Creek as the most likely sample location, as opposed to Dry Cottonwood Creek and Eldorado Bar (compare with, e.g., Guo et al., 1996; Gübelin and Koivula, 2008; Berg, 2007, 2014). Hexagonal zoning, enhanced by exsolved rutile needles, is regarded as the most evident inclusion feature in alluvial Montana sapphires (Gübelin and Koivula, 2008). The frequent absence of these inclusions, combined with the presence of blue halos around small rutile crystals, confirmed that the samples were heat-treated (compare with Emmett and Douthit, 1993; Gübelin and Koivula, 2008). The strong blue halos are caused by internal diffusion of titanium from rutile into the iron-bearing corundum host during high-temperature treatment (Koivula, 1987). In addition to the blue halos, the most common internal features in heat-treated blue to blue-green alluvial Montana sapphires are blue irregular spots, single blue straight lines, multiple parallel straight lines, and blue hexagonal patterns of parallel straight lines (Kane, 2008). Heat treatment might also be the reason why barite grains

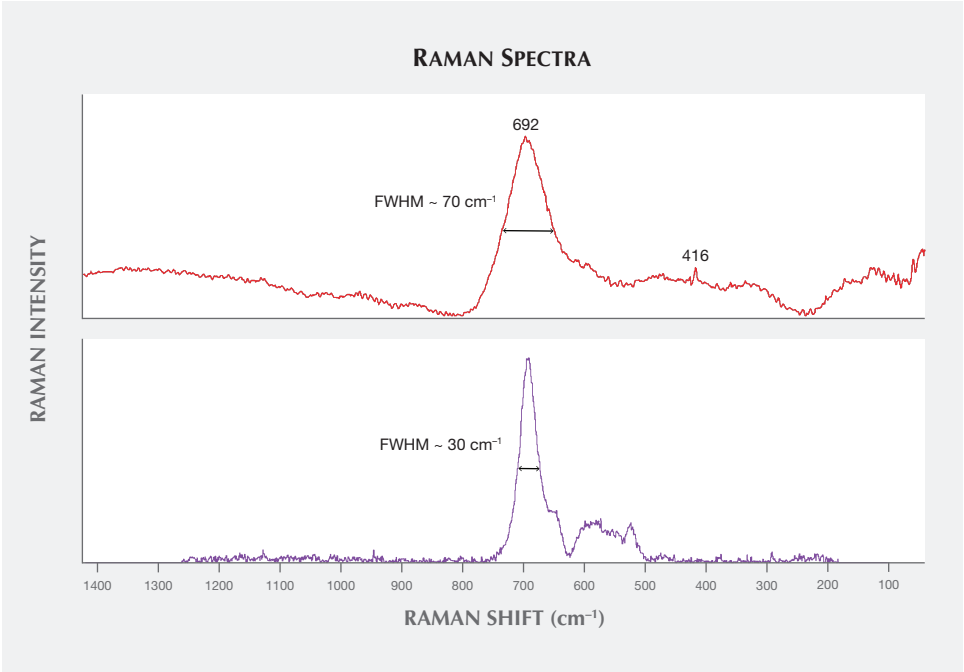


*Figure 20. The Raman spectrum of a spinel-group inclusion (top) showed a principal band at 692 $cm^{-1}$ with a FWHM around 70 $cm^{-1}$. This is broader than the reference spectrum of magnesiochromite and published chromite spectra (bottom), which could be due to heat treatment. The small peak at 416 $cm^{-1}$ was caused by the sapphire host.*

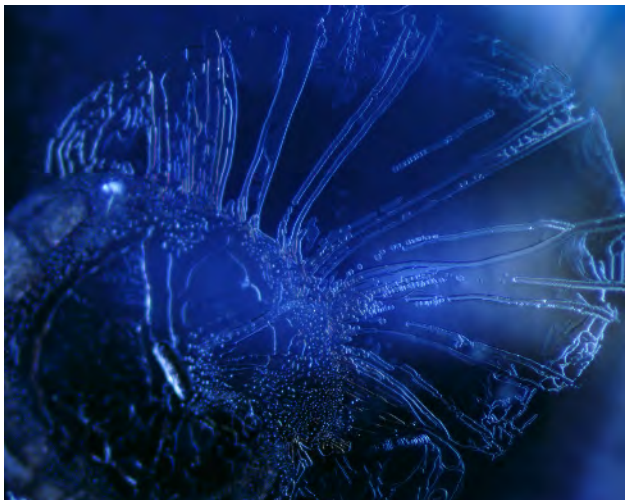

*Figure 21. Atoll-like inclusions were common, with a central mineral surrounded by roundish or elongated shapes. The inclusions are seen here with darkfield and oblique illumination. Photomicrograph by Hanco Zwaan; field of view 1.4 mm.*

showed a rounded and corroded or partially molten surface (figure 13), as blue and green sapphires are heated at 1650°C (Emmett and Douthit, 1993) and the melting point of barite is 1580°C.

The heat treatment routine demands further caution when interpreting the results. Aluminite, a clay-like hydrated/hydrous aluminum sulfate, and nahcolite ($NaHCO_3$), which occurred as a captured phase in a fluid inclusion, were both found in partially healed, surface-reaching fissures. In those fissures, several expanded "snowball"-like inclusions were also present, and therefore both minerals are interpreted as phases related to heat treatment, probably formed during post-treatment cooling. Nahcolite has been found in fluid inclusions in magmatic, metamorphic, and metasomatic rocks (e.g., pegmatites, carbonatites, basaltic glasses, eclogites, granulites, and alkaline metasomatic alteration zones), but is only stable at relatively low temperatures (<600°C, virtually pressure-independent). In natural occurrences, nahcolite is likely a daughter mineral that crystallized from the included fluids as temperature decreased (Liu and Fleet, 2009). As nahcolite was only encountered incidentally, and appears to be related to features caused by heating, it is highly unlikely to be a daughter mineral of natural origin in the sapphires we analyzed.

The low-pressure silica polymorph cristobalite, which is stable above 1470°C at 1 bar pressure but can persist metastably to much lower temperatures (e.g., Deer et al., 2004), was detected in relation to the atoll-like inclusions as ovoid or snowball-like features. Cristobalite is therefore regarded as another result of heat treatment, due to either crystallization out of a molten flux when cooling is not too rapid (compare with Emmett et al., 2003) or the heating of natural glass inclusions. Those inclusions were reported in unheated Rock Creek sapphires by Gübelin and Koivula (2008).

The interior surfaces of negative crystals strongly resembled the dendritic patterns of resolidified surfaces, seen in many high-temperature heat-treated sapphires (Gübelin and Koivula, 2008), and are therefore interpreted as a result of heat treatment as well.

**Mineral Inclusions and Provenance.** Topaz, barite, apatite, monazite, pyrochlore, anatase, allanite, and K-feldspar inclusions in corundum suggest the involvement of pegmatites and related veins during formation, and/or an environment rich in *incompatible elements* and volatiles such as in alkali magmas (Giuliani et al., 2007) and carbonatites (Guo et al., 1996). The presence of chromite-spinel and Ca-rich plagioclase, however, would indicate an ultramafic to mafic igneous source. As a result of metasomatism, phlogopite is often present in association with ultramafic intrusions. Metasomatism is critical to the genesis of many gem corundum deposits, and desilication of an intrusive pegmatite in ultramafic/mafic rock by contact metasomatism is described as a corundum-forming process (e.g., Giuliani et al., 2007; Simonet et al., 2008). Rutile occurred in many of the sapphires from the present study, but particularly in two stones that also contained either chromite-spinel or plagioclase. Yet rutile cannot be considered a possible indicator of source, as it is known to occur in corundum from various origins (e.g., Gübelin and Koivula, 1986, 2008; Smith, 2010).

Mineral inclusions that might be indicative of particular growth environments were found in different samples. This leaves open the possibility that the alluvial sapphires have different sources, as proposed by Berger and Berg (2006). Chemical analyses of the alluvial Montana sapphires containing the particular inclusions mentioned above were further evaluated for any supporting evidence.

**Chemical Composition.** Various geochemical plots of trace-element concentrations and ratios have been used to distinguish between sapphires of various localities and of different origins (e.g., Sutherland et al.,

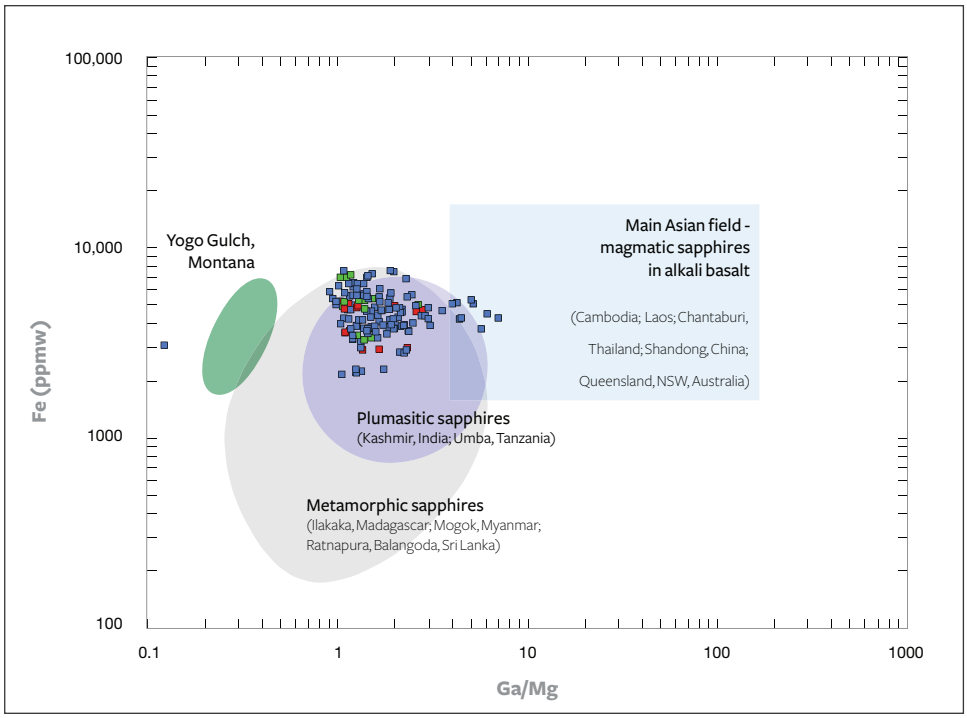


*Figure 22. Compositions of alluvial Montana sapphires (blue, green and red squares) in relation to metamorphic, magmatic and blue plumasitic sapphires (shaded compositional ranges), as shown by Peucat et al. (2007). Red symbols indicate sapphires that contained inclusions suggesting a volatile-rich formation environment, and green symbols represent sapphires that contained inclusions of possible ultramafic/mafic origin. The blue symbols refer to the compositions of the other sapphires analyzed. For further explanation, see text.*

1998; Zaw et al., 2006; Peucat et al., 2007; Sutherland and Abduriyim, 2009). The use of the Ga/Mg ratio versus Fe concentration appears to be an efficient tool to discriminate between the "metamorphic" sapphires, found mainly in metamorphic terrains, and the "magmatic" samples found mainly in alkali basalts and syenite (Peucat et al., 2007; Sutherland and Abduriyim, 2009). Metasomatic (specifically "plumasitic") sapphires can also be plotted in this diagram. These specimens, found in primary metasomatic rocks, are related to fluid interactions between ultramafic/mafic rocks such as serpentinites, amphibolites, and marbles, and aluminum-rich rocks, including granites, pegmatites, and paragneisses such as metapelites (Lawson, 1903; Du Toit, 1946; Peucat et al., 2007). Plumasites are corundum-bearing metasomatic rocks that result from the desilication of ultramafic-intruding pegmatites. Sapphire deposits in both Kashmir (India) and Umba (Tanzania) are closely related to plumasites (Simonet et al., 2008).

The alluvial Montana sapphires largely plotted in a restricted area (figure 22) and did not provide supporting evidence for different sources. The samples that contained inclusions indicative of different growth environments showed completely overlapping compositions. Even in one sapphire containing topaz inclusions (M037), the measured Ga/Mg ratio varied between 1.0 and 2.8 (with Fe between 5315 and 4795 ppmw, respectively), which comprised the Ga/Mg ratio of the bulk of the samples. Also, there were no discernible trends pertaining to Cr, Ti, V, and Ca.

*Figure 23. Compositions of alluvial Montana samples in an Fe-Mg-Ti (ppmw) diagram, showing overlap with metamorphic sapphires from Mogok, Myanmar; metasomatic sapphires from Umba, Tanzania; and sapphires from Rio Mayo, Colombia. Based on this diagram, metasomatic sapphires from Kashmir can be unambiguously separated from alluvial Montana samples.*

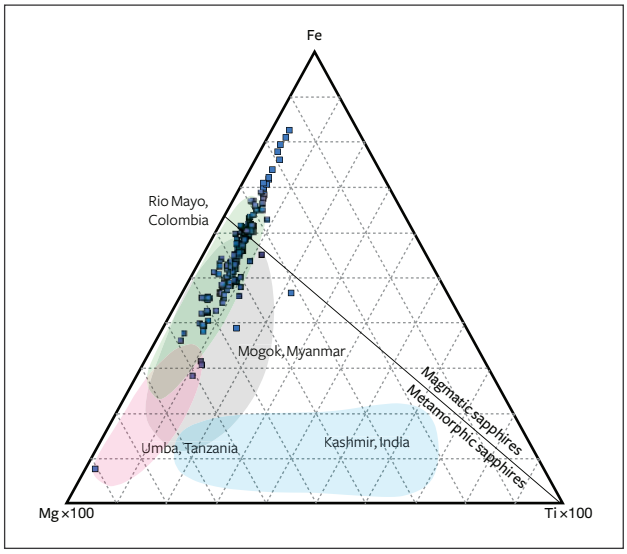

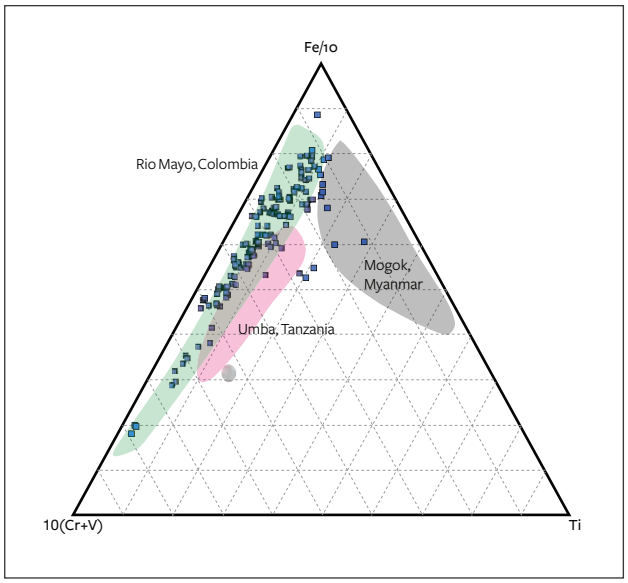


*Figure 24. Alluvial Montana sapphires follow the same trend as those from Rio Mayo, Colombia, and Umba, Tanzania, but can be separated from Mogok sapphires, although individual analyses may show overlap, based on this Fe-(Cr+V)-Ti diagram.*

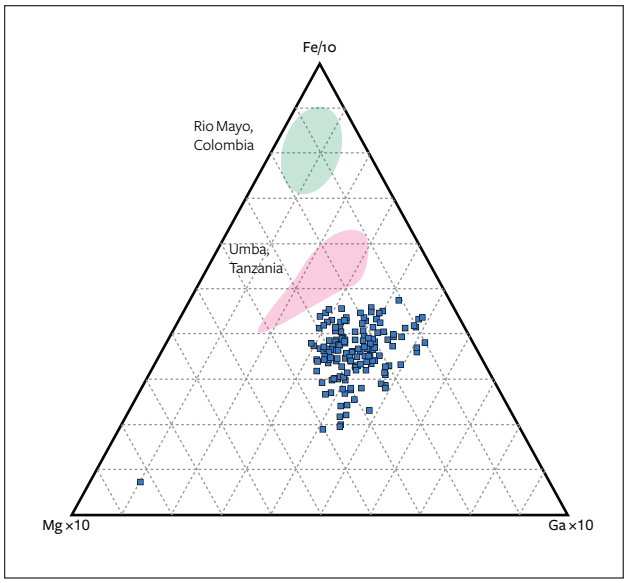


*Figure 25. This Fe-Mg-Ga diagram shows a clear compositional difference between alluvial Montana sapphires and sapphires from Umba and from Rio Mayo.*

Comparing chemical compositions with the large dataset of many sapphire occurrences published by Peucat et al. (2007), and with data for Australian samples (Sutherland and Abduriyim, 2009), the alluvial Montana sapphires can be separated clearly from primary sapphires found at Yogo Gulch, Montana, which are thought to be of mantle origin (see the introduction). Alluvial Montana sapphires plotted in the fields of metamorphic and plumasitic/metasomatic sapphires, with a slight overlap into the magmatic sapphires field (figure 22). Within the metamorphic sapphires, the most overlap occurred with those from Mogok, Myanmar (formerly Burma), which showed a relatively high Fe content (1200–4800 ppmw). The Montana sapphires' composition further overlapped with alluvial samples from Rio Mayo, Colombia. The Colombian sapphires were considered difficult to pinpoint (Peucat et al., 2007). They showed a heterogeneous Fe composition (light blue 2500–4000 ppmw, and dark blue approximately 14,000 ppmw) and a relatively low Ga/Mg ratio (an average ratio of 1.12), indicating that they are different from magmatic types of alkali basalts and geochemically more allied to metamorphic blue sapphires. Sutherland et al. (2008) concluded that Colombian sapphires geochemically fall within the limits of metasomatic, desilicated felsic/ultramafic "plumasitic" associations, supported by high U/Th ratios in included zircon, reflecting a direct metasomatic fluid-rich input for the corundum genesis.

Plotted on an Fe-Mg-Ti diagram, the Montana alluvial sapphires follow the same trend as sapphires from Umba and Rio Mayo and, like the Colombian sapphires, cross the magmatic and metamorphic fields (figure 23). In this diagram, the Montana samples also show an overlap with Mogok material but do not follow the Ti-rich trend of Kashmir sapphires. Although the Montana sapphires cross the magmatic field, they do not follow the clear Fe-Ti trend of most magmatic sapphires (compare Peucat et al., 2007).

The overlapping occurrences can be further separated using a ternary Fe-(Cr+V)-Ti diagram (figure 24). Again, the Montana sapphires follow the same trend as Colombian and Tanzanian sapphires but can largely be distinguished from Burmese sapphires. Plotting slightly toward Ga, they can also be separated from the sapphires of Umba and Rio Mayo in an Fe-Mg-Ga diagram (figure 25).

Other combinations and plots that appeared to be effective in characterizing corundum from Australia, such as Fe/Ti vs. Cr/Ga and Ga/Mg vs. Fe/Mg (Sutherland and Abduriyim, 2009; Sutherland et al., 2009), gave mixed results for alluvial Montana sapphires. They plotted in between metamorphic and magmatic fields, or in both fields, although in the latter combination most of the analyses plotted in the metamorphic field.

Another factor that clearly separates alluvial

Montana sapphires from both magmatic blue sapphires from alkali basalts and syenitic blue sapphires is their 10,000 × Ga/Al ratios, between 0.7 and 1.2. This range is in agreement with values of the continental crust (1.0–1.5) and much lower than that of magmatic sapphires, which vary between 2.5 and 3.7 (Peucat et al., 2007).

Regression is a technique for determining the statistical relationship between two or more variables where a change in a dependent variable is associated with, and depends on, a change in one or more independent variables. Discriminant analysis is a regression-based statistical technique that can be used to determine the classification or group of a particular stone on the basis of its characteristics or essential features. It differs from techniques such as cluster analysis (the demonstrated chemical plots are examples of cluster analysis) in that the classifications or groups to choose from must be known in advance. Each case must have a score on one or more quantitative predictor measures as well as a score on a group measure.

Statistical determination of the most probable deposit type for secondary placer corundum deposits is based on the calculation of discriminating factors from the concentration of oxides in corundum from the main primary deposits (Giuliani et al., 2014). As explained above, the discriminating factors are determined by a statistical analysis that tries to minimize the variance in a certain class (e.g., sapphires of plumasitic origin) while maximizing the variance between classes (e.g., between sapphires of plumasitic and syenitic origin).*

Discriminant analysis of sapphire and ruby deposits in Madagascar has shown its effectiveness in determining the most likely deposit type, although Giuliani et al. (2014) demonstrated that this method needs improvement. For example, for sapphires of plumasitic origin, the discriminant analysis showed two subclasses (P1 and P2), of which P1 shows slight overlap with samples of syenitic origin. Further systematic geological study of the plumasitic primary sapphire occurrences should lead to a more refined typology. Interestingly, when recalculating our analyses of Fe, Cr, V, Ti, Mg, and Ga from ppmw to oxides in weight percent and applying this technique, the alluvial Montana sapphires plot largely in or very close to the field of primary sapphires of plumasitic origin (subclass P1, figure 26). This independent statistical method appears to support a close geochemical affinity between alluvial Montana sapphires and sapphires of plumasitic/metasomatic origin.

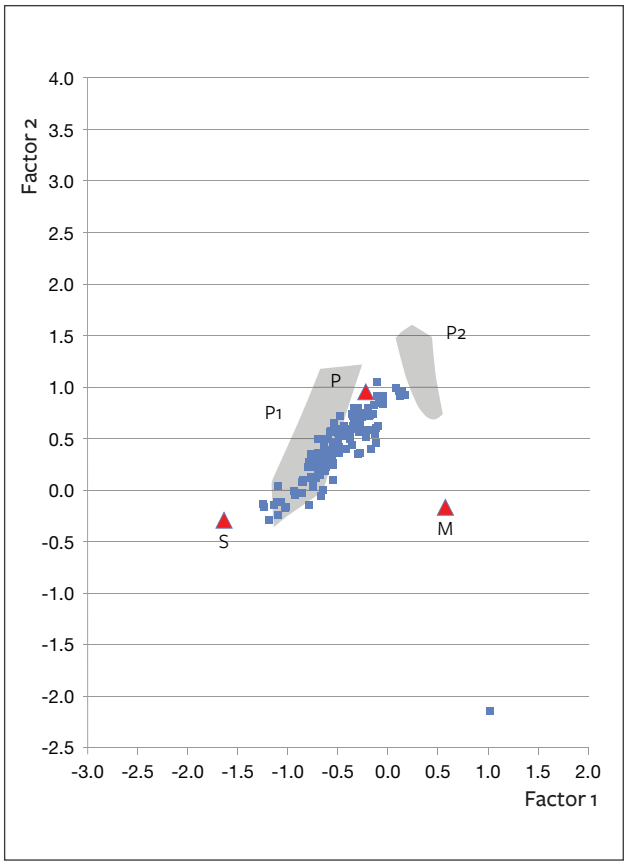


*Figure 26. Discriminant analysis of alluvial Montana samples shows that they plot approximately in the field of primary sapphires of plumasitic origin. P1 and P2 are two subclasses of primary sapphires of plumasitic origin. The red triangles represent the centroids of spaces related to sapphires of syenitic origin (S), plumasitic origin (P), and metasomatic/metamorphic origin (M; compare with Giuliani et al., 2014).*

*The two discriminant factors are defined as:

Factor 1 = 0.23095 × ($Cr_2O_3$ – 0.0613814)/0.0596296 – 0.723839 × (FeO – 0.489593)/0.372367 – 0.0403934 × ($Ga_2O_3$ – 0.0159195)/0.00946033 + 0.0767757 × (MgO – 0.00613983)/0.0040002 – 0.00901195 × ($TiO_2$ – 0.0236271)/0.0567399 + 0.0791335 × ($V_2O_3$ – 0.00402119)/0.00329669

Factor 2 = –0.530426 × ($Cr_2O_3$ – 0.0613814)/0.0596296 – 0.638704 × (FeO – 0.489593)/0.372367 – 0.00893226 × ($Ga_2O_3$ – 0.0159195)/0.00946033 – 0.200622 × (MgO – 0.00613983)/0.0040002 + 0.296868 × ($TiO_2$ – 0.0236271)/0.0567399 – 0.165072 × ($V_2O_3$ – 0.00402119)/0.00329669

*Figure 27. The features of Montana alluvial sapphires indicate a metasomatic origin. They can be separated from material with overlapping properties through their distinct chemical composition. Photo by Robert Weldon/GIA.*

**Implications for the Original Source of Corundum.** Geochemically, the samples in this study were most similar to plumasitic/metasomatic sapphires, as well as metamorphic sapphires from Mogok. The plumasitic sapphires from Kashmir and Umba are related to metasomatic alterations where pegmatites depleted in $SiO_2$ and ultramafic rocks are in contact (e.g., Solesbury, 1967; Atkinson and Kothavala, 1983; Seifert and Hyršl, 1999; Giuliani et al., 2007; Peucat et al., 2007). In the Mogok material, metasomatic exchanges are likely in a complex setting where sapphires are present in "urtite" dikes (rocks containing more than 70% nepheline) and have developed in marble during high-grade metamorphism, with probable interactions with nearby granites (Iyer, 1953; Kane and Kammerling, 1992; Harlow, 2000; Peucat et al., 2007).

The Montana sapphires, showing a similar homogeneous chemical composition, have inclusions that suggest an environment containing *volatile components* (F, OH, P) and incompatible elements (Ba, Ce, Nd, Nb, and possibly Y, La, Ta, Nd, and Th) but that also hint at the presence of ultramafic/mafic rocks. It is therefore also plausible that the alluvial sapphires from Montana were formed during metasomatic alterations between Al- and Mg-rich units.

Involvement of F-rich fluids is supported by the presence of topaz, apatite, and pyrochlore inclusions, and also by the low Ga/Al ratios in the sapphires, which may be caused by extraction of $GaF_6^{3-}$ ions during F-rich fluid circulation. Whalen et al. (1987) explained that this process occurred during partial melting in granulites in the presence of F-rich fluids, depleting granulite restites and enriching the melt in Ga.

Garland (2002) advocated a metamorphic *sensu stricto* origin in a closed system of Montana sapphires (see "Geology and Origin" above), but at the same time recognized that the assumption of equilibrium in the corundum-anorthite-clinozoisite-muscovite assemblage is a problem. No reaction between

corundum and clinozoisite became evident, and there is no indication of an equilibrium relationship between the host and inclusions. Moreover, neither clinozoisite nor zoisite inclusions were found in our study.

Garland (2002) also stated that the Montana sapphires may have formed in the metamorphic events related to the intrusion of the Idaho batholith into largely aluminous Proterozoic metamorphic rocks at the northern and western edge of the batholith (again, see figure 3). The main intrusive phases are late Cretaceous, with smaller associated Tertiary plutons, which developed large hydrothermal systems with associated metasomatism. This would suggest the presence of a more open system during the formation of Montana sapphires, in line with our data and observations.

## CONCLUSIONS

Geochemical features of alluvial sapphires from Montana (figure 27) show significant overlap with trends of plumasitic/metasomatic sapphires. These features and the mineral inclusions identified may reflect a metasomatic origin. Topaz inclusions were observed in one of the samples. Topaz has not been reported as an inclusion in sapphire from any other occurrence, and it may serve to prove a Montana origin. The alluvial Montana sapphires can further be geochemically characterized and distinguished from occurrences with the most overlapping properties (Umba, Tanzania, and Rio Mayo, Colombia) by using concentrations and ratios of Fe, Ga, Mg, Ti, Cr, and V and a combination of Fe-Ga/Mg, Fe-Mg-Ti, Fe-(Cr+V)-Ti, and Fe-Mg-Ga diagrams.

## GLOSSARY

**Batholith:** a large, igneous rock or intrusive body formed at great depth, having an aerial extent of at least 100 $km^2$ (40 sq. mi) and no known floor.

**Foreland basin:** a linear sedimentary basin at a foreland, the exterior area of an orogenic belt where deformation occurs without significant metamorphism. Generally the foreland is the portion of the orogenic belt closest to the continental interior.

**Hydrothermal breccia:** a rock composed of angular broken rock fragments held together by a mineral cement or in a fine-grained matrix. It is formed when hydrothermal fluid fractures a rock mass.

**Incompatible element:** 1. An element for which the ratio of mineral or mineral assemblage to liquid is much less than unity; in other words, the element is concentrated in the liquid. 2. A chemical element that tends to remain in the melt when a magma crystallizes.

**Nonconformity:** a substantial break or gap in the geologic record where a rock is overlain by another that is not next in stratigraphic succession, such as an interruption in the continuity of a depositional sequence of sedimentary rocks or a break between eroded igneous rocks and younger sedimentary strata. It normally implies uplift and erosion with loss of the previously formed record.

**Volatile component:** a material in a magma, such as water or carbon dioxide, whose vapor pressure is sufficiently high to be concentrated in a gaseous phase.

Main source: Jackson (1997)

ABOUT THE AUTHORS

*Dr. Zwaan is head of the Netherlands Gemmological Laboratory and researcher at Naturalis Biodiversity Center in Leiden, the Netherlands. Mr. Buter is associate researcher, also at Naturalis. Dr. Mertz-Kraus is a scientific staff member of the Petrology Group at the Institut für Geowissenschaften, Johannes Gutenberg-Universität, in Mainz, Germany. Mr. Kane is president and CEO of Fine Gems International, in Helena, Montana.*

ACKNOWLEDGMENTS

*The anonymous peer reviewers are thanked for their valuable comments and suggestions. Dirk van der Marel is thanked for assistance with photography and preparing graphics.*

## REFERENCES


Atencio D., Andrade M.B., Christy A.G., Gieré R., Kartashov P.M. (2010) The pyrochlore supergroup of minerals: nomenclature. *Canadian Mineralogist*, Vol. 48, No. 3, pp. 673–698, http://dx.doi.org/10.3749/canmin.48.3.673

Atkinson D., Kothavala R. (1983) Kashmir sapphire. *G&G*, Vol. 19, No. 2, pp. 64–76, http://dx.doi.org/10.5741/GEMS.19.2.64

Baker D.W. (1992) Central Montana alkali province: critical review of Laramide plate tectonic models that extract alkali magmas from abnormally thick Precambrian lithospheric mantle. *Northwest Geology*, Vol. 20/21, pp. 71–95.

——— (1994) Montana sapphires – the value of color. *Northwest Geology*, Vol. 23, pp. 61–75.

Berg R.B. (2007) *Sapphires in the Butte-Deer Lodge Area, Montana*. Montana Bureau of Mines and Geology, Bulletin 134, 59 pp.

——— (2011) Bedrock source of sapphires in alluvial deposits in the Rock Creek, sapphire district, Western Montana. *Geological Society of America, Abstracts with Programs*, Vol. 34, No. 4, p. 9.

——— (2014) *Sapphires in the Southwestern Part of the Rock Creek Sapphire District, Granite County, Montana*. Montana Bureau of Mines and Geology, Bulletin 135, 85 pp.

Berger A.L., Berg R.B. (2006) The Silver Bow sapphire occurrence, Montana: Evidence for a volcanic bedrock source for Montana's alluvial sapphire deposits. *Economic Geology*, Vol. 101, No. 3, pp. 679–684, http://dx.doi.org/10.2113/gsecongeo.101.3.679

Cade A., Groat L.A. (2006) Garnet inclusions in Yogo sapphires. *G&G*, Vol. 42, No. 3, p. 106.

Clabaugh S.E. (1952) *Corundum Deposits in Montana*. U.S. Geological Survey, Bulletin 983, 100 pp.

Deer W.A., Howie R.A., Wise W.S., Zussman J. (2004) *Rock-Forming minerals: Framework Silicates. Silica Minerals, Feldspathoids and the Zeolites*. The Geological Society, London, Volume 4B, 2nd ed., 982 pp.

Du Toit A.L. (1946) Discussion on 'corundum indicator basic rocks and associated pegmatites in the Northern Transvaal by J.W. Brandt'. *Transactions of the Geological Society of South Africa*, Vol. 49, pp. 51–102.

Emmett J.L., Douthit T.R (1993) Heat treating the sapphires of Rock Creek, Montana. *G&G*, Vol. 29, No. 4, 250–272, http://dx.doi.org/10.5741/GEMS.29.4.250

Emmett J.L., Scarratt K., McClure S.F., Moses T., Douthit T.R., Hughes R., Novak S., Shigley J.E., Wang W., Bordelon O., Kane R.E. (2003) Beryllium diffusion of ruby and sapphire. *G&G*, Vol. 39, No. 2, pp. 84–135, http://dx.doi.org/10.5741/GEMS.39.2.84

Evans K.V., Aleinikoff J.N., Obradovich J.D., Fanning M. (2000) SHRIMP U-Pb geochronology of volcanic rocks, Belt Supergroup, western Montana: evidence for rapid deposition of sedimentary strata. *Canadian Journal of Earth Sciences*, Vol. 37, No. 9, pp. 1287–1300, http://dx.doi.org/10.1139/e00-036

Freeman J.J., Wang A., Kuebler K.E., Jolliff B.L., Haskin L.A. (2008) Characterization of natural feldspars by Raman spectroscopy for future planetary exploration. *The Canadian Mineralogist*, Vol. 46, No. 6, pp. 1477–1500.

Fuentes F., DeCelles P.G., Constenius K.N. (2012) Regional structure and kinematic history of the Cordilleran fold-thrust belt in northwestern Montana, USA. *Geosphere*, Vol. 8, No. 5, pp. 1104–1128, http://dx.doi.org/10.1130/GES00773.1

Garland M.A. (2002) The Alluvial Sapphire Deposits of Western Montana. PhD thesis, University of Toronto, Canada, 343 pp.

Giuliani G., Ohnenstetter D., Garnier V., Fallick A.E., Rakotondrazafy M., Schwarz D. (2007) The Geology and Genesis of Gem Corundum Deposits. *Mineralogical Association of Canada, Short Course Series* Vol. 37, pp. 23–78.

Giuliani G., Caumon G., Rakotosamizanany S., Ohnenstetter D., Rakotondrazafy M. (2014) Classification chimique des corindons par analyse factorielle discriminante: application a la typologie des gisements de rubis et saphirs. *Revue de l'Association Française de Gemmologie*, No. 188, pp. 14–22.

Gübelin E.J., Koivula J.I. (1986) *Photoatlas of Inclusions in Gemstones*. ABC Edition, Zurich, Switzerland.

——— (2008) *Photoatlas of Inclusions in Gemstones*, Vol. 3. Opinio Publishers, Basel, Switzerland.

Guo J., O'Reilly S.Y., Griffin W.L. (1996) Corundum from basaltic terrains: a mineral inclusion approach to the enigma. *Contributions to Mineralogy and Petrology*, Vol. 122, No. 4, pp. 368–386, http://dx.doi.org/10.1007/s004100050134

Harlow G.E. (2000) The Mogok Stone Tract, Myanmar: minerals with complex parageneses. *Minerals and Museums 4 Conference Abstracts*, Melbourne, Australia, http://research.amnh.org/users/gharlow/MogokAbsDistrib.pdf

Iyer L.A.N. (1953) The geology and gemstones of the Mogok Stone Tract, Burma. *Memoirs of the Geological Survey of India*, Vol. 82, p. 100.

Jackson J.A. (1997) *Glossary of Geology*, 4th ed. American Geological Institute, Alexandria, VA, 769 pp.

Jochum K.P., Nohl U., Herwig K., Lammel E., Stoll B., Hofmann A.W. (2005) GeoReM: a new geochemical database for reference materials and isotopic standards. *Geostandards and Geoanalytical Research*, Vol. 29, No. 3, pp. 333–338, http://dx.doi.org/10.1111/j.1751-908X.2005.tb00904.x

Jochum K.P., Weis U., Stoll B., Kuzmin D., Yang Q., Raczek I., Jacob D.E., Stracke A., Birbaum K., Frick D.A., Günther D., Enzweiler J. (2011) Determination of reference values for NIST SRM 610-617 glasses following ISO guidelines. *Geostandards and Geoanalytical Research*, Vol. 35, No. 4, pp. 397–429, http://dx.doi.org/10.1111/j.1751-908X.2011.00120.x

Kane R.E. (2004) The sapphires of Montana: A rainbow of color. *Gem Market News*, Vol. 22, No. 1, Pt. 1, pp. 1–8.

——— (2008) American sapphires: Montana and Yogo. *World of Gems Conference 2008*, Gemworld International, Glenview, IL, pp. 59–64.

Kane R.E., Kammerling R.C. (1992) Status of ruby and sapphire mining in the Mogok Stone Tract. *G&G*, Vol. 28, No. 3, pp. 152–174, http://dx.doi.org/10.5741/GEMS.28.3.152

Koivula J.I. (1987) Internal diffusion. *Journal of Gemmology*, Vol. 20, Nos. 7/8, pp. 474–477.

Lawson A.C. (1903) Plumasite, an oligoclase corundum rock, near Spanish Peak, California. *University of California Publications in Geological Sciences*, pp. 219–229.

Liu X., Fleet M.E. (2009) Phase relations of nahcolite and trona at high *P-T* conditions. *Journal of Mineralogical and Petrological Sciences*, Vol. 104, No. 1, pp. 25–36, http://dx.doi.org/10.2465/jmps.080402

López A., Frost R.L. (2015) Identification of allanite $(Ce, Ca, Y)_2(Al, Fe^{3+})_3(SiO_4)_3OH$ found in marble from Chillagoe, Queensland using Raman spectroscopy. *Spectrochimica Acta Part A: Molecular and Biomolecular Spectroscopy*. Vol. 138, pp. 229–233, http://dx.doi.org/10.1016/j.saa.2014.11.052

May T.W., Wiedmeyer R.H. (1998) A table of polyatomic interferences in ICP-MS. *Atomic Spectroscopy*, Vol. 19, No. 5, pp. 150–155.

Mychaluk K.A. (1995) The Yogo sapphire deposit. *G&G*, Vol. 31, No. 1, pp. 28–41, http://dx.doi.org/10.5741/GEMS.31.1.28

Nasdala L., Grötzschel R., Probst S., Bleisteiner B. (2010) Irradiation damage in Monazite-(Ce): an example to the limits of Raman confocality and depth resolution. *Canadian Mineralogist*, Vol. 48, pp. 351–359, http://dx.doi.org/10.3749/canmin.48.2.351

Peucat J.J., Ruffault P., Fritsch E., Bouhnick-le Coz M., Simonet C., Lasnier B. (2007) Ga/Mg ratio as a new geochemical tool to differentiate magmatic from metamorphic blue sapphires. *Lithos*, Vol. 98, Nos. 1–4, pp. 261–274, http://dx.doi.org/10.1016/j.lithos.2007.05.001

Poitrasson F., Chenery S., Shepherd T.J. (2000) Electron microprobe

and LA-ICP-MS study of monazite hydrothermal alteration: Implications for U-Th-Pb geochronology and nuclear ceramics. *Geochimica et Cosmochimica Acta*, Vol. 64, No. 19, pp. 3283–3297, http://dx.doi.org/10.1016/S0016-7037(00)00433-6

Pratt J.H. (1906) *Corundum and Its Occurrence and Distribution in the United States*. U.S. Geological Survey, Bulletin 269, 175 pp.

Saeseaw S., Wang W., Scarratt K., Emmett J.L., Douthit T.R. (2009) Distinguishing heated spinels from unheated natural spinels and from synthetic spinels – a short review of on-going research. http://www.gia.edu/gia-news-research-NR32209A, 13 pp.

Schmetzer K., Schwarz D. (2005) A microscopy-based screening system to identify natural and treated sapphires in the yellow to reddish-orange colour range. *Journal of Gemmology*, Vol. 29, No. 7/8, pp. 407–449.

Schulze D.J. (2003) A classification scheme for mantle-derived garnets in kimberlite: A tool for investigating the mantle and exploring for diamonds. *Lithos*, Vol. 71, No. 2/4, pp. 195–213, http://dx.doi.org/10.1016/S0024-4937(03)00113-0

Schwieger R. (1990) Diagnostic features and heat treatment of Kashmir sapphires. *G&G*, Vol. 26, No. 4, pp. 267–280, http://dx.doi.org/10.5741/GEMS.26.4.267

Seifert A.V., Hyršl J. (1999) Sapphire and garnet from Kalalani, Tanga Province, Tanzania. *G&G*, Vol. 35, No. 2, pp. 108–120, http://dx.doi.org/10.5741/GEMS.35.2.108

Simonet C., Fritsch E., Lasnier B. (2008) A classification of gem corundum deposits aimed towards gem exploration. *Ore Geology Reviews*, Vol. 34, Nos. 1–2, pp. 127–133, http://dx.doi.org/10.1016/j.oregeorev.2007.09.002

Smith C. (2010) Inside sapphires. *Rapaport Diamond Report*, Vol. 33, No. 7, pp. 123–132.

Solesbury F. (1967) Gem corundum pegmatites in NE Tanganyika. *Economic Geology*, Vol. 62, No. 7, pp. 983–991, http://dx.doi.org/10.2113/gsecongeo.62.7.983

Sutherland F.L., Schwarz D., Jobbins E.A., Coenraads R.R., Webb G. (1998) Distinctive gem corundum suites from discrete basalt fields: a comparative study of Barrington, Australia, and West Pailin, Cambodia, gemfields. *Journal of Gemmology*, Vol. 26, No. 2, pp. 65–85.

Sutherland F.L., Duroc-Danner M., Meffre S. (2008) Age and origin of gem corundum and zircon megacrysts from the Mercaderes-Rio Mayo area, South-west Colombia, South America. *Ore Geology Reviews*, Vol. 34, pp. 155–168, http://dx.doi.org/10.1016/j.oregeorev.2008.01.004

Sutherland F.L., Abduriyim A. (2009) Geographic typing of gem corundum: a test case from Australia. *Journal of Gemmology*, Vol. 31, No. 5–6, pp. 203–210.

Sutherland F.L., Zaw K., Meffre S., Giuliani G., Fallick A.E., Graham I.T., Webb G.B. (2009) Gem corundum megacrysts from East Australian basalt fields: trace elements, O isotopes and origins. *Australian Journal of Earth Sciences*, Vol. 56, No. 7, pp. 1003–1020, http://dx.doi.org/10.1080/08120090903112109.

Wang A., Kuebler K.E. Bradley L., Haskin L.A. (2004) Raman spectroscopy of Fe-Ti-Cr-oxides, case study: Martian meteorite EETA 79001. *American Mineralogist*, Vol. 89, Nos. 5–6, pp. 665–680.

Whalen J.B., Currie K.L., Chappell B.W. (1987) A-type granites: geochemical characteristics, discrimination and petrogenesis. *Contributions to Mineralogy and Petrology*, Vol. 95, No. 4, pp. 407–419, http://dx.doi.org/10.1007/BF00402202

Williams T.J., Walters L. (2004) Mineral inclusions in alluvial sapphires from Browns Gulch, southwestern Montana; Implications for the origin of Montana alluvial sapphires. *Geological Society of America, Abstracts with Programs*, Vol. 36, No. 5, p. 225.

Zaw K., Sutherland F.L., Dellapasqua F., Ryan C.G., Yui T.F., Mernagh T.P., Duncan D. (2006) Contrasts in gem corundum characteristics, eastern Australian basaltic fields: trace elements, fluid/melt inclusions and oxygen isotopes. *Mineralogical Magazine*, Vol. 70, No. 6, pp. 669–687, http://dx.doi.org/10.1180/0026461067060356

# The Grand Sapphire of Louis XIV and The Ruspoli Sapphire: Historical and Gemological Discoveries

François Farges, Gérard Panczer, Nassima Benbalagh, and Geoffray Riondet

Since it was added to the French crown jewels in 1669, the 135.74 ct Grand Sapphire has been regarded as one of the world's most magnificent sapphires. Newly discovered archives indicate that Louis XIV obtained the Grand Sapphire at about the same time he acquired the Tavernier Blue diamond; both gems were mounted in gold settings in 1672. Although the Grand Sapphire is often referred to as the "Ruspoli" sapphire, this study shows that these are, in fact, two different gems. Microscopic and spectroscopic evidence (Raman, UV-Vis-NIR absorption, and laser-induced fluorescence) suggest that the Grand Sapphire originated in the metamorphic/detrital terrain of Sri Lanka.

Among the French crown jewels, four are preeminent. The 140.62 ct Regent and the 52.23 ct Grand Sancy diamonds (Balfour, 2009) are held in the Louvre Museum. The approximately 69 ct French Blue diamond was stolen in 1792 and recut to become what is now the Hope diamond (Farges et al., 2009; Post and Farges, 2014), housed at the Smithsonian Institution's National Museum of Natural History. The 135.74 ct Grand Sapphire, shown in figure 1, was donated to the National Museum of Natural History (MNHN) in Paris in 1796 (Morel, 1988) and has remained there ever since.

Like the Grand Sancy and French Blue diamonds, the Grand Sapphire was added to the French crown jewels during the 72-year reign of King Louis XIV (Bapst, 1889). Morel (1988) reports that the gem was purchased from a merchant named Perret, who acquired it from a German prince, who bought it from the Ruspolis, an Italian noble family. This is how the gem also became known as the Ruspoli sapphire. Morel added that it once belonged to a poor Bengali spoon merchant, explaining its other nickname, the Wooden Spoon Seller's sapphire.

While researching the historical archives for the French Blue diamond, we found no evidence of a jeweler named Perret serving Louis XIV. In fact, no such name is found among the registries of jewelers work-

*Figure 1. The 135.74 ct Grand Sapphire, measuring 38 × 29 × 28 mm, was acquired for the French crown jewels during the 72-year reign of Louis XIV (1643–1715). Since 1796, it has been housed in the National Museum of Natural History in Paris (MNHN, inventory number A.67). Photo by François Farges, © MNHN.*

See end of article for About the Authors and Acknowledgments.
Gems & Gemology, Vol. 51, No. 4, pp. 392–409,
http://dx.doi.org/10.5741/GEMS.51.4.392.

*Figure 2. The two designs created by royal jeweler Pierre-André Jacqumin (ca. 1749) for Louis XV's Order of the Golden Fleece emblem. The version on the left shows the approximately 69 ct French Blue diamond below the Côte de Bretagne, a 107.5 ct red spinel carved as a dragon. The version on the right, adorned with two large sapphires, probably would have entailed recutting the Grand Sapphire. Louis XV selected the first design, though the jewel was stolen in 1792. Courtesy of the Herbert Horovitz collection.*

ing in 17th century Paris (Bimbenet-Privat, 2002). Furthermore, no mention of the Ruspoli family surfaced until much later (Barbot, 1858); royal sources from the 17th and 18th centuries never refer to this origin. Because the connection between the Grand Sapphire and the Ruspolis appeared questionable, we conducted a thorough study of the French National Archives in Paris, along with the city's archives, to better understand this confusing pedigree. We also performed an on-site gemological study, using portable instruments, to determine the Grand Sapphire's physical properties. Due to the heightened precautions surrounding the preservation of the historical gemstone, this study was conducted in a single day, in the controlled confines of the MNHN, using portable spectrometers and complementary equipment. From the measurements obtained, we propose reasoned assumptions as to the geological and geographic origin of this famous sapphire.

## BACKGROUND

The earliest dated documentation of the Grand Sapphire is the 1691 inventory of the French crown jewels (Bapst, 1889). The sapphire is described as a "violet sapphire," "lozenge-shaped" and set in gold. Until the end of the 17th century, violet encompassed a color range from indigo blue to purple (Pastoureau, 2000). This range is consistent with the observed color, a medium blue with pale violet hues. The six-sided lozenge cut was rare for the 17th century (and even later). Its weight ("7 gros ½ et 12 grains," equivalent to 28.74 g) is given with its gold setting. That year, the gem was appraised at 40,000 livres, the standard French currency at the time. On average, one livre in 1691 is roughly equivalent to US$15 in 2015 (based on the calculation by Allen, 2001).

In 1739, King Louis XV was inducted as a knight of the Order of the Golden Fleece (Farges et al., 2009). His jeweler, Pierre-André Jacqumin (or Jacquemin), was commissioned to create an insignia of that chivalric order. We recently discovered (Farges et al., 2008) that Jacqumin submitted two proposals: one with two main diamonds, including the French Blue (figure 2, left), and another with two large sapphires (figure 2, right). For the second version, the Grand Sapphire almost certainly would have been recut, as the king asked Jacqumin to use the existing crown jewels in the emblem (Morel, 1988). Because the king chose the diamond insignia, the sapphire was preserved, though its 1672 gold setting had disappeared:

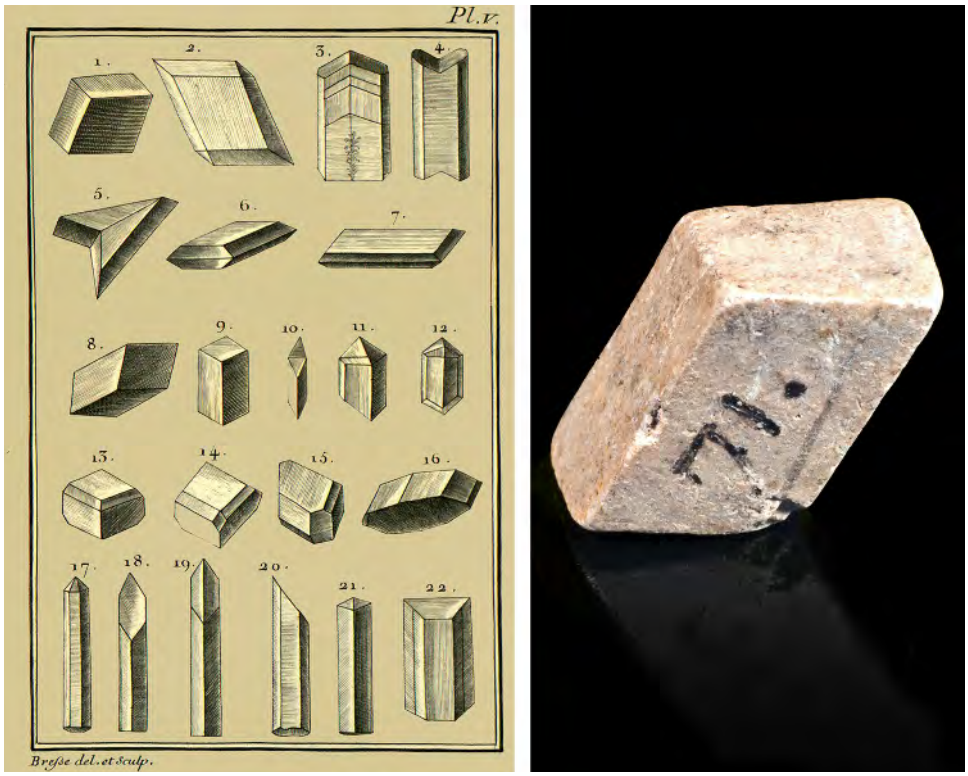


*Figure 3. Left: Plate IV from Romé de l'Isle's* Crystallographie *(1772) shows the Grand Sapphire (number 2 in this figure). Romé de l'Isle thought that sapphire, with calcite (number 1), exhibited the primitive shape of his fifth system of crystallography, the "rhombic parallelepiped." Right: An unglazed ceramic model of the Grand Sapphire (13 × 3 × 3 mm) made for Romé de l'Isle ca. 1770. This model, rediscovered in 2015 at the MNHN, is among the earliest ever produced. Photo by François Farges, © MNHN.*

The sapphire is described without any gold setting in the 1774 royal inventory, kept in the French National Archives. Its weight is listed as 132 old Paris carats, equivalent to 135.18 ct (Morel, 1988). Like all the other jewels of the French Crown, the sapphire was kept within the Garde-Meuble (the royal storehouse), which is now the Hôtel de la Marine on Place de la Concorde in Paris. Hence, it was also known as the "saphir du Garde-Meuble."

French crystallographer Jean-Baptiste Romé de l'Isle (1772) studied the unmounted sapphire and concluded that it was a natural, uncut gem. He even classified the Grand Sapphire as the most ideal crystal form for his fifth crystallographic system, the "rhombic parallelepiped" (figure 3). In the second edition of his *Crystallographie*, Romé de l'Isle (1783) seemed somewhat uncertain about his 1772 conclusion, writing that the gem's facets might be related to human polishing. But Romé de l'Isle later received two crystal models of ruby shaped like the Grand Sapphire, causing him to reassert his original hypothesis (Romé de l'Isle, 1787). That same year, Mathurin Jacques Brisson published the stone's density (equivalent to 3.9941 g/cm$^3$, consistent with corundum), but stated that the stone's shape was "most likely man-faceted" (Brisson, 1787). Despite this observation, the 1789 royal inventory (also kept in the National Archives) describes the sapphire as "not cut"; no appraisal is given. In 1791, another royal inventory now housed in the National Archives (Bion et al., 1791) characterized the sapphire as "a large chunk of sapphire, lozenge, six-sided, polished flat on all its facets. Two clear edges and rounded, bright and clear, weighing 132 k $^3/_{16}$." This was equivalent to 135.88 modern metric carats, with "k" representing old Paris carats. The sapphire's value was appraised at one hundred thousand livres, roughly equivalent to US$1.5 million in 2015.

In September 1792, at the height of the French Revolution, rioters looted the royal treasury and stole most of the crown jewels, including the Regent, Grand Sancy, and French Blue diamonds. According to Morel (1988), the Grand Sapphire was not stolen. In the National Archives, however, we found an inventory completed immediately after the theft, which did not list any sapphires among the few remaining gems (Farges and Benbalagh, 2013). We therefore conclude that the sapphire also disappeared. A subsequent inventory from the Paris archives, dated December 23, 1792, contains the Grand Sapphire and other important sapphires of the French crown jewels (see box A). Presumably, these were recovered shortly after the looting, along with other notable gems, including the Peach Blossom and Hortensia diamonds (Bapst, 1889).

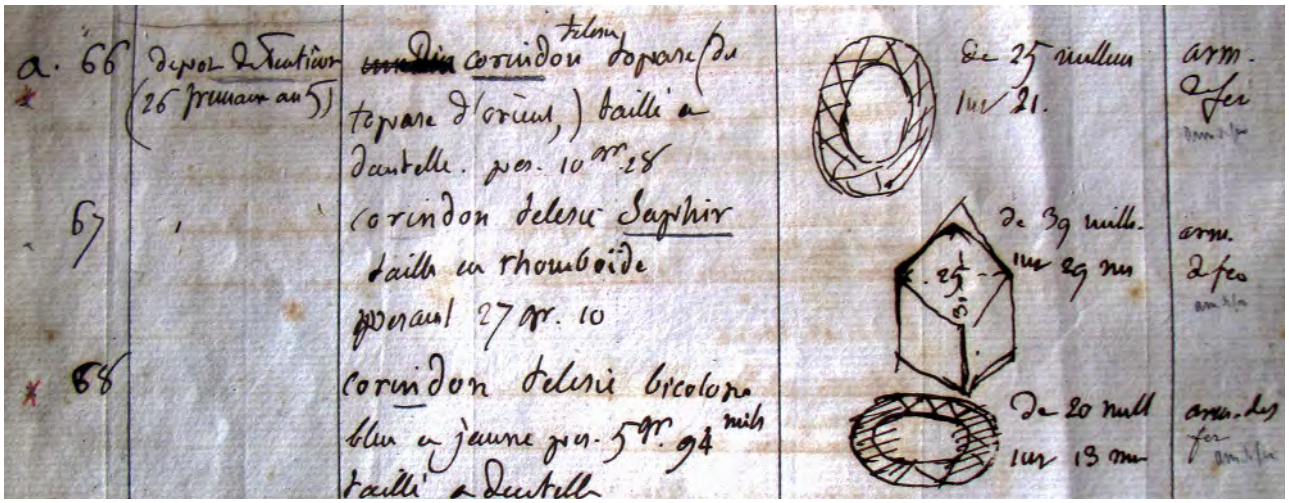

*Figure 4. In this official MNHN inventory, ca. 1800, the Grand Sapphire is seen in the middle row (item "a.67"). Photo by François Farges, © MNHN.*

The Grand Sapphire was among the royal gems donated to the MNHN's mineralogy gallery in 1796 (figure 4) for the purpose of "public education" (Morel, 1988), most likely because state officials accepted Romé de l'Isle's belief that the sapphire was an uncut crystal. Louis Jean-Marie Daubenton, head professor of mineralogy at the MNHN, probably knew of the gem's cut and prestigious pedigree (Morel, 1988). Indeed, his most distinguished scholar, René-Just Haüy (later regarded as the "father of modern crystallography"), soon recognized that the sapphire shape bore the "polish of art" (Haüy, 1801).

Since the sapphire's acquisition by the museum, little has happened with it. Barbot (1858) wrote:

> The most beautiful sapphire known is oriental; it is described in the Inventory of the French crown jewels, performed in 1791; its history is quite intriguing. This

## Box A: The French Crown Jewels Since the 1792 Looting

Soon after the looting of the royal storehouse, a first inventory was conducted on September 21, 1792. Officials established a loss of more than 95% of the treasure inventoried a year earlier (see Bion et al., 1791). But in October 1792, several of the thieves were identified. On his way to the guillotine, a man named Depeyron confessed (in exchange for his life) where he had hidden several large gems, including the Hortensia and one of the Mazarin diamonds (Bapst, 1889). As the investigation progressed, many jewels were eventually recovered. Inventories were thus regularly compiled to demonstrate that the police were conducting an efficient investigation. This is how the Grand Sapphire of Louis XIV resurfaced in December 1792. Eventually, the Grand Sancy and Regent diamonds were discovered during the spring of 1794. The only large gem never recovered was the French Blue, which was not considered as important as the colorless diamonds.

Once most of the French crown jewels were recovered, a committee decided to contribute the pieces to various museums for the public's benefit. Other royal collections were also dispersed, including artworks, precious books, and furniture. While jewels were assigned to the forthcoming Louvre museum, the Grand Sapphire was considered a mineral and thus went to the MNHN.

When the French Empire was established in 1804, the crown jewels were reconstructed, with new acquisitions compensating for the 1792 losses. In 1887, the French government sold off most of the treasures, and only two dozen pieces were preserved for historical purposes. Most pieces were purchased by private collectors and companies such as Tiffany. Many gems were then dismounted, recut, or altered to a more modern taste. Today, France is attempting to recover the surviving pieces as part of its cultural heritage. Since 2014, the crown jewels donated to the MNHN have been displayed in a permanent exhibit, "Treasures of the Earth."

> sapphire, with no flaws or defects, weighs 132 $^{1}/_{16}$ carats [old Paris carats, equivalent to 135.75 modern metric carats], it has a lozenge six-sided shape and is polished flat on all its facets. It is appraised at 100,000 francs.

Then, Barbot added this previously unpublished information:

> This marvelous sapphire was found in Bengal by a poor man who was selling wooden spoons, so the gem bears this nickname. Afterwards, it belonged to the Rospoli [*sic*] House in Rome from which it was then purchased by a Prince of Germany, who in turn sold it to Perret, a French jeweler, for 170,000 francs. This was the stone involved in the famous trial of the sapphire. Considering its qualities and its extraordinary weight, we think that this sapphire's valuation is not properly well estimated. It is now in the Musée de Minéralogie.

The first excerpt clearly refers to the Grand Sapphire. In the second excerpt, Barbot is the first to mention the sapphire's previous owners, including the Bengali spoon seller, the Ruspolis (an Italian noble family misspelled by Barbot), a German prince, and finally Perret. Barbot also refers to "the famous trial" in which the gem was supposedly involved (which will be discussed at greater length). Since then, the Grand Sapphire has often been referred to as the "Ruspoli" (Simonin, 1867) or the Wooden Spoon Seller's sapphire (Snively, 1872; Streeter, 1877; Tagore, 1879). The many inconsistencies in the gem's narrative prompted us to reexamine those references, in order to better understand the historical, geographical, and geological origins of this extraordinary gem.

## MATERIALS AND METHODS

**Archives.** We extensively investigated a series of unpublished documents uncovered in various locations, including the MNHN, the National Archives, the Paris city and departmental archives (Archives municipales and départementales), and the archives at the École Militaire and the National Library of France (BnF), all in Paris. We have also reviewed the diplomatic archives of the French Foreign Ministry in La Courneuve. This last search included the recently discovered books of royal gemstones (*Livres des Pierreries du Roi*), consisting of dozens of volumes produced between 1669 and 1789 and containing thousands of pages of unpublished information.

**On-Site Experiments.** Weight, goniometric, microscopic, and spectroscopic testing was conducted using portable instruments, as the sapphire was not allowed to leave the museum. These miniature instruments are well suited for examining highly valuable or oversized artifacts that cannot be transferred from the museum to a regular laboratory. The main limitation of portable instruments is their reduced specifications (low energy output, lateral resolution, and signal-to-noise ratio, among others) compared to larger versions of these instruments.

The analyses included Raman scattering spectroscopy using an Ocean Optics QE 65000 spectrometer, with 532 and 785 nm excitation lasers; near-ultraviolet to near-infrared (UV-Vis-NIR) spectroscopy with an Ocean Optics USB2000 spectrometer, covering a 350–1000 nm range with a spectral resolution of 1.5 nm (FWHM), using a tungsten lamp; and photoluminescence spectroscopy, induced by either a UV lamp (365 nm) or a continuous green laser operating at 532 nm excitation, all at ambient temperature. The fluorescence emission was collected with an optical fiber and analyzed by the Ocean Optics USB2000 spectrometer described previously (Panczer et al., 2013), using a UV lamp as the excitation source (254 and 365 nm, 6 W each). We also used a Marie Putois and Rochelle contact goniometer (from 1794), a binocular microscope (Krüss KSW4000 with 10× and 30× magnification), a Krüss GMKR10 professional refractometer with an LED source, and a Krüss GMKR13 polariscope.

**Off-Site Experiments.** For the items allowed to leave the exhibition gallery, such as the replica described below, 3-D laser scanning was performed at MNHN's Surfaçus facility using a Konica Minolta Range 7 operating with a 660 nm laser (accurate to approximately 4 µm). Scanned data were reduced (edge-collapse decimation) using MeshLab, GemCad, and DiamCalc

## In Brief

- The lozenge-shaped Grand Sapphire, acquired by Louis XIV in 1669, was lost during the theft of the crown jewels in 1792 but recovered soon thereafter.
- Since 1858, the gem has often been confused with the Ruspoli sapphire, a square cushion cut that belonged to H.P. Hope and later to Ileana of Romania.
- Gemological investigation indicates that the Grand Sapphire has a Sri Lankan origin. This unique gem is one of the main attractions at the National Museum of Natural History in Paris.

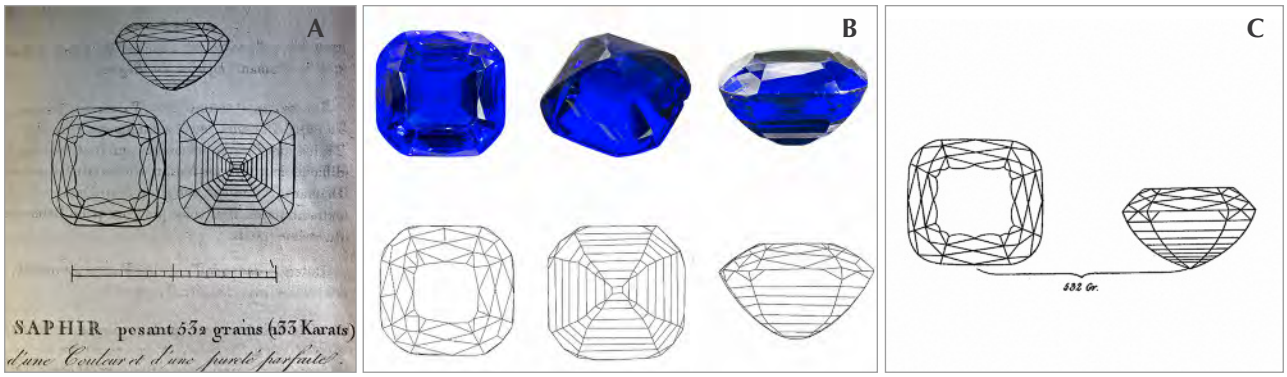


*Figure 5. Images of the Ruspoli sapphire. A: An illustration from the 1813 auction leaflet for the gem, © Bibliothèque National de France. B: The top row shows the historical replica of the Ruspoli sapphire, ca. 1830 (30 × 29 × 15 mm; MNHN inventory number 50.167). The bottom row shows the laser-scanned 3-D model after edge-collapse decimation, © MNHN. C: A drawing from Hertz (1839) of H.P. Hope's largest sapphire (private collection). Photos by François Farges.*

software packages for final adjustments of facets. Chemical analyses were performed with an SD3 Bruker solid-state X-ray detector (133 eV resolution) installed in a Tescan Vega II LSU scanning electron microscope operated in low-pressure mode (20 Pa) at 20 kV.

## RESULTS AND DISCUSSION

**The "Trial of the Sapphire."** In our archival search for a jeweler named Perret who might be involved in the story of the Grand Sapphire, only one match was found, from a trial conducted between 1811 and 1813 (Méjan, 1811; Berryer, 1839). A few months before the trial, Jean-François Perret purchased a large sapphire that allegedly once belonged to the Ruspoli family. He sold the gem to Milanese jeweler Antonio Fusi, who paid a deposit. A few days after this transaction, Fusi tried to cancel the sale and have his deposit refunded, but Perret refused. After the two-year trial, Fusi was ordered to pay Perret the balance due. To satisfy the judgment, the court seized the sapphire and sold it at auction in December 1813 ("Le procès du saphir," 1813).

At the time of this trial, the Grand Sapphire had been kept at the MNHN for nearly 20 years. We found no evidence showing that this gem was sold by the MNHN before the trial and recovered later. Therefore, those pieces of information are contradictory. But Pierre-Nicolas Berryer, the lawyer who represented Perret, described this sapphire involved in the 1811–1813 trial as "of the purest sky blue, with an oval shape with symmetrical facets … much more magnificent than the well-known one of the royal storehouse; unique for its kind, it was priceless" (Berryer, 1839).

While Berryer failed to mention the gem's weight, a legal expert named Maurice Méjan published an 1811 summary of recent trials, including that of the sapphire. Fortunately, Méjan recorded its weight as 133 old Paris carats (equivalent to 136.9 modern carats). Regardless, the shape and cut given by Berryer are not consistent with the Grand Sapphire. Notice, too, that Berryer compares the sapphire to one from "the royal storehouse," the well-documented nickname of the Grand Sapphire prior to the 1792 looting (Farges and Dubois, 2013). In other words, Berryer considered the Grand Sapphire and the Ruspoli sapphire two distinct stones.

**The Real Ruspoli Sapphire Rediscovered.** In 2013, during a search of the National Library in Paris, we found a leaflet connected to the December 1813 court-ordered auction (inventory number SZ-1350). The leaflet claims that the sapphire was owned by a poor Bengali wooden spoon seller, the Ruspolis, and even Charlemagne, "who is believed to have received the gem from an Indian prince." Yet there is no evidence within the document to support any of this. Therefore, we are skeptical of any historical provenance published in this leaflet, including the association with the Ruspoli family, and consider it the seller's attempt to influence the price.

The auction leaflet shows a drawing of the sapphire involved in the trial (figure 5A). This drawing had to accurately represent the gem, which was on public display at the Hôtel Bullion in Paris a few weeks before the sale ("Le procès du saphir," 1813). The stone depicted has a square cushion shape with rounded corners, brilliant faceting on the crown, and a step-cut pavilion. This drawing does not even re-

motely resemble the Grand Sapphire, but it does match Berryer's 1839 description of the sapphire from the trial. The weight of this gem (136.9 ct when converted to metric carats) is close, but not identical, to that of the Grand Sapphire (135.74 ct). Therefore, the gem attributed to the Ruspolis in the auction leaflet is not the Grand Sapphire. Barbot clearly confused them in his 1858 treatise. How did this happen?

In 2012, we found a blue glass replica of a large gemstone in the MNHN drawers. Inventoried as no. 50.167, the replica is composed of a potassic lead glass ("strass"), according to SEM/EDX data, and doped with minor amounts of cobalt (approximately 0.2 wt.% CoO) that account for its vivid blue color. The 3-D model for this replica, obtained through laser scanning, is similar to the drawing of the Ruspoli sapphire (figure 5B, bottom). Its volume corresponds to a sapphire weighing 163 ct. The MNHN inventory, dated 1850 (but donated much earlier; see Farges et al., 2009), states:

| Inv. no. | Origin | Description | Location |
|---|---|---|---|
| *(18)50.167* | *Mr. Achard* | *Model in strass of a very nice sapphire belonging to Mr. Hoppe, and sold by Mr. Achard* | *Technological showcase No. 9* |

"Mr. Achard" is most likely David Achard, a Parisian jeweler from 1807 to 1831, who also donated the lead casts of the French Blue (MNHN inventory number 50.165) and another diamond (MNHN inventory number 50.166). Haüy (1817) named Achard the leading Parisian lapidary and jeweler. "Mr. Hoppe of London" is none other than Henry Philip Hope, for whom the Hope diamond is named (Farges et al., 2009).

The sale of the sapphire to Hope is confirmed by his catalogue of gems, compiled in 1839 by Bram Hertz, a prominent London jeweler. This inventory confirms the MNHN records: the drawing of his largest sapphire (figure 5C) is identical to the glass replica (MNHN inventory number 50.167; figure 5B). Also, Hertz's 1839 drawing closely resembles the one from the 1813 auction leaflet (compare figures 5A and 5C). Furthermore, their weights correspond exactly with 532 grains (equivalent to 136.9 ct). Therefore, it would seem that Achard purchased the sapphire sometime after the 1813 auction and, before his death in 1831, sold the stone to Hope. At some point during this period, Achard donated the replica to the MNHN, where it was exhibited next to the Grand Sapphire in the same "Technological showcase No. 9" (described in Hugard, 1855). Our hypothesis is that Barbot examined both stones while visiting the MNHN's gallery of mineralogy and confused them in his book.

Hertz (1839) describes Hope's sapphire, now identified as the Ruspoli, as

> A very large and fine sapphire, of a square shape with rounded corners, and of a very fine velvet-blue colour, resembling the flower of the bluebottle found among the corn. It is of the purest and of a most charming hue, having, moreover, the advantage of displaying its beautiful colour equally as fine by candle as by day-light, a quality which is rarely met with in a sapphire. It is very finely cut, and shows an extraordinary refulgence…This beautiful sapphire is set as a medallion, surrounded by 23 fine large brilliants, averaging three grains each: it is kept in the 16th drawer—Wide plate 10… 532 grains.

The drawer mentioned above refers to a cabinet in which Hope stored his gem collection. The "wide plates" are a set of drawings for the most important gems from the collection, published by Hertz (1839) as an appendix to his inventory. Inside the tenth plate is the drawing of the sapphire (reproduced within figure 5C). Note that in Méjan (1811) and Hertz (1839), the weight of the sapphire remains unchanged at 532 grains, even though Paris and London used different units at the time. In other words, during his inventory of Hope's largest sapphire, Hertz simply repeated the French weight from 1811 without reweighing it in London units.

**Later Whereabouts of the Ruspoli Sapphire.** Emanuel (1867) wrote that "in the Russian treasury are some [sapphires] of an enormous size, amongst them one of a light-blue tint, which formerly was in the possession of the late Mr. Hope." Emanuel is most likely referring to the Ruspoli, easily the largest sapphire in Hope's collection (Hertz, 1839). A portrait of Empress Marie Fyodorovna of Russia, housed at the Irkutsk Regional Art Museum, shows an impressive set of sapphire jewels. Among them is a squared sapphire in the center that could be the Ruspoli. Later, the stone was reset as the centerpiece of a sapphire and diamond *kokoshnik* (a Russian headdress) created by Cartier in 1909 and owned by the Grand Duchess Maria Pavlovna of Russia (Munn, 2001). The *kokoshnik* later belonged to Queen Marie of Romania (figure 6) and her daughter Ileana. The latter revealed that she sold the headpiece to a famous jeweler in New York around 1950 (Ileana, 1951) but did not give additional details on that transaction. Thus, the recent whereabouts of this *kokoshnik* and the Ruspoli sapphire are unknown. Although Ileana

*Figure 6. In this portrait by Philip Alexius de Laszlo, Queen Marie of Romania is wearing the 1909 Cartier* kokoshnik *that most likely bears the Ruspoli sapphire as the center gem. Examination of a high-definition image of that jewel (courtesy of Cartier archives) confirms this. Courtesy of Peles National Museum.*

wrote that the sapphire weighed 124 ct, other sources indicate 137.2 ct (Munn, 2001) or even 137 ct (Nadelhoffer, 2007), values that closely correspond with the Ruspoli (136.9 ct).

## THE TRUE STORY OF THE GRAND SAPPHIRE

Supposedly purchased by Francesco-Maria Ruspoli (1672–1731; see Morel, 1988), the Ruspoli sapphire has a double series of crown facets that is more typical of the late 18th and early 19th century (Schrauf, 1869). In fact, there is no proof that this gem ever belonged to the Ruspolis, as jewelers and auction sellers often contrived aristocratic pedigrees and curse legends to increase gem values. Examples include the fake Spanish pedigree of the Wittelsbach Blue diamond (Dröschel et al., 2008) or the "curse" of the Hope diamond (Post and Farges, 2014). Charlemagne's purchase of the Ruspoli sapphire from an Indian prince appears to be another such legend. Therefore, the name "Ruspoli" is highly questionable. A more accurate alternative would be the "Achard-Hope sapphire," as this name is related to important personages actually involved with this historical gem.

For its part, the MNHN officially denies custody of the Ruspoli sapphire, claiming instead the Grand Sapphire of Louis XIV, the companion stone of the French Blue diamond.

**The Acquisition of the Grand Sapphire.** We searched the French royal archives to determine the exact provenance of the Grand Sapphire. In the Clairambault collection of the National Library of France, we discovered an unpublished financial record of royal expenses for gemstones, dated 1683. It lists a lozenge-cut sapphire worth 40,000 livres (see Farges and Benbalagh, 2013). This description is identical to the one given in the 1691 inventory for the Grand Sapphire. Because no other sapphire with such a shape and value is known, we conclude that this document deals with the acquisition of the Grand Sapphire. The 1683 record also provides a new piece of information: "the sapphire is not included in the purchases,"

meaning that of all gemstones acquired by Louis XIV between 1661 and 1683, this is the only one for which no money was spent. Some pagination details in this archive (see Farges and Benbalagh, 2013) suggest that the acquisition was acknowledged during the spring or summer of 1669, but we do not know its exact circumstances.

Based on these dates, we examined the French Foreign Ministry archives, where the records of the royal gemstones are kept. Newly revealed documents for 1669 (French diplomatic archives, inventory number 2040) show that the Grand Sapphire was among the faceted sapphires inventoried by the royal treasurer on July 1, 1669 (Farges and Benbalagh, 2013). Here again, no information is given on the gem's provenance. The inventory states that Jean Pittan the Younger, the king's jeweler, was responsible for setting the sapphire in gold. Another record from the same archives, dated August 20, 1672, reports that the setting was completed and the sapphire was returned by Pittan. The weight of the jewel is listed as "7 gros ½ et 12 grains" (28.74 g), the same weight as in the 1691 inventory of the French crown jewels. Based on the current weight of the Grand Sapphire (135.75 ct), we estimate the weight of the pure gold setting to be around two grams. This is a curiously small amount of gold for such a large stone. The most plausible interpretation is that the Grand Sapphire was set on a stand composed of gold filigree, a style favored by Louis XIV (Bimbenet-Privat, 2002, 2003). Because of its mechanical properties, such an intricate network of gold wires could support the weight of a relatively large and heavy sapphire, despite the low weight of the metal itself.

We found nothing in those archives that explains how the sapphire was obtained other than the words "not included in the purchases." This could mean a gift, plunder, inheritance, or deferred payment. We investigated these various possibilities (see Farges and Benbalagh, 2013) with no success. Since that study, one of the authors rediscovered the 1666 inventory of the French crown jewels (Farges, 2014a). This extensive manuscript does present important new information about the jewels, but none concerning the Grand Sapphire, suggesting that it had not yet entered the royal collection. Furthermore, nothing in the 1666 bequest of the Dowager Queen Anne of Austria or the record of the Russian diplomatic visit in 1668 provided fruitful hints. Also, there is no evidence of any gem purchase by Louis XIV between 1666 and February 1669, when gem merchants Jean-Baptiste Tavernier and David Bazeu (or Bazu) returned from their voyages to India (Morel, 1988). As the sapphire is not listed among the gems purchased from those merchants, the Grand Sapphire must have been obtained shortly after their return from India, but before its official recording in the royal books—in other words, between February and June 1669.

**Analogies with the Tavernier Blue Diamond.** Figure 7 shows the Grand Sapphire next to a cubic zirconia replica of the Tavernier Blue diamond that was cut and donated to the MNHN by Scott Sucher (see Sucher, 2009). The similarities between the Grand Sapphire and the Tavernier Blue, both acquired in 1669, are striking. They have roughly the same dimensions. The simple cuts and faceting allow the observer to easily study their purity, inclusions, and color (Farges, 2010).

According to Zemel (2015), the Grand Sapphire is a Mogul-cut gem, like the Tavernier Blue diamond. Mogul-cut gems are often faceted irregularly or asymmetrically, usually showing a large flat base and an array of radial facets, as in the Orlov and Taj-i-Mah diamonds. Other Mogul cuts include more symmetrical shapes such as pendeloques or tables (the Darya-i-Noor diamond, for instance). Those diamonds were faceted in India during the 17th and 18th centuries, and cutters there were expert in minimizing weight loss during polishing (Tavernier, 1676). Louis XIV decided to recut the asymmetrical Tavernier Blue as an apparently symmetrical brilliant; the resulting stone became known as the French Blue. Clearly, the sapphire was already symmetrical, but the king did not

*Figure 7. The Grand Sapphire (left) and a cubic zirconia replica of the Tavernier Blue diamond (right). Photo by François Farges, © MNHN.*

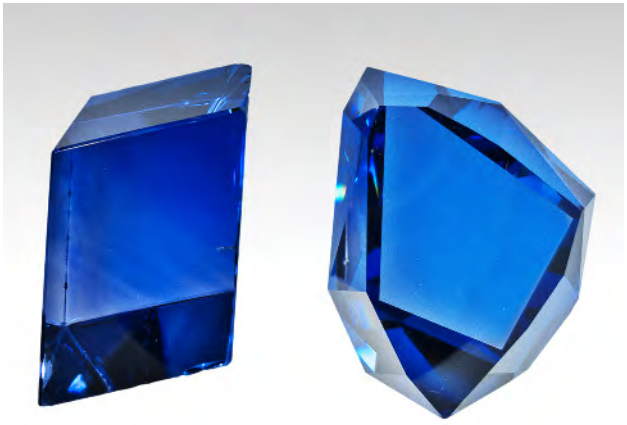

ask for more ornate recutting (for instance, as a cushion with a step cut on its pavilion). If the Grand Sapphire is a Mogul cut, then either Tavernier or Bazeu must have donated it, as they were the only merchants to return from India in 1669 with gemstones (Morel, 1988). While Tavernier sold diamonds to Louis XIV, Bazeu also traded magnificent pearls and several colored gems, including two yellow sapphires and a red spinel, the latter also cut as a lozenge (Morel, 1988).

Despite the assertions of Morel (1988), Louis XIV never wore the Grand Sapphire or the Tavernier Blue diamond (Farges and Benbalagh, 2013). Instead, the gems were kept in a gold chest adorned with elaborate filigree, a masterpiece created for the king by Jacob Blanck, a little-known jeweler who worked for Jean Pittan the Younger (Bimbenet-Privat and Pié, 2014). Blanck's creation is now known as the Louis XIV gemstone chest ("coffre des pierreries de Louis XIV," inventory number MS 159). Bimbenet-Privat and Pié (2014) showed that the king used the chest to display his gemstones and royal ornaments to prestigious visitors, just as the Mogul emperor Aurangzeb had with Tavernier in 1665 (Tavernier, 1676).

The acquisition of two large blue gems at about the same time (the spring of 1669) is no coincidence. Around 1672, both gems were set into gold, which was out of the ordinary for the French Court. In fact, most of the diamonds in the French crown jewels were set in silver-plated gold, which was considered more valuable at the time (Bimbenet-Privat, 2002). Therefore, the setting of both blue gems into gold is atypical of this period and could be a reference to the "azure and gold" colors of the French monarchy (Pastoureau, 2000).

## GEMOLOGICAL STUDY

We used the following orientation to identify the facets of the sapphire (again, see figure 1). "Top" is the upper horizontal, nearly square facet. "Front left" and "front right" are the two main frontal facets seen in figure 1, while the left rear, right rear, and bottom facets are not visible. There is a missing corner on the upper rear area of the sapphire, at the junction of the left rear, right rear, and top facets.

Visual examination of the Grand Sapphire shows that its blue color is not uniform; rather, it displays chevron-pattern zoning. The observed color is a medium blue with pale violet hues ranging from violetish blue to pure blue, with a medium to medium-dark tone and a strong saturation. The gem reveals abundant evidence of rough handling, containing many scratches, nicks, and pits. It weighs 27.148 grams (135.74 ct).

**Shape.** The dihedral angles of the Grand Sapphire rhomboid are 75°, 90°, and 71°. Its shape has nothing in common with a rhombohedron (whose dihedral angles are 75.5 or 76°). The shape is a parallelepiped, with two axes intersecting at oblique angles and a third orthogonal to the two other axes. Four edges are slightly recut, connecting the three front facets seen in figure 1 (as well as another edge on the upper left rear), while the other eight edges are actually quite sharp. On the upper rear, one significant missing corner shows a flat surface of a few square millimeters (figure 8A). This surface forms angles of 105°, 85°, and 105° with its three neighboring facets. The texture of this surface contrasts with the other facets of the gem. Closer microscopic examination reveals many imperfections such as micron-size cavities around approximately circular frosted areas that are much duller (figure 8A). Also, this surface lacks crystalline patterns such as the terraces that are typical of the naturally formed crystal habit of sapphire (see figures 8B and 8C). The irregularities observed suggest some abrasive polishing by water action. This might indicate that the Grand Sapphire was recut from a larger piece of sapphire found in weathered alluvial gravels, typical of corundum in Sri Lanka (see, among others, Hughes, 1997). If the Mogul origin of this faceting is confirmed (see Zemel, 2015), one can speculate that this rough was only slightly larger than the cut gem (see Tavernier, 1676), confirming Haüy's observation (1801) that the sapphire was cut "to preserve its volume as much as possible."

**Orientation.** A plane polariscope was used to better observe the chevron-patterned zoning of the Grand Sapphire (figure 8D). These chevrons correspond to the growth pattern of two of the six facet planes of the hexagonal corundum crystal (i.e., the m-planes of the hexagonal lattice system of the trigonal crystal system: $[1\bar{1}00]$, $[0\bar{1}10]$, $[\bar{1}010]$, $[\bar{1}100]$, $[01\bar{1}0]$, and $[10\bar{1}0]$). Using the polariscope, the direction of the c-axis was determined thanks to its total extinction (sapphire is uniaxial negative). The color zoning appeared in high contrast when set 15–20° off-axis. In the pictures taken from this direction (figure 8D), the apparent angle of the chevrons is approximately 125° (close to the theoretical value of 120° for a trigonal/hexagonal crystal-like sapphire). This confirms the previous determination of the crystal orientation using the polariscope. Otherwise, the apparent

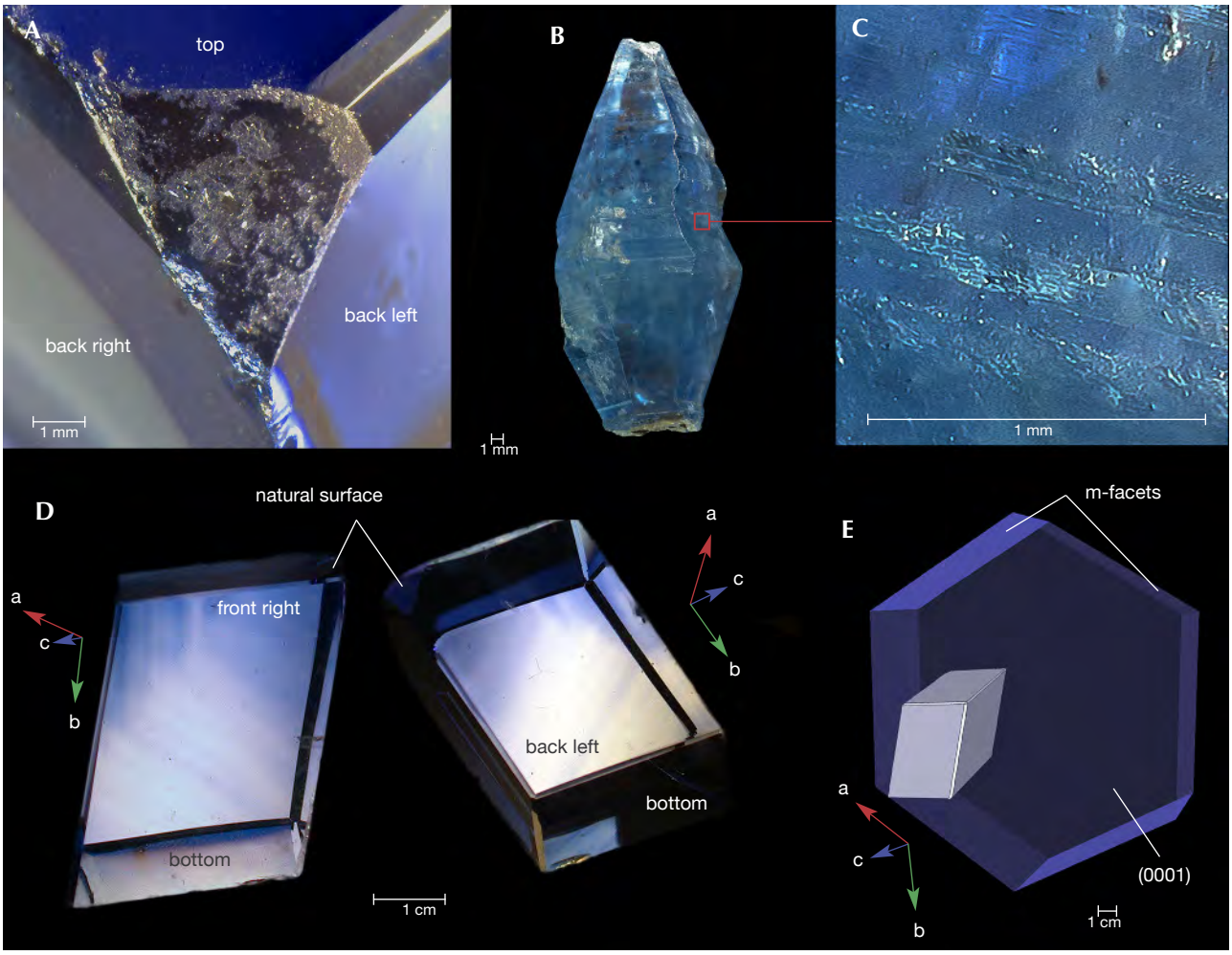


*Figure 8. A: Detail of the natural, uncut surface on the Grand Sapphire. B: A doubly terminated gem sapphire monocrystal from the Monaragala district, Sri Lanka (45 × 11 × 12 mm; MNHN inventory number 195.146). C: Detail of the Sri Lankan sapphire's surface, showing crystal growth terraces. D: Two "opposite" views of the Grand Sapphire examined under a polariscope and oriented slightly off the c-axis (shown in dark blue). E: Three-dimensional reconstruction showing the probable location of the Grand Sapphire within a hypothetical trigonal/hexagonal corundum crystal. Photos by François Farges, © MNHN.*

angle would be much larger from other viewing angles and the chevrons would not be visible when the viewing angle was too far from the c-axis. Using GemCad, we created a 3-D model of the Grand Sapphire based on direct goniometric measurements. This model is set in an orientated hexagonal preform (figure 8E) to illustrate how the gem represented a small portion of the original crystal (assuming it crystallized isotropically) before it was smoothed by erosion.

**Refraction.** The Grand Sapphire's refractive indices are 1.772 ($n_\omega$) and 1.764 ($n_\varepsilon$). The gem is uniaxial negative, with a birefringence of 0.008. These values are consistent with corundum (see Bariand and Poirot, 1985).

**Inclusions.** We observed oriented rutile needles (figure 9) and a globe-shaped opaque black inclusion with highly reflective surfaces and a high refractive index. The opaque black inclusion resembles an iron oxide such as hematite or ilmenite.

**Fluorescence.** The Grand Sapphire showed moderate red fluorescence under long-wave UV (365 nm) illu-

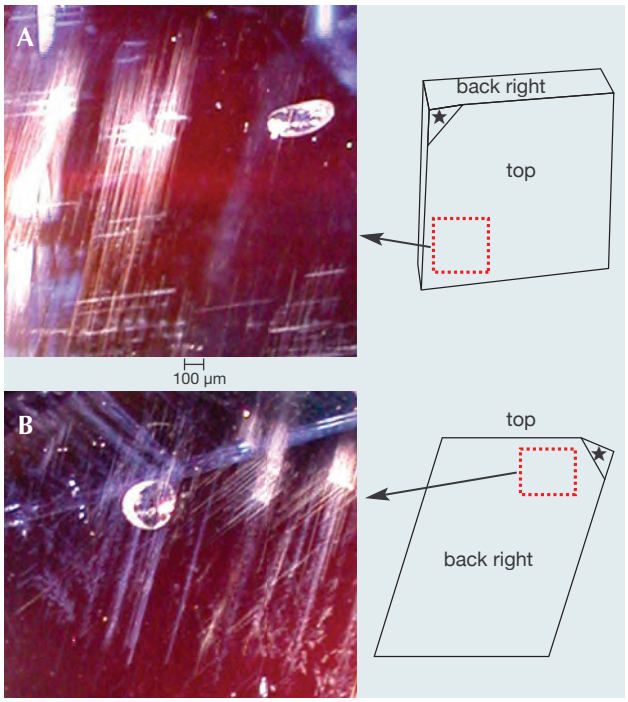


*Figure 9. Inclusions in the Grand Sapphire, observed from the top facet (A) and the right rear facet (B). Rutile needles and a large hematite-like inclusion are visible from both facets. Photos by Gérard Panczer, © MNHN; field of view 1.35 mm.*

mination, but weaker fluorescence under short-wave UV (254 nm). Moreover, its fluorescence was a more intense red along the green 532 nm laser beam through the stone (figure 10).

**Raman Scattering Spectroscopy.** Raman spectra collected with 532 and 785 nm laser excitation were comparable (figure 11). With 785 nm excitation, the baseline was not uniform, most likely due to the gem's fluorescence in the Raman range (Panczer et al., 2012). In both cases, clearly detected Raman scattering peaks corresponded to their associated vibration modes (Al-O bonds in a six-fold octahedral coordination).

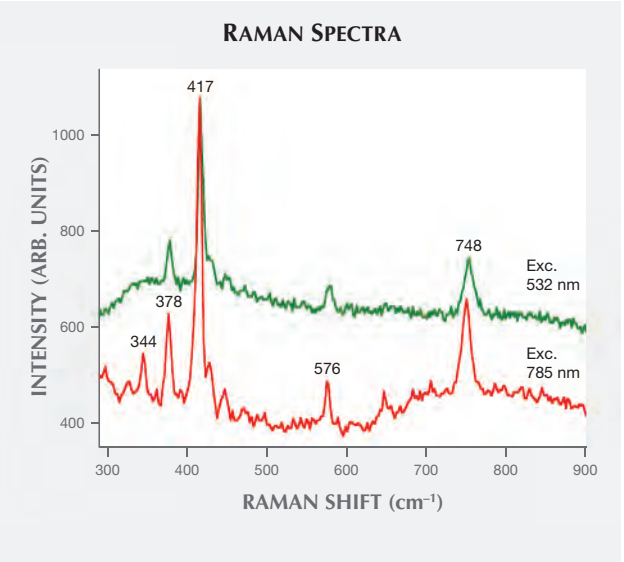


*Figure 11. Raman scattering spectra for the Grand Sapphire, with laser excitation at 532 nm (green curve) and 785 nm (red curve). The peaks are indicative of octahedrally coordinated Al.*

**UV-Vis-NIR Spectroscopy.** Three zones of the gem were selected for UV-Vis-NIR spectroscopy (figure 12). One zone corresponded to the central part of the sapphire. The second and third zones had the highest and lowest color saturation, respectively. The spectra for the three zones were comparable. An absorption band

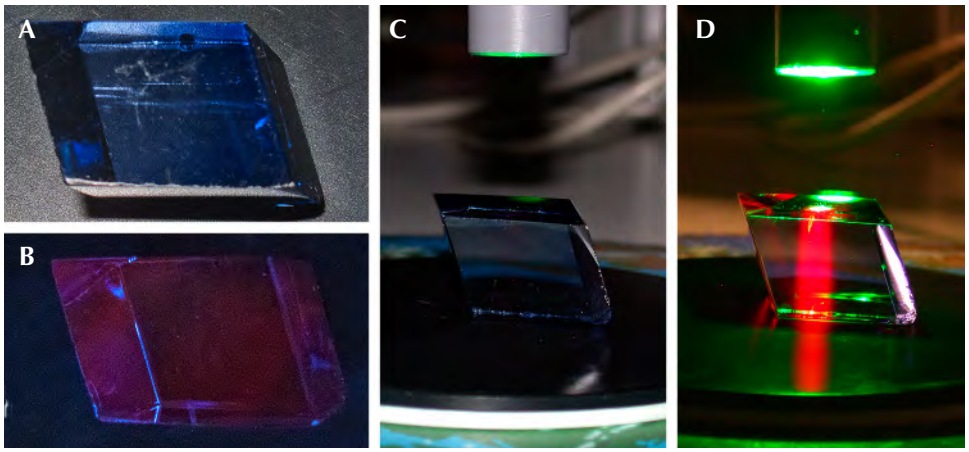


*Figure 10. Fluorescence of the Grand Sapphire. A and B: Before and after illumination with long-wave UV (red fluorescence). C and D: Before and after exposure to 532 nm laser excitation results in a strong red fluorescence along the laser beam. Photos by François Farges, © MNHN.*

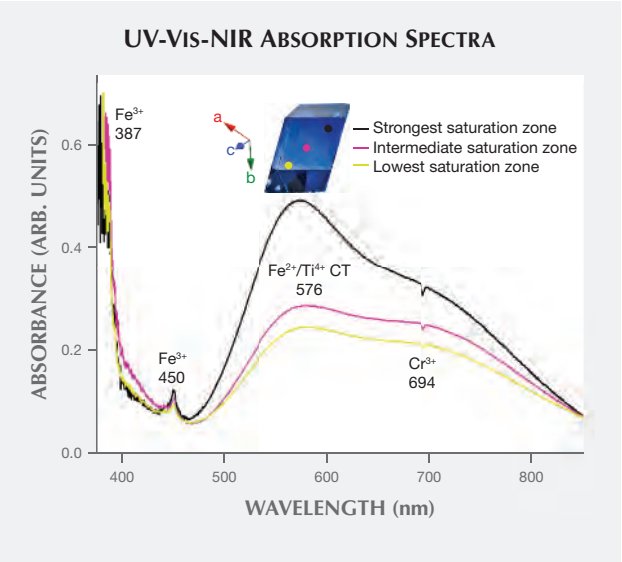


*Figure 12. Unpolarized UV-Vis-NIR absorption spectra (with the hexagonal unit cell shown as a, b, and c vectors) for three different zones of the front right facet show variation in the intensity of blue color.*

was detected in the green to red spectral range for all zones, with a maximum centered near 576 nm. A more narrow absorption contribution, though less intense, was observed near 450 nm. Also, a negative-intensity line corresponded to an emission peak at 694 nm (again, see figure 12).

**Luminescence Spectroscopy.** Luminescence spectroscopy, induced by either a 365 nm UV source or by a 532 nm continuous laser, showed a sharp, intense emission line at 694 nm (figure 13). This phenomenon indicated that the two wavelengths excited an extrinsic luminescent center whose electrons were subjected to a radiative transition—in this case, the presence of $Cr^{3+}$ atoms. The portable apparatus used did not discriminate between the transitions related to $Cr^{3+}$ (referred to here as R1 and R2, centered at 692.9 and 694.3 nm, respectively; Gaft et al., 2015). The other weak bands observed in the spectra are secondary peaks related to the main doublet (Panczer et al., 2013). These results also explain the negative absorption measured by UV-Vis-NIR spectroscopy near 694 nm, as seen in figure 12.

**Interpretation.** Despite the use of portable instruments with lower resolution than laboratory or synchrotron-based instruments, the gem shows the physical properties of a sapphire. Its Raman scattering spectrum (again, see figure 11) matched that for corundum from

## Timeline of Five Famous French Gems

**1666:** In India, Jean-Baptiste Tavernier purchases an approximately 115 ct blue diamond with Mogul faceting. This will become the Tavernier Blue.

No sapphires are listed in the inventory of the French crown jewels.

**Spring 1669:** The Mogul-faceted diamond is sold by Tavernier to King Louis XIV.

The Grand Sapphire is acquired by Louis XIV and inventoried among the faceted sapphires.

**Summer 1669:** The Tavernier Blue diamond and the Grand Sapphire are in the possession of Jean Pittan the Younger, the king's primary jeweler.

**1672:** The Tavernier Blue is recut to create the French Blue. The Grand Sapphire is kept intact. Both gems are set in gold before Pittan returns them to the king.

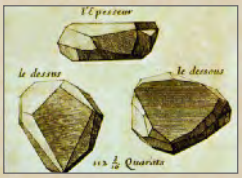

**1675:** The French Blue and the Grand Sapphire are placed in a gold chest for display.

**1691:** First official appearance of both the French Blue and the Grand Sapphire in the inventory of the crown jewels.

**1749:** The French Blue and the Grand Sapphire are removed from their settings by Pierre-André Jacqumin, Louis XV's jeweler, for his Order of the Golden Fleece pendant.

Eventually, the Golden Fleece insignia will be completed with the French Blue.

The Grand Sapphire returns to the royal storehouse without its gold setting.

*The "Ruspoli" sapphire is supposedly purchased by the Ruspolis, a noble Roman family. There is no record of the purchase, however, and this ownership is highly questionable.

the RRUFF database. The rutile inclusions were not weathered or dissolved. Therefore, the Grand Sapphire did not undergo any thermal treatment above 1600°C. Its optical absorption showed a maximum at 576 nm, consistent with an electron exchange between $Fe^{2+}$+ $Ti^{4+}$ and $Fe^{3+}$+ $Ti^{3+}$ (Ferguson and Fielding, 1971; Fritsch and Rossman, 1988). The 694 nm "negative" absorption peak seen in figures 12 and 13 was related to the presence of $Cr^{3+}$ substituting for six-fold coordinated $Al^{3+}$ (high crystal field) in corundum (Gaft et al., 2005; Panczer et al., 2012) and was responsible for the narrow and intense red emission. $Cr^{3+}$ is a frequent impurity in corundum, including sapphires (Bariand and Poirot, 1985).

**Geological and Geographical Origins.** Determining the geologic or geographic origin of sapphire remains a challenge even with advanced analytical methods (Mumme, 1988; Notari and Grobon, 2002; Shigley et al., 2010). For instance, blue sapphires from Sri Lanka and Madagascar show similar mineralogical and gemological properties (Gübelin Gem Lab, 2006). However, the determination of geographical origin of a rare historical gemstone such as the Grand Sapphire is based on limited but convergent criteria (inclusions, growth zones, absorption patterns, luminescence, and the like). In addition, the number of possible geographical occurrences for the Grand Sapphire is historically limited: The only ac-

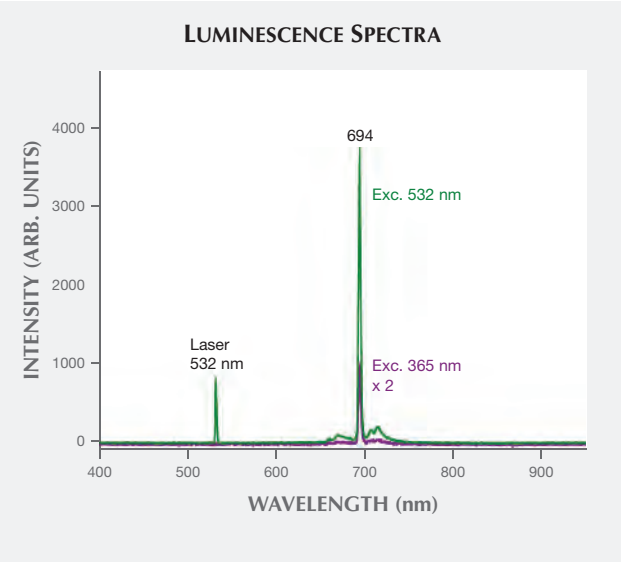


*Figure 13. Luminescence spectra for the Grand Sapphire with excitation by a 532 nm laser (green curve) and a 365 nm UV source (purple curve, with intensity doubled for comparison with the green spectrum). The 532 nm line corresponds to the laser scattering.*

## Tavernier, French Blue, and Hope Diamonds | Grand Sapphire of Louis XIV | Ruspoli Sapphire*

**1768–1772:** French mineralogist Jean-Baptiste Louis Romé de l'Isle studies the sapphire and is convinced the gem bears a natural habit. A bisque model of the gem is made.

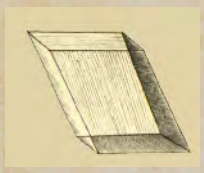

**1774:** In the 1774 inventory of the French crown jewels, the Grand Sapphire is listed as a faceted gem.

**1783:** Romé de l'Isle changes his mind and concludes that the Grand Sapphire is hand-polished.

**1787:** M.J. Brisson publishes the previously measured dimensions and densities of the French Blue and the Grand Sapphire. He considers the gem faceted.

Based on wooden models of ruby crystals sent by German mineralogist Abraham Gottlob Werner, Romé de l'Isle reverts to his original hypothesis: The Grand Sapphire "must be a natural crystal of sapphire."

**1789:** In the inventory of the French crown jewels, the Grand Sapphire is described as "not cut."

**1791:** In the inventory of the French crown jewels, the French Blue and the Grand Sapphire are still the most magnificent colored gemstones of this collection. The appraised value for both gems has increased approximately three times since 1774–1789.

**Fall 1792:** The Golden Fleece insignia is stolen (along with the French Blue), and the Grand Sapphire is missing as well.

**Winter 1792:** The Grand Sapphire reappears and is transferred to a safer storage area in Paris at the Hôtel de la Monnaie.

**Spring 1796:** Cadet Guillot, who participated in the 1792 looting of the crown jewels, dismounts the Golden Fleece insignia and sells parts of it in Brittany, Normandy, and London.

The Grand Sapphire is selected by French mineralogist Louis Jean-Marie Daubenton for donation to the recently created National Museum of Natural History (MNHN) in Paris.

**Summer 1796:** The 107 ct Côte de Bretagne spinel from the Golden Fleece pendant is recovered in London from Cadet Guillot. The whereabouts of the French Blue remain unknown.

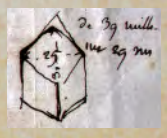

tive deposits before 1669 were in modern-day Myanmar, Sri Lanka, and Thailand-Cambodia. The rutile inclusions observed in Burmese sapphires are usually shorter and more densely packed (see Hughes, 1997) than those observed in the Grand Sapphire, which appear more typical of Sri Lanka (L. Thoresen, pers. comm., 2015).

According to the Gübelin Gem Lab (2006), the Grand Sapphire's UV-Vis-NIR spectrum is typical of sapphires that crystallized in metamorphic rocks. Their absorption is dominated by an intense $Fe^{2+}/Ti^{4+}$ charge transfer, with absorption maxima centered at 575 and 700 nm. The absorption bands related to $Fe^{3+}$ are usually weaker (Hughes, 1997). Therefore, the Grand Sapphire probably originated from the charnokitic series (an orthopyroxene-bearing metamorphic rock with granitic composition) of Sri Lanka or their fragmented clastic (detrital) sediments, as suggested by the examination of the small natural, uncut facet of the Grand Sapphire. The use of a laboratory UV-Vis-NIR apparatus should not affect the conclusions drawn from luminescence spectroscopy, as the charge transfer bands of interest are well probed with sufficient resolution by the portable apparatus. This study therefore shows how portable instruments, despite their intrinsic limitations, can assist with the examination of museum pieces that cannot be transferred to a laboratory setting.

## CONCLUSIONS

Through a historical and gemological study of the Grand Sapphire, we have rediscovered some of its lost secrets. The stone is likely from Ceylon, present-day Sri Lanka. It may have been cut originally by Indian lapidaries (Zemel, 2015) before being purchased by a European (possibly David Bazeu) and given to Louis XIV around 1669, about the same time the monarch purchased the Tavernier Blue diamond. Both gems were set in gold under the supervision of jeweler Jean Pittan the Younger at about the same time (1672–1673). A gold setting was used, possibly to highlight the "azure and gold" colors of the French monarchy (Farges, 2010; Post and Farges, 2014). There is no evidence that Louis XIV ever wore those gems as part of his regalia. Instead, the gems were placed in a remarkable gold chest that was exhibited to impress selected visitors (see Farges, 2010; Bimbenet-Privat and Pié, 2014: Post and Farges, 2014).

### Timeline of Five Famous French Gems (continued)

**1801:** French mineralogist René-Just Haüy demonstrates that the Grand Sapphire's facets are "handmade."

**1792–1812:** The French Blue is owned by Henry Philip Hope, according to Parisian lapidary David Achard. The gem is cast and recut as the Hope diamond. Achard recovers the cast of the French Blue.

The gem that would later be known as the "Ruspoli" sapphire first appears in Rome and Paris. One of its previous owners is said to be a Ruspoli prince. In Paris, the sapphire is the subject of a lengthy trial between two jewelers, Perret and Fusi.

**Fall 1812:** The Hope diamond makes its first appearance in London. Nobody connects the gem to the French Blue.

**Winter 1813:** The Ruspoli sapphire is auctioned by court order. An accurate drawing is printed in an auction leaflet, but the sapphire's previous owners are falsely listed as a Bengali wooden spoon seller, an Indian prince, and Charlemagne.

**1814–1831:** David Achard donates the lead cast of the French Blue to the MNHN.

Achard recovers the Ruspoli sapphire and sells it to H.P. Hope. Achard cuts a strass replica of the sapphire and donates it to the MNHN.

**1837:** The Grand Sapphire and the strass replica of the "Ruspoli" sapphire are displayed in the same showcase in the new gallery of mineralogy at the MNHN.

**1839:** An inventory of H.P. Hope's collection includes the Hope diamond. The same inventory included a detailed drawing of the Ruspoli sapphire.

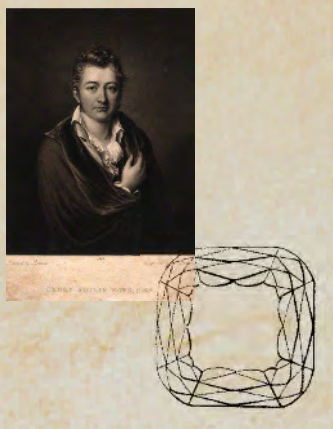

**1839–1867:** Henry Philip Hope sells the Ruspoli sapphire to Czar Nicholas I.

The faceting of the Grand Sapphire is relatively simple but remarkable nonetheless. Recutting it as a cushion would have resulted in significant weight loss with no dramatic increase in brilliance. In this regard, Louis XIV proved to have eclectic tastes, collecting both minimally faceted (possibly Mogul) gems such as the Grand Sapphire and complex brilliant-cut faceted gems such as the French Blue, one of the first brilliant-cut diamonds ever documented (Farges, 2014b).

In 1739, the sapphire was removed from its gold setting, most likely to consider recutting it into two stones for Louis XV's Order of the Golden Fleece insignia. Fortunately, this idea was eventually abandoned. Sometime between 1739 and 1774, the Grand Sapphire became an object of scientific study; M.J. Brisson measured its density, while Jean-Baptiste Romé de L'Isle examined its shape and eventually concluded that it was an uncut crystal. From the crystal, Romé de L'Isle shaped a model in bisque (1772). Apparently stolen in September 1792 and recovered a few months later, the sapphire entered the national collection of mineralogy at the MNHN in Paris, where Haüy (1801) once again identified it as a faceted gem.

Since 1858, the Grand Sapphire has often been confused with another gem, known as the Ruspoli sapphire, for which the MNHN possesses a historical replica that was once exhibited near the Grand Sapphire. The stones have approximately the same weight, but their faceting is dramatically different. Whereas the Grand Sapphire is a six-sided "lozenge" cut, the Ruspoli is a more conventional cushion cut. This sapphire was then sold at an auction in 1813 and acquired by the French jeweler David Achard, who subsequently sold it to Henry Philip Hope. Czar Nicholas I is said to have obtained the stone, which may have adorned a great Russian *kokoshnik* designed in 1909 by Cartier. Princess Ileana of Romania sold the piece to a jeweler in the United States in the 1950s, and its current whereabouts are unknown.

Unearthing elements of the true story of the Grand Sapphire reaffirms its rightful standing as one of the most important gemstones of the 17th century. Its unusual shape makes it one of the singular cut stones of all time. It is celebrated in a permanent exhibit named "Treasures of the Earth" (*Trésors de la Terre*), which opened in December 2014 at the MNHN. This exhibit places the sapphire in its appropriate context with the other magnificent gems and art objects of the French crown jewels.

## Tavernier, French Blue, and Hope Diamonds | Grand Sapphire of Louis XIV | Ruspoli Sapphire*

**1858:** In his *Traité*, Charles Barbot is the first to connect the French Blue with the Hope diamond.

Barbot also describes the Grand Sapphire and the gem later referred to as the "Ruspoli" while they are on exhibit at the MNHN, in a way that suggests the Grand Sapphire was once owned by a Bengali wooden spoon seller and the Ruspoli family.

**1867–1881:** Edwin William Streeter (1877) shows a model of the Tavernier Blue diamond.

When translating L. Simonin's *Underground Life, or Mines and Miners* (1867) from French to English, Henry William Bristow apparently misinterprets Charles Barbot's writings and calls the Grand Sapphire the Ruspoli for the first time.

Streeter and Sir Sourindro Mohun Tagore (1879) perpetuate the confusion. John H. Snively (1872) is among the first to mistakenly refer to the Grand Sapphire as the "Wooden Spoon Seller's Sapphire."

**1909:** The Hope diamond is reset by Cartier in Paris for Evalyn Walsh MacLean.

The Ruspoli sapphire is possibly reset by Cartier into a diadem for Grand Duchess Maria Pavlovna of Russia.

**1949:** Harry Winston purchases the Hope diamond.

**ca. 1950:** Princess Ileana of Romania sells the Ruspoli sapphire to a jeweler in New York. Its whereabouts remain unknown.

**1958:** Harry Winston donates the Hope diamond to the Smithsonian's National Museum of Natural History in Washington, DC, where it has been exhibited ever since.

**1980s:** The Grand Sapphire, still commonly referred to as the "Ruspoli," is occasionally displayed at the MNHN.

**2007–present:** Historical artifacts concerning the lead cast of the French Blue diamond, the 18th century bisque model of the Grand Sapphire, and the strass replica of the actual Ruspoli sapphire are found within the MNHN collections in Paris. The Grand Sapphire and the lead cast of the French Blue are placed on permanent exhibit at MNHN in December 2014.

ABOUT THE AUTHORS

*Dr. Farges is a professor of mineralogy at the Institut de Minéralogie, Physique des Matériaux et Cosmochimie (IMPMC), Muséum National d'Histoire Naturelle, and UMR CNRS 7590 (Paris). He is former curator of the French national collections of minerals, gems, and art objects and formerly a professor at Stanford University. Dr. Panczer is a professor of physics at University of Lyon, working at the Institut Lumière-Matière (ILM), Claude Bernard University Lyon 1 and UMR CNRS 5306 (Lyon). Mrs. Nassima Benbalagh is a former research associate at the MNHN. Mr. Riondet is an antiquarian in Lyon who graduated in gemology at the University of Lyon 1.*

ACKNOWLEDGMENTS

*We thank Herbert Horovitz, Christophe Dubois, Michèle Bimbenet-Privat, Stéphane Castelluccio, Cristiano Ferraris, the Centre Commun de Microspectrométrie Optique (CECOMO, Lyon 1 University), the staff of the French National Library (BnF, Paris), the National Archives (AN, Paris), the diplomatic archives of the French Foreign Ministry (La Courneuve), and everyone who helped us conduct these exhaustive searches. Lisbet Thoresen is thanked for her critical reading of this manuscript. We also thank the Cartier archives in Paris for the photo of the* kokoshnik, *and the J. Paul Getty Museum in Los Angeles for the use of Hyacinthe Rigaud's portrait of Louis XIV, both seen in the timeline.*

## REFERENCES

Allen R. (2001) Great divergence in European wages and prices from the Middle Ages to the First World War. *Explorations in Economic History*, Vol. 38, No. 4, pp. 411–447, http:dx.doi.org/10.1006/exeh.2001.0775.

Balfour I. (2009) *Famous Diamonds*. Antique Collectors' Club, Woodbridge, UK.

Bapst G. (1889) *Histoire des Joyaux de la Couronne de France [History of the Crown Jewels of France]*. Hachette, Paris [in French].

Barbot C. (1858) *Traité Complet des Pierres Précieuses [Comprehensive Treatise of Gemstones].* Morris et Compagnie, Paris [in French].

Bariand P., Poirot J.P. (1985) *Larousse des pierres précieuses, fines, ornementales, organiques [Larousse Precious, Fine, Decorative, Organic Stones]*. Librairie Larousse, Paris [in French].

Berryer P.N. (1839) *Les souvenirs de M. Berryer, doyen des avocats de Paris de 1774 à 1838 [Memories of M. Berryer, Senior Lawyer of Paris from 1774 to 1838]*. A. Dupont, Paris [in French].

Bimbenet-Privat M. (2002) *Les orfèvres et l'orfèvrerie de Paris au XVIIe siècle [Goldsmiths and goldsmithery in Paris during the XVIIth century]*, Vol. I (Les Hommes [the People]). Association Paris-Musées, Paris [in French].

—— (2003) Les pierreries de Louis XIV [The gemstones of Louis XIV of France]. In B. Barbiche and Y. M. Berc, Eds., *Etudes sur l'ancienne France offertes en hommage à Michel Antoine*. École nationale des Chartes, Paris, pp. 81–96 [in French].

Bimbenet-Privat M., Pié E. (2014) Le coffre des pierreries de Louis XIV (1675) [the gemstone chest of King Louis XIV (1675)]. La Revue des musées de France, *Revue du Louvre*, No. 2014-3, pp. 63–72 [in French].

Bion J.-M., Delattre F.-P. and Christin C.-G.-F. (1791) *Inventaire des diamans de la couronne, perles, pierreries, tableaux, pierres gravées, et autres monumens des arts & des sciences existans au garde-meuble* (...) *[Inventory of diamonds of the crown, pearls, precious gems, paintings, engraved stones, and other monuments of arts & sciences in the royal storehouse]*. Imprimerie Nationale, Paris [in French].

Brisson M.J. (1787) *Pesanteur Spécifique des Corps [Specific Gravity of Matter*]. Imprimerie Royale, Paris [in French].

Dröschel R., Evers J., Ottomeyer H. (2008) The Wittelsbach Blue. *G&G*, Vol. 44, No. 4, pp. 348–363, http://dx.doi.org/10.5741/GEMS.44.4.348.

Emanuel H. (1867) *Diamonds and Precious Stones*. John Camden Hotten, London.

Farges F. (2010) Sur les traces du diamant bleu [On the trail of the blue diamond]. *Pour la Science*, Vol. 398, pp. 54–62 [in French].

—— (2014a) The gem peridots of the Muséum national d'Histoire naturelle, Paris: An historical overview. In L. Thoresen, Ed., *Twelfth Annual Sinkankas Symposium – Peridot & Uncommon Green Gem Minerals*, Pala International, Inc., Fallbrook, CA, pp. 52–65.

—— (2014b) Les grands diamants de la Couronne de François Ier à Louis XVI [The great diamonds of the Crown from Francis I to Louis XVI]. *Versalia*, Vol. 17, pp. 55-79 (in French].

Farges F., Benbalagh N. (2013) La véritable histoire du "*Grand Saphir*" de Louis XIV: Est-il le "*Ruspoli*"? [The true story of the "Grand Saphir" of Louis XIV: Is it the "Ruspoli"?] *Revue de Gemmologie*, No. 185, pp. 61–66 [in French].

Farges F., Dubois C. (2013) À la recherche du véritable "Ruspoli" [In search of the true "Ruspoli"]. *Revue de Gemmologie*, No. 186, pp. 20–30 [in French].

Farges F., Sucher S., Horovitz H., Fourcault J.-M. (2008) Deux découvertes majeures autour du "diamant bleu de la Couronne." [Two major discoveries about the "Blue Diamond of the Crown"]. *Revue de Gemmologie*, No. 165, pp. 17–24 [in French].

—— (2009) The French Blue and the Hope: New data from the discovery of a historical lead cast. *G&G*, Vol. 45, No. 1, pp. 2–17, http://dx.doi.org/10.5741/GEMS.45.1.4.

Ferguson J., Fielding P.E. (1971) The origins of the colours of yellow, green and blue sapphires. *Chemical Physics Letters*, Vol. 10, No. 3, pp. 262–265, http://doi:10.1016/0009-2614(71)80282-8

Fritsch E., Rossman G.R. (1988) An update on color in gems. Part 2: Colors involving multiple atoms and color centers. *G&G*, Vol. 24, No. 1, pp. 3–15, http://dx.doi.org/10.5741/GEMS.24.1.3.

Gaft M., Reisfeld R., Panczer G. (2015) *Luminescence Spectroscopy of Minerals and Materials*, 2nd ed. Berlin, Heidelberg, New York: Springer-Verlag, 606 pp.

Gübelin Gem Lab (2006) The limitations of origin determination. *Jewellery News Asia*, No. 264, pp. 52–62.

Haüy R.J. (1801) *Traité de Minéralogie [Treatise of Mineralogy]* (5 volumes). Chez Louis, Paris [in French].

——— (1817) *Traité des caractères physiques des pierres précieuses… [Treatise of the physical characters of precious stones…]*. Courcier, Paris [in French].

Hertz B. (1839) *A Catalogue of the Collection of Pearls and Precious Stones Formed by Henry Philip Hope Esq.* William Clowes and Son, London.

Hugard J.-A. (1855) *Muséum d'histoire naturelle de Paris, Galerie de minéralogie et de géologie [Natural History museum in*

*Paris, Gallery of mineralogy and geology]*. Hugard, Paris [in French].
Hughes R.W. (1997) *Ruby & Sapphire*. RWH Publishing, Boulder.
Ileana, Princess of Romania (1951) *I Live Again*. Rinehart & Co., New York.
Méjan M. (1811) *Recueil des Causes Célèbres [Collection of Famous Cases]*, No. 12, Lahü, Paris [in French].
Morel B. (1988) *The French Crown Jewels*. Fonds Mercator, Antwerp.
Mumme I.A. (1988) *The World of Sapphires: Their Occurrence, Discrimination, Synthesis, and Valuation*. Mumme Publications, Port Hacking, Australia.
Munn G.C. (2001) *Tiaras: A History of Splendor*. Antique's Collector's Club, Woodbridge, UK.
Nadelhoffer H. (2007) *Cartier*. Chronicle Books, San Francisco.
Notari F., Grobon C. (2002) Gemmologie du corindon et du spinelle [Gemology of corundum and spinel]. *Le Règne Minéral* (special issue), Vol. 15, pp. 48–59 [in French].
Panczer G., de Ligny D., Mendoza C., Gaft M., Seydoux-Guillaume A-M., Wang X. (2012) Raman and fluorescence. In J. Dubessy, M.-C. Caumon, and F. Rull, Eds., *Applications of Raman Spectroscopy to Earth Sciences and Cultural Heritage*. EMU Notes in Mineralogy, Vol. 12. European Mineralogical Union and the Mineralogical Society of Great Britain and Ireland, pp. 61–82.
Panczer G., Riondet G., Farges F. (2013) Analyses gemmologiques sur site du "Grand Saphir" de Louis XIV. *Revue de Gemmologie*, Vol. 185, pp. 67–71 [in French].
Pastoureau M. (2000) *Bleu. Histoire d'une couleur [Blue, History of a Color]*. Le Seuil, Paris [in French].
Post J.E., Farges F. (2014) The Hope diamond: rare gem, historic jewel. *Rocks & Minerals*, Vol. 89, No. 1, pp. 16–26, http://dx.doi.org/10.1080/00357529.2014.842831.
Le procès du saphir [The trial of the sapphire] (1813) *Journal de Paris*, No. 353 (19-XII-1813), pp. 2–3 [in French].
Romé de l'Isle J.B. (1772) *Essai de cristallographie [Essay of Crystallography]*. Didot jeune, Knapen & Delaguette, Paris [in French].
——— (1783) *Cristallographie [Crystallography]*. Imprimerie de Monsieur, Paris [in French].
——— (1787) Note envoyée par M. de Romé de Lisle, relativement à la figure primitive des Rubis, Saphirs & Topazes [Note sent by M. de Romé de Lisle about the primitive figure of rubies, sapphires and oriental topazes]. *Journal de Physique, de Chimie, d'Histoire naturelle et des Arts*, No. 30, pp. 368–370 [in French].
Schrauf A. (1869) *Handbuch der Edelsteinkunde*. Druck und Verlag von C. Gerold's Sohn, Vienna [in German].
Shigley J.E., Laurs B.M., Janse A.J.A., Elen S., Dirlam D.M. (2010) Gem localities of the 2000s. *G&G*, Vol. 46. No. 3, pp. 188–216, http://dx.doi.org/10.5741/GEMS.46.3.188.
Simonin L. (1867) *Underground Life: Or Mines and Miners*, trans. H.W. Bristow. Appleton, New York.
Snively J.H. (1872) The sapphire. *Appletons' Journal*, Vol. 8, No. 180, p. 274.
Streeter E.W. (1877) *Precious Stones and Gems (...)*. Chapman and Hall, London.
Sucher S. (2009) A crystallographic analysis of the Tavernier Blue diamond. *G&G*, Vol. 45, No. 3, pp. 178–185, http://dx.doi.org/10.5741/GEMS.45.3.178.
Tagore S.M., Sir (1879) *Mani-Mani, Part 1: or a Treatise on Gems*. Bose and Co., Calcutta.
Tavernier J.B. (1676) *Les Six Voyages de Jean Baptiste Tavernier, Ecuyer Baron d'Aubonne, qu'il a Fait en Turquie, en Perse, et aux Indes [The Six Voyages of Jean Baptiste Tavernier, Baron d'Aubonne, that He Made to Turkey, Persia, and the Indies]*. Clouzier, Paris [in French].
Zemel F. (2015) *The Esoteric Codex: Curses*. Lulu.com, 182 pp.

# Characterization of Tarnish Spots in Chinese High-Purity Gold Jewelry

Taijin Lu, Jian Zhang, Yan Lan, Ying Ma, Hua Chen, Jie Ke, Zhenglong Wu, and Miaomiao Tang

In recent years, red, brown, and black tarnish spots on high-purity gold jewelry (99.9% Au) have been widely reported, mainly in China but also in other parts of the world. Yet the cause of these spots and their possible formation mechanism are unclear. In this study, high-purity gold with typical tarnish spots was systematically investigated using differential contrast microscopy, laser scanning confocal microscopy, SEM, X-ray fluorescence, and X-ray photoelectron spectroscopy. The study detected silver and sulfur along with gold within the tarnish spots. The tested samples all had a gold purity of 99.9%, regardless of whether there was tarnish. Higher-magnification 3-D microscopic observations revealed the typical presence of an "impurity center" within the tarnish spot and a thin film of stain that varied from several nanometers to several hundred nanometers thick. XPS analysis confirmed the presence of both Ag and S in the thin film. An *in situ* Ar ion sputtering experiment for removing the spot revealed that the sulfur could only be detected at the surface, where the film was less than 12 nm thick. To prevent these tarnish spots, we recommend careful cleaning during the gold manufacturing process and proper care and maintenance to eliminate the possibility of silver contamination.

Tarnish spots or stains with different colors on the surface of gold jewelry or coins, particularly low-purity gold jewelry, have been a concern for several centuries. The low-purity gold jewelry produced in the past usually contained internal impurities such as Ag, Cu, Zn, Ni, Fe, and S, and some external contamination particles that were introduced while in storage or during the plating process. These tarnish spots can be attributed to both a common natural electrochemical reaction and corrosion caused by these impurity metals and contamination particles (Zhen and Wu, 1991).

During the last two decades, surface spots ranging from red to brown and black have been reported on high-purity gold coins from Austria, France, and the United States, as well as Chinese panda coins. Collectors have referred to this as "gold corrosion" (Griesser et al., 2003; Rupprecht et al., 2003; Gusmano et al., 2004; Mayerhofer et al., 2005; Yang et al., 2007a), though it is highly unlikely that gold oxidizes even in a very polluted environment (Yang et al., 2007b). The colored spots on the coins were reported to be mainly composed of $Ag_2S$ (Gusmano et al., 2004; Yang et al., 2007a,b).

With the development of gold purification technology in the late 1990s, jewelry with greater than 99.9% purity has become popular in the Chinese market. In recent years, particularly in 2013, colored tarnish spots on the surface of high-purity gold jewelry have been the subject of media speculation (Lu et al., 2013). These reports have raised fundamental questions and concerns for consumers about the quality of gold products. What are these spots, and what are their characteristic features? Why do spots on the same piece of gold jewelry occur in different colors? What is the origin of these spots, and how can they be avoided?

To understand the nature of the various spots, high-purity gold samples with typical tarnish spots were systematically investigated using differential contrast microscopy, laser scanning confocal microscopy, scanning electron microscopy (SEM), as well as X-ray fluorescence (XRF) spectrometry and X-ray photoelectron spectroscopy (XPS).

## SAMPLES AND EXPERIMENTAL METHODS

High-purity gold products with typical tarnish spots were collected from four gold retail companies in Hong Kong, Shenzhen, and Beijing. All samples were

See end of article for About the Authors.
Gems & Gemology, Vol. 51, No. 4, pp. 410–417,
http://dx.doi.org/10.5741/GEMS.51.4.410.

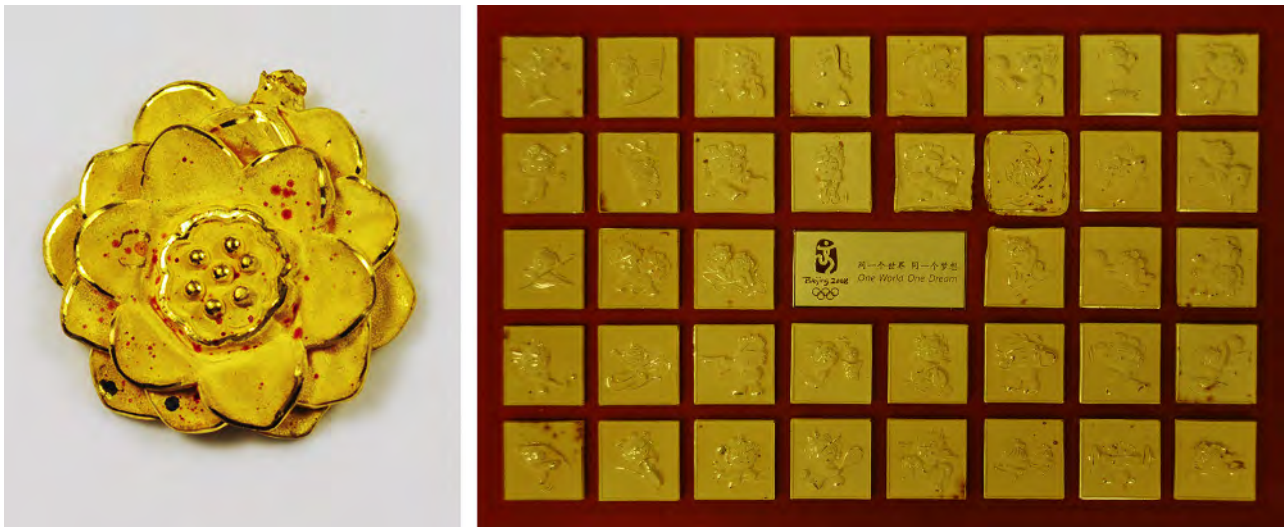


*Figure 1. A high-purity gold jewelry piece with tarnish spots (left) and a set of commemorative gold pins from the 2008 Summer Olympics in Beijing (right). Photos by Jian Zhang.*

stated as having gold purity greater than 99.9%. Three of the pieces were curved with artistic patterns and weighed 3.50 g (figure 1, left), 10.00 g, and 63.75 g, respectively. Also tested was a set of 40 high-purity gold collectible pins from the 2008 Summer Olympics in Beijing (figure 1, right), each weighing 1 gram and measuring 32.0 × 32.5 mm. Red, brown, and black spots were clearly visible on the surface of the pins, independent of location. All the samples were stored for at least one year, and the Olympic souvenirs were stored for five years. Flower-patterned pieces such as the one in figure 1 (left) were said to be without spots when first acquired. They were stored in the city of Shenzhen, and spots were clearly visible one year after purchase. The Olympic souvenirs were sealed and stored in a safe deposit box in Beijing, until spots were apparent to the unaided eye in 2012. They were kept in air atmosphere before being shipped for our investigation.

The spots' color, color distribution, structure, and microstructure were observed using a gem microscope with darkfield illumination, a differential interference contrast microscope (Nikon LV100), a laser scanning confocal microscope (Olympus LEXT OLS4000 3D), and a scanning electron microscope (JSM5600 LV SEM), using various magnifications and illumination conditions. Three-dimensional images and spot thicknesses were obtained and measured using the laser scanning confocal microscope system with image software. The purity of the gold and the chemical composition of the spots were analyzed quantitatively using an X-ray fluorescence spectrometer (Thermo Scientific Quant'X EDXRF analyzer). After the samples were cleaned with ethanol in an ultrasonic bath, their detailed chemical composition was measured using XPS (Thermo Scientific ESCALAB 250 and ESCALAB 250Xi). The XPS was calibrated with two reference points (Ag 2d5/2: 368.3 eV and C 1s: 284.5 eV). To obtain profile depth information on the spots, we removed them using $Ar^+$ ions and performed elemental analysis by XPS etching. Four tarnish spots were removed in this manner. The XPS experiments were conducted using a water-cooled Al Kα anode at 200W and a photoelectron beam spot size of 650 μm.

To identify possible links between the tarnish spots and "pollutant source" technologies, we visited two factories in Shenzhen that produce high-purity gold jewelry. We observed the entire process, represented by the flowchart below:

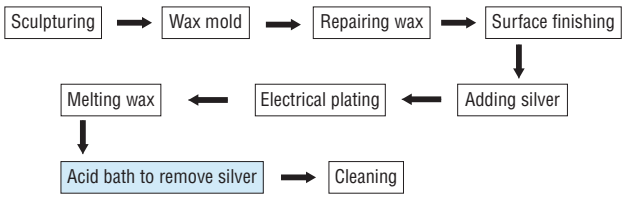


Once the wax object has gone through the carving process, it is painted with silver so that it will be electrically conductive and allow the gold plating. The silver paint is often applied by hand with a fine brush to make sure all the intricately designed areas will receive the coating. Applying with a brush also gives the

technician more control in laying down an even coating across the various design elements of each object. The silver paint must be constantly kept swirling in a beaker so that the contents are properly mixed. After the object is completely painted, fine sandpaper is used to remove any imperfections or excess paint buildup. After the electroplating, the thin silver paint layer under the gold is removed by submersing the piece in an acid bath that removes the silver paint but does not affect the gold. But in some cases the removed silver from underneath the gold layer may be deposited on the surface of the gold object, causing spots.

Exposure to the contaminant occurs during the acid bath step. Each piece is supposed to be cleaned in water ten times after the acid bath to remove the silver, but this does not always happen.

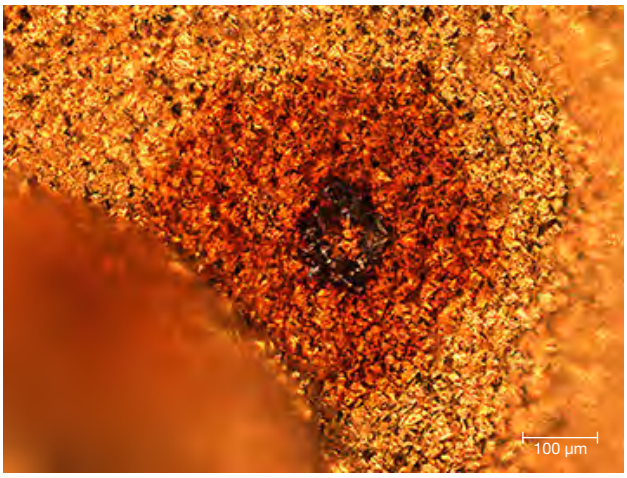


*Figure 2. Microstructure of a brown tarnish spot seen on the surface of high-purity gold jewelry, revealed by differential interference contrast microscopy. Photomicrograph by Jian Zhang.*

## RESULTS

**Color Characteristics and Fine Structure.** It was easy to recognize the tarnish spots, either visually or at low magnification, due to their clear color contrast with the gold background. Their size, shape, and color (including color distribution) varied from sample to sample. The diameter of individual stains ranged from 150 to 1500 µm, with most between 300 and 800 µm; some were as small as 100 µm and others as large as 2 mm. Red, brown, dark brown, and black spots were commonly seen in this study. The spots displayed relatively uniform color distribution at low magnification. They were usually dark circular dots, though irregular shapes also appeared when the spots were connected in patches.

To find the possible growth features and/or microstructures, color distribution, and relationships between the color and the thickness of the thin films of the spots, we performed higher-magnification observations and measurements using differential interference contrast microscopy, laser scanning confocal microscopy, and scanning electron microscopy. The observations are summarized as follows.

*Color Distribution.* The color distribution within each spot was usually uneven. In most cases, the spots appeared as a film-like substance on the gold's surface, consisting of numerous tiny gold crystallites. At the center of each spot was a black circle (figure 2) composed of flaky material that strongly contrasts with the thin film, showing a clear boundary. Most of the films were brown. The film-like material covering the surfaces of the gold crystals was also observed with SEM.

*Impurity Particles.* The dark center of the spot had an irregular shape with a relatively smooth surface and clear edges with the surrounding thin film. The size of the center varied but usually ranged from 20 to 80 µm. Figure 3 shows a typical example of a black impurity center seen in a brown spot.

*Distribution of Tarnish Spots.* The distribution of the spots was not random and followed some general pat-

*Figure 3. Photomicrography with a laser scanning confocal microscope system reveals an irregularly shaped impurity center within a brown spot. Image by Jian Zhang.*

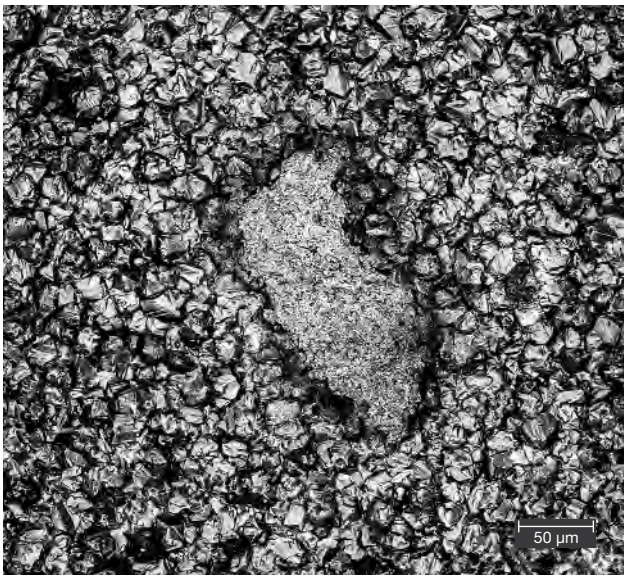

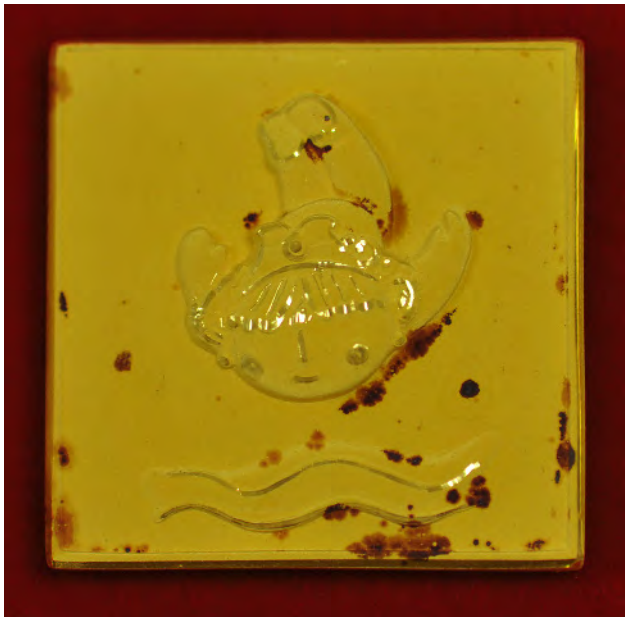

*Figure 4. Brown spots are mainly distributed along the edges of features in this 32.0 × 32.5 mm gold pin from the 2008 Olympic Games. Photo by Jian Zhang.*

terns. The spots often appeared at intersections, corners, edges, curves, or other geometrically preferential sites on the high-purity gold. Figure 4 shows the distribution of the brown spots observed on a gold collectible pin from the 2008 Olympics. These spots are mainly distributed along the corners and along the edges of features.

## In Brief

- Red, brown, and black tarnish spots on high-purity gold jewelry have been reported in recent years.
- Samples from China with 99.9% gold purity were tested using microscopic and spectroscopic techniques to identify the features and origin of their tarnish spots.
- Analysis of the tarnish spots identified the presence of silver and sulfur. The spots were caused by silver deposited on the gold objects during a special electroplating process.

*Unusually Colored Zones.* While the color distribution within a spot was usually uneven, occasionally pink and/or blue zones were seen within a brown spot in a gold Olympic pin, as shown in figure 5.

*Thickness.* There was a direct relationship between the depth of color and the thickness of the thin films. The thicker spots tended to be darker. The red spots were not as thick as the brown ones, which in turn were not as thick as the black ones. When we observed and measured the thickness at higher magnification with the laser scanning confocal microscope, we measured from the surface of the tarnish spot to the top of the gold plating. We found that most spots ranged from 190 to 320 nm thick. On very rare occasions, the thickness was more than 1 µm. Figure 6 shows that the thickness of the thin layer on the surface of the gold studied is 190–320 nm, measured by the laser scanning confocal microscope with measurement software.

**Gold Purity Analysis.** All samples were tested with EDXRF spectrometry to determine their gold purity. Each sample was tested at least three times to confirm the homogeneity, by selecting the areas with and without the brown spots. We found that the gold content in all the tested samples was greater than 99.9%, consistent with the national standard for high-purity gold jewelry (GB 11887-2008). From table 1, we can see that the average gold content was 99.93% for one of the flower-patterned pieces studied. The main trace elements were Cu and Ag, while Ir and Zn were not detected.

*Figure 5. Pink and blue zones together with an impurity center were visible within a brown spot in this high-purity gold commemorative pin from the 2008 Olympics in Beijing. Photomicrograph by Jian Zhang.*

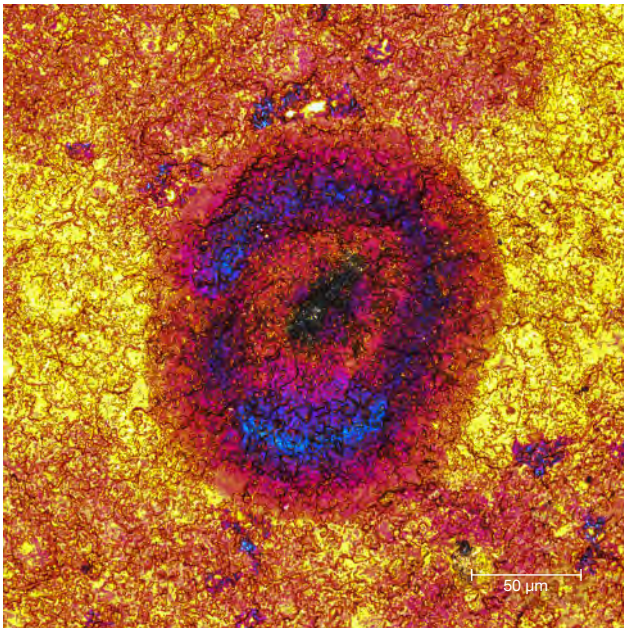

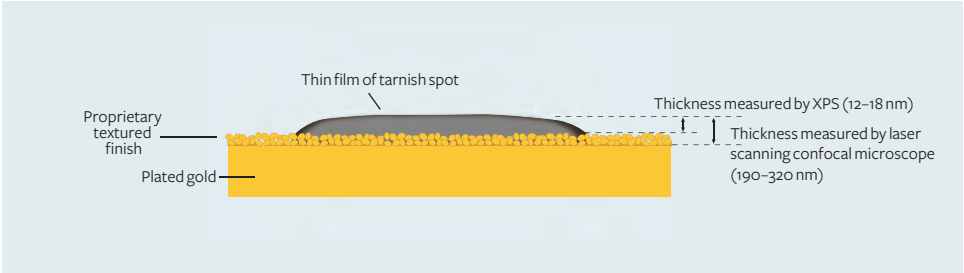


*Figure 6. This drawing illustrates the structure of the gold tarnish spot and the materials beneath it. The thicknesses measured by the various instruments are also illustrated.*

**XPS Analysis.** The chemical composition of the spots was analyzed using X-ray photoelectron spectroscopy (XPS). No silver impurity was recorded in the areas without the spots, but carbon (C 1s, 284.81 eV), oxygen (O 1s, 531.68 eV), sodium (Na 1s, 1069.8 eV), and silicon (Si 2p, 102.2 eV) were detected. These impurities could be attributable to pollution (Yang et al., 2007a). The area with a spot clearly showed two silver peaks located at 367.83 eV and 373.83 eV, which are Ag 3d5/2 and Ag 3d3/2 transitions, respectively, with a difference in binding energy of about 6 eV (figure 7).

The results of quantitative analysis by $Ar^+$ ion sputtering etching are summarized as follows:

1. At the surface of the spot, the concentrations of gold (Au 4f7, 83.6 eV) and silver (Ag 3d5/2) were similar: 0.54 atomic % and 0.56 atomic %, respectively. According to XPS analysis, the Ag 3d5/2 peak at 367.83 eV represents zero-valent silver metal, while Ag 3d3/2 is attributed to monovalent silver. Comparing the known binding energy positions for possible silver and sulfur compounds (Briggs and Seah, 1990; Wang, 1992; Yang et al., 2007a), we concluded that the spots likely have major $Ag_2S$ or $Ag_2SO_4$ components, similar to the results reported by Yang et al. (2007a).
2. The silver and sulfur were mainly found at or just under the surface of the tarnish spots, judging from the *in situ* $Ar^+$ ion etching XPS analysis. In figure 8, the depth profile quantitative data show that the atomic percentage of sulfur was highest at the surface of the spot. After etching approximately 12 nm below the surface, almost no sulfur could be detected. The silver could still be detected, although the peak intensity was much weaker.
3. By plotting a diagram of the $Ar^+$ etching time vs. atomic percentages of Au 4f (83.6 eV), Ag 3d (373.83 eV), and S 2p (161.8 eV) in figure 9, we noted that the Au 4f composition was lowest at the surface, gradually increasing until reaching a saturated level about 8.0 nm below the surface. The atomic percentage of Ag 3d was highest about 1.8 nm from the surface, and S 2p displayed similar behavior.

**TABLE 1.** EDXRF quantitative chemical analysis (wt.%) of a high-purity gold jewelry piece with tarnish spots.

| Element | Spot 1 (tarnished) | Spot 2 (tarnished) | Spot 3 (untarnished) |
|---|---|---|---|
| Au | 99.91 | 99.93 | 99.95 |
| Cu | 0.075 | 0.048 | 0.055 |
| Zn | 0.00 | 0.00 | 0.00 |
| Ir | 0.00 | 0.00 | 0.00 |
| Ag | 0.019 | 0.020 | 0.00 |
| S | bdl* | bdl | bdl |

**Abbreviation: bdl = below detection limit.*

*Figure 7. X-ray photoelectron spectroscopy detected silver peaks at 367.83 eV and 373.83 eV in the brown spot area.*

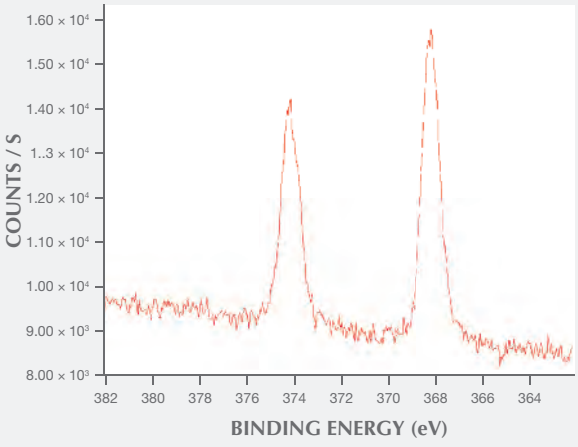

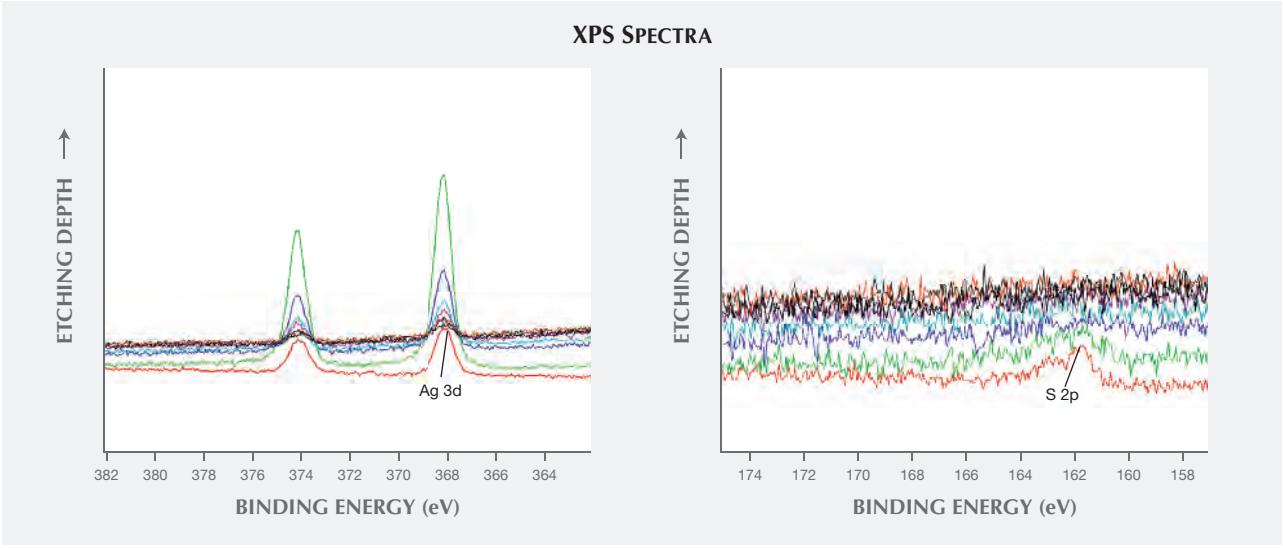


*Figure 8. Depth XPS spectra of Ag (left) and S (right) measured by* in situ *$Ar^+$ ion etching, with the concentrations of Ag and S decreasing as the depth increases.*

4. Most brown tarnish stains were removed when the $Ar^+$ etching time exceeded about 210 seconds. The calculated thickness of the brown stains, based on the etching rate of 0.06–0.08 nm/s, mostly ranged from 12 to 18 nm. This value was dramatically lower than the laser scanning confocal microscope result because it did not include the textured finish layer (again, see figure 6).

*Figure 9. This diagram shows the relationships between etching time (with an etching rate of 0.06 nm/s) and the atomic percentages of S (red line), Au (green line), and Ag (blue line). Since the beam is only focused on the surface and there are other detected elements such as O, C, and N, the Au atomic percentage is only about 70%.*

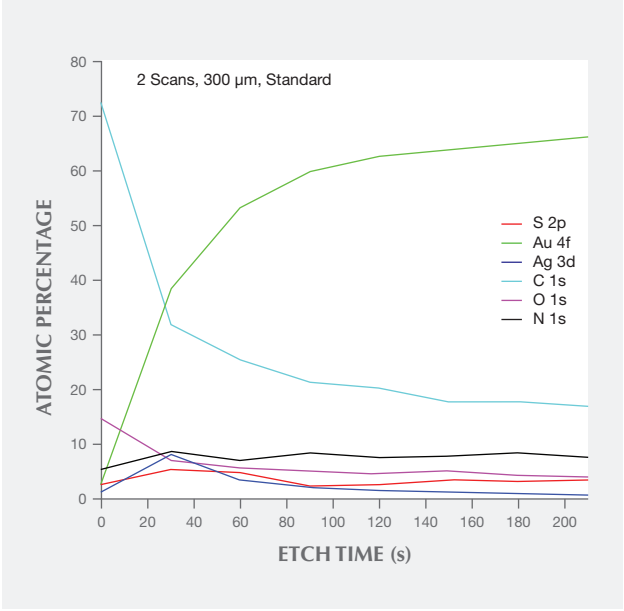


The distribution of Au 4f, Ag 3d, and S 2p laterally across a stain with a diameter of roughly 1000 µm was measured and analyzed (figure 10). It was clear that the Au 4f content was lowest at the center, while both Ag 3d and S 2p were highest at the center; Au, Ag, and S contents were almost flat at the center, which measured about 400 µm wide.

## DISCUSSION

As we know, gold is a noble metal that is highly stable in air. The $Au/H_2O$ system known as the Pourbaix diagram (Yang and Yang, 1991) clearly shows that at a pH range of 2 to 12, the potential of gold is about 0.3 V higher than that of oxygen. This suggests that gold cannot be oxidized by oxygen or air pollution (Yang and Yang, 1991; Yang et al., 2007a). Theoretically, the tarnish spots of high-purity gold jewelry cannot be attributed to chemical corrosion or oxidation of the gold. In fact, our EDXRF testing of gold jewelry samples confirmed their purity was higher than 99.9%, and the main trace elements were Cu and Ag. XPS quantitative analysis, particularly the *in situ* etching experiments in both depth and horizontal directions for removing the stains, confirmed that the major chemical components of the stains were Ag and S, in the form of the $Ag_2S$ thin film. Judging from the depth profile analysis results, the formation of the

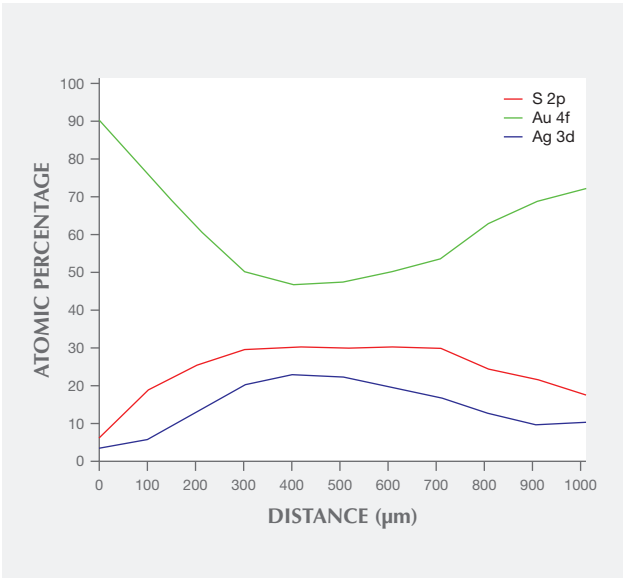


*Figure 10. The atomic percentages of Au 4f, Ag 3d, and S 2p across a brown spot from edge to edge, as detected by XPS.*

tarnish spots is related to silver metal surface contamination. This could stem from external contamination or incomplete cleaning of the silver from the gold piece, which is much closer to the final packing process, based on our factory field investigation. The source of the sulfur could be air pollution. In recent years, the air quality monitoring authority has reported elevated daily concentrations of $SO_2$, CO, $CO_2$, $NO_2$, $NH_3$, $H_2S$, HF, and other gases in Beijing.

Based on experiments related to the formation of tarnish spots on silver, an $Ag_2S$ thin film could form around a silver particle nucleus when the environment contains even very low $H_2S$ and $H_2SO_4$ at room temperature (Kim and Payer, 1999; Payer and Kim, 2002; Kim, 2003; Yang et al., 2007a,b). Figure 11 shows the possible formation process of tarnish spots on high-purity gold jewelry.

In short, silver particle contaminants on the surface of gold jewelry are the nucleation centers for the $Ag_2S$ thin film, and the atmospheric sulfur concentration affects the formation as well as the size of this film.

## CONCLUSIONS

Red, brown, and black tarnish spots on the surface of high-purity gold jewelry samples were investigated by differential contrast microscopy, laser scanning confocal microscopy, SEM, X-ray fluorescence, and X-ray photoelectron spectroscopy. Each sample had a gold purity of 99.9%, regardless of the presence of

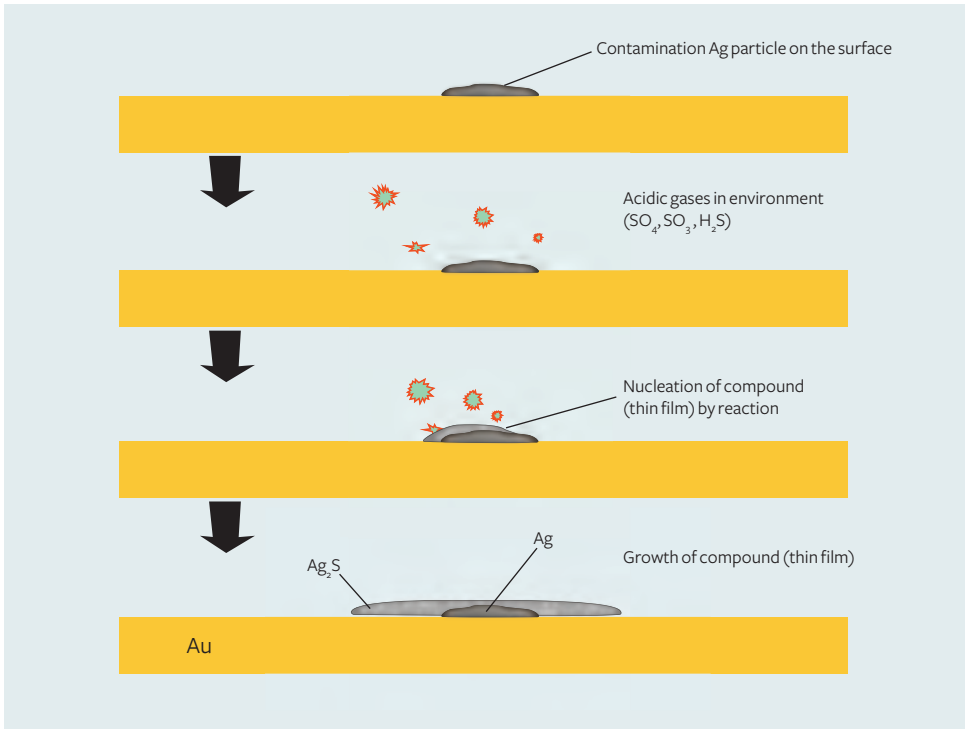


*Figure 11. Possible formation process for the tarnish spots on high-purity gold.*

tarnish. Higher-magnification 3D microscopic observations typically revealed an "impurity center" within the tarnish spot, and the thickness of the thin films typically ranged from several nanometers to several hundred nanometers, including the textured finish layer. The "impurity centers" consisted of silver particles, and the thin films of the tarnish spots were composed of $Ag_2S$, judging from the XPS analysis. The *in situ* Ar ion etching experiment for removing the thin film revealed that the sulfur was only detected at the surface of the tarnish spots where the thickness was less than 12 nm. Therefore, the colored tarnish spots are formed by the chemical reaction between the silver particle contaminants on the surface, and the sulfur-containing components result from air pollution. To prevent these tarnish spots from forming, we recommend improving the cleaning process during gold manufacturing, to eliminate the possibility of silver particle remnants on the surface of high-purity gold jewelry.

ABOUT THE AUTHORS

*Dr. Lu is chief researcher, Mr. Zhang is a senior engineer, Ms. Chen is director of the Beijing Institute, and Ms. Ke is deputy director at the National Gems & Jewellery Technology Administrative Center (NGTC) in Beijing. Mr. Lan is director of, and Ms. Ma is an engineer at, the Shenzhen Institute at the National Gems & Jewellery Technology Administrative Center (NGTC). Mr. Wu is a professor at Beijing Normal University, and Ms. Tang is an engineer at Thermo Fisher Scientific in Beijing.*

## REFERENCES

Briggs D., Seah M.P., Eds. (1990) *Practical Surface Analysis: Auger and X-ray Photoelectron Spectroscopy*, 2nd ed. John Wiley & Sons, New York, 657 pp.

GB 11887-2008 (2008) National Standard of the People's Republic of China: Jewellery – Fineness of precious metal alloys and designation (in Chinese).

Griesser M., Denk R., Griebel M., Traum R., Winter H. (2003) The past and the future—investigating brown spot corrosion on historic gold coins and metals to advance their preservation. In *Proceedings of Numismatics and Technology: Question and Answers*. KHM, Vienna, pp. 91–98.

Gusmano G., Montanari R., Kaciulis S., Montesperelli G., Denk R. (2004) "Gold corrosion": red stains on a gold Austrian Ducat. *Applied Physics A*, Vol. 79, No. 2, pp. 205–211, http:dx.doi.org/10.1007/s00339-004-2534-0

Kim H. (2003) Corrosion process of silver in environments containing 0.1 ppm $H_2S$ and 1.2 ppm $NO_2$. *Materials Corrosion*, Vol. 54, No. 4, pp. 243–250, http://dx.doi.org/10.1002/maco.200390053

Kim H., Payer J.H. (1999) Tarnish process of silver in 100 ppb $H_2S$ containing environments. *Journal of Corrosion Science and Engineering*, Vol. 1, paper 14.

Lu T. J., Zhang J., Lan Y., Ma Y., Chen H., Ke J. (2013) Characterization of tarnish spots on the surface of high-purity gold jewelry. *2013 China Gems & Jewelry Academic Conference*, Oct. 30, pp. 247–250 (in Chinese).

Mayerhofer K.E., Piplits K., Traum R., Griesser M., Hutter H. (2005) Investigation of corrosion phenomena on gold coins with SIMS. *Applied Surface Science*, Vol. 252, No. 1, pp. 133–138, http://dx.doi.org/10.1016/j.apsusc.2005.01.111

Payer J.H., Kim H. (2002) The tarnish process of silver in atmospheric environments containing hydrogen sulfide and nitrogen dioxide. *Electrochemical Society Meeting Abstracts*, www.electrochem.org/dl/ma/199/pdfs/0148.pdf.

Rupprecht L., Gusmano G., Montanari R. (2003) Corrosion damage in modern gold coins. *Numismatic & Technology: Question and Answers*, Vienna, 25–26 April, p. 113.

Wang J.Q. (1992) *Other Electronic Spectroscopy (XPS/XAES/UPS)—Introduction*. National Defense Industry Press, Beijing.

Yang C., Liang C., Wang P. (2007a) Investigation of the tarnish on the surface of a panda gold coin. *Rare Metals*, Vol. 26, No. 1, pp. 68–73, http://dx.doi.org/10.1016/S1001-0521(07)60030-8

Yang C.J., Liang C.H., Liu X. (2007b) Tarnishing of silver in environments with sulphur contamination. *Anti-Corrosion Methods and Materials*, Vol. 54, No. 1, pp. 21–26.

Yang X.Z., Yang W. (1991) *Electrochemical Thermodynamic Potential-pH Diagram and Its Application in Corrosion of Metals*. Chemical Industry Press, Beijing, 256 pp. (in Chinese).

Zhen Y.X., Wu Y. (1991) *Metal Corrosion Thermodynamic Potential-pH Map and Its Application*. Chemical Industry Press, Beijing, 256 pp. (in Chinese).

# SPLENDOR IN THE OUTBACK: A VISIT TO AUSTRALIA'S OPAL FIELDS

Tao Hsu, Andrew Lucas, and Vincent Pardieu

With more than 170 years of opal mining and trading activity, Australia is synonymous with opal. Many world-renowned deposits are distributed in and along the margin of the Great Artesian Basin (GAB). Opal exports contribute roughly $85 million annually to the nation's GDP. The industry employs thousands in the Outback communities and attracts more than 231,000 tourists per year. Opal tourism brings an estimated $324 million each year to these remote mining communities (National Opal Miners Association, n.d.).

To better understand the deposits, collect samples, and experience the opal culture, the authors traveled to Australia in June 2015 and visited four important opal fields: Lightning Ridge, Koroit, Yowah, and Quilpie (figure 1).

## OPAL FORMATION IN THE GREAT ARTESIAN BASIN

Almost all of Australia's opal deposits are geographically related to the GAB; therefore, the influence of this special environment on opalization is of particular interest. Opal is recovered predominantly from the sandstone or claystone units of Cretaceous age in all producing areas within or along the margin of the GAB. Back in the Cretaceous period, sea level fluctuation and general withdrawal occurred along the Australian shoreline. The local balance between rapid sedimentation and subsidence played a role in basin formation. During this period, the GAB was covered by a shallow, stagnant inland sea known as the Eromanga Sea, and the climate was dramatically different from today.

While experienced opal miners always follow certain structures in the rocks to mine the material, scientists have formed opalization models based on samples and field observations (figure 2). A variety of opalization theories have been proposed, including weathering theory, microbe theory, and syntectonic theory (Pecover, 2007). The most recent proposal is redox theory (Rey, 2013), which portrays a cold and poorly connected Eromanga Sea that lacked carbonates but was full of sediments rich in iron and organic matter. These sediments favored an anoxic environment in which anaerobic, pyrite-producing bacteria thrived. Thus, these sedimentary lithologies were extremely reactive to oxidation. During the Late Cre-

*Figure 1. Australia's opal deposits are distributed in or along the margin of the Great Artesian Basin. Coober Pedy, Andamooka, White Cliffs, and Lightning Ridge are some of the world's best-known opal-producing areas. In June 2015, the authors visited Lightning Ridge in New South Wales, as well as Koroit, Yowah, and Quilpie in Queensland.*


See end of article for About the Authors and Acknowledgments.
GEMS & GEMOLOGY, Vol. 51, No. 4, pp. 418–427,
http://dx.doi.org/10.5741/GEMS.51.4.418.

*Figure 2. In Koroit's underground mine, owner Mark Moore showed the authors the fault line he followed to find opals. Photo by Vincent Pardieu/GIA.*

taceous period (about 97 to 60 million years ago), Australia experienced extensive acidic and oxidative weathering. Rey (2013) proposed that precious opal might form via this prolonged weathering and the opalized redox front, which was later buried and therefore well preserved by Cenozoic sediments.

Unfortunately, none of these models can resolve all the problems associated with opal formation. The different types of occurrences, such as black opal nodules and boulder opal ironstone concretions, also create challenges for researchers. Although an opalization model is not the purpose of this report, some of the most critical questions scientists must answer before forming any theories involve the supply of silica and water, space for opal growth, sedimentation conditions, and the ion exchange process. Not all opals formed the same way, and therefore multiple models may be required.

## LIGHTNING RIDGE AND BLACK OPAL

Our first stop was Lightning Ridge, the traditional source for fine-quality black opal. The Lightning Ridge area is located in New South Wales, just south of the border from Queensland (figure 3). Opal was first discovered here in the late 1880s. The town of Lightning Ridge grew quickly after miners from other areas realized the value of this beautiful gem. Today, active mining operations are distributed both around the township and in the outlying areas such as Sheepyard, Grawin, Glengarry, and Carters Rush (again, see figure 3). Exploration is carried out in different areas of Lightning Ridge, and the authors visited one to the north of the township.

In Lightning Ridge, opal is generally recovered from the Finch Claystone unit of the Early Cretaceous age. This unit is directly below the Wallangulla Sandstone, which contains some Finch Claystone lenses; some of these lenses are opal bearing as well (figure 4). Previous underground mining channels are

*Figure 3. Map of the Lightning Ridge region. The group visited one underground mine in the town of Lightning Ridge and one in Sheepyard.*

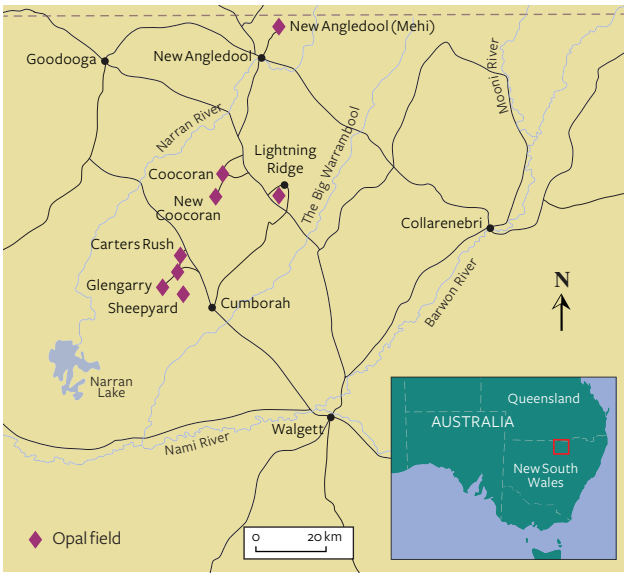

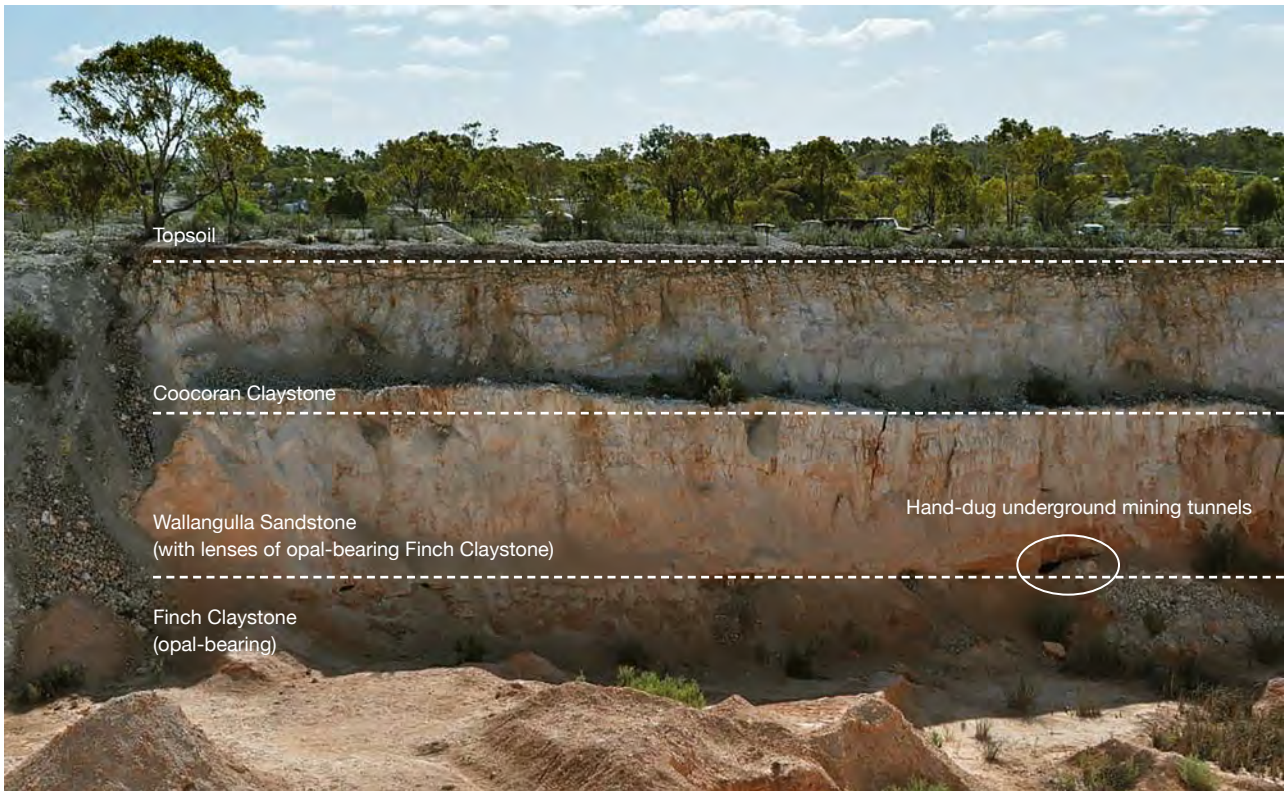


*Figure 4. An exposed stratigraphic profile of the Lunatic Hill mine. Previous mining channels from the beginning of the 20th century can be seen at the boundary between the Wallangulla Sandstone and Finch Claystone units. The claystone is usually found at a depth of less than 30 meters. Photo by Vincent Pardieu/GIA.*

clearly visible at the contact zone between the two units on a well-exposed profile in the Lunatic Hill mine. The deposits are usually found less than 30 meters from the surface. Opal is found as nodules contained in the whitish clays; local miners refer to these as "nobbies" (figure 5). Opal is also recovered as thin seams in the outlying areas. The miners often follow structural features such as fractures and faults to look for opals.

*Figure 5. These spectacular black opal nobbies were found in claystone. The nodule was cut into two parts, and we can clearly see the areas with precious opal, while the rest is composed of dark gray potch. Photo by Vincent Pardieu/GIA, courtesy of Vicky Bokros.*

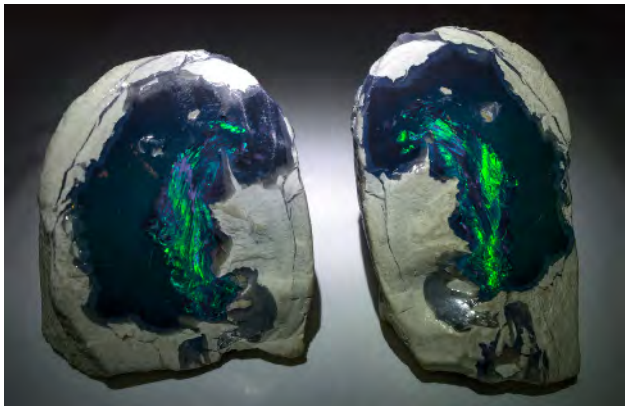

Miners seeking black opal usually start with an underground operation. They will switch to an open pit (which Australians refer to as an "open cut") only when they feel that it is more profitable. We saw mainly underground mining operations in this area.

A custom-designed digger extracts opal-bearing clays from the Finch Claystone unit, with the Wallangulla Sandstone unit acting as the roof of the underground mine (figure 6). Mined materials are drawn to the surface by a "blower" and transported to the washing plant (figure 7). A black opal washing plant generally consists of a water source, an agitator, and a sorting table. The washing process often takes one week to finish (figure 8). Opal, clay, and sandstone fragments are rotated in water within the agitator; this removes most of the clay from the opal without damaging the stone. At the end of the week, miners

*Figure 6. This customized digger is specifically designed to extract opal-bearing clay. Joints on the machine allow for greater flexibility. Photo by Andrew Lucas/GIA.*

open the agitator and let the slurry flow out onto the sorting table, where they pick out the opals by hand (figure 9).

The clay is not very hard and is easily removed from the opals by washing and/or polishing. Due to their shape, opals from Lightning Ridge can be processed as cabochons and other freeforms (figure 10). Special care and design are necessary to use the black seam opal in jewelry (figure 11). White, crystal, and black opals can all be found in the Lightning Ridge region, but the fine-quality black opal is sought worldwide.

*Figure 7. The "blower" is in fact a giant vacuum sucking everything mined to the surface. It is powered by a generator mounted on a truck above ground. The mined materials are loaded onto dump trucks and carried to the washing plant. Photo by Vincent Pardieu/GIA.*

*Figure 8. The agitator, a converted concrete mixer, is the core facility in the washing plant. When it rotates, the opal nodules and other materials within it circulate, removing much of the clay from the opal. Photo by Vincent Pardieu/GIA.*

*Figure 9. This handful of opal is the result of several weeks of underground mining and a few days in the agitator. Photo by Vincent Pardieu/GIA.*

*Figure 11. Black seam opal occurs as thin lines in claystone. According to the mine owner, seam opal requires a different processing method than the nodules. Photo by Vincent Pardieu/GIA.*

Fine black opal owes its beauty to its dark background and bright play-of-color (figure 12). A whole spectrum of colors can be found in black opals, with shades of blue and green the most common. Every piece is unique because of the pattern of the play-of-color, the number of colors exhibited, and the thickness of the finished pieces; this makes the stone extremely hard to grade. Although opal's beauty is very subjective and choosing a stone is a deeply personal experience, market demand determines the overall price range. According to the miners and cutters, any play-of-color with an element of red dramatically increases the value of the stone. This was reflected in the prices of the loose stones we saw in the local market.

Opalized fossils are also found in Lightning Ridge. Plant and animal fossils of Cretaceous age, from microscopic organisms to giant dinosaur skeletons, are found in the GAB, and some have been partially or completely opalized (figure 13). With their precious play-of-color, these fossils are both a national treasure and excellent material for scientific research. They have attracted the attention of paleontologists all over the world. According to Dr. Elizabeth T.

*Figure 10. Experienced cutters guided the authors through the entire process of polishing an opal cabochon. Photo by Andrew Lucas/GIA.*

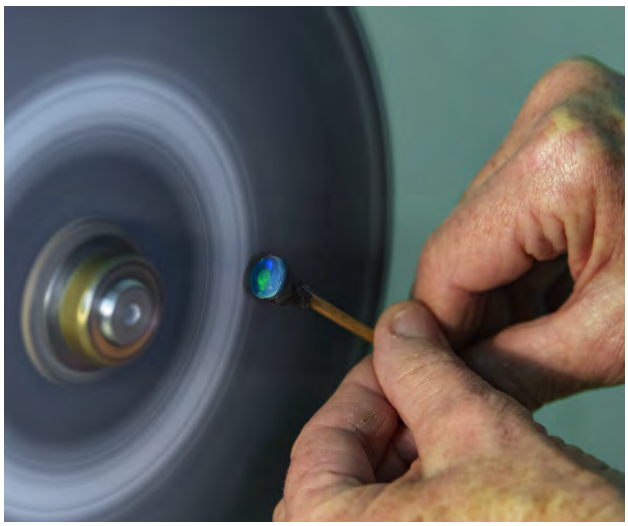

*Figure 12. This 92 ct black opal, held by cutter and carver Justine Buckley, was recovered in 2014 from Lightning Ridge. It took Buckley about a year to design and polish the stone, which shows a whole spectrum of colors. Photo by Andrew Lucas/GIA.*

*Figure 13. These well-preserved bivalve fossils are from the freshwater mollusks that lived in Lightning Ridge during the Cretaceous period. This type of fossil is usually found in mining operations that intersect with paleochannels. Photo by Vincent Pardieu/GIA.*

*Figure 14. Isolated flat-topped hills are a common topographic feature in the central part of Queensland. Many of these hills host opal mines. Photo by Andrew Lucas/GIA.*

Smith from the University of New South Wales, the transparency of precious opal provides an unprecedented view inside the fossil.

## QUEENSLAND FIELDS AND BOULDER OPAL

Across the state border north of Lightning Ridge is Queensland, considered the home of boulder opal. Opal was discovered in Queensland in the 1870s. In his geological survey report, Jackson (1902) reported: "At present about 295 men are engaged in the industry… The total value of gem stones produced from all opal-fields in Queensland is, as nearly as can be estimated, £131,000, or, up to the end of 1899, £116,000." By the turn of the century, opal was popular among European consumers.

The state of Queensland has more than 300,000 $km^2$ of land and about a dozen fields dedicated to opal exploration (again, see figure 1). Unlike other locations, the Queensland fields mainly produce boulder opal, which is extracted from the Desert Sandstone formation of Upper Cretaceous age. This formation, which experienced high erosion after its deposition, covers most of the state today as low ranges, tablelands, and isolated flat-topped hills (figure 14). A lower and softer opal-bearing sandstone and clay subunit is capped by a hard reddish siliceous subunit 5 to 16 meters thick (figure 15). This profile can be clearly seen at multiple mining operations. To better understand the boulder opal industry, the authors visited Koroit, Yowah, and Quilpie in central Queensland.

While underground and open-cut operations are found in all three fields, open-cut mining seems to be more prevalent. Opal is recovered from siliceous ironstone concretions, called "lily pads" or "nuts" by local miners depending on their morphology (figure 16). Miners examine certain structures to look for ironstone concretions, which are sometimes grouped along a line. As opposed to the washing process we saw in Lightning Ridge, miners need to split each concretion by hand to unveil the contents; only a limited number yield opal (figure 17).

Boulder opal is quite different from other varieties in terms of appearance. The term "boulder" refers to the host rock that is naturally attached to the fin-

*Figure 15. The large open-cut mining operation in Alaric, about 65 km north of the Quilpie mine, shows a well-defined profile of the Desert Sandstone formation. Photo by Vincent Pardieu/GIA.*

*Figure 16. Boulder opal is mainly found in siliceous ironstone concretions. The flat ones from Koroit are called "lily pads," while the small round ones from Yowah are known as "nuts." Some of the ironstone concretions in Quilpie can be very large. Photo by Vincent Pardieu/GIA.*

ished product. When an opal-bearing ironstone concretion is opened, the distribution of precious opal is easy to see. Sometimes it is found in between the "skin" layers of the concretion or at its core (figure 18). Although opal at the kernel of a concretion may

*Figure 17. Boulder opal miners must split every ironstone concretion they find to reveal its contents. Photo by Andrew Lucas/GIA.*

*Figure 18. An open ironstone concretion displays the precious opal within. Opal can also occur on the surface of the concretion. Photo by Vincent Pardieu/GIA.*

be large enough to separate from the host rock, most opals are too thin to be removed without being damaged (figure 19). Some opals occur on the surface of siliceous ironstone and follow the natural surface feature of the host rock; therefore, keeping it together with the rock adds more appeal to the stone. When precious opal occurs in cracks of the host rock, a well-polished stone can show truly spectacular abstract patterns (figure 20).

*Figure 19. This opal is the kernel of an ironstone concretion. When this happens, the opal is usually large enough to be separated from the matrix, but cutters often choose to keep it to add aesthetic appeal. The host seen here is a piece of tree trunk. Photo by Vincent Pardieu/GIA; courtesy of the Maguire Collection.*

*Figure 20. A boulder opal from Koroit showing abstract patterns is positioned next to a flat "lily pad" ironstone concretion. Photo by Vincent Pardieu/GIA.*

## OPAL CULTURE

In all the mining towns we visited, we were impressed by the pride and passion of the locals, including some miners from overseas. For them, opal mining has become a way of life. Even during long periods without finding a gem-quality stone, the miners choose to stay. In our interviews, we were struck by their remarkable perseverance and drive. These were not the type of people who needed a steady paycheck or job security. They were willing to struggle and search for a discovery of opal, realizing that it might never come but also aware that with hard work it is possible. The economies of these small communities are largely based on opal mining, as well as opal-related tourism and recreational fossicking.

The Australian Opal Centre is under construction in Lightning Ridge (figure 21). Ms. Jenni Brammall, the manager of this project, informed us of the progress being made. While the foundation of the building was completed in 2014, fundraising is under way to support further operations. The opal center currently operates out of a small facility on the town's main street. The new facility will serve as a museum, an educational center, and a platform to promote the national gemstone.

In Yowah, the authors met miner turned opal artist Eddie Maguire, who showed us his outstanding collection. He fashioned these stones in his home studio, applying creative cuts and unique displays (figure 22). Mr. Maguire's collection consists entirely of carvings. In polishing the opal, he tries to preserve the natural form as much as possible. Many pieces are displayed on a frame or host, also designed and carved by Mr. Maguire. This method works very well with boulder opals since they are usually attached with their host rock, though many of the boulder opals in this collection stand on their own. He is working on opening a private museum in Yowah to exhibit his collection and educate people about opal.


*Figure 21. The manager of the Australian Opal Centre project, Jenni Brammall, is a paleontologist, photographer, and expert on opalized fossils. Photo by Vincent Pardieu/GIA.*

*Figure 22. Eddie Maguire's collection does not include jewelry pieces. Instead, he tries to keep the opals in their natural state and add some elegant or eclectic elements to the display. Shown in the background is Terry Coldham. Photo by Vincent Pardieu/GIA.*

## CONCLUSION

Despite its dominance in the international market, the Australian opal industry still faces many challenges. A regional drought is one of the major obstacles for opal mining. The drought in the GAB has lasted for several years, and finding a water source is a problem for many miners. Although opal is well known, consumers need a better understanding of the stone's varieties to truly appreciate its uniqueness. As in many other mining regions, a new generation of prospectors will be needed to sustain the future of Australia's opal industry. From our conversations with miners we learned that many of the younger generation are moving to the cities. It is not a problem for now, but in another 20 to 30 years there could be a serious shortage of labor.

Meanwhile, many Australians are working hard to promote this spectacular gem, including miners, dealers, and collectors. At the beginning of our trip, Andrew Cody of Cody Opal hosted us in his Sydney flagship store. The store hosts the National Opal Collection, which features some of the rarest opalized fossils, including a three-meter-long intact skeleton of a pliosaur (figure 23). Australian opal formed

*Figure 23. Opalized fossils are a national treasure of Australia. The National Opal Collection in Sydney features an intact three-meter-long skeleton of an opalized pliosaur. Photo by Tao Hsu/GIA.*

around the same time as these prehistoric creatures. Mr. Cody and his brother Damien have been promoting Australian opal globally for years and in mainland China since 2012.

Since its discovery in the late 19th century, Australian opal has had a rich mining culture and a loyal consumer base. Despite the challenges the industry faces, the gem continues to fascinate scientists and jewelry enthusiasts with its unique formation and vivid play-of-color.

ABOUT THE AUTHORS

*Dr. Hsu is technical editor of* Gems & Gemology*, and Mr. Lucas is manager of field gemology education, at GIA in Carlsbad. Mr. Pardieu is senior manager of field gemology at GIA's Bangkok laboratory.*

ACKNOWLEDGMENTS

*The authors want to thank Terry Coldham, who was instrumental in planning this field expedition and drove tirelessly across the Australian Outback; the Lightning Ridge Miners Association; the Australian Opal Centre; the Gemmological Association of Australia; Andrew Cody; and all of the miners, cutters, wholesalers, and retailers in Lightning Ridge, Koroit, Yowah, and Quilpie.*

## REFERENCES

Jackson C. F. V. (1902) *The Opal-Mining Industry and the Distribution of Opal Deposits in Queensland*. G.A. Vaughan, Government Printer, Brisbane.

National Opal Miners Association (n.d.) Model work health and safety regulations for mining, https://submissions.swa.gov.au/SWAforms/Archive/mining/documents/022%20-%20National_Opal_Miners_Association.PDF

Pecover S. R. (2007) Australian opal resources: Outback spectral fire. *Rocks & Minerals*, Vol. 82, No. 2, pp. 102–115, http://dx.doi.org/10.3200/RMIN.82.2.102-115

Rey P.F. (2013) Opalisation of the Great Artesian Basin (central Australia): An Australian story with a Martian twist. *Australian Journal of Earth Sciences*, Vol. 60, No. 3, pp. 291–314, http://dx.doi.org/10.1080/08120099.2013.784219

## For More on Australian Opal

Learn more about the different types of opal found in Australia. Our exclusive video and photo galleries explore the fields of Lightning Ridge and Queensland and introduce the people who spend their lives pursuing this phenomenal gem.

Visit http://www.gia.edu/gia-news-research/australia-opal-fields-expedition, or scan the QR code on the right.

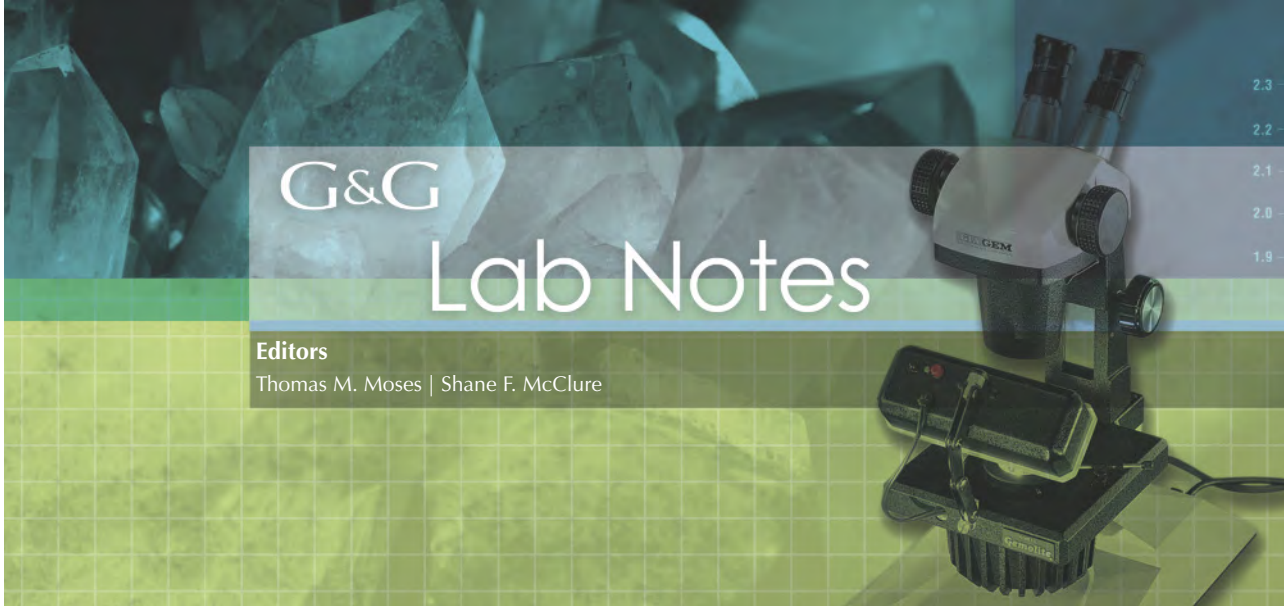


## Graphite Inclusions Forming Octahedral Outline in DIAMOND

Primary diamond deposits are usually found in mantle-derived igneous rocks, with the principal hosts being kimberlite and lamproite. During the ascent to the earth's surface, diamonds may be converted, partially or entirely, to graphite and chemically dispersed and eliminated (A.A. Snelling, "Diamonds – Evidence of explosive geological processes," *Creation*, Vol. 16, No. 1, 1993, pp. 42–45). GIA's New York laboratory recently received a 1.30 ct Fancy brownish greenish yellow diamond (figure 1) containing an octahedral-shaped inclusion outlined by minute crystal inclusions along the junctions of the crystal faces.

Gemological examination at 60× magnification reveals that the octahedral-shaped inclusion is outlined by numerous irregular dark crystals (figure 2). Advanced gemological analysis with UV-Vis and FTIR spectroscopy confirmed that this was a natural diamond with a natural color origin.

Further analysis using Raman spectroscopy reveals that the dark inclusions are graphite crystals with a Raman peak at 1590 $cm^{-1}$ (figure 3), which corresponds to the graphite G band (I. Childres et al., "Raman spectroscopy of graphene and related materials," in J.I. Jang, Ed., *New Developments in Photon and Materials Research*, Nova Science Publications, 2013). Since this G band is at a slightly higher energy level than that from the primary graphite, which usually peaks at around 1580 $cm^{-1}$, we propose that the crystals tested are likely the secondary graphite converted from part of the original diamond into graphite form during the specific growth episode when oxidized fluids rich in $CO_2$ and $H_2O$ passed through diamond bearing horizons. This also explains the shift of the G band to a higher energy, due to the higher strain near these newly formed secondary graphite crystals (J. Hodkiewitcz, "Characterizing graphene with Raman spectroscopy," *Application Note: 51946*, Thermo Fisher Scientific, Madison, Wisconsin, 2010). Late formation of additional diamond layers on top of the graphites would have converted them to covered internal features within the larger diamond (R.H. Mitchell, *Kimberlites and Lamproites: Primary Sources of Diamond*, Geoscience Canada Reprint Series 6, Vol.

*Figure 1. This 1.30 ct Fancy brownish greenish yellow diamond contains an octahedral-shaped inclusion.*

*Figure 2. Minute graphite inclusions outline the octahedral crystal faces in this diamond. Field of view 7.19 mm.*

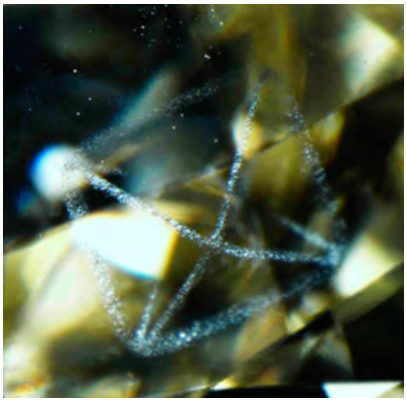

*Editors' note: All items were written by staff members of GIA laboratories.*

GEMS & GEMOLOGY, Vol. 51, No. 4, pp. 428–440.

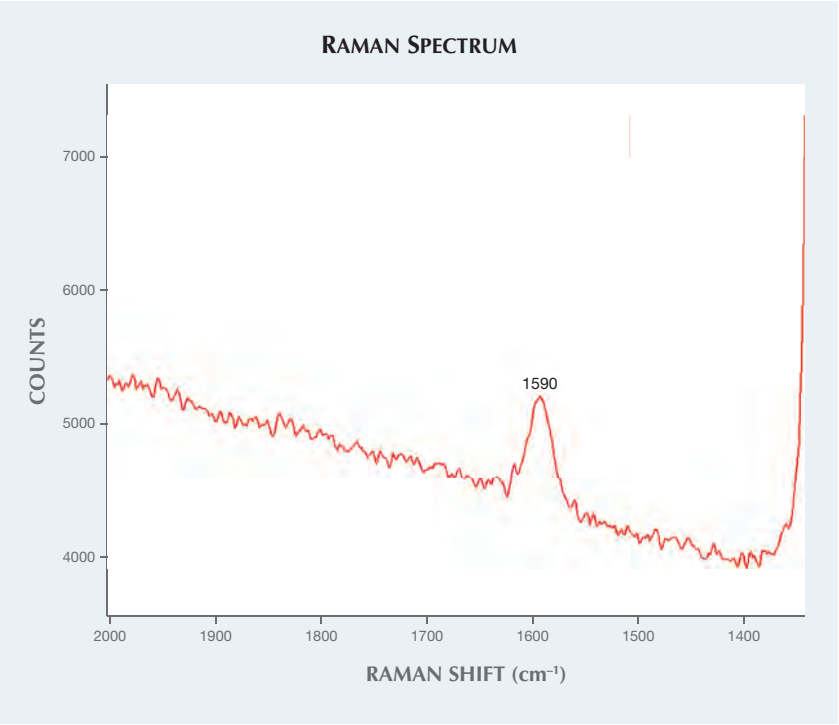


*Figure 3. The graphite G band at 1590 cm$^{-1}$ is found on the minute crystals along the crystal junctions, confirming that they are graphite crystals.*

18, No. 1, 1991, pp. 1–16). Primary graphite crystals could also mix into the crystal clouds during the diamond's growth due to changes in environmental temperature, pressure, and the growth fluid's chemical elements. These minute graphite crystals would tend to form along the junctions of crystal faces, since they usually have a higher surface energy. Thus, we believe that both primary and secondary graphite formation, occurring between the diamond's growth episodes, contributed to this phenomenal octahedral outline.

Graphite inclusions are commonly seen in diamonds as isolated crystals or jointed crystal clouds. It is very unusual to see these minute graphite inclusions formed at the junctions of the original diamond crystal faces and outlining the octahedral growth pattern. This stone not only captures the amount of stress and extreme conditions under which the diamond grew, but also shows the beauty of the formation of crystalline diamond.

*Yixin (Jessie) Zhou*

## Treated Pink with HPHT Synthetic Growth Structure

HPHT synthetic diamonds are grown using high pressure and high temperature but with a much higher growth rate than natural diamond. Consequently, their growth structures are different. GIA's New York lab recently examined a multi-step treated diamond with a growth structure similar to that of HPHT synthetics. The 1.62 ct Fancy pink type IIa round brilliant seen in figure 4 showed spectral characteristics suggestive of HPHT treatment, irradiation, and annealing. This diamond was internally clean, except for the presence of strong, colorless internal graining (figure 5). Tatami and banded strains with strong interference colors could be seen under cross-polarized light (again, see figure 5). Based on these microscopic features, we concluded that this was a natural diamond.

DiamondView imaging of the stone showed cuboctahedral growth with dark sectors and pink coloration (figure 6). This crystal habit is usually observed in HPHT-grown synthetic diamonds. As seen in figure 6 (left), the cubic {100} sector can be located in the pavilion, along with octahedral {111} sectors. In order to understand more about this growth, we compared it with a type IIa 0.27 ct HPHT synthetic, which was treated post-growth to induce a Fancy Intense orangy pink color (figure 6, right). Both specimens showed similar fluorescence patterns; however, the natural diamond's greenish blue phosphorescence was evenly distributed, as seen in the middle image of figure 6. This is unlike the dark images yielded from type IIa pink HPHT synthetics, which are not phosphorescent.

Although most natural diamonds show octahedral growth structure in DiamondView images, some natural gem-quality colorless and yellow diamonds may show cuboctahedral growth (Winter 2010 Lab Notes, pp. 298–299; Winter 2011 Lab Notes, p. 310; Spring 2013 Lab Notes, pp. 45–46). Some non-gem-quality diamonds possess cuboctahedral form (D.G. Pearson et al., "Orogenic ultramafic rocks of UHP (diamond facies) origin," in R.G. Coleman and X. Wang, Eds., *Ultrahigh Pressure Metamorphism*, Cambridge University Press, 1995, pp. 456–510). Growth rate, pressure, and temperature of geological environment control the habit of a di-

*Figure 4. This multi-step treated 1.62 ct Fancy pink natural diamond shows what appears to be HPHT synthetic growth structure.*

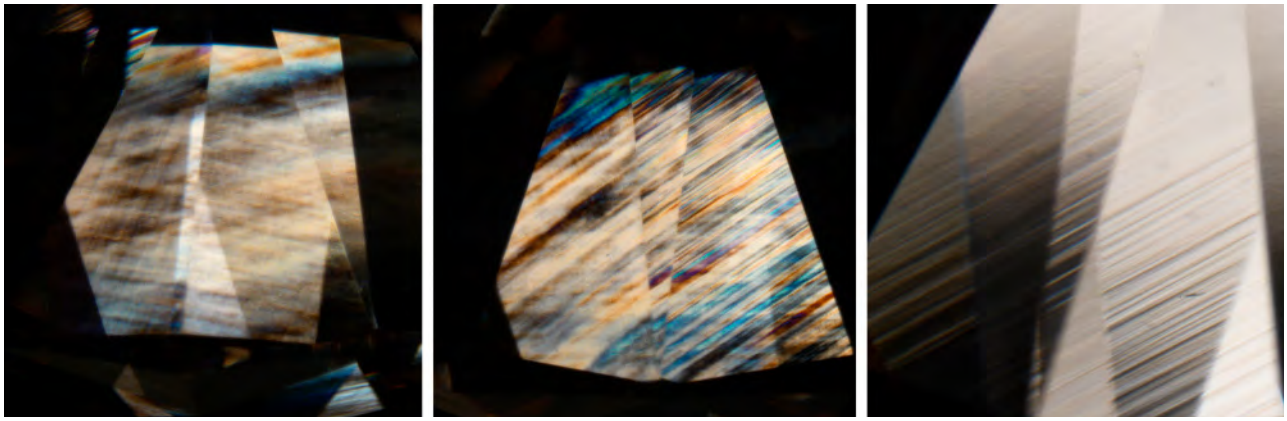

*Figure 5. Tatami strain (left, field of view 3.20 mm), banded strain (middle, field of view 3.20 mm), and heavy internal graining (right, field of view 2.45 mm) are evidence of a natural diamond.*

amond crystal. A slow growth rate causes octahedral crystal growth, but a high growth rate can facilitate cubic {100} and octahedral {111} sectors developing simultaneously. As a result, cuboctahedral habit can be formed naturally.

While the DiamondView is very reliable at revealing the growth structure of natural vs. synthetic diamond, it is important to correctly interpret all identifying characteristics. When cuboctahedral growth structure is observed, one should look for other features to support the origin. Microscopic features and spectral characteristics are useful for this purpose.

*Kyaw Soe Moe and Wuyi Wang*

## Very Large Type Ib Natural Diamond

Nitrogen is the main impurity in diamond and during growth it is initially incorporated in the diamond lattice as isolated nitrogen atoms (C centers). Diamonds where the majority of nitrogen occurs in C centers are known as type Ib. While C centers are common in lab-grown HPHT diamonds, the occurrence of C centers in natural cratonic diamonds is extremely rare (<1% of all natural diamonds). Natural diamonds form deep in Earth's mantle, where high temperatures result in nitrogen aggregating to form A centers ($N_S$) and B centers ($N_4V$).

GIA's New York laboratory recently tested a large 13.09 ct gem-quality natural type Ib rough diamond. The diamond measured 13.51 × 11.56 × 10.18 mm, with rounded dodecahedral morphology and clear dissolution pits on some faces in a symmetrical pattern (figure 7). The diamond had a highly saturated, slightly orangy yellow color evenly distributed throughout the whole crystal. The diamond contained two tiny sulfide inclusions with their associated graphitic rosette fracture systems.

The infrared absorption spectrum revealed typical features of natural type Ib diamonds: a sharp peak at 1344 $cm^{-1}$ and a broad band at 1130 $cm^{-1}$. The absorption attributed to the

*Figure 6. DiamondView fluorescence images of the treated 1.62 ct pink natural (left) and the post-growth treated 0.27 ct pink HPHT synthetic (right) showed similar growth patterns, containing cubic {100} sector and octahedral {111} sectors. The middle image of phosphorescence of the 1.62 ct pink natural diamond showed even color distribution without growth sectors. Type IIa pink HPHT synthetic diamonds are usually not phosphorescent.*

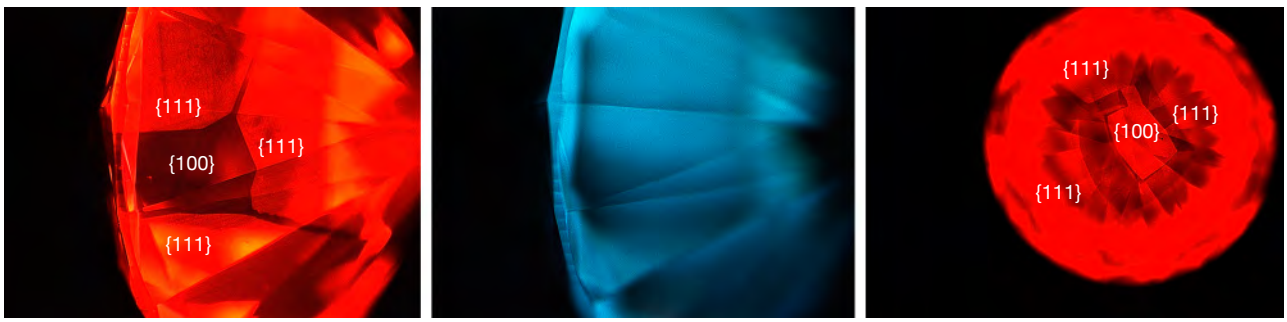

*Figure 7. The yellow color of this gem-quality 13.09 ct type Ib natural diamond rough is due to the presence of isolated nitrogen (C centers).*

A center (1280 $cm^{-1}$) was rather weak. Spectral fitting showed that 75% of the nitrogen existed as C centers and 8% as A centers. This diamond did not contain any amber centers, which is consistent with the lack of plastic deformation lines or brownish hue.

The UV-Vis-NIR absorption spectrum, collected at liquid nitrogen temperature, showed a smooth and gradual increase in absorption from the near-infrared region to about 560 nm, and then a sharp increase to the high-energy side. C centers were the only color-introducing defect in this large diamond.

Photoluminescence (PL) spectra were collected at liquid nitrogen temperature with various laser excitations. Under 514 nm laser excitation, $[N\text{-}V]^0$ at 574.9 nm and $[N\text{-}V]^-$ at 637.0 nm were detected. Many sharp emissions with unknown assignments were also observed (figure 8). With 830 nm laser excitation, weak emissions at 882/884 nm from Ni-related defects were observed.

Large type Ib diamonds with intense yellow color are rarely seen. GIA continues to study these rare diamonds to understand the geological processes that allow isolated nitrogen to be preserved in some natural diamonds. Preservation of C centers in these natural diamonds is typically attributed to very young formation ages or to storage of these diamonds at cooler temperatures in Earth's mantle than most other diamonds. Ongoing isotopic age dating of sulfide inclusions, combined with temperature constraints, will provide the opportunity to evaluate how these enigmatic type Ib diamonds are preserved in natural cratonic settings.

*Wuyi Wang and Karen Smit*

## Uranium Contents of HYALITE

Hyalite is a colorless variety of common opal with strong greenish fluorescence. Rough specimens have interesting glassy botryoidal shapes formed by vapor transport in volcanic or pegmatitic environments (O.W. Flörke, "Transport and deposition of $SiO_2$ with $H_2O$ under supercritical conditions," *Kristall und Technik*, Vol. 7, 1972, pp. 159–166). Hyalite from a new source in Zacatecas, Mexico, discovered in 2013, shows strong green fluorescence even under daylight conditions. This material was spotlighted for the first time at the 2014 Tucson gem and mineral shows (E. Fritsch et al., "Green-luminescing hyalite opal from Zacatecas, Mexico," *Journal of Gemmology*, Vol. 34, 2015, pp. 490–508).

GIA's Tokyo laboratory recently had an opportunity to examine several faceted hyalites from Zacatecas, Mexico, along with several rough hyalites from other locations, including Japan, Hungary, and Argentina. There were two different types of Japanese hyalites in the study samples: botryoidal and spherical. The botryoidal one (figure 9) was from Gifu's Naegi granitic pegmatite (H. Ogawa et al., "Fluorescence of hyalite in pegmatite from Naegi granite, Nakatugawa," 2008 Annual Meeting of Japan Association of Mineralogical Sciences), while the spherical one was from Toyama's Shin-yu hot spring (Y. Takahashi et al., "On the occurrence of opal at the Shin-yu hot spring, Tateyama," *Tateyama Caldera Research*, Vol. 8, 2007, pp. 1–4.). Hungarian hyalite is known to form in the clefts of trachytic rocks in Bohemia, Czech Republic, and Auvergne, France (B. von Cotta, *Rocks Classified and Described: A Treatise on Lithology,* Longmans, Green, and Company, London, 1866, p. 425). Argentinean hyalite is widely distributed, but the original rocks are not described.

*Figure 8. The diamond's PL spectrum, collected at liquid nitrogen temperature with 514 nm laser excitation, showed emissions related to N-V centers along with many sharp peaks of unknown assignment.*

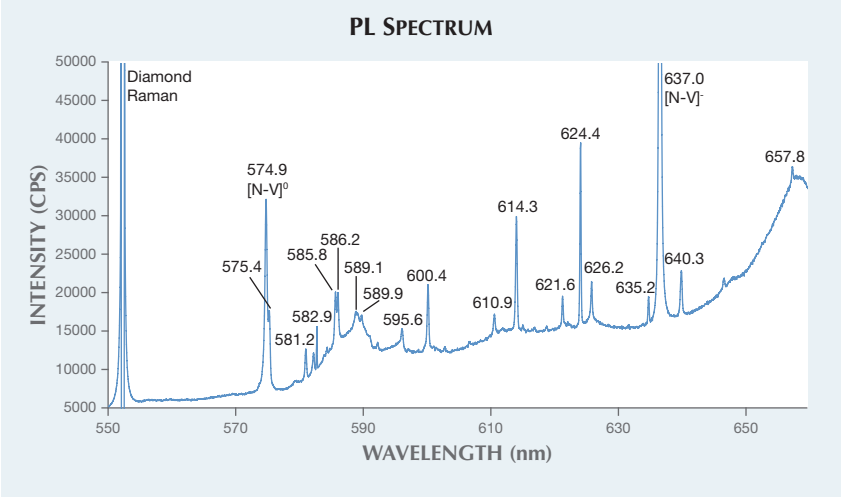

*Figure 9. Two different types of Japanese hyalite rough specimens under daylight (left) and short-wave UV light (right). The photo on the right demonstrates the strong yellow-green fluorescence of pegmatite hyalite, while the spherical hyalite samples do not show the fluorescence.*

Standard gemological testing of the faceted Mexican stones revealed RI values of 1.460–1.461 and a hydrostatic SG of 2.13. Prominent fluorescence was observed under short-wave UV light, but only the Japanese spherical samples were inert (figure 10). Strong graining flow structures were visible at 64× magnification. Raman analysis (figure 11) revealed typical amorphous silica spectra composed of a major band between 430 and 460 $cm^{-1}$ (vibration of bridging oxygen) and a band centered at 790 $cm^{-1}$ representing the stretching of isolated $SiO_4^{4-}$ (P. McMillan, "A Raman spectroscopic study of glasses in the system CaO-MgO-$SiO_2$," *American Mineralogist*, Vol. 69, 1984, pp. 645–659). Laser ablation–inductively coupled plasma–mass spectrometry (LA-ICP-MS) detected a very wide range of uranium contents; the maximum was 1060–1330 ppmw for the Japanese pegmatitic hyalite, while the Japanese spherical hyalite had zero uranium content. The amounts are quite inhomogeneous, but seem to correlate with the intensities of fluorescence, decreasing from Mexican (1180–3.55 ppmw) to Argentinian (2.48–2.49 ppmw) to Hungarian (0.39–0.15 ppmw) (figure 11). Interestingly, only the Japanese pegmatitic hyalite sample was rich in rare earth elements (REE). Since Naegi granitic pegmatite is known to be an REE-enriched pegmatite (T.S. Ercit, "REE-enriched granitic pegmatites," in R.L. Linnen and I.M. Samson, Eds., *Rare-Element Geochemistry and Mineral Deposits*, Geological Association of Canada, GAC Short Course Notes 17, 2005, pp. 175–199), the host rock chemistry appears to affect the silica-rich fluid.

*Figure 10. Clockwise from top center, one Hungarian botryoidal hyalite with matrix, one Japanese pegmatite rough hyalite with matrix, twenty-three pieces of Japanese spherical hyalite, one rough and three faceted Mexican specimens, and one Argentinian botryoidal hyalite under short-wave UV light. The intensity of yellow-green fluorescence vary in the different specimens.*

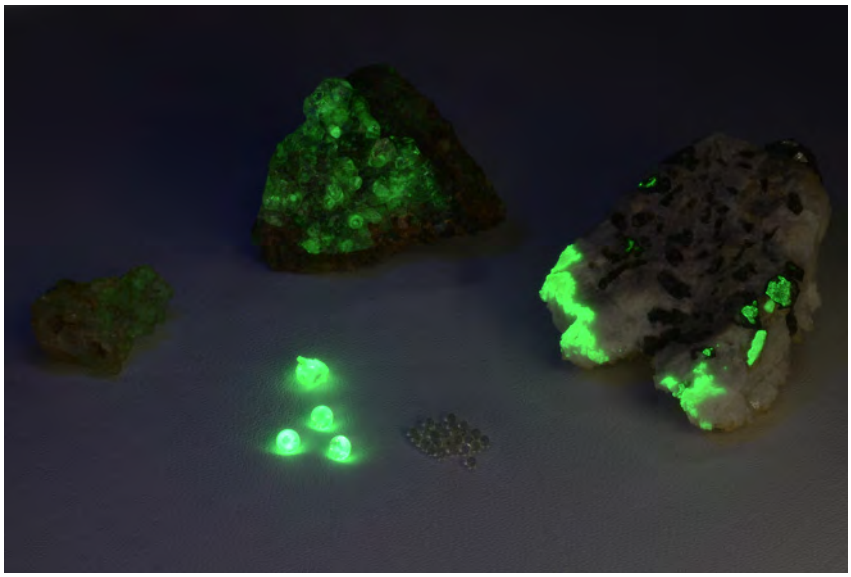

*Kazuko Saruwatari, Yusuke Katsurada, Shoko Odake, and Ahmadjan Abduriyim*

---

**Large Natural Fossil Blister PEARLS from *Tridacna* (Giant Clam) Species**

Fossil pearls, first mentioned in 1723 in John Woodward's "An essay towards a natural history of the earth and terrestrial bodies," were described in greater detail by R. Bullen Newton in 1908 ("Fossil pearl-growths," *Journal of Molluscan Studies*, Vol. 8, pp.

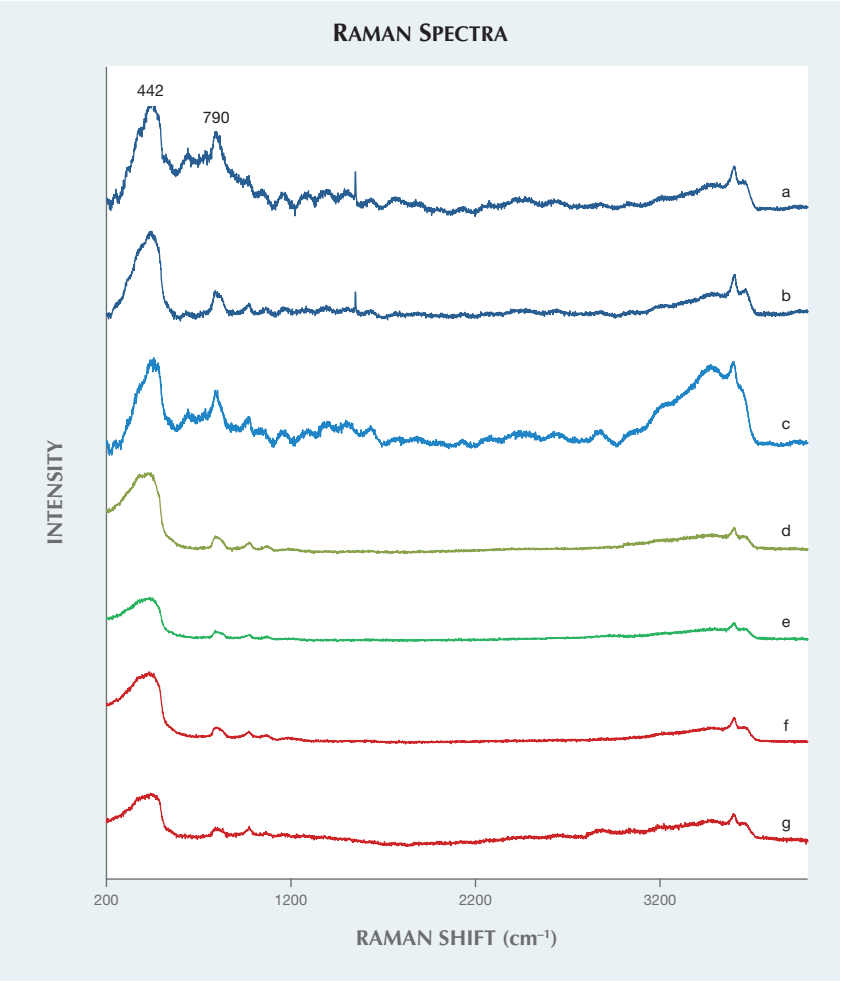


*Figure 11. Raman spectra from (a–b) Mexican hyalites, (c) Japanese pegmatitic hyalite, (d) Hungarian hyalite, (e) Argentinean hyalite, and (f–g) Japanese spherical hyalite. All spectra show similar patterns, with the Mexican specimens showing the unknown specific peak at 1548 cm$^{-1}$.*

318–320). It is a rare occurrence to receive such pearls at GIA, which is why two large fossil blister pearls recently submitted to the New York laboratory immediately caught our attention.

According to the client, the pair of fossil blister pearls were found near Lunga Lunga, a region in southeastern Kenya bordering Tanzania. They were found attached to a fossilized giant clam shell that weighed approximately 297 kg and was discovered 4.3 meters below ground (figure 12) along with some fossilized corals. The shell, along with the attached pearls, was presented to the client as a gift from a local Digo tribe. It took a month to remove the entire shell from the ground. Similar fossilized giant clam shells have been recovered from areas along the Kenyan coastline (G. Accordi et al., "The raised coral reef complex of the Kenyan coast: *Tridacna gigas* U-series dates and geological implications," *Journal of African Earth Sciences*, Vol. 58, No. 10, 2010, pp. 97–114). These two blister pearls were subsequently removed from the shell and submitted to GIA for identification after cleaning and removing the outermost fossilized debris.

The blister pearls measured approximately 58 × 47 × 45 mm and 85 × 70 × 46 mm and weighed 758 ct and 1256 ct, respectively. The faces of

*Figure 12. Two natural fossil blister pearls attached to their giant clam host, courtesy of Volker Bassen London Auction Rooms.*

these pearls had a porcelaneous appearance and were smoother than the bases, which were attached to the clam shell. These bases showed chalky rough surfaces and flared forms (figure 13). Numerous natural indentations and cavities were present on their surfaces. In some areas, subtle flame-like structures were also observed at 10× magnification with the use of fiber-optic lighting (figure 14). Microradiography was not helpful owing to the specimens' sizes, but Raman spectroscopy was able to detect calcite on both specimens and aragonite on the larger pearl, although it is possible there was aragonite in untested areas on the small pearl. The presence of aragonite in the larger pearl indicates that some of those structures had been replaced by calcite during fossilization.

According to the client, the shell in figure 12 was found in the upper layers of secondary fossil reef buildup, suggesting that it lived there during the later Pleistocene period. To the authors, the shell looks similar to that of the present-day *Tridacna gigas* giant clam, but the client stated that the clam was a precursor called *Tridacna gigantea*. The large size of

*Figure 13. The two natural fossil blister pearls after removal from the giant clam shell. The left image shows the face-up view, while the right image shows the base of the pearls, where the clam shell was previously attached.*

these fossil blister pearls, their unique appearance, and the story behind their discovery proved fascinating, and offered valuable gemological and scientific information for future reference.

*Chunhui Zhou and Joyce Wing Yan Ho*

### A Natural Pearl with an Intriguing Internal Structure

Aspects of natural pearl formation remain a mystery in many cases; however, one generally accepted principle is that an intruder finds its way into the mantle or gill areas of a mollusk and instigates the pearl formation process. Gemologists are never sure what they will find when natural pearls are examined using microradiography. Substantial real-time X-ray microradiography (RTX) work by GIA staff in various locations has shown evidence of formation cause in only a few pearls.

Early in 2015, a cream semi-baroque button pearl measuring 5.22 × 5.04 mm and weighing 0.95 ct (figure 15) was submitted to GIA's Bangkok laboratory with nine other pearls. Externally the pearl appeared similar to many other previously examined natural pearls, but the microradiography uncovered something that was far from normal.

After initial RTX examination, the apparent initiator of this specimen's formation was found to be very different from anything encountered, to our knowledge, in a natural pearl. RTX revealed an attractive radiating structure within a central conchiolin-rich boundary and associated external arcs within the surrounding nacreous overgrowth (figure 16). The radial object displayed clear solid arms extending from the central core of the structure. Given the nature of the core, further investigation was performed in order to identify the radial feature and see whether the pearl was natural or formed via human intervention using an organic nucleus as a "bead."

Computed microtomography (μ-CT) analysis was used to perform a 3-D examination of the radial feature. The μ-CT results revealed a magnificent structure with a snowflake-like

*Figure 14. Porcelaneous and flame-like structures, seen here on the surface of the larger fossil blister pearl, were observed in some areas under fiber-optic lighting. Field of view 15 mm.*

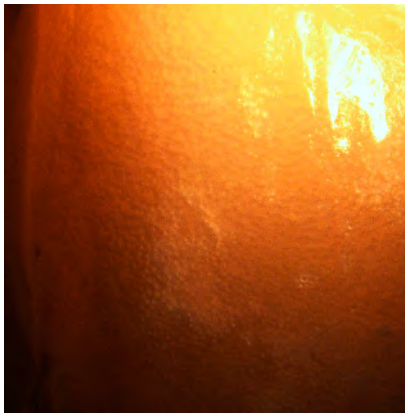

*Figure 15. The 0.95 ct pearl measuring 5.22 × 5.04 mm is shown with a GIA triplet loupe for scale.*

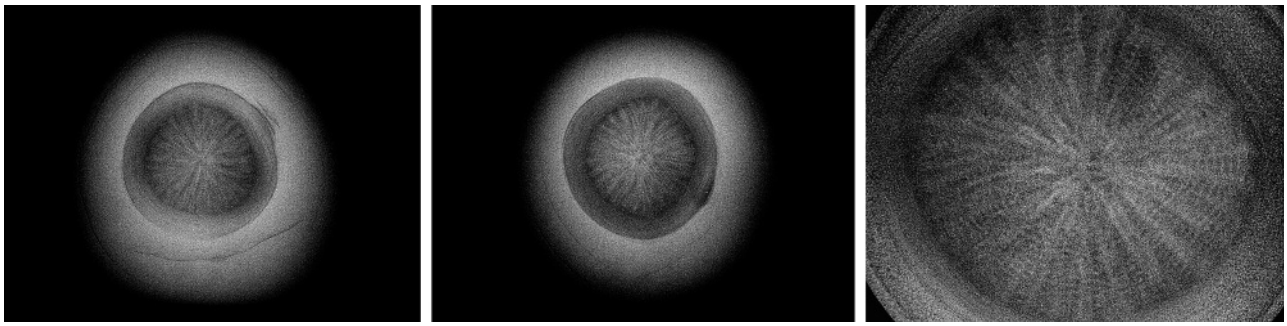

*Figure 16. The RTX images of the pearl's structure (left and right viewed from the side; center viewed from the top) revealed an intricate feature that might be an example of a foraminifera. The central feature measures approximately 1.95 × 1.93 mm, as determined by RTX and µ-CT.*

intricacy to its form (figure 17). The structure created some doubts about the natural formation of the pearl. The dark organic/conchiolin-rich growth structure, with some gaps between the nucleus and the surrounding nacre, has been noted in other unusual natural pearls of known origin. This differs from the so-called "atypical bead-cultured pearls" that almost always display a tight structure (lacking growth arcs) around the inserted nucleus. Almost all of the whole shell nuclei experimentally inserted into *Pinctada maxima* hosts have shown the boundary of the shell/nacre interface to merge tightly with one another, with very little in the way of organic arcs within the surrounding nacre. This curious structure led to further investigations into published claims of natural organic nuclei within natural pearls.

Similar but not identical structures have been documented in RTX and µ-CT work carried out on two pearls recovered from natural *P. maxima* shells by GIA staff ("An expert's journey into the world of Australian pearling," 2014, www.gia.edu/gia-news-press/malaysia-jewellery-fair). Pearls with unique structures have also been reported by others (K. Scarratt et al., "Natural pearls from Australian *Pinctada maxima*," Winter 2012 *G&G*, pp. 236–261). The exact origin of the pearls studied in Scarratt et al. is unclear, although they are more likely to be natural in at least two of the examples cited. For instance, the whole shell of one sample mentioned by Scarratt et al. showed characteristics similar to the specimen described here, with visible arcs within the nacre surrounding a shell nucleus that has a notable void/organic interface between the shell and nacre. The very small drill hole present in the shell, as opposed to the larger drill holes commonly found in cultured pearls, also strongly suggests a natural origin.

The nucleus of the 0.95 ct pearl under discussion appeared to be an organism such as coral. In order to find a match, coral samples were analyzed by RTX and µ-CT methods to compare their structures. Results indicated that the feature within the pearl may well be coral, but no exact match was noted. During the recent International Gemmological Conference (IGC) in Vilnius, Lithuania, it was suggested that the similar internal feature of a different pearl (N. Sturman et. al, "X-ray computed microtomography (µ-CT) structures of known natural and non-bead cultured *Pinctada maxima* pearls," *Proceedings of 34th International Gemmological Conference*, 2015, pp. 121–124) could well be a re-

*Figure 17. The µ-CT images reveal the structure in even more detail. Here, the nature of the organic-looking natural core is shown in three different µ-CT slices in the three different directions examined.*

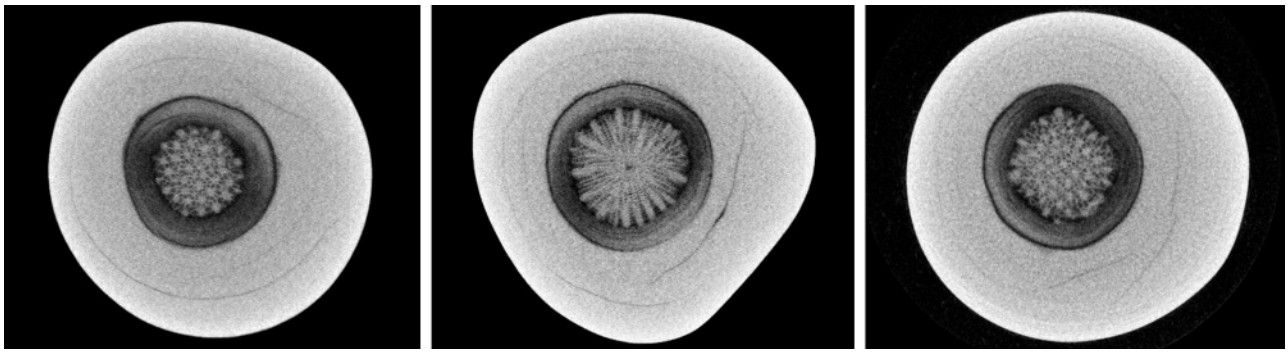

markably preserved foraminifera, a marine micro-skeleton member of a phylum of amoeboid protists. They are usually less than 1 mm in size; their structures vary, and many live on the sea floor. Given the environment, size, and features evident in the form within the pearl under discussion, it may well be that the internal structure is a type of foraminifera sphere with a porous structure for passive filtration (see figure 6 at www.mdpi.com/1660-3397/12/5/2877/html). The µ-CT results revealed the interconnecting channels and radial structure characteristic of these spherical foraminifera.

Whatever the true nature of the central form, the author considers the structure of this pearl to be natural based on the characteristics noted. It is also interesting to see that this pearl was small and not of particularly fine quality, other characteristics of natural pearl samples collected from the field. GIA's own experiments with small pieces of shell and coral using *P. maxima* hosts have produced larger pearls with different external appearances and generally finer quality than the specimen studied here. Further research into the differences between unusual structures in natural and atypical bead-cultured pearls will continue.

*Nanthaporn Somsa-ard*

*Figure 18. Left: A large natural pearl reportedly from a* Spondylus *species. Right: A large natural pearl reportedly from a* Trochoidea *species. Courtesy of Sunghee Caccavo.*

## Two Large Natural Pearls Reportedly from *Spondylus* and *Trochoidea* Species Mollusks

In a Fall 2014 Lab Note (pp. 241–242), GIA reported on four natural pearls ranging from 5.72 to 12.40 ct that were reportedly from a *Spondylus* (thorny oyster) species. These interesting non-nacreous pearls showed porcelaneous surfaces with unique bluish flame structures. Another even larger natural pearl, also reportedly from a *Spondylus* species, was recently submitted to the New York laboratory for identification. This pearl measured approximately 24 × 16 mm and weighed 42.96 ct (figure 18, left). It was formed in an attractive drop shape with a homogeneous yellow-brown bodycolor, abundant surface grooves, and a distinct bluish flame structure (figure 19). As with previous examples, microradiography showed only a tight structure, lacking obvious growth arcs. In addition, aragonite and natural polyenic pigment peaks were detected by Raman spectroscopy. Its unique appearance, coloration, and bluish tinted flame structures consistent with *Spondylus* pearls we previously reported. There is no known cultured pearl from this species, and the tight structure is commonly seen in other non-nacreous pearls, which further confirmed its natural origin.

The same client also submitted a large natural nacreous pearl reportedly from an unknown *Trochoidea* (turban snail) species (figure 18, right). The specimen, which measured approximately 27 × 19 × 12 mm and weighed 39.30 ct, had a cream color, high luster, and strong orient. Its smooth surface showed a unique wavy pattern. Previously GIA reported on a natural pearl from the turban snail species *Astraea undosa* that also showed high luster and strong iridescent colors, with an undulating wave-like pattern (Winter 2003 GNI, pp. 332–334). Both pearls share many common characteristics, and their appearances closely resemble one another.

Our client claimed that the *Spondylus* pearl is from Baja, Mexico; the turban pearl is from Mexico's Pacific coast. Although it is extremely challenging to identify the exact mollusk species these rare pearls originated from, their unique and interesting appearances are consistent with previously studied materials of similar claims. Regardless of their

*Figure 19. Distinct bluish flame structures were observed on this large non-nacreous pearl, similar to previously studied samples that also reportedly formed within* Spondylus *(thorny) oysters. Field of view 7.9 mm.*

exact origin, these beautiful large natural pearls prove just how wonderful Mother Nature is at creating spectacular wonders of great variety and eye-pleasing form.

*Chunhui Zhou and Joyce Wing Yan Ho*

## Two Large CVD-Grown SYNTHETIC DIAMONDS Tested

The quality and size of near-colorless and colorless synthetic diamonds grown by chemical vapor deposition (CVD) have rapidly improved in recent years due to advances in growth techniques and the introduction of post-growth decolorizing treatments. Near-colorless CVD synthetics have now passed the three-carat threshold. In September 2015, a 3.09 ct sample (I color, $VS_2$ clarity) of unknown provenance was submitted to HRD Antwerp (www.hrdantwerp.com/en/news/hrd-antwerp-recently-examined-a-309-ct-cvd-lab-grown-diamon). This was preceded by Pure Grown Diamonds' announcement of a 3.04 ct synthetic (I color, $SI_1$ clarity) in December 2014 (www.businesswire.com/news/home/20141229005491/en/ADDING-MULTIMEDIA-Worlds-Largest-Laboratory-Pure-Grown#.VOtnbS63raQ).

GIA's New York laboratory recently tested two large CVD synthetic diamonds (figure 20) submitted for grading services. These synthetics, weighing 2.51 and 3.23 ct, are the largest CVD-grown diamonds GIA has examined to date. The results of the examination underscore the continued improvements in CVD synthetic diamonds.

The 2.51 and 3.23 ct round brilliants received H and I color grades, respectively. Microscopic examination revealed pinpoint and black inclusions in both, while small fractures along the girdle were only observed in the 2.51 ct round (figure 21). The 3.23 ct synthetic contained a small black inclusion measuring approximately 125 µm. As a result, $SI_1$ and $VS_2$ clarity grades were given to the 2.51 and 3.23 ct samples, respectively. Both revealed irregular stress patterns with high-order interference colors when viewed under cross-polarized light (figure 22), indicating high levels of strain.

*Figure 20. The I-color 3.23 ct round on the left (9.59–9.61 × 5.83 mm) and H-color 2.51 ct round on the right (8.54–8.56 × 5.43 mm) are the largest CVD synthetic diamonds GIA has tested.*

The synthetics showed weak orange fluorescence to conventional short-wave UV and were inert to long-wave UV radiation. Exposure to the deep UV radiation (< 230 nm) of the DiamondView revealed an overall strong red-pink fluorescence attributed to nitrogen-vacancy centers with dislocation bundles that fluoresced violet-blue (figure 23), followed by weak greenish blue phosphorescence. Both samples were characterized by a layered growth structure, suggesting that the crystals were grown using a multi-step technique to maximize their volume. The sharp boundaries between the different growth layers are a result of changes in the fluorescent impurity uptake during the starting, stopping,

*Figure 21. Left: These pinpoint inclusions were observed in the 2.51 ct synthetic diamond. Right: A small black inclusion measuring approximately 125 µm was observed in the 3.23 ct sample. Field of view 4.72 mm (left) and 6.27 mm (right).*

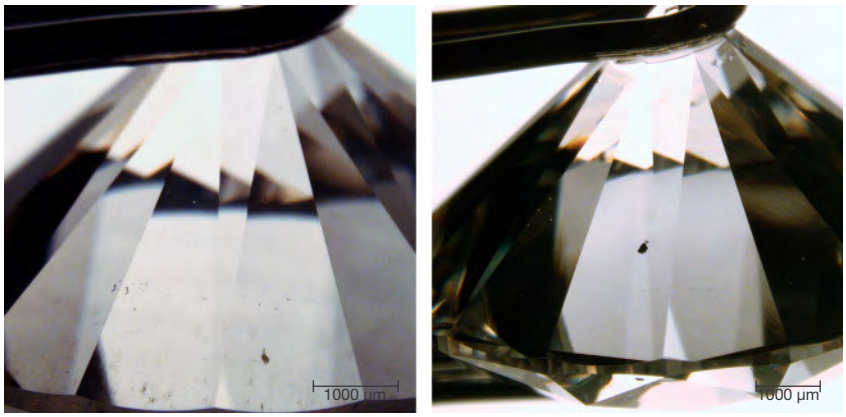

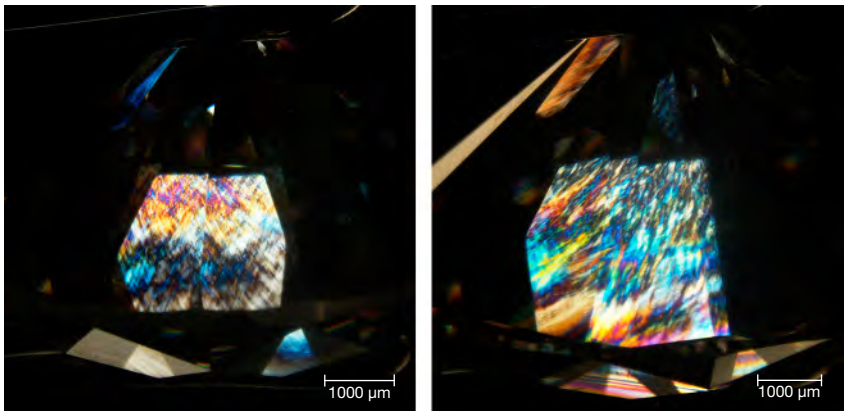


*Figure 22. Irregular stress patterns were observed under the microscope with cross-polarized light. Both the 2.51 ct (left) and 3.23 ct (right) synthetic diamonds showed high-order interference colors. Field of view 5.76 mm and 6.27 mm, respectively.*

and restarting of growth. These images clearly revealed that at least five growth layers were applied to produce these large crystals. The patterns suggest that the table of the 2.51 ct sample was cut parallel to the growth layers, while the table of the 3.23 ct synthetic was cut at an angle to the growth layers. The dislocation bundles are seen to propagate through the different growth layers. The formation of the two blue bands of highly concentrated dislocations crossing the table of the 2.51 ct specimen is not understood.

Infrared absorption spectroscopy in the mid-IR range (6000–400 $cm^{-1}$) showed no major nitrogen-related absorption in the one-phonon region, which classified both samples as type IIa. No hydrogen-related defects were detected, either. UV-Vis-NIR absorption spectra collected at liquid-nitrogen temperature revealed a smooth increase in absorption from the infrared region to the high-energy end of the spectrum, with a 737 nm peak in both samples and a small absorption peak at 596 nm in the 3.23 ct synthetic. The 737 nm peak is an unresolved doublet at 736.6/736.9 nm attributed to $[SiV]^-$. This center is often inadvertently introduced during CVD growth (P. Martineau et al., "Identification of synthetic diamond grown using chemical vapor deposition (CVD)," Spring 2004 *G&G*, pp. 2–25; W. Wang et al., "CVD synthetic diamonds from Gemesis Corp.," Summer 2012 *G&G*, pp. 80–97) but is rarely observed in natural diamonds, especially using absorption methods. The 596 nm feature is particularly useful for identification purposes, as it has only been reported in CVD synthetic material (again, see Martineau et al., 2004).

Photoluminescence (PL) spectra acquired with 514 nm laser excitation at liquid-nitrogen temperature revealed a doublet at 596/597 nm, nitrogen-vacancy centers at 575 $[NV]^0$ and 637 $[NV]^-$ nm, and $[SiV]^-$ at 736.6/736.9 nm for both samples, with the $[NV]^{0/-}$ luminescence dominating. The strength of the $[NV]^{0/-}$ centers was consistent with the red-pink fluorescence colors (figure 23). Although the 596/597 nm doublet is not thought to arise from the same center as the 596 nm feature seen in the absorption spectrum of the 3.23 ct sample, it has only been detected in CVD synthetics, thus revealing the samples' CVD origin (Martineau et al., 2004). The doublet also indicated that the samples had not undergone post-growth HPHT (high-pressure, high-temperature) processing to improve their color, as the treatment would have removed this feature.

*Figure 23. DiamondView imaging of both samples revealed strong red-pink fluorescence superimposed with dislocation patterns that fluoresced violet-blue. A layered growth structure indicating start-stop growth was clearly observed on the pavilion of both. The orientation of the layers reveals that the 2.51 ct sample (top) was cut with its table approximately parallel to the growth plane, whereas the layers intersect the table facet in the 3.23 ct sample (bottom).*

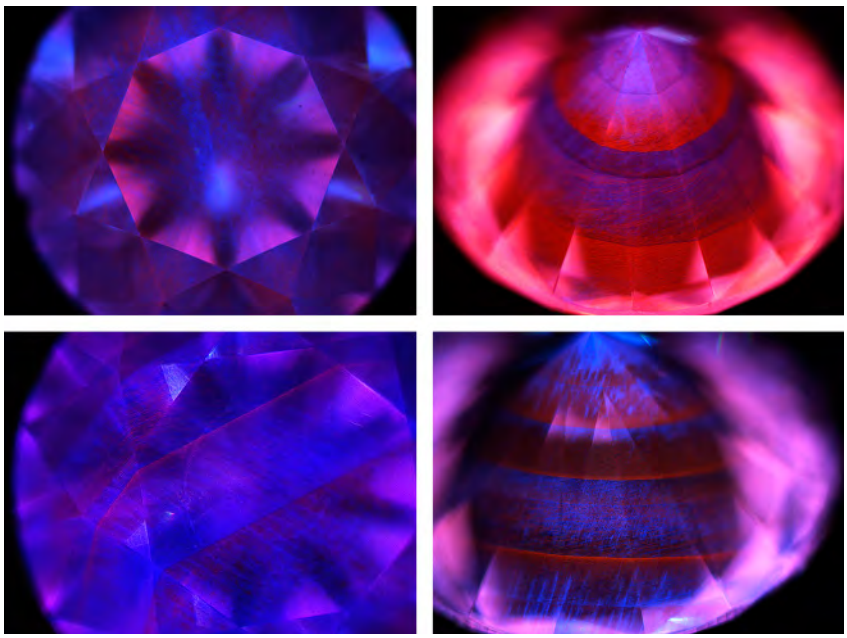

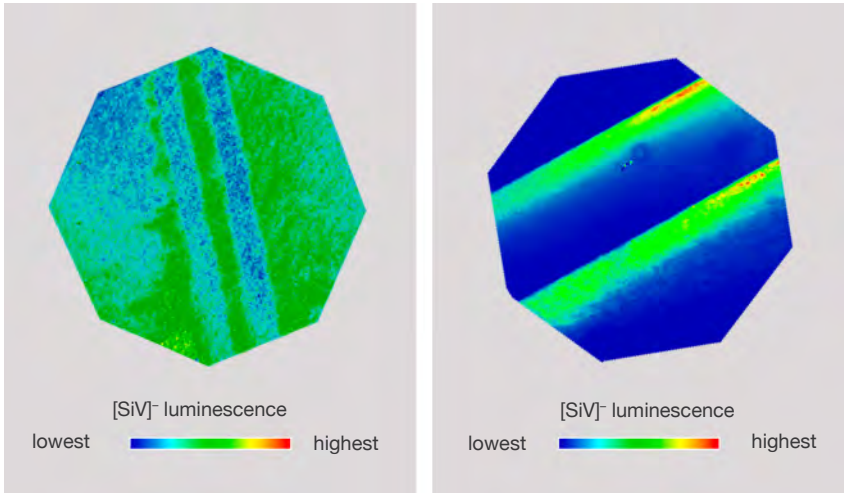


*Figure 24. PL [SiV]⁻ silicon distribution maps were collected with 532 nm laser excitation. Left: Less luminescence from [SiV]⁻ centers is observed in two broad bands on the 2.51 ct sample. Right: More intense [SiV]⁻ luminescence is found at the diamond layer boundaries in the 3.23 ct sample.*

The distribution of [SiV]⁻ centers was investigated through PL mapping of the 736.6/736.9 nm doublet at liquid-nitrogen temperature using 532 nm laser excitation (figure 24). The distribution was different between the two samples, forming patterns that corresponded directly with their DiamondView images (again, see figure 23). For the 2.51 ct sample, the [SiV]⁻ luminescence decreased along the bands with higher concentrations of dislocation bundles. This may indicate that there are fewer [SiV]⁻ centers in this region, or an increased concentration of defects (either structural or impurity-based) that effectively quench the [SiV]⁻ luminescence. Where the growth layers intersect the table in the 3.23 ct sample, the [SiV]⁻ luminescence appeared to be highest at the start of a layer's growth, decreasing as the growth progressed. This could mean that the concentration of silicon in the growth gas fell over time, or that the concentration of defects that may quench the [SiV]⁻ luminescence increased during growth. Notably, the concentration of dislocations increased as growth progressed.

Analysis of these two large samples demonstrates that high-quality CVD synthetic diamonds can be produced even without post-growth decolorizing HPHT treatment, marking a significant improvement in CVD growth. Using advanced spectroscopic and fluorescence imaging technologies, it is nevertheless possible to detect low concentrations of impurity centers, allowing conclusive determination of these samples' synthetic origin. GIA is monitoring the development of laboratory-grown diamonds and conducting research to ensure that we can continue identifying every single synthetic diamond.

*Caitlin Dieck, Lorne Loudin, and Ulrika D'Haenens-Johansson*

## SYNTHETIC ROCK CRYSTAL QUARTZ Bangle with Unusual Inclusions

Synthetic quartz is grown by the hydrothermal technique, which can produce large single crystals of high quality (K. Byrappa and M. Yoshimura, *Handbook of Hydrothermal Technology: A Technology for Crystal Growth and Material Processing*, William Andrew Publishing, 2001). This process, widely used in the jewelry trade, has led to difficulty in separating synthetic quartz from its natural counterpart (R. Crowningshield et al., "A simple procedure to separate natural from synthetic amethyst on the basis of twinning," Fall 1986 *G&G*, pp. 130–139). The presence of Brazil-law twinning and certain inclusions, such as tourmaline or golden rutile needles, can be used to distinguish natural from synthetic quartz. But high-quality quartz, whether of natural or synthetic origin, typically has no inclusions or twinning. In this case, standard gemological testing may not be able to identify the origin. Advanced instruments, including infrared absorption spectroscopy (S. Karampelas et al., "An update in the separation of natural from synthetic amethyst," *Bulletin of the Geological Society of Greece*, 2007, pp. 805–814) and LA-ICP-MS are considered useful tools for separating natural from synthetic material from material with synthetic origins (C.M. Breeding, "Using LA-ICP-MS analysis for the separation of natural and synthetic amethyst and citrine," *GIA News from Research*, 2009, www.gia.edu/gia-news-research-nr73109a).

The Bangkok lab recently examined a high-clarity, transparent, near-colorless bangle (figure 25). Standard gemological testing revealed a spot RI of 1.54 and an SG of 2.65, consistent with quartz. Magnification revealed irregular two-phase inclusions (figure 26). These inclusions are more likely to be present in natural quartz than in

*Figure 25. A synthetic rock crystal quartz bangle measuring approximately 80 × 22 × 10 mm.*

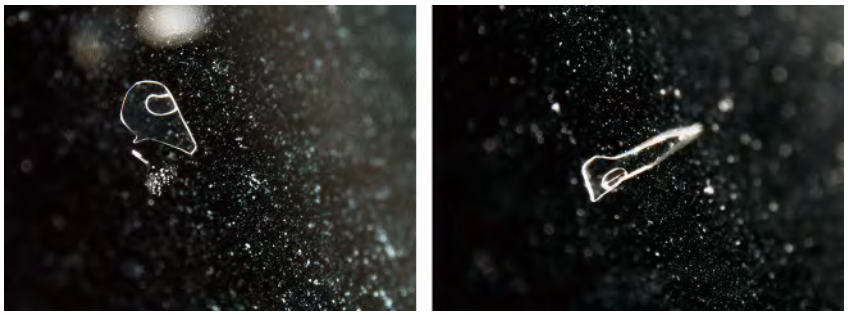

*Figure 26. Irregular two-phase inclusions seen in the bangle using dark-field illumination (left and right) are similar to those found in natural specimens but are rarely found in hydrothermal synthetic quartz. Field of view 4.1 mm.*

hydrothermal synthetic quartz, which typically shows nail-head spicule and breadcrumb inclusions. This bangle also gave an IR absorption spectrum unlike that of natural rock crystal quartz. The characteristic IR absorptions of natural rock crystal quartz occurred at 3379, 3483, and 3595 $cm^{-1}$. These features are never seen in synthetic rock crystal quartz. The IR spectrum of the bangle showed absorption peaks at 3610, 3585, 3431, 3294, and 3194 $cm^{-1}$ (figure 27), which matches the IR absorption features of synthetic rock crystal quartz (P. Zecchini and M. Smaali, "Identification de l'origine naturelle ou artificielle des quartz," *Revue de Gemmologie*, No. 138/139, 1999, pp. 74–80). The IR spectrum confirmed that this material was grown by hydrothermal methods.

*Figure 27. Infrared spectra of the synthetic rock crystal quartz bangle and a 17.50 ct natural rock crystal quartz faceted bead show different absorption patterns. The characteristic absorptions of natural rock crystal quartz at 3379, 3483, and 3595 $cm^{-1}$ are never seen in synthetic rock crystal quartz. The bangle showed absorption peaks at 3610, 3585, 3431, 3294, and 3194 $cm^{-1}$, matching the IR absorption of synthetic rock crystal quartz.*

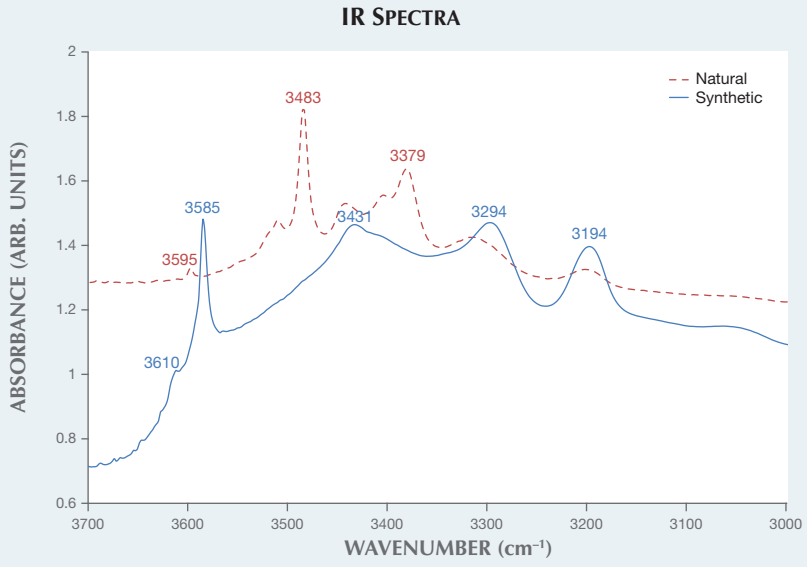


Large transparent colorless quartz can be found in natural and synthetic forms, but synthetic quartz is usually seen as a flat crystal. This bangle is an interesting example of large, high-clarity synthetic quartz used in jewelry. The presence of the irregular two-phase inclusions in this example serves as an important reminder that natural and synthetic quartz can show a similar appearance and contain internal inclusion features that are identical.

*Nattida Ng-Pooresatien*

*PHOTO CREDITS:*
*Jian Xin (Jae) Liao—1, 7, 20; Yixin (Jessie) Zhou— 2; Sood Oil (Judy) Chia—4, 13, 18; Kyaw Soe Moe—5, 6; Masumi Saito—9, 10; Joyce Wing Yan Ho—14, 19; Caitlin Dieck—21, 22, and 23; Lorne Loudin—24; Nuttapol Kitdee—25; Nattida Ng-Pooresatien—26.*


## "Dragon's Eye" Fire Agate

Found in only a few places in the southwestern United States and Mexico, fire agate is a very finely layered golden brown to reddish brown agate with a botryoidal multi-layered structure. Each of the individual layers in a fire agate is dusted with the iron hydroxide mineral goethite, which provides the brown bodycolor.

What makes fire agate particularly special is that the ultra-thin coatings of goethite cause a very colorful iridescence, primarily in red, golden orange, and green, but occasionally in violet to blue. The vibrant colors result from interference between light rays that are reflected and refracted while traveling through the gem and reflecting from these ultra-thin layers.

The finest-quality fire agates can rival Australian black opal. Because they are a form of chalcedony quartz, fire agates are also more durable than opal, making them suitable for virtually any jewelry application.

*Figure 1. Upon close examination, the polished botryoidal knob in this Mexican fire agate resembles a reptilian eye. Photomicrograph by John Koivula; field of view 8.12 mm.*

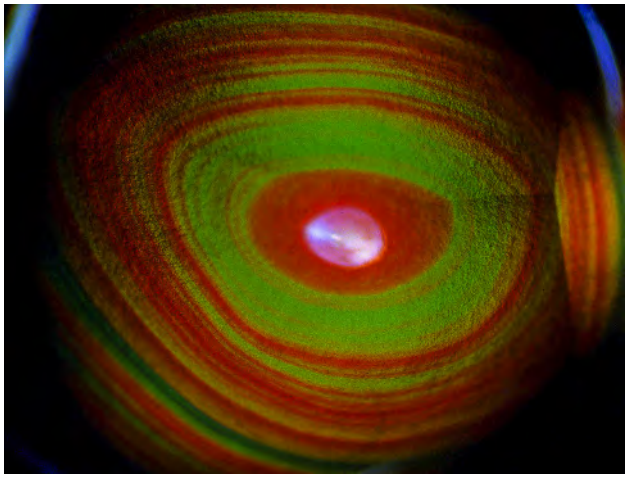

The 4.62 ct (10.22 × 9.16 × 7.19 mm) Mexican fire agate studied here, a polished high-dome cabochon, is from the El Terrero mine in the Calvillo Mountains of Aguascalientes State, Mexico. Under close examination (figure 1), its somewhat ovoid botryoidal structure and fine granular texture, together with the banded red, orange, and green coloration, project the image of a reptilian "dragon's eye." As an added bonus, the hotspot created by the fiber-optic light at the apex of the gem adds an elegant finishing touch to the overall image.

*John I. Koivula*
*GIA, Carlsbad*

## Red Heart Inclusion in Diamond

Diamonds, like colored gemstones, contain a variety of interesting inclusions. Although some would call them flaws, I prefer to think of them as Mother Nature's artwork or fingerprint. I have seen inclusions resembling angels and animals of all sorts, some requiring more imagination than others. It is fascinating to think of what might have been captured inside a diamond more than two billion years ago.

The 2.00 ct round brilliant diamond shown in figure 2 has I color, $I_1$ clarity, and a wonderful cut. But its most remarkable feature is a red heart-shaped inclusion, identified as pyrope garnet based on microscopic examination by GIA's Carlsbad laboratory. The inclusion is not visible to the eye but jumps out at 10× magnification. It measures approximately 140 microns across where it is exposed at

*About the banner: Epigenetic iron oxide staining is seen in a thin section of chalcedony using polarized light and a quarter-wave plate. Photomicrograph by Nathan Renfro; field of view 0.25 mm.*

*Editors' note: Interested contributors should contact Nathan Renfro at nrenfro@gia.edu and Jennifer-Lynn Archuleta at jennifer.archuleta@gia.edu for submission information.*

Gems & Gemology, Vol. 51, No. 4, pp. 441–445.

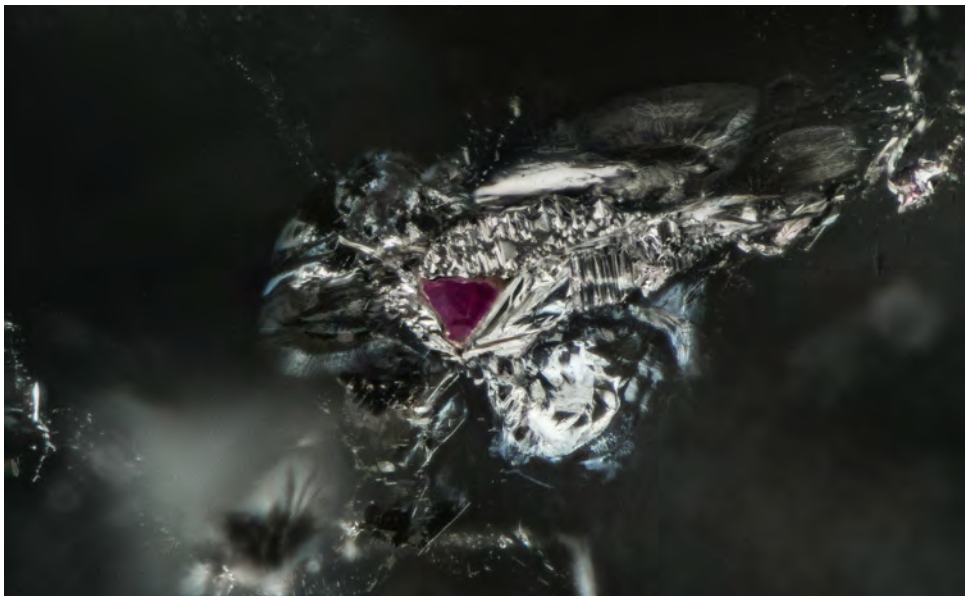

*Figure 2. A unique expression of romance: Breaking the surface of this 2.00 ct diamond is a red heart-shaped inclusion. Photomicrograph by Nathan Renfro; field of view 1.58 mm.*

the table facet. The inclusion is much larger and extends along almost half of the image frame, but the reflective interface makes it difficult to see the underlying garnet. We only see the pink color where the inclusion breaks the surface and the mirror-like interface has been removed.

With the combination of the red heart and diamond, both universal symbols of love, this is a one-of-a-kind gem. We have named it the Forsythe diamond and plan to auction it around Valentine's Day 2016, in keeping with the theme of romance, and part of the proceeds will go toward a local charity. How lucky are we to be able to work with beautiful gemstones containing hidden secrets just waiting to be unlocked every day.

*Matt Wahl*
*Forsythe Jewelers*
*Pittsford, New York*

## Trapiche Muscovite

For collectors who appreciate crystals that display distinctive trapiche structure, muscovite offers a very interesting and unusual variety known to mineralogists as cerasite or "cherry blossom stones" due to its form. With a pseudohexagonal habit and a silvery luster, these muscovite pseudomorphs after indialite-cordierite intergrowths may, on rare occasion, show a well-developed trapiche structure (figure 3) virtually identical to that of fine-quality trapiche emerald.

Trapiche muscovites come from only one locality, the Japanese city of Kameoka in Kyoto Prefecture, where they are locally known as "cherry blossom stones" (*sakura-ishi* in Japanese). Small and attractive, well-formed specimens are occasionally found when they weather out of a contact metamorphic hornfels.

*Figure 3. Muscovite mica, known from a single locality in Japan, can display trapiche structure with both open (left) and closed (right) centers. Photomicrographs by Nathan Renfro; field of view 4.05 mm (left) and 4.56 mm (right).*

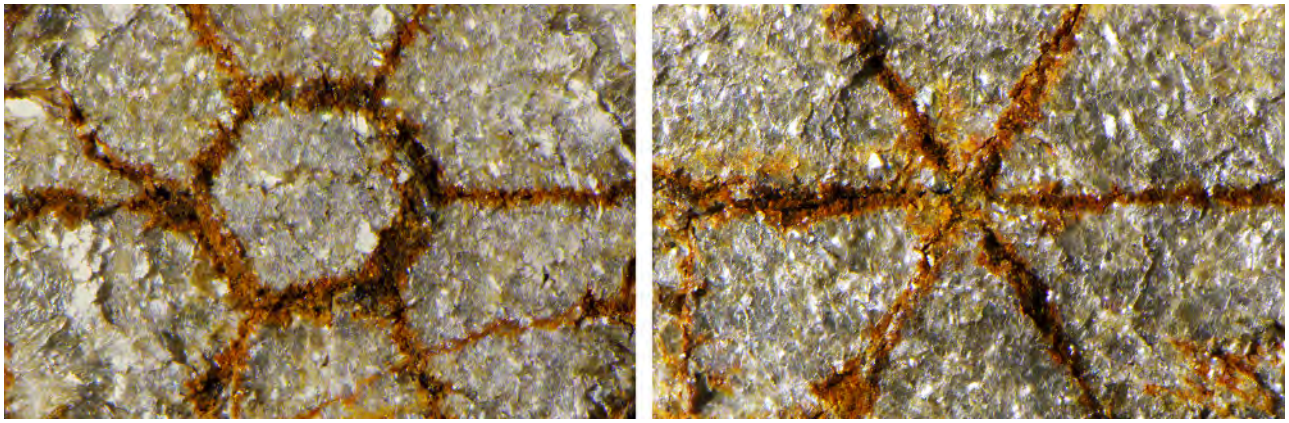

*Figure 4. These muscovite trapiches, or "cherry blossom stones," formed through alteration of complex indialite-cordierite intergrowths. Photo by Nathan Renfro.*

In figure 4, the closed-center specimen measures approximately 6.49 × 6.44 × 4.48 mm with a corresponding weight of 0.90 ct, while the one with the open center measures 4.71 × 4.27 × 5.21 mm and weighs 0.62 ct. Fine examples of these unusual muscovite pseudomorphs measuring over 6 mm and weighing over 1 ct are considered very rare.

*John I. Koivula*

### Parisite in Colombian Quartz

The brownish rare earth carbonate parisite is known as an unusual Colombian mineral specimen, and as a diagnostic inclusion indicative of Colombian origin when observed in emeralds (E.J. Gübelin and J.I. Koivula, *Photoatlas of Inclusions in Gems*, Vol. 1, ABC Edition, Zurich, 1986, p. 252). This rare mineral has also been reported to occur in quartz from Muzo, Colombia (E.J. Gübelin and J.I. Koivula, *Photoatlas of Inclusions in Gemstones*, Vol. 2, Opinio Verlag, Basel, Switzerland, 2005, p. 621).

A particularly striking example of rock crystal quartz with numerous brown crystals of parisite (figure 5) was recently examined at GIA's Carlsbad laboratory, where the inclusions' identity was confirmed by Raman analysis. Interestingly, three of the most prominent parisite inclu-

*Figure 5. These three crystals captured in Colombian rock crystal quartz host three crystal morphologies of the rare mineral parisite: bipyramidal, hexagonal tabular prism, and pyramidal forms. Photomicrograph by Jonathan Muyal; field of view 4.79 mm.*

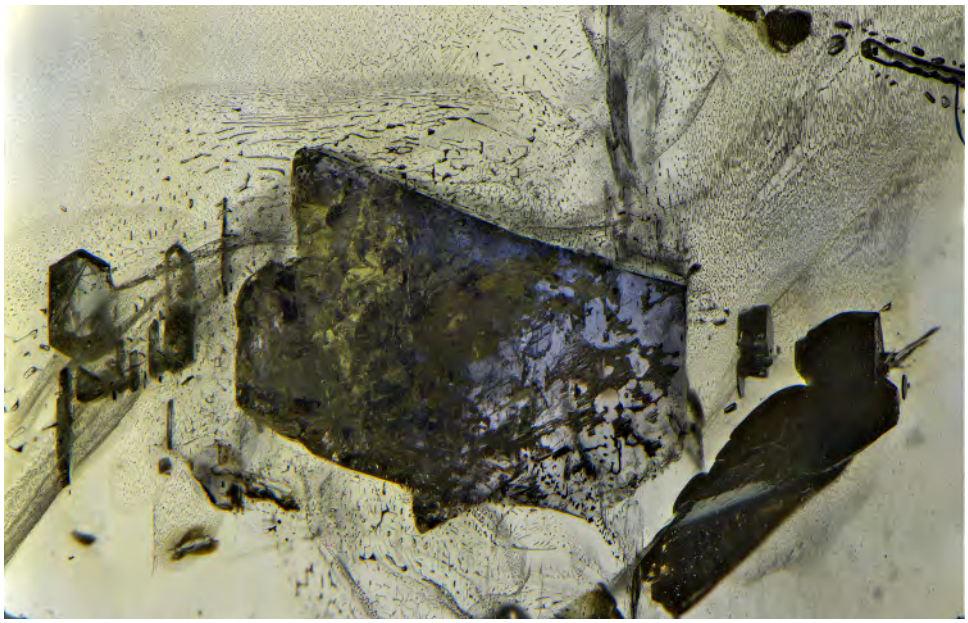

*Figure 6. This violetish blue inclusion in a Sri Lankan yellow sapphire was identified as spinel. Photomicrograph by Nathan Renfro; field of view 5.63 mm.*

sions in this rock crystal quartz displayed multiple crystal habits: a well-formed bipyramid, a tabular hexagonal prism, and a pyramidal form. Due to their euhedral nature, these inclusions are presumed have formed simultaneously with their host quartz and are therefore termed *syngenetic*. Also present in the stone were numerous fluid inclusions and an iridescent interface on the bipyramidal crystal.

This is the finest example of parisite as an inclusion in quartz that has been documented by GIA.

*Jonathan Muyal*
*GIA, Carlsbad*

### Violetish Blue Spinel in Yellow Sapphire

Spinel as an inclusion in sapphire has been previously documented in blue and yellow sapphires from Sri Lanka (E.J. Gübelin and J.I. Koivula, *Photoatlas of Inclusions in Gemstones*, Vol. 1, ABC Edition, Zurich, 1986, pp. 353–354). Typically these inclusions are green zinc-rich ghanospinels. Recently the authors examined a transparent light yellow sapphire crystal with a prominent violetish blue octahedral inclusion (figure 6). Interestingly, microscopic examination showed the violetish blue inclusion to be an intergrowth of at least two gemmy crystals, with the larger one crystallographically aligned with negative crystals that were also present in the host.

When further examined with polarized light, the violetish blue inclusion appeared to be singly refractive, which meant spinel was a possibility, considering their similar formation environments. The sample was polished down to a plate in order to place the violetish blue inclusion closer to the surface for Raman analysis, which conclusively confirmed that it was spinel. Also present in this sapphire were numerous carbon dioxide–filled negative crystals, fingerprints, and open cracks. The presence of the intact $CO_2$ inclusions and the pristine condition of the spinel inclusion provided clear evidence that the sapphire host had not been subjected to any form of heat treatment. This is the first example of a violetish blue spinel inclusion in sapphire that the authors have examined.

*Nathan Renfro and John Koivula*
*GIA, Carlsbad*

### Stars Are Out in Paraíba Tourmaline

The rarity of Brazilian Paraíba tourmaline, with its vibrant, almost unearthly colors, makes it a coveted gem the world over. What a delight to discover a pair of stars shining out from among many non-phenomenal stones in a parcel. This was a fruitful result of gemologist Elaine Rhorbach's regular use of a point-source light for examination of all materials she encounters in the marketplace. Wherever she is in the world, this former nurse carries her powerful otoscope—no longer examining ears, but rather checking for any optical phenomena in gems, even where none is expected.

The phenomenon of asterism is seen in a variety of gem materials fashioned as cabochons. The multiple chatoyant bands of light forming these stars are caused by the scattering of planar light by sets of parallel structures. These are often inclusions such as minerals, voids, and structural defects, but they may also be manifested by natural surface features of the crystal left intact on the gem's base (e.g., tourmaline prism face striations) or etched into the surface by hand. The crystal structure of the host dictates the number of bands, and with mineral inclusions in particular, the orientations are a result of complex chemical interactions between the inclusions and their host. Orientation of the cut gem also determines what effect is seen. For instance, multi-star quartz is a member of the same trigonal crystal class as tourmaline; it displays four-

and six-ray stars, depending on viewing orientation in relation to its crystallographic axes of symmetry.

In the case of the 1.06 and 0.90 ct Paraíba tourmaline cabochons seen in figure 7, the c-axis of the larger gem is along its length and that of the smaller specimen is across its width. Thus, the view from above is perpendicular to the crystal's c-axis. Fluid-filled inclusions paralleling the c-axis dominate the gems' microworld, causing a distinct chatoyant band perpendicular to the axis. A faint band seen crossing this appears to be caused by the slight widening of the fluid-filled inclusions (figure 8). Since the inclusions are roughly rectangular as they are aligned parallel to the c-axis of the crystal, they produce two directions of reflections oriented at 90°. The elongate direction has more reflective surface area and therefore produces a brighter chatoyant band, while the width has less surface area and produces a weaker chatoyant band from the same reflective inclusion set. While EDXRF detected the presence of copper in these vibrant gems, affirming their Paraíba nature, the subtle stars elevated them into the class of rarefied connoisseur gems—another example of the power of inclusions!

*Elise A. Skalwold*
*Ithaca, New York*
*Nathan Renfro*

*Figure 7. Under point-source light, these 1.06 and 0.90 ct Paraíba tourmaline cabochons purchased in Brazil in the early 1990s display four-ray stars. Photo by Robert Weldon.*

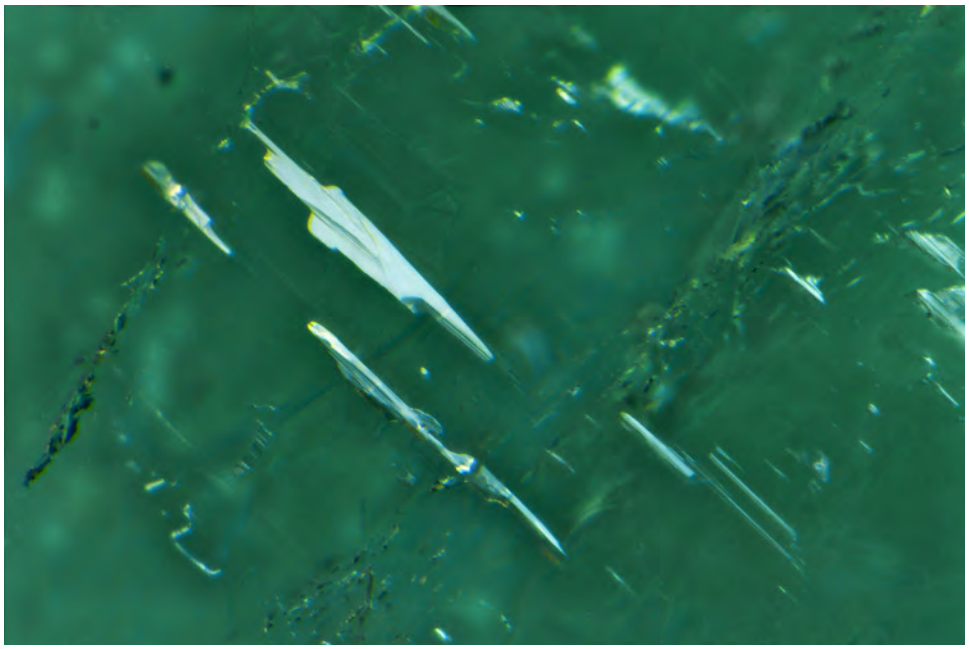

*Figure 8. Reflective fluid-filled inclusions parallel to the c-axis of the Paraíba tourmaline scatter the light, forming the stronger chatoyant band. A faint band seems to be caused by a slight widening of these inclusions. Photomicrograph by Nathan Renfro; field of view 1.20 mm.*

# G&G Gem News International

**Contributing Editors**
Emmanuel Fritsch, *University of Nantes, CNRS, Team 6502, Institut des Matériaux Jean Rouxel (IMN), Nantes, France* (fritsch@cnrs-imn.fr)
Gagan Choudhary, *Gem Testing Laboratory, Jaipur, India* (gagan@gjepcindia.com)
Christopher M. Breeding, *GIA, Carlsbad* (christopher.breeding@gia.edu)

## COLORED STONES AND ORGANIC MATERIALS

**Demantoid garnet with giant fluid inclusion.** Since 2009 the Antetezambato demantoid garnet deposit, near Ambanja, in the Ambato peninsula of northern Madagascar, has yielded a huge quantity of rough gem material. This skarn-related deposit continues to produce fine crystals for the international market in a wide range of colors (F. Pezzotta et al., "Demantoid and topazolite from Antetezambato, northern Madagascar: Review and new data," Spring 2011 *G&G*, pp. 2–14). Mineralogical curiosities were also found, such as demantoid garnet fossil pseudomorphs of gastropod and coral (Winter 2013 GNI, pp. 257–258; J. Raoul et al., "Pseudomorphose de fossiles en andradite 'démantoïde' à Antetezambato, Madagascar," *le Règne Minéral*, Vol. 123, 2015, pp. 21–26). An andradite crystal (figure 1) hosting a giant two-phase (liquid + vapor) fluid inclusion (FI) was extracted from the mangrove swamps and is now the property of M. J. Raoul.

The greenish gem crystal, measuring 1.5 × 0.6 cm (figure 2A), exhibits some faces that follow a more dodecahedral habit {110} while others are more trapezoidal {110}. Micro-Raman spectroscopy clearly showed the four main peaks of andradite at 352, 371, 515, and 874 $cm^{-1}$ (figure 3, top). The bubble of the FI cavity is visible to the naked eye and moves when the sample is turned, similar to some giant FI in quartz. The demantoid garnet was investigated by X-ray computed tomography (CT) scanning to reveal its 3D interior morphology. Images were made with a Phoenix Nanotom S scanner using a resolution of 7.59 µm/voxel and an X-ray tube on nanofocus tension of 115 kV. The calculation of all the phases was computed by VGStudio software, and the volumes of the respective phases are the sums of voxels. The 3D tomography images show a unique fluid inclusion cavity (figure 2B) with a morphology like a negative crystal with polygonal outlines parallel to the faces of the host garnet crystal (figures 2C, D). All the criteria define a primary two-phase FI. The total volume of the garnet is 896.1 $mm^3$, of which 6.2 vol.% is occupied by the FI cavity. The volume of the liquid phase is 52.16 $mm^3$ and the volume of the vapor phase is 3.52 $mm^3$, which corresponds to a liquid/vapor ratio of 6.75%.

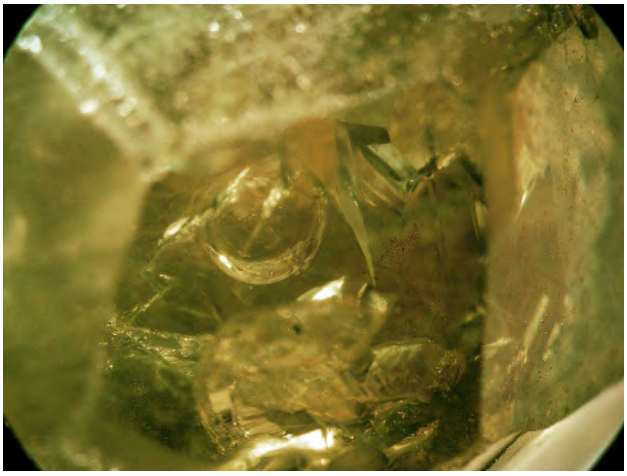

*Figure 1. The demantoid crystal from Madagascar contains a giant two-phase fluid inclusion. The photomicrograph shows the FI cavity with its bubble trapped by the garnet. The bubble's diameter is around 2 mm. Photo by Michel Cathelineau.*

*Editors' note: Interested contributors should send information and illustrations to Stuart Overlin at soverlin@gia.edu or GIA, The Robert Mouawad Campus, 5345 Armada Drive, Carlsbad, CA 92008.*

Gems & Gemology, Vol. 51, No. 4, pp. 446–462.

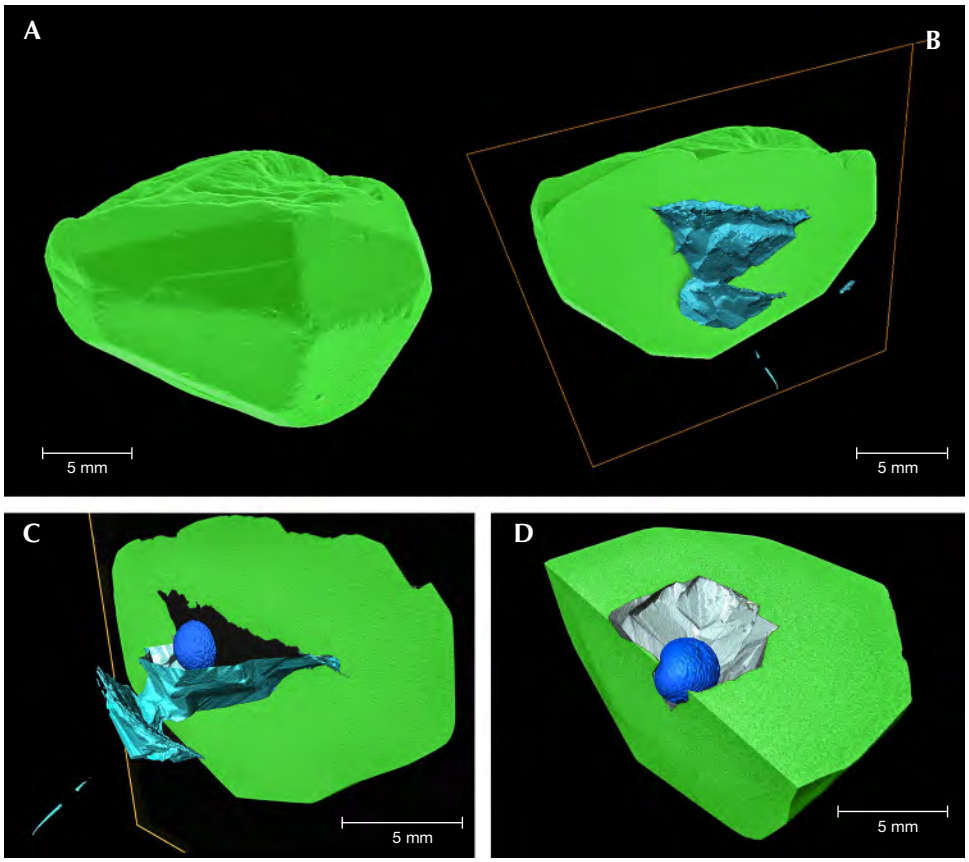


*Figure 2. 3-D tomography images of the demantoid and the giant fluid inclusion cavity. Top left: Morphology of the crystal. Top right: Tomographic section of the crystal showing the morphology of the fluid inclusion cavity. Bottom left: The internal view of the cavity showing the gas bubble. Bottom right: The cavity displays a negative crystal morphology with polygonal outlines parallel to the faces of the host garnet crystal, as well as the bubble phase (blue).*

The Raman spectrometry data show that the fluid is free of $CO_2$, $CH_4$, $H_2S$, and $N_2$: the FI is a primary two-phase aqueous FI (liquid + vapor). The salinity of the aqueous FI was determined by analyzing the Raman spectrum of $H_2O$ based on the weakening of the hydrogen bond by chloride. A deformation of the OH stretching vibration band of water appears in the range between 2900 and 3700 $cm^{-1}$ (figure 3, bottom). Even if the cationic composition of the natural FI differs from pure sodium, the experimental approach yields the salinity of any inclusion accurately if NaCl is the main species (M.-C. Caumon et al., "Fused-silica capillary capsules (FSCCs) as reference synthetic aqueous fluid inclusions to determine chlorinity by Raman spectroscopy," *European Journal of Mineralogy*, Vol. 25, No. 4, 2014, pp. 755–763). Under these conditions the calculated salinity for the demantoid garnet FI is about 8 wt.% equivalent NaCl.

The gem garnet mineralization of Antetezambato is described as a skarn-type deposit related to Upper Mesozoic to Cenozoic magmatism affecting the limestones of the Mesozoic Isalo Group (again, see Pezzotta et al., 2011). Similar demantoid-bearing skarns are described in the Ampasindava Peninsula at Ambohimirahavavy, 50 km west of Ambanja (G. Estrade et al., "REE and HFSE mineralization in peralkaline granites of the Ambohimirahavavy alkaline complex, Ampasindava peninsula, Madagascar," *Journal of African Earth Sciences*, Vol. 94, 2014, pp. 141–155). The skarns of the Ambohimirahavavy alkaline granitioid complex are host to rare-metal mineralization. Peralkaline dykes intruded (at 24.2 ± 0.6 Ma) the limestone of the Isalo groups (G. Estrade et al., "Unusual evolution of silica-under- and -oversaturated alkaline rocks in the Cenozoic Ambohimirahavavy Complex (Madagascar): Mineralogical and geochemical evidence," *Lithos*, Vol. 206–207, 2014, pp. 361–383) and developed a bi-metasomatic skarn. The metasomatic zone was formed at the contact with the calcareous rocks by calc-silicate rocks (exo-skarn zone) with diopside, garnet andradite (demantoid variety), calcite, apatite, phlogopite, fluorite, and wollastonite. At the contact of the granite (endo-skarn zone), the associated minerals are quartz, albite, aegirine-augite, and calcite (G. Estrade, "Le complexe cénozoïque alcalin d'Ambohimirahavavy à Madagascar: origine, évolution et minéralisations en métaux rares," PhD thesis, Paul Sabatier University, Toulouse, France, 2014, 299 pp.) Exo-skarn paragenesis is also found as inclusions in the demantoid of Antetezambato, such as fluorine-(arsenic)-bearing apatite, fluorite, calcite, wollastonite, fluorine-bearing vesuvianite, diopside, calcite, and quartz (W. Barrois et al., "Caractéristiques minéralogique et chimique des grenats démantoides de Bagh Borj (Iran) et d'Antetezambato (Madagascar): conséquences géologiques. 2ème partie, Études minéralogique

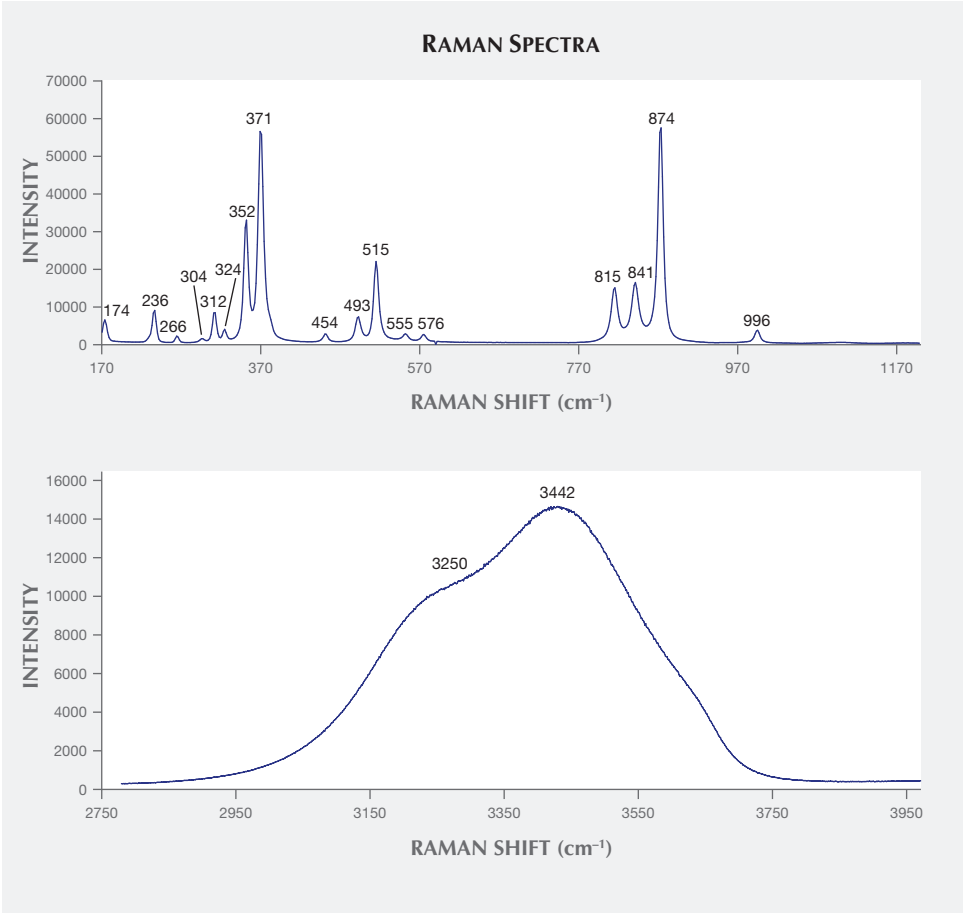


*Figure 3. The micro-Raman spectra of the Antetezambato demantoid garnet in the 170–1200 cm$^{-1}$ range (top) and the 2750–4000 cm$^{-1}$ range (bottom).*

et chimique," *Revue de Gemmologie a.f.g.*, Vol. 183, 2013, pp. 10–15, in French).

Fluid inclusions were observed in all the minerals of the exo- and endo-skarns of the Ambohimirahavavy alkaline complex, but they were too small in the garnet for microthermometric studies. In quartz, calcite, and diopside, three types of primary aqueous FI, free of $CO_2$, $CH_4$, $H_2S$, and $N_2$, were characterized (see Estrade's PhD thesis). The main FI type (liquid + vapor) consists of 20 to 40 vol.% vapor, and homogenizes to liquid between 255 and 375°C for quartz, and 350 to 370°C for diopside, with a wide range of salinity between 0.5 and 25 wt.% equivalent NaCl. There is also a vapor-rich (V) FI and a halite-bearing FI (liquid + vapor + halite). The giant liquid-rich FI (liquid + vapor) trapped by the demantoid of Antetezambato has a salinity of 8 wt.% equivalent NaCl that falls within the salinity range of the (liquid + vapor) FI type found for all the minerals from the Ambohimirahavavy skarn.

Such chemical and salinity similarities of the fluids between the two settings confirm that the Antetezambato deposit is associated with a skarn deposit linked to the intrusion of Oligocene alkaline magmatism. In the Ambohimirahavavy deposit, fluid inclusions in garnet are too small to be studied by microthermometry. The giant inclusion trapped in the demantoid from Antetezambato testifies to the presence of cavities favorable for fluid inclusion studies and proves that the parental fluid of demantoid garnet was aqueous.

Demantoid at Ambato peninsula is linked to the presence of alkaline magmas intruding limestones of the Isalo group. These garnets are Cr-free but contain Al (Barrois et al., 2013). The source of aluminum and iron is the alkaline magma (syenite, nepheline syenite, and alkaline granite), while calcium originated from the limestone. The fluorine and phosphorus-bearing inclusions trapped by the andradite from both occurrences were carried by the alkaline magma, which was rich in fluorine, phosphorus, and rare earth elements. In the future, primary skarn-type demantoid-bearing deposits in northwestern Madagascar at the contact between alkaline granite dykes and limestone from the Isalo Group should be prospected for this material.

*Gaston Giuliani*
*Paul Sabatier University, Toulouse, France*
*Marie-Christine Boiron and Christophe Morlot*
*University of Lorraine, Nancy, France*
*Julien Raoul*
*Beryl International, La Varenne St Hilaire, France*
*Pierre-Yves Chatagnier*
*Borel GC, Lausanne, Switzerland*

**Grandidierite from Madagascar.** Grandidierite was first described in southern Madagascar in 1902. The mineral is very rare; gem-quality material of facetable size was almost unheard of in the market before the summer of 2015.

In September 2015, GIA's Bangkok lab issued identification reports for several faceted grandidierite samples, which reached the consumer market the following month. The submitted stones ranged from 0.9 to 2.3 ct. Around the same time, one of the authors (VP) returned from a field expedition to Madagascar, where he had received some unidentified stones from Jack Mampihao. Included with the material was one unfamiliar rough fragment, weighing 8.26 ct and measuring approximately 14 × 11 × 7 mm (figure 4), which Mr. Mampihao said came from a mine near Tolianaro, in the Tranomaro area at the southern tip of the country. Mr. Mampihao reported that a large number of these stones were found, but they were unknown to local miners and dealers. Currently, we have no information about the exact amount and quality of this material.

Gem-quality grandidierite has been attributed to deposits in southern Madagascar, near Tolianaro (formerly Fort-Dauphin), and in Sri Lanka. With a chemical formula of $(Mg, Fe^{2+})Al_3(BO_3)(SiO_4)O_2$, the mineral belongs to the orthorhombic crystal system. All anisotropic minerals display pleochroism to varying degrees; grandidierite shows dark blue-green, dark green, and colorless (M. O'Donoghue, *Gems: Their Sources, Descriptions and Identification*, 6th ed., Butterworth-Heinemann, London, 2006). Its bodycolor ranges from bluish green to greenish blue (A. Thomas, *Gemstones: Properties, Identification and Use*, New Holland Publishers Ltd., London, 2009). Grandidierite has an RI of 1.590–1.639 (O'Donoghue, 2006) and a birefringence of 0.037–0.039. Its SG is close to 2.98 (O'Donoghue, 2006; Thomas, 2009), but this value may vary between 2.85 and 3.00, according to other sources (H. N. Lazzarelli, *Gemstones Identification Blue Chart*, 2010, www.gembluechart.com). A previous study has shown an absorption line at 479 nm (K. Schmetzer et al., "The first transparent faceted grandidierite, from Sri Lanka," Spring 2003 *G&G*, pp. 32–37). In that study, Raman spectroscopy was carried out on a single gem-quality grandidierite, and the same sample was subjected to composition analysis. The gemological properties of our rough sample were compared with the literature; the results are given in table 1.


*Figure 4. This grandidierite sample, weighing 8.26 ct and measuring approximately 14 × 11 × 7 mm, was acquired in Madagascar by one of the authors. Photo by Victoria Raynaud.*

**TABLE 1.** Comparison of grandidierite sample with the published literature.[a]

| | Grandidierite in the literature | Rough sample from Madagascar |
|---|---|---|
| SG | 2.85–3.00 | 2.91[b] |
| RI | 1.590–1.639; biaxial negative | 1.579–1.620; biaxial negative |
| Birefringence | 0.037–0.039 | 0.041 |
| Pleochroism | Dark blue-green, colorless, and dark green | Very light blue, colorless, and light grayish blue[c] |
| Handheld spectroscope | Absorption line at 479 nm | Faint absorption line in the blue spectrum around 470–490 nm[d] |
| Raman peaks | 492, 659, 717, 868, 952, 982, and 993 $cm^{-1}$ | **127**, **160**, **230**, 240, 263, 346, 362, 376, **426**, 440, **491**, 512, 585, 620, **659**, 685, 715, 743, **865**, **951**, **993**, and **1042** $cm^{-1}$ [e] |

[a] *Schmetzer et al. (2003), O'Donoghue (2006), and Lazzarelli (2010).*
[b] *Constant at three hydrostatic measurements.*
[c] *The pleochroism observed was very light and might have been influenced by the stone's bodycolor.*
[d] *Using a diffraction grating handheld spectroscope (OPL).*
[e] *The values printed in bold are the largest Raman peaks.*

**TABLE 2.** Analysis of a previously studied grandidierite and a recent sample from Madagascar (wt.%).

| Oxides (wt. %) | Grandidierite from Schmetzer et al. (2003)[a] | Recent sample from Madagascar[b,c] |
|---|---|---|
| $SiO_2$ | 20.20 | 16.41 (0.05) |
| $Al_2O_3$ | 52.64 | 53.89 (0.51) |
| $B_2O_3$ | 11.91 | 12.33 (0.58) |
| $Cr_2O_3$ | 0.07 | 0.01 (0.00) |
| FeO | 1.71 | 0.30 (0.05) |
| MnO | 0.03 | 0.01 (0.00) |
| MgO | 12.85 | 17.01 (0.32) |
| **Total** | **99.41** | **99.95** |

[a] *Electron microprobe analysis (EPMA), with total iron as FeO. $TiO_2$, $V_2O_3$, and CaO were detected (each 0.01%) but are not included here.*
[b] *Laser ablation–inductively coupled plasma–mass spectrometry (LA-ICP-MS).*
[c] *The standard deviations are listed between parentheses.*

The stone was analyzed using LA-ICP-MS (table 2). Three spots were analyzed and compared to data obtained by Schmetzer et al. (2003). The sample had a very low iron content compared to the earlier study. This may be explained by the elevated Mg content, since the two elements often substitute for each other. An exact comparison of the datasets should be done with care, since different techniques were used to analyze the composition. Schmetzer (2003) used electron microprobe analysis (EPMA), while the present authors used LA-ICP-MS. Using a diffraction grating handheld spectroscope, we observed a very faint line in the blue region of the visible spectrum (approximately 470–490 nm). The Raman spectrum matched closely with the RRUFF spectrum for grandidierite (figure 5). Both spectra were taken on unoriented samples.

All the characteristics of the unknown stone obtained in Madagascar matched with grandidierite. Some values fell outside the previously reported ranges, but they were within acceptable ranges for a mineral that has not been studied in depth and for a sample that is from an unknown deposit. With field collection and lab testing pointing to new sources of grandidierite, this could be a step toward a larger market presence for this material.

*Wim Vertriest, Stanislas Detroyat, Supharart Sangsawong, Victoria Raynaud, and Vincent Pardieu*
*GIA, Bangkok*

**Mexican demantoid from new deposits.** Gemologists have recognized three andradite varieties: melanite (black), topazolite (yellow-brown), and demantoid. Demantoid, the yellowish green to green variety, is the most important to the jeweler-gemologist. The traditional demantoid garnet sources are Russia (Ural Mountains) and Italy (Val Malenco and Sondrio). More than 20 years ago, small garnet crystals of pale yellowish green color were found in the Sonora andradite occurrence near the Mexican city of Hermosillo (Fall 1994 GNI, p. 194). This garnet has been classified as demantoid without any detailed gemological and mineralogical analysis.

It is very interesting to note that in some deposits of metamorphic skarns (e.g., Kamchatka, Russia; Val Malenco, Italy; and Arizona, USA), the demantoid crystals are associated with topazolite (E.P. Kievlenko, *Geology of Gems*, Ocean Pictures, Littleton, Colorado, 2003). In late 2014, our investigations showed that the same mineralogical association (figure 6, left) is characteristic for the Las Vigas Mexican topazolite source (Fall 2014 GNI, pp. 246–247). These green to yellow-green garnet crystals, measuring 1.5–5.5 mm, are also hosted by the Las Vigas skarn deposits (Cerro de la Concordia, in Las Vigas de Ramirez municipality and the Piedra Parada mine in Tatatila municipality). These deposits are located in Veracruz State, about 50 km southeast of the town of Valle de Veracruz. Studying crystals from these two new Mexican deposits with different analytical techniques, the mineral was identified as demantoid garnet (figure 6, right).

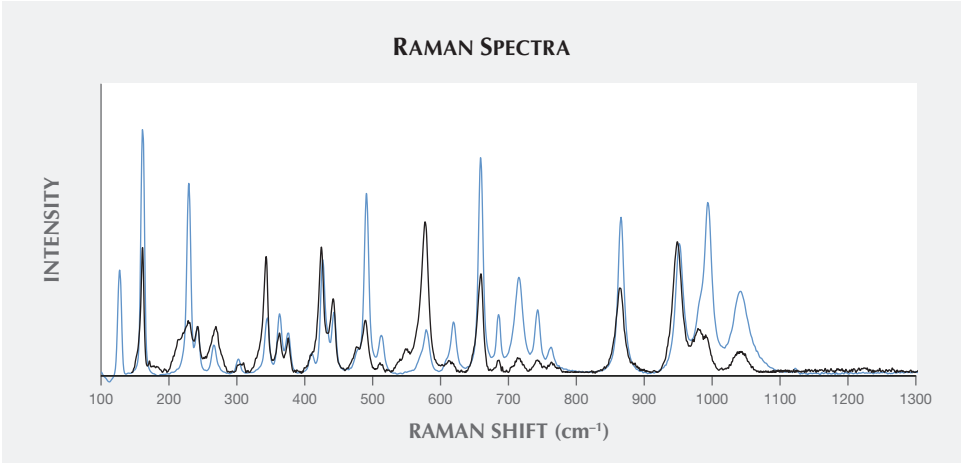


*Figure 5. This comparison of the Raman spectra of the grandidierite from Madagascar (blue spectrum) and a sample in the RRUFF database (black spectrum) provides further confirmation that the previously unidentified material is grandidierite.*

*Figure 6. Demantoid was recently discovered in Veracruz State, Mexico. The photo on the left shows an association of topazolite + demantoid. Demantoid crystals are seen in the photo on the right. Photos by Mikhail Ostrooumov.*

Three samples of rough demantoid (measuring 4.0–5.5 mm in the longest dimension) were characterized for this report, and the following gemological properties were determined: color—green; polariscope reaction—isotropic and weakly anisotropic; weak strain birefringence; RI—$n_\alpha$ = 1.888–1.889; very strong dispersion, at 0.055 (visual indicator identification); hydrostatic SG—3.82–3.88; fluorescence—inert to both long- and short-wave UV radiation.

The garnet composition was determined by means of electron microprobe analysis (EPMA), using a total of 15 analysis points. Standard conditions of 20 kV, 20 mA, and 1 µm beam size were used with a JEOL JSM-35c microprobe. The analyses showed little compositional heterogeneity or zonation. The structural formula was calculated on the basis of 12 oxygen atoms, yielding an average approximate composition of $(Ca_{2.96}Fe^{2+}_{0.08})_{3.04}Fe^{3+}_{2.05}Si_{2.94}O_{12}$. This structural formula has an abundance at the X-site and Y-site cations but is close to electroneutrality due to the sum of the positive and negative charges (Wc = +23.99; Wa = –24.00). The EPMA-WDS data showed that these green garnets were almost pure andradite (And > 95.60 mol.%). No chromium was detected in the chemical composition of the studied crystals.

Infrared transmission spectra were measured with a Bruker Tensor 27 FTIR spectrometer, scanning from 4000 to 400 $cm^{-1}$ and using the KBr pellet method. The pellets were prepared by mixing approximately 3 mg of the sample with 300 mg KBr. OPUS software was used for the spectroscopic interpretation of the infrared spectra. Raman (figure 7, left), mid-infrared (figure 7, right) and X-ray analysis confirmed that the crystals belonged to the demantoid variety (http://rruff.info). The mid-IR spectra showed the presence of hydroxyl groups. The infrared spectra consisted of a prominent band at 3420 $cm^{-1}$, with a secondary band at about 3610 $cm^{-1}$ due to the fundamental OH stretching vibration of water molecules, as well as the water bending vibration at approximately 1650 $cm^{-1}$.

*Figure 7. Raman (left) and infrared (right) spectra of the samples confirm their demantoid garnet identity.*

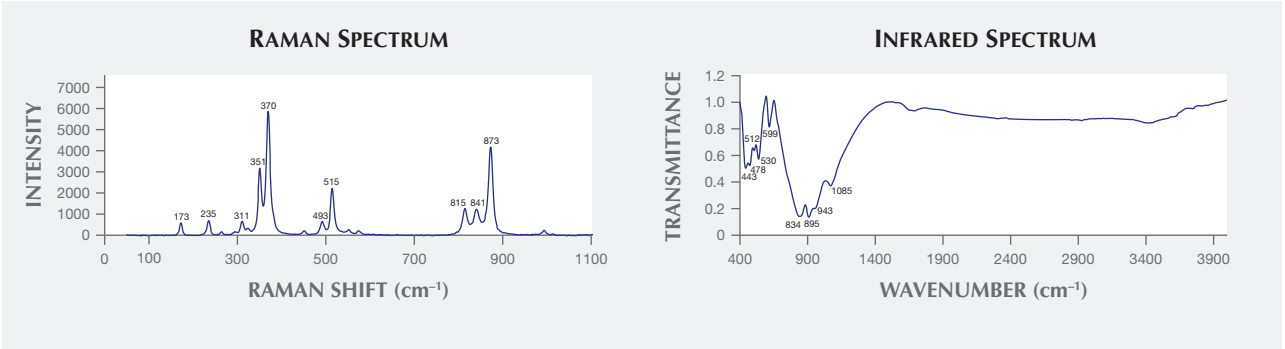

UV-Vis-NIR spectroscopy showed absorption bands at 403, 444, 574, 617, 854, and 1170 nm, which can be assigned to spin-forbidden crystal-field transition of $Fe^{3+}$, substituted on the octahedral $Al^{3+}$ site of the garnet structure. Our EPMA analyses of garnet generally indicated the presence of some divalent iron. The spectra showed absorption bands in the 900–1000 nm and 1150–1250 nm ranges, which are assigned to $Fe^{2+}$, and corresponding absorption features were observed at about 860 and 1170 nm. The simultaneous presence of both $Fe^{3+}$ and $Fe^{2+}$ means that intervalence charge transfer is possible (in accordance with A.S. Marfunin, *Advanced Mineralogy*, Vol. 2, Springer-Verlag, Berlin, 1995, pp. 113–114), and the 574 nm band is therefore assigned to an $Fe^{2+} \rightarrow Fe^{3+}$ intervalence charge transfer band. The typical absorption bands of $Cr^{3+}$ in the visible region between 630 and 690 nm are absent, consistent with the EPMA results. Our investigations have also shown that some demantoid garnets from Russia do not show any chromium absorption, and their color is due to the presence of $Fe^{3+}$ alone.

The color measuring system of the International Commission of Illumination (ICI) has been found useful for describing the color characteristics of minerals (K. Langer et al., "Optical absorption spectroscopy," in A.S. Marfunin, Ed., *Advanced Mineralogy*, Vol. 2, Springer-Verlag, Berlin, 1995, pp. 119–122). The color of a mineral is assigned to a point in the x-y coordinates of the ICI color chart. Special computer programs are used to calculate the color parameters (x-y coordinates, λ—dominant wavelength, P—saturation or purity, Y—lightness) of a mineral directly from the measured optical absorption spectrum. The dominant wavelength λ, or hue, is the human eye's psycho-sensory interpretation of wavelengths that are identified by the x-y coordinates of the ICI color chart. Preliminary colorimetric calculations showed that the colors of the Mexican demantoid have low saturation (P=20%) and lightness (Y=17%). Therefore, they are darker than pure green demantoid from other deposits (e.g., Bobrovka River in the Ural Mountains). The dominant wavelength of Mexican demantoid (λ=560 nm) is a slightly yellowish green. This combination of colorimetric parameters defines a color different from that of chromium-bearing demantoid. Measurements on the demantoid from the Urals showed higher values of saturation (P=44–50) and lightness (Y=20–37%) and a purer green hue, with λ=530–545 nm (M. Ostrooumov, "Colorimetry of minerals," *Priroda*, No. 6, 1987, pp. 43–53, in Russian). Such demantoids are more attractive to the gem trade.

Thus, electron microprobe (EPMA-WDS) chemical analyses, various spectroscopic techniques, X-ray diffraction, and standard gemological testing have confirmed the discovery of demantoid in the Las Vigas skarn deposits of Veracruz State. The discovery could represent an interesting mineralogical and gemological opportunity. Although the full range and economic potential of this demantoid has not been determined, it may well have features that distinguish it from other important deposits worldwide.

*Mikhail Ostrooumov (ostroum@umich.mx)*
*University of Michoacan, Institute of Earth Sciences*
*Morelia, Michoacan, Mexico*

**A new natural-color bluish green chalcedony.** A new type of chalcedony (figure 8) was recently submitted to GIA's Carlsbad laboratory by Yianni Melas of Greece. According to Melas, this material originated in Africa (figure 9), although a more precise location has not been made available. The translucent material displayed a vibrant bluish green color and is currently marketed under the trade name "Aquaprase." Although chalcedony varieties such as chrysoprase and Gem Silica are well known and occur in

*Figure 8. This bluish green chalcedony, colored by chromium and nickel, is marketed under the trade name "Aquaprase." Photo by Kevin Schumacher.*

*Figure 9. A large piece of chalcedony rough recovered from the mining area. Photo by Yianni Melas.*

yellowish green and greenish blue colors, the color of this material was distinctly different from any African chalcedony examined by GIA to date.

From a gemological perspective, it was important to conclusively determine that this material was naturally colored and not artificially dyed. Since the quartz crystals present in this material were colorless rather than brown, we ruled irradiation out as a possible treatment. Microscopic examination of rough and cut stones in conjunction with chemical analysis and visible spectroscopy were used to characterize this chalcedony. Standard gemological testing revealed an RI range from 1.531 to 1.539, with no observable birefringence. The SG, measured hydrostatically, ranged from 2.55 to 2.57. A handheld spectroscope revealed faint, narrow lines in the red end of the spectrum, rather than the broadband absorption one would expect if the material had been dyed with an organic pigment. All of these features were consistent with natural-color chalcedony.

Microscopic examination revealed a granular aggregate structure with a few areas showing subtle banding and faint green concentrations of color between some of the coarser quartz grains, which appeared to be a greenish mineral phase located along the grain boundaries. A waxy luster was observed on fractured areas, consistent with an aggregate material. Some areas contained small cavities that were filled with colorless drusy quartz crystals (figure 10, left and center). Dark brown and black inclusions of various metal oxides were also observed scattered throughout most of the samples examined, along with some areas of whitish cloudy inclusions that were not identified (figure 10, right).

Raman analysis confirmed the material was quartz. EDXRF was used to analyze the trace-element metals that might be responsible for the bluish green color. All seven finished gemstones tested showed the presence of chromium and nickel. Interestingly, iron, vanadium, and copper were also detected in one of the cut samples, but these elements might not be related to the color, as other bluish green samples did not contain them. Visible spectroscopy (figure 11) revealed broad absorption bands centered at approximately 420 and 600 nm, with a large transmission window at approximately 500 nm producing the bluish

*Figure 10. The Aquaprase samples contained minute pockets of colorless drusy quartz (left and center) and irregular brown and black metal oxide inclusions (right). Photomicrographs by Nathan Renfro; field of view 2.83 mm (left), 4.76 mm (center), and 4.62 mm (right).*

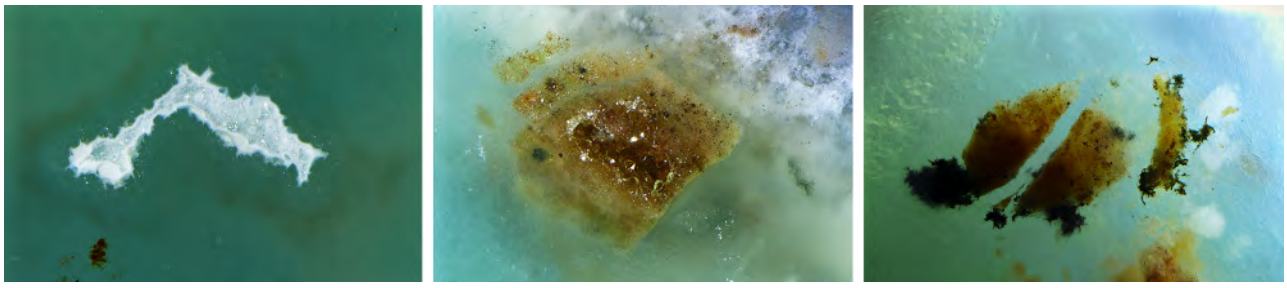

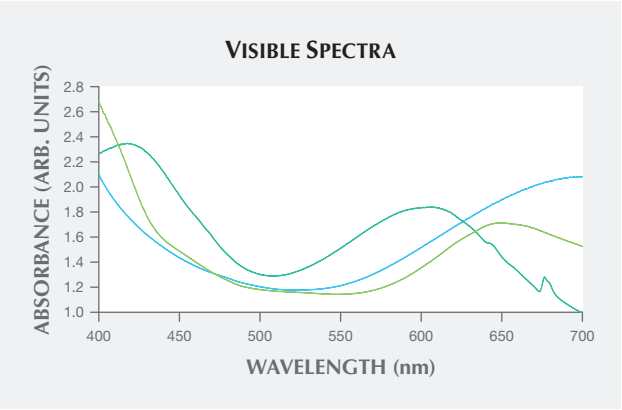


*Figure 11. The visible spectrum for the Aquaprase (bluish green trace) showed two broad absorption bands at 420 and 600 nm in addition to sharper peaks at 646, 676, and 679 nm. This absorption pattern is clearly different from that of chrysoprase (yellowish green trace) and Gem Silica (greenish blue trace).*

green color. Sharp absorption peaks at 646, 676, and 679 nm were presumably related to chromium (http://www.gia.edu/gia-news-research-nr7809).

This new type of African chalcedony is easily recognized by its unique composition and absorption spectrum, which is significantly different from the chrysoprase and Gem Silica varieties. The attractive bluish green color of Aquaprase, which may be caused by chromium and nickel, should prove to be a popular and welcome addition to the gem trade.

*Nathan Renfro*
*GIA, Carlsbad*

**Rubies from a new deposit in Zahamena National Park, Madagascar.** In July 2015, news circulated through the trade about a ruby discovery south of Andilamena, near Lake Alotra (figure 12). Photos of clean, attractive stones of over 10 carats were shared on social media by Malagasy and Sri Lankan gem merchants. Several thousand unlicensed miners quickly descended on the area, creating serious conservation concerns as the new deposit was located inside Zahamena National Park. In August 2015, the Malagasy government sent soldiers to close the mining site. But because the area is very remote, they could not maintain their presence longer than a month. As soon as the soldiers departed, the miners returned in numbers.

Gem-quality rubies and sapphires are not unknown in northeastern Madagascar: They were first found in 2000, east of Andilamena and west of Vatomandry (Summer 2001 GNI, pp. 147–149). These discoveries were followed by a blue sapphire deposit near Andrebabe, a few kilometers south of Andilamena, in 2002 (www.ruby-sapphire.com/madagascar_ruby_sapphire.htm). Ruby mining was limited until 2004, when demand for the heavily fractured material from Andilamena dramatically increased with the advent of the lead-glass filling treatment developed in Thailand between 2001 and 2004. Visiting the deposit in June and September 2005, author VP could see that more than 10,000 miners were living and working in the jungle (www.rwwise.com/madagascar1.html). In 2011 and 2012, two new discoveries occurred in the region. The first was a pink and blue sapphire deposit near Mandraka village, north of Toamasina. In 2012, a deposit was discovered east of Didy (www.giathai.net/pdf/Didy_Madagascar_US.pdf). That deposit produced some large, clean, and attractive rubies and blue sapphires. More discoveries followed—near Bemainty, north of Didy, for instance—but either the gems were ordi-

*Figure 12. Rough rubies from Zahamena National Park with a combination of good shape, transparency, and attractive color. Photo by Vincent Pardieu/GIA.*

*Figure 13. A young Malagasy miner searches for rubies in Zahamena with simple homemade tools: a pierced plastic oil can used as a sieve and an empty water bottle to store his gems. Photo by Vincent Pardieu/GIA.*

nary or the rush was short-lived. In 2015, a new blue sapphire rush occurred near Andrebabe in February, followed by a ruby discovery near Ambodivoangy village in July (http://lotusgemology.com/index.php/library/articles/322-blood-red-rubies-from-madagascar-lotus-gemology).

From September 23 to October 6, 2015, a GIA field expedition team collected samples at the mines. After three days of walking in the jungle, the team was able to visit the new mining sites (figure 13), located about four hours' walking distance from Ambodivoangy. There they witnessed some illegal ruby mining activity by artisanal miners at two different sites, located in a valley at 17°37'60"S 48°52'19"E and along a creek in a forested area at 17°38'26"S 48°52'38"E. They confirmed that the deposit was indeed located inside Zahamena National Park. Approximately 500 people were seen at the lower mining site, while about the same number worked in the forest along a stream where ruby-rich gravels were collected (figure 14).

The local trading center was in Andrebakely, with mainly Malagasy buyers, while foreign buyers (typically from Sri Lanka) waited for local miners and businessmen at Tanambe and Andilamena. In both towns, more than 20 Sri Lankan buying offices were visible, mostly in houses with painted signs for the different companies.

The new deposit is located about halfway between the old ruby deposit in the jungle east of Andilamena (discovered in 2000) and the rush that occurred at Didy in 2012 (www.giathai.net/pdf/Didy_Madagascar_US.pdf). The rubies from Zahamena share obvious similarities with those from Andilamena, such as their inclusions (mainly zircon and rutile crystals associated with rutile needles) and trace-element composition. Therefore, it is likely that these deposits are related, and a huge ruby and sapphire deposit could be hidden under the jungle in northeastern Madagascar.

Back at GIA's Bangkok lab in October 2015, the samples were fabricated and data was collected from them; a more extensive study is in progress. At this point it is interesting to note that the rubies from the Zahamena deposit have a very similar aspect to those from amphibole-related African deposits such as Montepuez in Mozambique, Chimwadzulu in Malawi, and Winza in Tanzania. Their iron content is indeed much higher than that of the marble-type rubies mined in Myanmar, Vietnam, Afghanistan, or Tajikistan. The shape of the crystals is generally tabular but not as flat as what is commonly found in Mozambique, meaning that

*Figure 14. Artisanal Malagasy ruby miners wash gem-rich gravels in the stream that runs through the jungle of the Zahamena National Park. Photo by Vincent Pardieu/GIA.*

faceted stones with good proportions can be produced. The new material is on average more included than the ruby from Montepuez. But ultimately the limiting factor for this deposit is its location inside Zahamena National Park, where gem mining is illegal.

*Vincent Pardieu, Supharart Sangsawong, and Stanislas Detroyat*
*GIA, Bangkok*

## SYNTHETICS AND SIMULANTS

**Golden coral imitated by plastic.** As one of the seven Buddhist treasures, coral is a symbol of importance in Chinese culture. Golden-colored coral is considered "sublime," since both red and gold represent prosperity and prestige. Golden coral, which is usually treated black coral, can be identified by its appearance and structure, with concentric growth layers and a pitted texture (figure 15, left). Imitations lack these characteristic features, which is of relevance to those deal with coral.

The Lai Tai-An Gem Laboratory in Taipei recently received a bracelet for identification; the client claimed the material was golden coral. The bracelet was composed of several evenly sized bright gold to deep brown beads, strung together with thread, that exhibited a waxy luster and an interesting "swirl" pattern (figure 15, right). Identical spot RIs of 1.55 were obtained from each bead, and there was no reaction under LW or SWUV light. The material did not exhibit the characteristic pitted texture of golden coral. Further analysis by FTIR and Raman spectroscopy identified the beads as plastic (resin). Peaks at 2934, 2862, 1731, 1285, 1128, 1072, 745, and 703 $cm^{-1}$ in the infrared spectrum (figure 16) and peaks at 619, 649, 1000, 1038, 1448, 1578, 1599, and 1725 $cm^{-1}$ in the Raman spectrum (figure 17) were indicative of plastic. Further inspection at 60× magnification with high-intensity fiber-optic illumination showed that

*Figure 15. These photos compare the appearance of golden coral (left) and a plastic imitation (right). Photo by Lai Tai-An Gem Lab.*

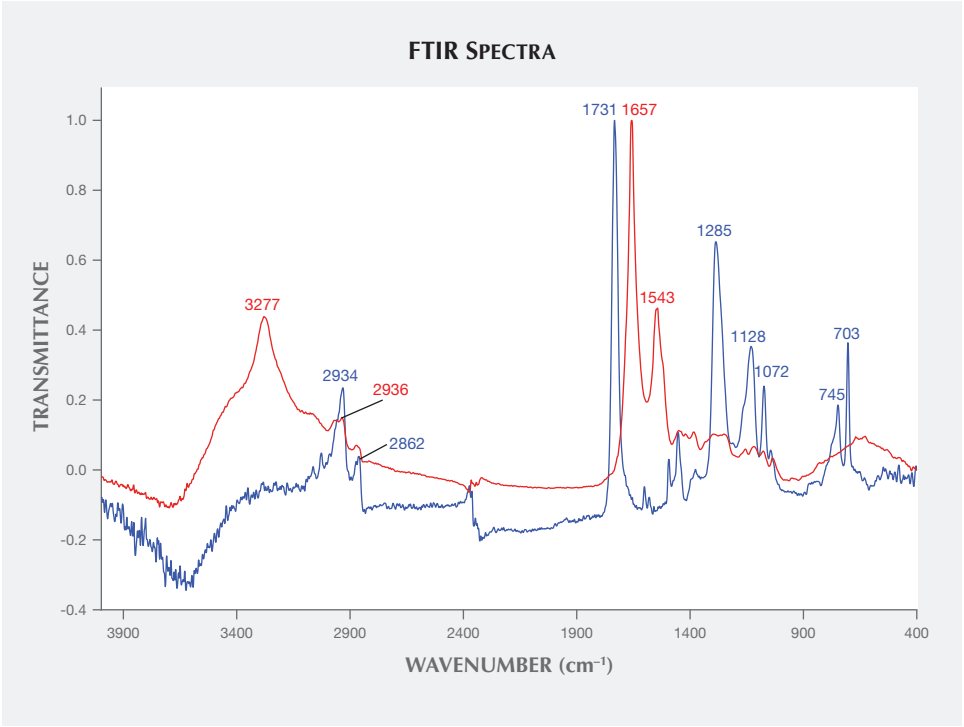


*Figure 16. FTIR analysis reveals the difference between the spectra for a tested coral sample (red line, peaks at 3277, 2936, 1657, and 1543 cm$^{-1}$) and plastic (blue line, peaks at 2934, 2862, 1731, 1285, 1128, 1072, 745, and 703 cm$^{-1}$).*

these translucent beads had the same swirl texture extending to the center from the surface, indicating that they were composed of plastic. The aforementioned natural characteristics were not seen at all in this material.

Golden coral may possess a degree of instability, so some material is coated with resin to strengthen the structure. In this case, however, each bead was entirely formed of plastic made to imitate golden coral. Plastics, along with glass, are among the most adaptable materials and can be fabricated to imitate virtually any natural material imaginable. Some imitations are more difficult to identify than others, but in this example identification was fairly simple owing to the structural differences of the two materials, observed with either a microscope or a loupe.

*Larry Tai-An Lai*
*Lai Tai-An Gem Laboratory, Taipei*

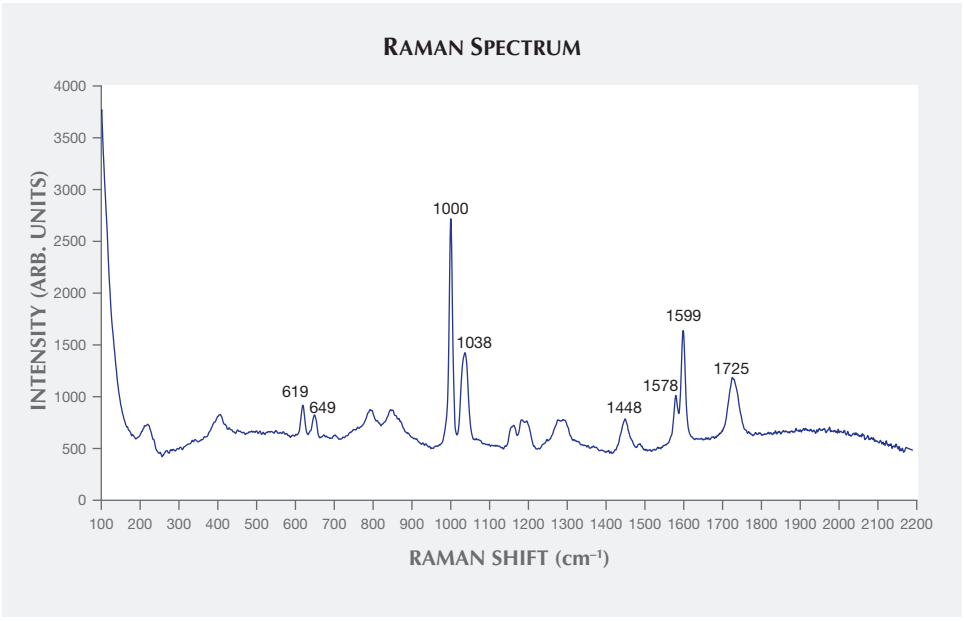


*Figure 17. Raman analysis (excitation wavelength of 785 nm) confirmed the beads' identity as plastic.*

## CONFERENCE REPORTS

**GSA 2015 annual meeting.** The Geological Society of America's annual meeting, held in Baltimore November 1–4, attracted more than 6,000 geoscientists from around the world. Two technical sessions, one oral and one poster, were devoted to the gemological field. The poster session's flexible presentation time and format, along with the wide range of topics covered (including diamond defect formation and low-pressure, high-temperature [LPHT] treatment of type Ia diamonds), allowed for dynamic discussion between exhibitors and viewers.

**George Harlow** (American Museum of Natural History, New York) opened the oral session by discussing how gemological studies provide insight into the geological developments of Earth. **Wuyi Wang** (GIA) presented the discovery and distribution of $[Si\text{-}V]^-$ defects in HPHT synthetic diamonds. This study challenged the widely accepted theory that $[Si\text{-}V]^-$ defects only occur in CVD synthetic diamonds, while also showcasing photoluminescence mapping as a powerful research technique.

**Laurent E. Cartier** (Swiss Gemmological Institute, Basel) applied DNA analysis to the origin determination of organic gems, and this presentation focused on pearls. For the first time, gemologists can conclusively identify the mollusk species of a pearl; Dr. Cartier's team is exploring similar possibilities with coral and ivory.

**Karen Smit** (GIA) studied the Re-Os isotope of sulfide inclusions in type Ib diamond from West Africa. The isotopic study was used to explain the assembly of the Gondwana supercontinent. **Steven Shirey** (Carnegie Institution of Washington) presented his Re-Os geochronology study on a sulfide inclusion within a superdeep diamond from Brazil. The age of this inclusion indicated crystal recycling facilitated by mental convection beneath. Both studies demonstrated the vital role gem materials play in earth science research.

Gemological studies of famous stones and historical jewelry pieces were also represented. **Alan Hart** (Natural History Museum, London) studied the creation of the Mogul cut. Using the Koh-i-Noor diamond as a case study, Mr. Hart found that differential hardness was the key factor that brought about the Mogul cut with the primitive cutting tools available in the mid-19th century. **Raquel Alonso-Perez** (Harvard University) used both spectroscopic and trace-element analysis to study the tourmalines mounted in the Hamlin Necklace, a piece of 19th-century North American jewelry.

Inclusion study is one of the pillars of modern gemology. **John Koivula** (GIA) pointed out the possibility of misidentifying synthetic corundum as heat-treated natural material. Experimental studies have demonstrated that heat-fused cracks generated in both pulled and flame-fusion synthetic corundum appear virtually identical to the features associated with so-called flux-healed natural stones. **Aaron Palke**, also of GIA, hypothesized that unusual glassy melt inclusions found in sapphires from southwestern Montana are crystallized as peritectic minerals formed during high-grade metamorphism, generating silica-rich melt and an alumina-rich restite. Future research on this topic may shed light on the source and transportation of Montana sapphires.

Phenomenal gems were also explored. **Keal Byrne** (Smithsonian Institution) investigated the luminescence of "chameleon" diamonds, which show an intriguing color-change response to temperature and/or light. **Xiayang Lin** (Pennsylvania State University) discovered the microscopic surface feature that causes iridescence in natural quartz crystals from India.

Researchers also spoke about American gem deposits. **Michael Wise** (Smithsonian Institution) discussed his work on the hydrothermal emerald and hiddenite mined in the Hiddenite area of North Carolina, while **Yury I. Klyukin** (Virginia Polytechnic Institute and State University) investigated the fluid evolution of the emerald deposit at the North American Emerald Mine, also in the Hiddenite region. **William B. "Skip" Simmons** (Maine Mineral and Gem Museum) shared the recent discovery of gem-quality pollucite in Mt. Mica pegmatite.

The details of all oral presentations from the GSA meeting can be found at https://gsa.confex.com/gsa/2015AM/webprogram/Session37638.html. GSA's 2016 annual meeting will be held September 25–26 in Denver.

*Tao Hsu, James E. Shigley, and Dona M. Dirlam*
*GIA, Carlsbad*

**First International Emerald Symposium.** Hosted by Fedesmeraldas, the Colombian Emerald Federation, the International Emerald Symposium was held October 13–15, 2015, in Bogotá. Approximately 350 participants attended sessions featuring Colombian and international speakers. The theme for the symposium was "Be Part of the Change," and there was a strong emphasis on the future and a cooperative effort that would benefit the entire emerald industry. The speakers were from source, manufacturing,and consuming countries, representing all levels of the value chain.

Day one started with Colombian government officials. **Maria Isabel Ulloa** (Vice Minister of Mines) spoke on the transparency, traceability, and control of gem commerce. She emphasized the progress made and the need to further formalize Colombia's emerald industry. This issue was addressed by several others during the symposium, including **Javier Octavio Garcia Granados** (Agencia Nacional de Mineria, ANM). **Santiago Angel** (Asociación Colombiana de Minería, ACM) spoke on Colombia's over-all mining outlook, including emerald, and emphasized that the country welcomes foreign investment and partnerships in mining.

In addition to the Colombian government officials from the opening presentations, **Christopher B. Yaluma** (Zambian Minister of Mines, Energy and Water Development) described how Zambia steered its emerald industry toward

formalization and outlined the ensuing benefits in tax revenue and consistent supply.

The next group of speakers represented trade organizations, including **Oscar Basquero** (Fedesmeraldas), **Gerry Manning** (American Gem Trade Association, AGTA), **Benjamin Hackman** (International Colored Gemstone Association, ICA), and **Roland Naftule** (World Jewellery Confederation, CIBJO). These presentations demonstrated the benefits trade organizations can provide in trading, networking, and addressing issues such as transparency and disclosure through their guidelines.

The afternoon session was devoted to laboratory officials. **Shane McClure** (GIA) spoke on the need for harmonization between laboratories regarding protocols and wording in reports. **Dietmar Schwarz** (Asian Institute of Gemological Sciences) and **Carlos Julio Cedeño** (CDTEC Gemlab, Bogotá; figure 18) discussed origin determination of emerald. Dr. Schwarz examined overall geographic determination, while Dr. Cedeño focused on the parameters to identify Colombian origin and specific locality. Also from CDTEC, **Darwin Fortaleche** presented information regarding a new enhancement process for natural emerald, currently under development in Colombia, that is expected to become a viable alternative to oil and polymer resin treatment.

In the second morning session, **Philippe Scordia** (Christian Dior Jewellery) offered insight into luxury jewelry brands and their criteria for gemstones. His talk included quality considerations in selecting gemstones for jewelry as well as corporate transparency and ethical sourcing and standards for selecting suppliers. Next were presentations on corporate social responsibility and traceability. **Charles Burgess** (Mineria Texas Colombia) discussed MTC's policies on transparency, including tracking rough, employee benefits (with approximately 500 locals employed), and corporate taxes paid.

ICA's **Jean Claude Michelou**, who served as the international coordinator of the symposium, presented the initiatives by the United Nations, governments, and non-government organizations to improve colored gemstone traceability throughout the value chain. He emphasized that 80% of colored gemstone production comes from small-scale and informal mining (figure 19) and stressed the importance of transparency to this sector in ensuring consumer confidence. This portion of the symposium was followed by a spirited discussion of the need for changes in the colored gemstone supply chain, including the role of large, well-funded corporations and traditional small-scale local miners as well as the issue of theft at the mines. Overall security improvements in Colombian mining areas were confirmed by a GIA field gemology team that traveled to the major sites after the symposium.

After lunch, the speakers included **Gaston Giuliani** (Paul Sabatier University, Toulouse) who gave an impassioned presentation on emerald deposits from around the world and their geological differences. **Marcelo Ribeiro** (Belmont Group) overviewed the investment in exploration, mining, and processing at the Belmont mine in Itabira, Brazil. Mr. Ribeiro addressed the use of optical sorters in processing rough as well as the move up the value chain into cutting rough. Representing manufacturing in a global hub, **Vijay Kedia** (Jewellers Association of Jaipur) discussed how emeralds from all over the world come to Jaipur for cutting and trading.


*Figure 18. Dr. Carlos Julio Cedeño discussed the origin determination of Colombian emerald, a crucial first step to branding. Photo by Andrew Lucas/GIA.*

The beginning of day three emphasized branding and education, featuring talks by **David Lightle** (Wright Brothers), **Gabriel Angarita** (Colombian Association of Emerald Exporters, ACODES), and **Andrew Lucas** (GIA). Mr. Lightle examined the potential of the "Mother Gem" brand for Colombian emerald, citing the success of branding Colombian coffee. He also noted the need to overcome Colombia's negative associations with drugs and violence. Mr. Angarita described the role of ACODES and the industry's efforts to brand and promote Colombian emerald. Mr. Lucas displayed articles and documentaries from GIA's website that are designed to educate the public about colored gemstones from mine to market.

Of great interest to the symposium was the presentation by **Sean Gilbertson** (Gemfields) on the company's mining operations in Zambia and Mozambique as well as their social responsibility and transparency programs. This talk was set against the backdrop of Gemfields' purchase of 70% of mining in Cosquez, and their acquisition of mining concessions totaling 20,000 hectares in the Muzo and Quipama areas. Later in the day, **Adolf Peretti** (Gem Re-

*Figure 19. The role of the small-scale independent miner is an important topic not only in Colombia, but in all colored gemstone producing countries. Photo by Andrew Lucas/GIA.*

search Swisslab, GRS) discussed color terminology as a communication and marketing tool. Dr. Peretti presented "Muzo green" as a color term on laboratory grading reports, sparking a lively panel debate regarding that and other grading terms, including the use of Minor, Moderate, and Significant for treatment classification.

*Andrew Lucas and Jonathan Muyal*
*GIA, Carlsbad*

**34th International Gemmological Conference.** The 34th IGC was held in Vilnius, August 26–30. Pre- and post-conference field trips visited Lithuanian cultural heritage sites, as well as the historical amber-producing area along the Baltic seacoast. This event takes place every two years, with the 2017 conference scheduled for Windhoek, Namibia. Several oral and poster presentations of interest are summarized here. Abstracts of all presentations can be viewed on the conference website at http://www.igc-gemmology.net/igc34-proceedings/.

Amber was one of several topics presented at the conference. **Albertus Bitinas** (Klaipeda University, Lithuania) summarized the geologic setting of amber deposits in the southeast Baltic region. The amber originated from pine trees (*Pinus succinifera*) that thrived during the Paleogene period (65–23.5 million years ago), when the climate of northern Europe was humid. The subsequent flow of rivers redistributed pieces of amber in sediments in this region. **Jonas Satkünas** (Lithuanian Geological Survey, Vilnius) recounted efforts to document the country's amber potential. He reported that 2,250 tons were recovered in the 19th century from the Curronian Lagoon along the Baltic seacoast. A recent survey of the lagoon revealed additional amber deposits with potential for development. Amber from Canada has never been seriously considered as a gem material, but **Willow Wight** (Canadian Museum of Natural History, Ottawa) discussed its importance for entomologists and botanists who have, over the past century, studied the animal and plant life from the Cretaceous period that became trapped and then preserved in the fossilized tree resin. **Lore Kiefert** (Gübelin Gem Lab, Lucerne, Switzerland) discussed the occurrence of natural green amber near Alem Ketema, Ethiopia. Green amber has been of gemological interest because of concerns that some material in the market is of natural or treated origin. Amber from the Hukawng Valley in northern Myanmar has been known for a millennium. **Tay Thye Sun** (Far East Gemmological Laboratory, Singapore) described a new amber locality in the Hti Lin township, in the central part of the country. Characterization of this new material demonstrated that it has many features similar to the Hukawng amber.

**Thomas Hainschwang** (Gemlab Liechtenstein) investigated 20 naturally colored, polycrystalline black diamonds of unknown origin, and one diamond from the Popigai impact crater in Siberia. The samples exhibited photoluminescence features suggesting micro-inclusions of carbon dioxide and lonsdaleite.

In the realm of synthetic diamonds, **Hiroshi Kitawaki** (Central Gem Laboratory, Tokyo) examined 15 type Ib yellow to brownish yellow synthetic diamonds that had been submitted for grading without disclosure. Visual features and spectroscopic evidence suggested post-growth high-temperature annealing, presumably to alter their color. The means of identifying both small HPHT and large CVD synthetic diamonds was reviewed by **Joe Yuan** (Taiwan Gemmological Institute, Taipei). Of particular importance for detection are anomalous birefringence ("strain") patterns, UV fluorescence reactions, and spectroscopic features.

Gem occurrences along the coast of Greenland were discussed by **Anette Juul-Nielsen** (Ministry of Natural Resources, Nuuk). Small-scale mining of ruby and pink sapphire from Archean metamorphic rocks is currently un-

derway in the Fiskenæsset area. The Greenland government is issuing licenses for both exploration and extraction of mineral resources.

**Kentaro Emori** (Central Gem Laboratory, Tokyo) discussed the value of three-dimensional plots of chemical composition data to support the country-of-origin determination of ruby and blue sapphire.

**Emilie Elmaleh** (University of Geneva) presented a study of zircon inclusions in metamorphic-related blue sapphires of sufficient size (< 150 microns) to allow age dating by the U/Pb method and quantitative chemical analysis. While potentially useful for country-of-origin determination, this method may be of more value for rough corundum samples because both techniques require that the zircon inclusion be present at the surface of the sample for analysis.

**Hanco Zwaan** (Netherlands Gemmological Laboratory, Leiden) investigated a suite of alluvial sapphires from deposits in Montana. Identification of mineral inclusions and geochemical analysis suggest that these sapphires originated in a metasomatic geologic environment.

**Karl Schmetzer** (Petershausen, Germany) investigated the origin of dual-color double stars in oriented needle-bearing corundum and quartz. The study concluded that the silvery white star is formed by light reflection and scattering, while the body-colored second star originated by the reflection and scattering of light from a layer near the base of the cabochons. The light producing the second star travels twice the distance down and up through the cabochon, undergoing selective absorption. The color of the second star is identical to the bodycolor of the host material.

**Visut Pisutha-Arnond** (Gem and Jewelry Institute, Bangkok) presented a heat-treatment study of sapphires to understand the role of beryllium in coloration. The researchers concluded that this trace element is made inactive by heating in a reducing environment, and that beryllium-diffusion treatment is only effective by heating under oxidizing conditions.

**Walter Balmer** (SSEF Swiss Gemological Institute, Basel) explored the presence of infrared bands at 3053 and 2490 wavenumbers as spectral evidence of beryllium diffusion treatment of sapphires.

**Ahmadjan Abduriyim** (GIA) investigated how residual pressure was distributed three-dimensionally by measuring such pressure around mineral inclusions in natural corundum from the New England sapphire field in New South Wales, Australia.

**Shane McClure** (GIA) described emeralds from the Belmont mine in Minas Gerais. The operation is the largest and most technologically advanced emerald mine in Brazil. He also followed a large rough emerald through the manufacturing process to create two cut stones (the largest weighing 18.17 ct) that were set in jewelry.

Gemological properties of pallasitic peridot from six different meteorites were presented by **Masaki Furuya** (Japan Germany Gemmological Laboratory, Kofu). Samples from the different meteorites could be distinguished from one another by inclusions, visible and infrared spectra, and trace element composition.

**Roman Serov** (Gemological Center, Lomonosov Moscow State University) investigated the heat treatment of green Russian demantoid garnet. Color changes were reversible and detected at heating temperatures as low as 400°C. Heating under reducing conditions was more effective in removing any brown component of demantoid color.

**Andy Shen** (China University of Geosciences, Wuhan) investigated nephrite jade samples from eight locations in China, using the linear discriminant analysis of trace element composition data as a criterion for determining their geographic origin.

Mining operations in the three main opal-producing areas of Australia—Lightning Ridge, Queensland, and Coober Pedy—were detailed by **Karen Fox** (Waterloo, Canada). She also explained the geologic conditions that favor opal formation in sedimentary environments.

**Emmanuel Fritsch** (University of Nantes, France) studied a yellow gem hyalite opal from Mexico with intense uranium-related, daylight-excited green luminescence. This is one of the few gem materials whose color is dominated by luminescence due to the presence of the uranyl ion.

Three gem minerals exhibiting photochromism, all showing a reversible change of color when exposed to ultraviolet radiation—hackmanite, tugtupite, and sodalite—were investigated by **Claudio Milisenda** (DSEF German Gem Lab, Idar-Oberstein). Within several hours to a day, the transient color reverted to the original color when the samples were exposed to daylight.

**Henry Hänni** (GemExpert, Basel, Switzerland) described the use of two imaging techniques—X-ray phase contrast and X-ray scattering—to investigate the internal structure of natural and cultured pearls. Both methods provide more valuable information for pearl identification than the images obtained by conventional absorption radiography.

In a study of natural and non-bead cultured *Pinctada maxima* pearls, **Nick Sturman** (GIA) discussed the use of X-ray computer microtomography to image internal features, which provide an important means of identification. A comprehensive database of internal features is being developed to assist in the identification of unusual pearls submitted for examination. **Sutas Singbamroong** (Gemstone and Precious Metal Laboratory, Dubai) characterized features of natural non-nacreous pearls reported to be from the *Tridacna* (clam) species.

**Lutz Nasdala** (Institute for Mineralogy and Crystallography, University of Vienna) outlined efforts to locate large gem-quality faceted zircons for use as analytical reference materials for chemical analysis and geological age dating of rocks. These gemstones must be chemically homogeneous and untreated, since they will be sectioned into small pieces for distribution to a number of analytical laboratories involved with geological studies.

**Brendan Laurs** (Gem-A) discussed methods being used to exploit primary and secondary gem deposits in the

Mogok region of Myanmar. Easily accessed rich surface deposits are increasingly exhausted, requiring deeper mining operations that involve greater costs, more sophisticated equipment, and increased risk.

In the poster session, **Gagan Choudhary** (Gem Testing Laboratory, Jaipur) presented the properties of emeralds from a new occurrence in the Indian state of Jharkhand. **Helmut Pristacz** (Institute for Mineralogy and Crystallography, University of Vienna) studied the properties of natural and various synthetic turquoise samples. **Antonello Donini** (CISGEM Laboratory, Milan) presented information on unusual gem materials—rhinoceros horn and ambergris—encountered by their laboratory. **Guanghai Shi** (China University of Geoscience, Beijing) compared the infrared spectroscopy characteristics of amber from the Baltic Sea, the Dominican Republic, and Myanmar, indicating the key differences in their spectral features. **Elizabeth Su** (Gemsu Rona, Shanghai) reported on the main jadeite markets in China. Finally, **Thanong Leelawatanasuk** (Gem and Jewelry Institute, Bangkok) described black sapphires treated by titanium diffusion.

*James E. Shigley*
*GIA, Carlsbad*

## ERRATA

1. In the Fall 2015 article on Colombian trapiche emerald, table 1 (p. 237), each listing in the "Section c-axis" column was reversed. The online edition has been corrected.

2. Also in the Fall 2015 issue, in the Lab Note on dyed and natural green jadeite (pp. 316–317), the images in figure 13 were reversed.

3. In the Fall 2015 Micro-World entry on a rough diamond fragment (p. 325), the weight of the fragment was incorrectly listed as 0.40 ct. The correct weight was 2.02 ct.

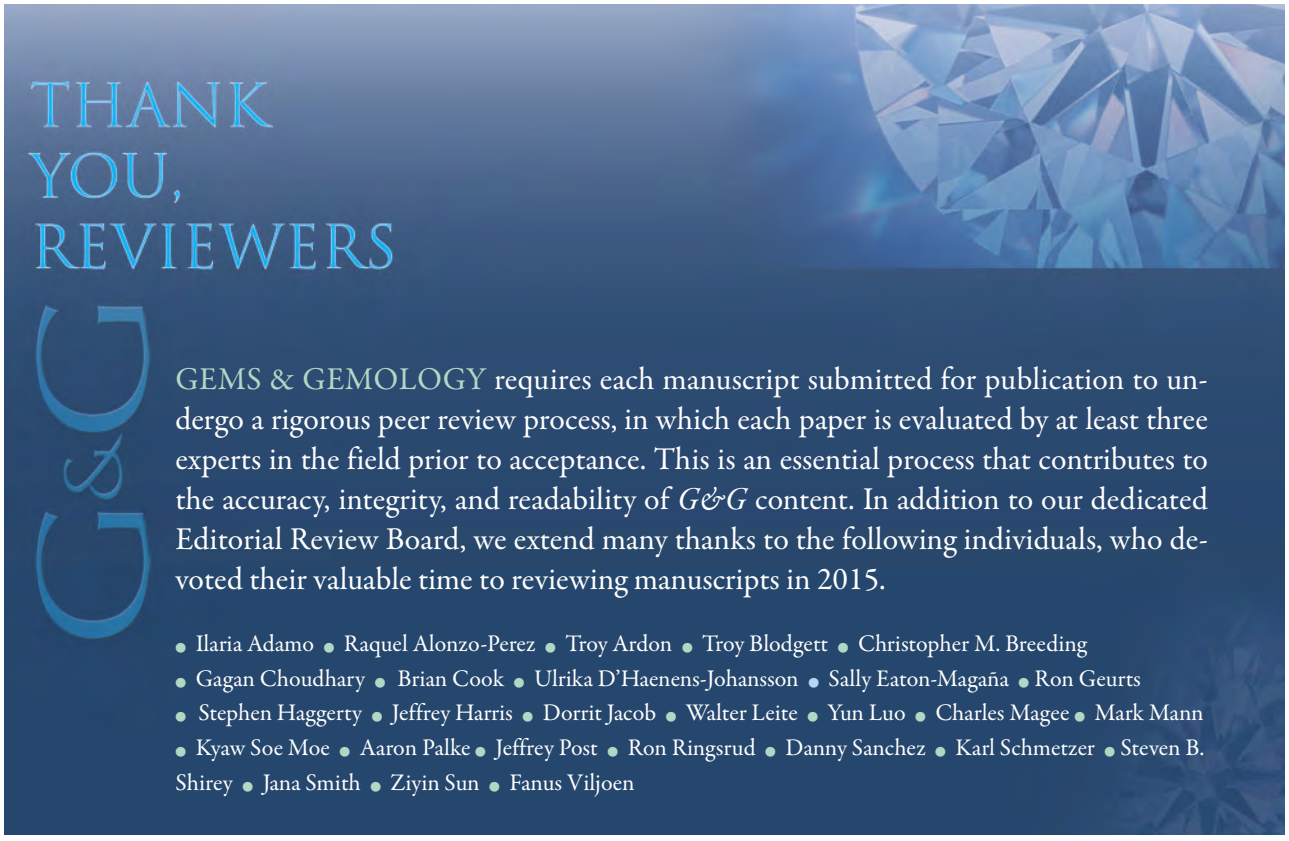

# LETTERS

## TRAPICHE NOMENCLATURE

I wanted to offer hearty congratulations for the Fall 2015 issue. Robert Weldon's cover is stunning, and the lead article on Colombian trapiche emeralds is a thought-provoking, important addition to crystallography and gemology.

I was interested in the authors' trapiche nomenclature discussion in box A (p. 224). I understand the desire to distinguish sectoral zoning formed by inclusions or texture as "trapiche-like"; the trapiche pezzottaite reported in the Micro-World section of that same issue probably falls under that category (Skalwold and Koivula, 2015). I would argue that the cordierite-indialite intergrowths known as "cherry blossom stones," described by the authors as "trapiche-like," actually qualify as true trapiche growth on the basis that each sector is the result of individual crystal growth. These unique trapiches are the result of a very complex indialite-cordierite intergrowth phenomenon in which cordierite crystals grow epitaxially on the six prism faces of an indialite crystal. The latter's remaining faces continue to grow and later alter to cordierite while grains of this intergrowth's host accumulate along the sectors, forming the trapiche appearance. The indialite later alters to cordierite and eventually the entire intergrowth is replaced by muscovite, while retaining the outward appearance of the original mineral intergrowth (see Rakovan et al., 2006; Kitamura and Yamada, 1987).

Also, in Nassau and Jackson's defense, I would add that later in 1970 they corrected the trapiche emerald locality information from their original *American Mineralogist* paper:

> Based on information supplied by E.J. Tripp and L.H. Hernandez and E.J. Tripp (private communications) the actual origin of the trapiche emeralds previously attributed … to the Chivor mine is the Peña [*sic*] Blanca mine, near Muzo, Colombia. These have the clear center and are distinct from specimens from Muzo itself, which have a dark center. Most Peña Blanca trapiche emeralds were purchased and distributed by Mr. W.F. Bronkie, then manager of the Chivor mine, and were accordingly attributed to the Chivor locality (Nassau and Jackson, 1970).

This erratum by the authors themselves is generally overlooked in articles that reference the original study.

Once again, congratulations on a superb paper, which is sure to be a classic reference across geological disciplines.

*Elise A. Skalwold*
*Ithaca, New York*

## REFERENCES


Kitamura M., Yamada H. (1987) Origin of sector trilling in cordierite in Daimonji hornfels, Kyoto, Japan. *Contributions to Mineralogy and Petrology*, Vol. 97, No. 1, pp. 1–6.

Nassau K., Jackson K.A. (1970) Trapiche emeralds from Colombia: Correction. *American Mineralogist*, Vol. 55, No. 10, pp. 1808–1809.

Rakovan J., Kitamura M., Tamada O. (2006) *Sakura ishi* (cherry blossom stones): Mica pseudomorphs of complex cordierite-indialite intergrowths from Kameoka, Kyoto Prefecture, Japan. *Rocks & Minerals*, Vol. 81, No. 4, pp. 284–292.

Skalwold E., Koivula J. (2015) *G&G* Micro-World: Pezzottaite debuts as the newest trapiche gem material. *G&G*, Vol. 51, No. 3, pp. 326–328.


## REPLY

We are glad you appreciated our work. Our judgment on "trapiche pezzottaite" can be based only on your account and not on a direct analysis of the sample. Looking at the accompanying figures, above all figure 7 on p. 327, we think that this pezzottaite sample can be classified as "trapiche-like" because the texture seems related to the zoning (probably sector zoning). There is another sample from Myanmar with similar features (http://www.mindat.org/photo-718381.html); thus, the zoning is likely due to the growth condition in this specific locality. Moreover, there are two other reasons to classify this sample as "trapiche-like": The first is that the inclusions do not form sharp boundaries separating the equivalent sectors. The second is the absence of organic matter observed in all trapiche minerals.

We disagree with your assessment, because in cherry blossom stones the trapiche-like aspect is due to the first formation of indialite, a mineral with the same point group as beryl. As a result, they have the same growth sectors. But the formation mechanism of cherry blossom stones is completely different, and even more complex, than that of trapiche minerals. In fact, the formation of cherry blossom stones requires intergrowth, phase transition, and pseudo-twinning. On the contrary, a trapiche is a single crystal where the growth sectors are separated by inclusions.

Thank you for the complementary information about trapiche emerald origin from Nassau and Jackson. We were not aware of their correction, which is never cited in the literature. At the October 2015 International Emerald Symposium in Bogotá, researchers consistently referred to Chivor trapiche emerald. We are pleased to see that our field investigations in the Chivor-Macanal-Gachala mining districts were in keeping with the correction, and that in fact trapiche emerald is only present in the western emerald zone. Your letter will help to definitively correct this error of location.


*Isabella Pignatelli*
*University of California, Los Angeles*

*Gaston Giuliani*
*Institute of Research for Development, Toulouse, France*
*French National Center of Research, Vandœuvre*